

**A Study on Middle-scale Variations of
Thermospheric Neutral Winds Associated with
Auroral Activity over Syowa Station, Antarctica**

南極昭和基地におけるオーロラ活動に伴う
熱圏中性風の中規模変動に関する研究

Minoru Kubota
久保田 実

Department of Geophysics, Faculty of Science,
Tohoku University

東北大学大学院理学研究科地球物理学専攻

**Thesis Presented for the Degree of Doctor of Science,
Tohoku University**

December, 1996

Acknowledgments

I would like to acknowledge the people who helped and encouraged me throughout this study. I am grateful to Prof. H. Fukunishi for his guidance and encouragement from the beginning to the completion of this study. I am especially indebted to Prof. S. Okano in the National Institute of Polar Research for valuable discussion on development of the Fabry-Perot Doppler Imaging System. I wish to thank Profs. H. Oya, A. Morioka and Dr. T. Ono for their useful comments. I express my deep appreciation to Drs. S. Watanabe, I. Murata and Y. Takahashi for their useful advice. I would also like to acknowledge Mr. Y. Niihara and Mrs. K. Sakanoi for their helpful suggestions in dealing with the FPDIS data, Mr. Y. Yamada and other members of the Laboratory for helpful assistance and encouragement.

Appreciation is extended to Profs. G. Hernandez and R. W. Smith in University of Alaska, Dr. H. Nakajima in the Solar Terrestrial Environment Laboratory, Dr. M. Ishii in the Communication Research Laboratory for their helpful comments and suggestions in the FPDIS data analysis. I would like to express my appreciation to Prof. K. Yokoyama, the leader of the 35-st wintering party of Japanese Antarctica Research Expedition, for his kind suggestions and help, and to all members of the wintering party of JARE35 for their warmhearted encouragement and support during my stay at Syowa station, Antarctica.

I greatly appreciate my parents, Isao and Yoshiko Kubota, for their support and encouragement throughout my study in the graduate school.

Geomagnetic data and all-sky auroral images were provided by the World Data Center-C2 for aurora in NIPR. The TIGCM model results were provided by Prof. R. G. Roble in the National Center of Atmospheric Research. This thesis was edited and printed by a desk-top publishing software \LaTeX . A free graphic software Gp were used for plotting the figures in this thesis.

Abstract

The solar wind energy injected into the high-latitude thermosphere primarily through auroral processes often exceeds the energy due to solar EUV/UV radiation during geomagnetically active periods. Further, auroral activity variation is so quick that thermospheric temperature and wind at high-latitude change rapidly. The observational and theoretical studies of thermospheric response to auroral activity are therefore significantly useful for the understanding of the dynamical processes of the thermosphere.

In order to investigate the response of the thermospheric neutral winds in the high-latitude E- and F-region to auroral activity, we have made an overall improvement of the prototype Fabry-Perot Doppler imaging system (FPDIS) which had been developed by the Tohoku University optical group in 1989. The FPDIS measures the Doppler shifts and widths of aurora and/or airglow emission lines of OI557.7 nm and OI630.0 nm over a wide field of view (165°) to obtain two-dimensional distributions of winds and temperatures in the E- and F-region. The characteristic of the improved FPDIS used in this study is high temporal and spatial resolution in the thermospheric wind measurements. The maximum time resolution is 1 min for the OI557.7 nm emission and 3 min for the OI630.0 nm emission, while the typical spatial resolution is about 50 km for the OI557.7 nm emission and about 100 km for the OI630.0 nm emission.

We installed the improved FPDIS at Syowa station (69.00°S , 39.58°E in geographic coordinates; -66.23° , 71.75° in corrected geomagnetic coordinates; $L=6.15$), Antarctica, and carried out observations of thermospheric neutral winds for 57 nights covering various auroral conditions during one austral winter period in 1994. The important results obtained from these observations are summarized as follows:

- 1) It was found that nighttime variations of the thermospheric neutral winds depend on geomagnetic activity. The magnetic southward winds during geomagnetically active periods were stronger than during quiet periods, and the difference in the wind velocities was

largest around midnight. The difference is supposed to be associated with the auroral energy injection and the relative location between the auroral oval and Syowa station.

2) In the vicinity of auroral arcs, strong outward flows were often observed. These flows seem to be caused by forced convection which is the response to heating or the divergent component of ion drag around auroral arcs. However, the velocity of outward flows were much greater than the prediction of numerical models.

3) Periodic enhancements of meridional winds which are classified into middle-scale atmospheric gravity waves (AGWs) were observed on the night of 3-4 June 1994 during geomagnetically active periods. The period of the variations was 1.3 – 2 hr and 1.2 hr in the F- and E-region, respectively, while the phase velocity of the poleward propagation was ~ 80 m/s and ~ 110 m/s in the F- and E-region, respectively. These middle-scale AGWs appear to be generated in the auroral oval staying at a few hundred kilometers north of Syowa station. This is the first case that the generation and propagation of middle-scale AGWs were clearly observed by an optical method.

4) Strong divergent wind patterns which suggest the existence of strong upward thermospheric winds were observed three times on the same night of 3-4 June 1994. The events appeared on the poleward side of the auroral oval at 0246 UT and 0302 UT seemed to be similar events reported by *Price et al.* [1995]. The event which occurred at 0404 – 0413 UT on 4 June 1994 showed a dramatic enhancement of the divergent wind which has not been reported yet. The upwelling region and the OI630.0 nm auroral emission region overlapped each other, and the strong divergent wind was generated simultaneously with an auroral emission enhancement. Its duration was ~ 15 min, and the horizontal scale of the upwelling region was estimated to be more than 680 km in the F-region.

These observational results demonstrate that the FPDIS is an outstanding tool for remote sensing of rapid variations of the thermospheric neutral winds associated with auroral activity, and make clear the existence of several types of thermospheric responses to auroral activity. Furthermore, it is demonstrated that the upwelling motion observed near the active auroral region is closely related with the AGW generation.

Contents

Acknowledgments	i
Abstract	iii
Contents	v
List of Figures	viii
List of Tables	xv
1 Introduction	1
1.1 The Earth's thermosphere	1
1.2 Modeling and simulation of the thermosphere	3
1.2.1 Thermospheric general circulation models	3
1.2.2 Empirical models	4
1.2.3 Other modeling and simulations	5
1.3 Satellite observations of the thermospheric neutral wind	6
1.4 Ground-based observations of the high-latitude thermospheric neutral wind	8
1.4.1 Upper thermosphere	8
1.4.2 Lower thermosphere	11
1.4.3 Vertical winds	13
1.5 Purpose of this thesis	14
2 Development of the Fabry-Perot Doppler Imaging System	17
2.1 Basic principle of the Fabry-Perot interferometer	17
2.2 Principle of the Fabry-Perot Doppler imaging	19
2.3 Prototype of the Fabry-Perot Doppler Imaging System	24

2.3.1	Optics	24
2.3.2	Correction of the image distortion caused by the photon imaging head	26
2.3.3	Problems in the image integration	27
2.4	New version of the Fabry-Perot Doppler Imaging System	30
2.4.1	Optical system	30
2.4.2	Fabry-Perot etalon	35
2.4.3	Interference filters	35
2.4.4	Two-dimensional photon detecting system	39
2.4.5	Image data processor and recording system	42
2.4.6	Calibration laser	42
3	Observations	45
3.1	Installation of the FPDIS at Syowa station, Antarctica	45
3.2	FPDIS observations at Syowa station	46
4	Procedures of Data Analysis	61
4.1	Determination of etalon parameters and fringe center using a calibration laser	61
4.1.1	Determination of fringe center	61
4.1.2	Conversion of image coordinates	63
4.1.3	Correction of drifting etalon parameters	64
4.2	Derivation of line-of-sight wind velocities from Doppler image data	67
4.3	Error estimation in wind velocity measurement	69
4.3.1	Photon noise	69
4.3.2	Influence of non-uniform auroral emission intensity	72
5	Thermospheric Neutral Winds over Syowa Station Derived from Doppler Imaging Data	79
5.1	F- and E-region wind patterns on quiet and disturbed days	79
5.1.1	F- and E-region wind patterns on quiet days	80
5.1.2	F- and E-region wind patterns on disturbed days	85
5.2	Strong outward flows from the auroral arc region	85
5.3	Periodic enhancements of meridional winds on 3-4 June 1994	95
5.4	Strong divergent winds observed simultaneously with an enhancement of auroral emission	100

6	Discussions	117
6.1	Nighttime variations of thermospheric winds on quiet and disturbed days . . .	117
6.2	Thermospheric neutral winds in the vicinity of auroral arcs	125
6.3	Middle-scale atmospheric gravity waves generated by auroral energy injection	127
6.4	Localized vertical winds associated with auroral activity	131
7	Conclusions	135
	References	137
A	Sequential wind data in the F-region	145
B	Sequential wind data in the E-region	155

List of Figures

1.1	Scheme of thermospheric phenomena and physical processes	2
2.1	Schematic diagram showing the optical path of the Fabry-Perot interferometer. The optical path difference of adjoining rays is given by the relation $m\lambda = 2nd \cos \phi$	18
2.2	Transmittance of a Fabry-Perot etalon as a function of the phase retardation of a beam for various values of the reflectance R . Four profiles from the narrowest to the widest one correspond to the values of R 0.98, 0.81, 0.65 and 0.45, respectively.	20
2.3	Schematic diagram showing the concept of the Fabry-Perot Doppler imaging system.	21
2.4	An example of interference fringes of a Fabry-Perot etalon. These are fringes of a He-Ne laser source with a etalon of 12 mm spacer and a reflectance of 0.88.	23
2.5	System diagram of the prototype of the Fabry-Perot Doppler Imaging System [after <i>Nakajima</i> , 1993]	25
2.6	Diagram of the photon imaging head (PIH) detector [after <i>Nakajima</i> , 1993]	26
2.7	Example of a grid image used for the grid calibration: (a) an image before correction and (b) a corrected image. It is apparent that distortions and nonlinearities of the image are eliminated [after <i>Nakajima</i> , 1995].	28
2.8	Conceptual sketches of the thresholding and integration process: (a) normal photon spots and (b) photon spots which overlap each other because of an overexposure. In both sketches, top, middle and bottom panels show photon spot images, thresholding images and fringe patterns obtained by the integration process, respectively.	29
2.9	System diagram of the further developed Fabry-Perot Doppler Imaging System (FPDIS)	31

2.10	Schematic diagram of the Fabry-Perot Doppler Imaging System (FPDIS). The list of the components (1)-(15) is given in Table 2.2.	33
2.11	View of the servo-stabilized Fabry-Perot etalon and its controller used for the FPDIS. Several connectors which are seen on the side of the etalon container are used for cables connecting the servo-control circuit to keep the parallelism and spacing of the etalon.	36
2.12	Dependence of the reflectivity of the etalon coating on the wavelength of incident light.	37
2.13	Filter transmission functions.	38
2.14	Schematic diagram of the proximity focused photon counting imager (PFPCI).	39
2.15	Radiant sensitivity and quantum efficiency of the photocathode as a function of wavelength. The photocathode used for the PFPCI is sensitive between 250 and 850 nm.	40
2.16	Schematic diagram of the PFPCI cooling unit.	41
2.17	View of a laser head and a power supply unit.	44
3.1	Overall view of the FPDIS installed in the information processing building at Syowa station(The picture was taken by a camera with a fish-eye lens). The optical system is seen in the middle, while the data processing system is seen on the left hand.	47
3.2	(a) The optical system for the FPDIS. A He-Ne laser tube is attached on the left side of the FPDIS, and a monochromatic laser enters into the optical path with an optical fiber which is seen as a blue string on the color picture. A CCD camera and a focusing lens are attached at the bottom of the FPDIS. (b) The instruments for image data processing and data storage of the FPDIS. An image data processor EXCEL and a monitor are seen in the middle, while a personal computer PC-9801 which controls both the EXCEL and a filter selection unit is seen on the right hand.	49
3.3	View of the roof of the information processing building at Syowa station, Antarctica. A lens projecting from the cover of the roof opening is the objective fish-eye lens of the FPDIS.	51
3.4	Conceptual sketch of the configuration of observations with the FPDIS.	55
3.5	Example of OI630.0 nm fringe image obtained by the FPDIS.	57

- 3.6 Time sequence of the FPDIS observation: (a) alternation of OI630.0 nm and OI557.7 nm, (b) only OI630.0 nm, and (c) only OI557.7 nm. These time sequences are repeated during observations. 60
- 4.1 (a) Slicing of the fringe image. Here, X and Y-coordinates denote the horizontal and the vertical direction, respectively. C_{y0} is an initial guess for the center position in Y-coordinate. (b) Example of the sliced image data. The abscissa represents the radius-squared coordinate $((x - C_x)^3/|x - C_x|)$, while the ordinate represents the count number of the image data. 62
- 4.2 Conversion of real-pixel coordinates (R space) on the image plane into radius-squared coordinates (X space). Sliced fringes of a calibration laser image are shown with the abscissa of (a) R space, and (b) X space. 65
- 4.3 Variations of the He-Ne laser fringes over the observation time on 4-5 June, 1994. Laser fringe images are obtained every one hour. The ordinate represents the X-position of the image. The scale for the inner fringe is indicated on the left hand, while the scale for the outer fringe is indicated on the right hand. Symbols '*' and '◇' stand for the radii of inner and outer fringes, respectively. The lower panel shows a variation of room temperature for the same time interval. 66
- 4.4 Partition of the fringes. Symbol '●' indicates the locations where Doppler wind velocities are derived. 68
- 4.5 Calculated standard deviation (SD) versus maximum counts at fringe peaks. The SD of wind velocities is given for inner (solid lines) and outer (broken lines) fringes of the OI630.0 nm emission. The temperatures assumed in this simulation are 500, 1000, 1500, and 2000 K. 71
- 4.6 Source emission intensity profiles used for investigating the influence of the non-uniformity of auroral emission intensity. Five kinds of source emission patterns corresponding to $\beta = 0, 1, 2, 4,$ and 8 were prepared in this simulation. 73
- 4.7 Examples of source emission intensity profiles and calculated fringe profiles for (a) a uniform emission source and (b) a non-uniform emission source. The OI630.0 nm emission with a kinetic temperature of 1000 K is assumed as the emission source. 74

4.8	Fringe profiles for a uniform source (solid line) and a non-uniform source (broken line). The OI630.0 nm emission with a kinetic temperature of 1000 K is assumed as the emission source.	75
4.9	Error dv in the wind velocity estimation. (a) Errors calculated for the OI630.0 nm emission with temperatures of 500, 1000, 1500, and 2000 K. (b) Errors are calculated for the OI557.7 nm emission with temperatures of 100, 200, 300, and 500 K.	77
5.1	Geometry for deriving the averaged meridional and zonal wind velocities from the OI630.0 nm fringe image data. The average values of horizontal wind velocities at the positions indicated by symbols of 'o' or 'o' are adopted as the averaged meridional or zonal wind velocities, respectively. Note that geomagnetic coordinates are rotated by 42 degrees against geographical coordinates at Syowa station.	81
5.2	Geometry for deriving the averaged meridional and zonal wind from the OI557.7 nm fringe image. The average values of horizontal wind velocities at the positions indicated by symbols of 'o' or 'o' are adopted as the averaged meridional or zonal wind velocities, respectively. The wind velocities in the magnetic southern sector of the OI557.7 nm fringe, which are represented with the symbol '*', are excluded from the averaging, because these data have a deviation caused by an instrumental problem.	82
5.3	Variations of meridional (solid lines) and zonal (broken lines) winds derived from Doppler imaging data of OI630.0 nm emission. Wind velocity data on the 4 nights from 10 July 1994 to 13 July 1994 are displayed together. The values of Kp during this period ranged from 0 to 2 ₋ , while the values of F10.7 solar flux ranged from 84.1 to 88.9.	83
5.4	Variations of meridional (solid lines) and zonal (broken lines) winds derived from Doppler imaging data of OI557.7 nm emission in the period of 10-13 July 1994.	84
5.5	Variations of meridional (solid lines) and zonal (broken lines) winds derived from Doppler imaging data of OI630.0 nm emission. Wind velocity data on the 4 nights from 1 June 1994 to 4 June 1994 are displayed together. The values of Kp during this period ranged from 3 ₋ to 5, while the values of F10.7 solar flux ranged from 69.5 to 70.3.	86

5.6	Variations of meridional (solid lines) and zonal (broken lines) winds derived from Doppler imaging data of OI557.7 nm emission in the period of 1-4 June 1994.	87
5.7	Line-of-sight neutral wind velocities and all-sky images observed at Syowa station in the nighttime from 2357 UT to 0029 UT on July 10-11, 1994. Upper panels, LOS wind velocities superposed on OI630.0 nm fringes; middle panels, LOS wind velocities superposed on OI557.7 nm fringes; lower panels, all-sky images obtained simultaneously by the SIT camera.	89
5.8	Line-of-sight neutral wind velocities and all-sky images observed at Syowa station in the nighttime from 0031 UT to 0102 UT on July 10-11, 1994. The format is the same as Figure 5.7.	91
5.9	Line-of-sight neutral wind velocities and all-sky images observed at Syowa station in the nighttime from 0104 UT to 0134 UT on July 10-11, 1994. The format is the same as Figure 5.7.	93
5.10	Location of four points at which wind velocities and aurora emission intensities are investigated.	95
5.11	Variations of LOS wind velocities at four locations on the inner and outer fringes illustrated in Figure 5.10, for the OI630.0 nm emission in the nighttime on 10-11 July 1994.	96
5.12	Same as Figure 5.11 except for the OI557.7 emission.	97
5.13	Variations of the OI630.0 nm emission intensities at four locations on the inner and outer fringes illustrated in Figure 5.10, for the night of 10-11 July 1994.	98
5.14	Same as Figure 5.13 except for the OI557.7 nm emission intensities.	99
5.15	Same as Figure 5.11 except for the night of 3-4 June 1994.	101
5.16	Same as Figure 5.12 except for the night of 3-4 June 1994.	102
5.17	Same as Figure 5.13 except for the night of 3-4 June 1994.	103
5.18	Same as Figure 5.14 except for the night of 3-4 June 1994.	104
5.19	All-sky images between 2250 UT and 0440 UT on the night of 3-4 June 1994, observed by the SIT camera at Syowa station.	105
5.20	Same as Figure 5.7 except for the time interval from 0238 UT to 0305 UT on 3-4 June 1994.	107
5.21	Same as Figure 5.20 except for the time interval from 0306 UT to 0331 UT.	109
5.22	Same as Figure 5.20 except for the time interval from 0333 UT to 0400 UT.	111

5.23	Same as Figure 5.20 except for the time interval from 0401 UT to 0426 UT.	113
6.1	Diurnal variation of the meridional neutral wind in the altitude range of 97 – 500 km above Syowa station calculated by the TIGCM.	118
6.2	Diurnal variation of the zonal neutral wind in the altitude range of 97 – 500 km above Syowa station calculated by the TIGCM.	119
6.3	Comparison between the meridional and zonal winds in the F-region calculated by the TIGCM model (thick lines) and the observed wind variations given in Figure 5.3.	120
6.4	Comparison between the meridional and zonal winds in the E-region calculated by the TIGCM model (thick lines) and the observed wind variations given in Figure 5.4.	121
6.5	Variations of magnetic north-south (solid lines) and east-west (broken lines) winds derived from the FPDIS OI630.0 nm emission data. Wind velocities on the 4 nights of 10-13 July 1994 are displayed together. The values of Kp ranged from 0 to 2 ₋ , and the value of F10.7 solar flux ranged from 84.1 to 88.9 during this period.	123
6.6	Same as Figure 6.5 except for the 4 nights of 1-4 June 1994 with Kp values of 3 ₋ to 5 and F10.7 solar flux of 69.5 to 70.3.	124
6.7	Schematic representation of meridional circulation forced by (a) the ion drag momentum force and (b) the heat source. The broad open arrows denote axes of maxima in the north-south ion drag force. The shaded area represents a strongly heated region [<i>Walterscheid et al.</i> , 1985].	126
6.8	Variations of LOS wind velocities observed at Syowa station on the night of 12-13 June 1994. The format is the same as Figure 5.15.	128
6.9	All-sky images observed in the nighttime of 12-13 June 1994 using the SIT camera at Syowa station.	129
6.10	Schematic model showing the location of the aurora oval and the events observed on the night of 3-4 June 1994. Symbols '⊗' indicate the location of Syowa station.	133
6.11	Triaxial magnetometer data at Syowa station on the night of 3-4 June 1994.	134

List of Tables

2.1	Summary of the instrumental parameters for the new version of the Fabry-Perot Doppler Imaging System (FPDIS)	32
2.2	List of the optical components used for the FPDIS.	34
3.1	Summary of Fabry-Perot Doppler Imaging observations at Syowa station, Antarctica from March to September, 1994. The symbol 'o' in the column of condition indicates that full observation was made, while the symbol 'Δ' indicates that observation was made partially. The notation $\sum K_p$ Pre/Next represents the summation of K_p values on the day of observation start and the next day.	53

Chapter 1

Introduction

1.1 The Earth's thermosphere

The Earth's thermosphere is defined as the high temperature region extending from the mesopause located at an altitude of 80-90 km to the thermopause located at an altitude of 300-500 km. The temperature increases rapidly with height in the lower thermosphere, and becomes asymptotic to a value of the order of 1000 K in the upper thermosphere. The fundamental structure of the thermosphere is determined by a balance of heating and cooling. The thermosphere is characterized by a coexistence of neutral gases and ionized gases and thus the dynamics of this region is governed by a combination of physical and chemical processes of the neutral gases and electrodynamical processes of the ionized gases. These interactive processes were reviewed by *Hunsucker* [1982], *Foster and St.-Maurice* [1983], *Rees et al.* [1983], *Killeen* [1987], *Crowley* [1991], *Solomon* [1991], and *Titheridge* [1995].

Figure 1.1 shows a scheme of thermospheric phenomena and physical processes. Of various thermospheric heat sources, solar extreme ultraviolet (EUV) and ultraviolet (UV) radiation is the most important source in a globally-averaged sense, and it is primarily responsible for maintaining high thermospheric temperature and for producing a pressure-gradient force that drives a fundamental day-to-night thermospheric circulation. Heating due to absorption of solar EUV flux, particularly heating due to absorption of solar radiation in the Schumann-Runge continuum region (~ 130 to 175 nm), is a dominant energy source in the middle and upper thermosphere above ~ 150 km [*Killeen*, 1987]. The thermospheric heating efficiency of solar ultraviolet photons for varying seasonal and solar cyclical conditions was calculated by *Torr et al.* [1980a, b] from the data of the Atmosphere Explorer (AE) satellites. The solar heating rate was estimated from the heating efficiency, and it was used in the thermospheric general circulation models (TGCMs) and other thermospheric

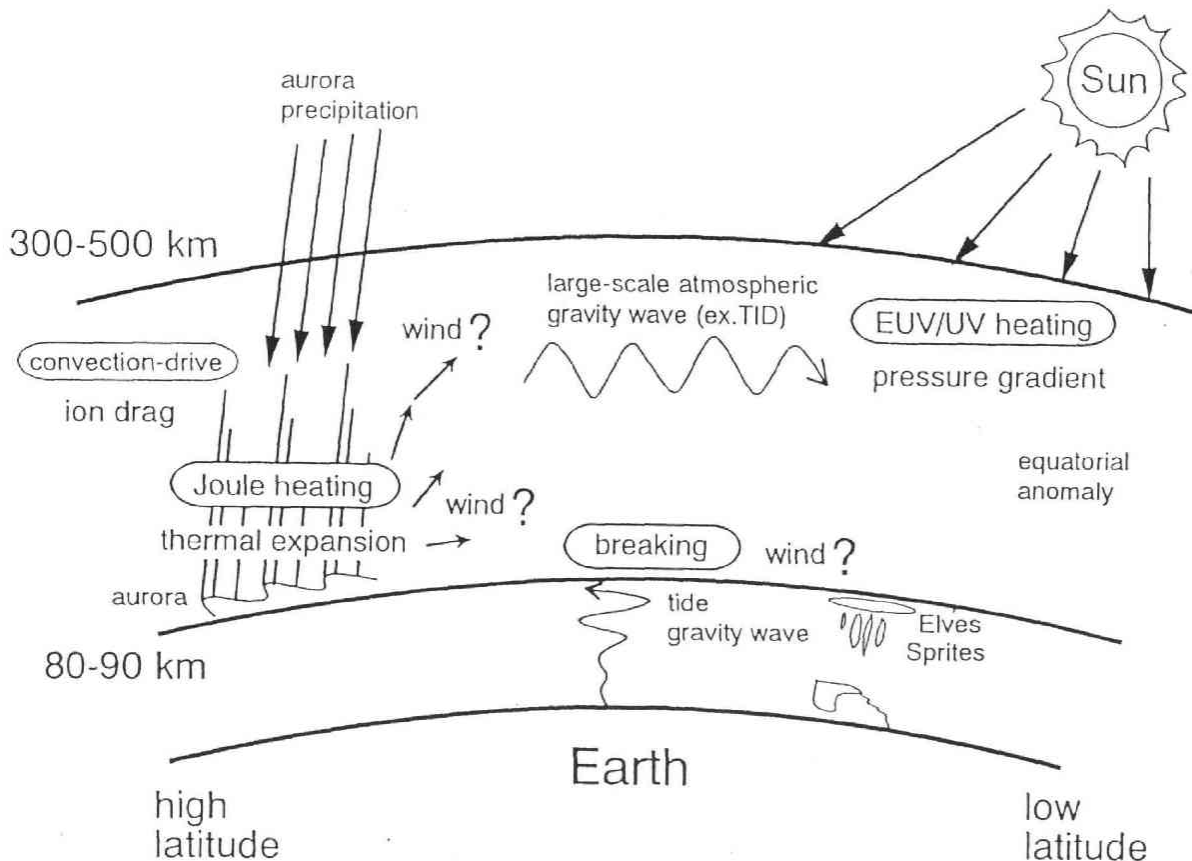


Figure 1.1. Scheme of thermospheric phenomena and physical processes

models. It is well known that thermospheric densities and temperatures vary with solar activity and that such variations follow those of solar decimetric (F10.7) flux. This radio flux, which has been catalogued continuously over many years, does not act directly on the upper atmosphere itself, but correlates with the experimental data sets of thermospheric temperatures [Hernandez, 1983].

The second important energy sources for the thermosphere is solar wind energy injected primarily through auroral processes. Auroral energy often exceeds the energy due to solar EUV/UV radiation during geomagnetic storms or substorms. Further, auroral activity changes so quickly that thermospheric temperature and wind at high-latitude change momentarily. Consequently a study of thermospheric response to auroral activity is essential for the investigation of dynamical processes of the thermosphere. The auroral energy heats the thermosphere through Joule heating and the collisional slowing-down process of energetic particles precipitating from the magnetosphere. The rate of Joule and particle heating can be estimated from ionospheric parameters. Foster *et al.* [1983] calculated the Joule heating

rate at high latitude using the electric field intensity and the Pederson conductivity which were derived from simultaneous measurements of ion drift velocity and precipitating charged particle flux by the AE-C satellite. Their result indicated that high-latitude Joule heating occurs in a roughly-oval pattern consisting of three distinct heating regions: the dayside cleft, the region of sunward ion convection at dawn and dusk, and the midnight sector. The total global thermospheric heating due to particle precipitation was estimated to be lower than Joule heating from recent satellite measurements of precipitating particle fluxes [Evans, 1986; Fuller-Rowell and Evans, 1986].

Another important energy source for the thermosphere is wave energy coming from the middle and lower atmosphere. The energy transport processes due to such waves have been studied by Garcia and Solomon [1985], Fritts *et al.* [1996] and many other researchers. The effect of such waves on the global thermospheric heat budget, however, has not been parameterized yet.

1.2 Modeling and simulation of the thermosphere

1.2.1 Thermospheric general circulation models

In recent years various kinds of numerical models have been developed to study the global thermospheric circulation, energetics, composition structure and their response to solar and auroral activities. The developed thermospheric general circulation models (TGCMs) have been used to simulate the various patterns of the thermospheric winds and temperatures, e.g., the solar-driven thermospheric circulations in equinox and solstice conditions, the response of the thermosphere to auroral particle precipitation and substorm energy input, and the mean high-latitude thermospheric circulation. Furthermore, in order to investigate the dynamical features of the thermosphere, comparative studies of model calculations and a large number of satellite observations have been made.

Killeen *et al.* [1986] obtained the mean global-scale circulation in the northern hemisphere F region by collecting and averaging all available data from the DE-2 satellite and the network of ground-based Fabry-Perot interferometers. The mean circulation patterns were compared with the predictions of the National Center of Atmospheric Research (NCAR) TGCM. From this study they concluded that (1) instrumentation deployed around the globe and on satellites can provide powerful, composite data sets that can be used to monitor the mean dynamical state of the earth's thermosphere and that (2) the mean thermospheric (F

region) neutral circulation for given geophysical situations (solar maximum, near solstice) can be modeled reasonably using a three-dimensional, time-dependent model with appropriate parameterizations for the energy and momentum inputs. *Killeen et al.* [1988] extended the NCAR TGCM to accommodate a time-dependent prescription of auroral particle precipitation and magnetospheric convection.

The thermospheric neutral winds driven by motion of convecting plasma in turn produce a dynamo effect. It was noted by *Banks* [1972] that these winds can generate an electric field that drives plasma motion, even if magnetospheric electric field is cut off. This phenomenon is called the 'flywheel' effect. *Deng et al.* [1991] investigated the flywheel currents by simulating a storm which occurred on 23 November 1982 using the NCAR TIGCM. The resulting height-integrated Hall currents at high-latitude were dominated by the neutral wind-driven component for several hours after the end of the storm main phase. The direction of these currents was reversed from normal. Furthermore, *Deng et al.* [1993] extended the previous work to include a comparison between the calculated time-dependent ionospheric Hall current system and the field-aligned currents measured by DE-2 satellite in the storm-time recovery period. As a result, DE-2 measurements demonstrated 'local' (satellite-altitude) flywheel effects. *Richmond* [1995] examined the flywheel effect by the NCAR thermosphere-ionosphere-electrodynamics general circulation model (TIE-GCM) which was an extension of the NCAR TIGCM. It was found that, after a field-aligned current between the ionosphere and the outer magnetosphere has been cut off, ion drifts become similar to high-latitude neutral winds at altitude of 145 km, with a total potential drop of 7.5kV, or 25% of originally imposed one.

1.2.2 Empirical models

The MSIS (mass spectrometer incoherent scatter) model has gone through several revisions. The MSIS-83 model [*Hiden*, 1983] was based on data from seven satellites, numerous rocket probes, and five ground-based incoherent scatter (IS) radars. The MSIS-86 model [*Hiden*, 1987] combined these earlier measurements with the DE-2 data and is capable of providing temperature and densities of N, N₂, O₂, O, He, Ar, and H as functions of exospheric temperature, local time, latitude, longitude, universal time, F10.7, and A_p. The MSIS-86 model has been adopted as the new CIRA empirical model [*Hiden et al.*, 1988], which is available in a computer compatible form for the first time.

Analogous to the MSIS model, the empirical horizontal wind model (HWM90) is based on thermospheric wind data from DE-2, Atmosphere Explorer (AE), ground based incoherent scatter radars, and Fabry-Perot interferometers [Hiden *et al.*, 1988, 1991]. The model uses a limited set of vector spherical harmonics and has a low-altitude limit of 100 km. The dependence on solar and magnetic activities is included in the HWM90 model. The HWM90 has been revised to include the mesosphere and lower atmosphere and to provide a single analytic model for calculating zonal and meridional wind profiles [Hiden *et al.*, 1996]. Since these empirical models run on small computers, various observational data can be compared with them [Smith *et al.*, 1994; Wu *et al.*, 1994; Fagundes *et al.*, 1996].

The vector spherical harmonic (VSH) model [Killeen *et al.*, 1987] involves a spectral compilation of calculations from the NCAR TIGCM. It provides a computational, efficient rendition of TIGCM results through use of a series of (truncated) coefficients to select functions which collectively describe the temporal and spatial dependence of various atmospheric parameters. The VSH model also incorporates empirical neutral wind data from DE-2, suitably merged with theoretical model predictions. The lower boundary of the model is set at 110 km. The model can provide neutral wind, temperature, and densities of several neutral and ionic constituents as functions of magnetic and solar activity levels.

1.2.3 Other modeling and simulations

Walterscheid *et al.* [1985] simulated the neutral gas response to changes in the energy source associated with an appearance of a symmetric stable aurora arc using a sophisticated two-dimensional numerical model. The main results of their study are as follows: (1) a zonal ion drag force drives strong counterstreaming zonal winds on either side of the arc; (2) the nonhydrostatic interplay of buoyancy and vertical pressure gradient forces sets up a large-scale buoyancylike oscillation. Walterscheid and Lyons [1992] performed new simulations about a stable aurora arc, and investigated the effect of cross-arc winds generated by solar, particle, and Joule heating and ion drag occurring over the whole polar region.

Brinkman *et al.* [1995] compared E region neutral winds observed by the Atmospheric Response in Aurora (ARIA 1) rocket with winds predicted by a high-resolution nonhydrostatic dynamical thermosphere model. The ARIA 1 rocket was launched into postmidnight diffuse aurora during the recovery phase of a substorm. Model inputs included electron densities derived from ground-based airglow measurements, precipitating electron fluxes and electron densities measured on the rocket, electric fields derived from the magnetometer and

satellite ion drift measurements, and large-scale background winds derived from a thermospheric general circulation model [Walterscheid and Lyons, 1989]. Their model predicted a strong jet of eastward wind at the E-region height, and showed modest agreement with the observed winds.

Fujiwara et al. [1996] performed a numerical simulation of the thermospheric response to magnetospheric substorm energy injection using a zonal averaged, time-dependent model of neutral composition, dynamics, and energy budget. In their simulation with an energy injection of 1 hour, large-scale atmospheric gravity waves (AGWs) generated by substorm energy via Joule heating of ionospheric currents were clearly identified in the wind field in a meridional plane as well as in the temporal and spacial variations of the total energy density of atmosphere above about 130 km height. It was suggested that short-duration energy injection preferentially generates AGWs which dominate energy oscillations at low latitudes through adiabatic heating and cooling.

1.3 Satellite observations of the thermospheric neutral wind

Killeen and Roble [1988] reviewed the synopsis of the progress made during the first 5 years of the NASA's Dynamics Explorer (DE) dual-spacecraft mission. The mission plan was designed involving two companion spacecraft in coplanar orbits: a high-altitude spacecraft (DE-1) instrumented to probe the Earth's inner magnetosphere and plasmasphere and a low-altitude spacecraft (DE-2) instrumented to probe the ionosphere and neutral upper atmosphere simultaneously with the DE-1 measurements. DE-2 has two instruments for thermospheric wind measurements. They are a Fabry-Perot interferometer (FPI) and a wind and temperature spectrometer (WATS). Remote sensing measurements of the meridional thermospheric winds using FPI have been combined with in situ measurements of the zonal component using WATS. The two data sets, with appropriate phasing and averaging, determined the vector wind along the track of the polar orbiting spacecraft [Killeen et al., 1982]. The DE-2 satellite has made a significant contribution to our overall understanding of the thermospheric dynamics at high-latitude and its response to various magnetospheric and ionospheric disturbances. *McCormac et al.* [1987] used several hundred orbits of DE-2 over six-month period to investigate quantitatively the dependence of the high-latitude

thermospheric circulation on geomagnetic activity, and showed average neutral wind patterns for active and quiet geomagnetic conditions in both hemispheres. In all four cases, the mean neutral circulation showed the imprint of momentum transferred from the two-cell ionospheric convection pattern. The magnitudes of the neutral winds for the high K_p case were generally greater than those for the low K_p case, as would be expected from the stronger auroral forcing.

Killeen et al. [1988] superposed vector neutral wind measurements from DE-2 and auroral images from DE-1, and unambiguously demonstrated a relationship between reversals in the F-region neutral wind and the location of the auroral oval. The simultaneous data sets indicated that the neutral wind reversals follow the substorm dependent expansion and contraction of the auroral oval, consistent with the measured variation of the Kp-dependent width of the antisunward neutral wind region obtained by *McCormac et al.* [1987].

Thayer and Killeen [1993] derived global semiempirical neutral wind fields representing quiet and active geomagnetic conditions using the averaged DE-2 measurements and the modeled winds from the NCAR thermosphere-ionosphere general circulation model (TIGCM), and performed a detailed 'kinetic analysis'. From this investigation, the following conclusions were obtained. (1) The nondivergent component of the high-latitude thermospheric neutral wind, which is primarily driven by ion-drag and Coriolis forces, makes up a large percentage of the total wind field for both quiet and active geomagnetic conditions. (2) The irrotational component of the high-latitude thermospheric neutral wind, which is mostly driven by the pressure-gradient-, Coriolis- and Pederson-drag (nonconvective-ion drag) forces, is representative of the solar-driven component of the neutral winds at F-region altitudes, directed primarily along the 14-02 MLT plane. *Thayer et al.* [1987] investigated the interplanetary magnetic field (IMF) B_y dependence of the neutral circulation for both southern (summer) and northern (winter) hemispheres, using the average neutral wind measurements from the same data base as the *McCormac et al.* [1987] study. They found significant differences in the mean thermospheric circulation pattern for B_y positive and negative.

The Upper Atmosphere Research Satellite (UARS) is a NASA program aimed at improving our knowledge of the physical and chemical processes controlling the stratosphere, mesosphere, and lower thermosphere, emphasizing those levels that are known to be particularly susceptible to change by human activities. Measurements include vertical profiles of temperature, many trace gases, and horizontal wind velocities, as well as solar energy inputs. Many

of the limb-scanning instruments can measure to as high as 80° latitude, providing near-global coverage [Reber *et al.*, 1993]. The UARS has two instruments for thermospheric wind measurements. They are a high resolution Doppler imager (HRDI) and a wind imaging interferometer (WINDII). The HRDI is a triple-etalon Fabry-Perot interferometer/-photometer which measures the horizontal wind and atmospheric temperature from the Doppler shift of the O_2 atmospheric band ($b^1\Sigma_g^+ - X^3\Sigma_g^-$) absorption and emission features, respectively. Morton *et al.* [1993] and Burrage *et al.* [1994] presented preliminary results of a study of mesospheric and lower thermospheric diurnal tidal winds obtained with the HRDI on the UARS. The obtained maximum amplitude of meridional wind is approximately 75 m/s. The observed vertical wavelength is about 20 km, with amplitudes increasing linearly with height. The WINDII takes advantage of airglow emission lines photochemically produced from species in the upper mesosphere (OH), the lower thermosphere (O_2 , $O(^1S)$) and the middle thermosphere ($O(^1S)$, $O(^1D)$ and $O(^2P)$) for the measurement of winds and temperatures in the altitude range 80 to 300 km. The instrument consists essentially of a charge coupled device (CCD) camera viewing the Earth's limb through a field-widened Michelson interferometer. Shepherd *et al.* [1995] presented a review of the Doppler imaging concept, its implementation in the WINDII and the current status of validation and data processing. McLandress *et al.* [1996] analyzed thermospheric winds measured by the WINDII for migrating solar tides, and reported some interesting features of thermospheric tides.

1.4 Ground-based observations of the high-latitude thermospheric neutral wind

1.4.1 Upper thermosphere

Fabry-Perot interferometers have been used for many years to measure winds and temperatures in the upper thermosphere from line-of-sight Doppler shifts of the $OI630.0$ nm emission line, for example Armstrong [1969], Hays and Roble [1971], Hernandez and Roble [1976], Sipler and Biondi [1979], Jacka *et al.* [1979], Hays *et al.* [1979], Burnside *et al.* [1981] and others. A classical Fabry-Perot interferometer has a photomultiplier at the center of a pinhole in the image plane of interference fringes by a Fabry-Perot etalon. Scanning of the etalon by changing the pressure within the etalon cavity or by a physical change of the etalon's plate separation has widely been used as a mean of producing an emission line spectrum.

Okano and Kim [1987] observed the thermospheric response to stable aurora red arcs (SAR-arcs) from two ground stations in New York state. They reported that both the thermospheric temperatures and equatorward wind velocities showed sharp increases approximately 1 hour after the onset of an isolated magnetic substorm, as a definite signature of the thermospheric response to auroral heating associated with an isolated magnetic substorm. *Murty and Kim* [1987] observed the meridional winds blowing away from the main heating region of the SAR-arcs. *Steen et al.* [1988] showed a decrease of the meridional neutral winds, using wind data from a Fabry-Perot interferometer and an incoherent scatter radar, global auroral images from the Viking satellite, and data from other ground-based measurement. They concluded that this phenomenon appears to be associated with intense Joule/frictional heating caused by enhanced ionospheric electric fields.

Meriwether et al. [1988] presented ground-based measurements of neutral winds from the central polar cap at Thule in the solar minimum condition for the first time. Winds in the geomagnetic polar cap had a fundamentally diurnal antisunward character, in accord with model predictions, with a typical speeds of ~ 200 m/s. A large degree of variability in both the magnitude and direction of winds was observed, including evidence for curvature in the neutral flow within the ~ 400 km diameter field of view. They concluded that even at solar minimum, the forcing by the polar cap convection pattern remains strong enough to significantly influence the geometry of the polar cap neutral wind field. The characteristic wind signatures are well correlated with positive and negative changes in the IMF B_y component. If B_y is positive, a jet is seen in the morning sector. Conversely, if B_y is negative, the jet appears in the evening sector. The formation of the 'jet' explains why the magnitude of the wind in the central polar cap is sometimes small in geomagnetically active conditions. *Sica et al.* [1989] found a significant IMF B_y -dependence in their Fabry-Perot data from the auroral zone station College, Alaska. The temperatures become higher and winds exhibit stronger sunward zonal flow in the evening (morning) sector for B_y negative (positive) condition. Furthermore, the night time zonal wind changed from westward to eastward earlier for B_y positive than for B_y negative, consistent with the Harang discontinuity shifting to earlier magnetic local times in the northern hemisphere as B_y becomes more positive. The wind averages for B_y negative and positive were compared with NCAR TGCM predictions that use a B_y -dependent model of ionospheric convection.

Hernandez et al. [1990] reported the result of the first ground-based measurements of F-region neutral atmosphere dynamics at the South Pole showing a rich variety of dynamic

phenomena and strong couplings with the ionospheric plasma. The data obtained on two days, in geomagnetic quiet-to-moderate and disturbed conditions were compared with the average pattern obtained at a similar geomagnetic latitude and similar conditions but in the northern hemisphere (Longyearbyen, Spitsbergen), and also with the NCAR TIGCM predictions for the average dynamics at the South Pole. The measured winds at the South Pole had a stronger prevailing westward component in its diurnal cycle than those observed at Longyearbyen or predicted by the TIGCM. *Smith et al.* [1994] observed neutral upper thermosphere winds and temperatures at the South Pole, Antarctica (90°S , 75° invariant latitude (INV)), and Mt Jone, New Zealand (44°S , 171°E , 52° INV) during a substorm period. Winds peaking at about 800 m/s and typical temperatures reaching up to 2000 K were found at the South Pole, while peak winds above Mount Jone reached 300 m/s in response to the strong high-latitude forcing which spread toward midlatitudes. These observational results were compared with predictions by the MSIS 86 model and the vector spherical harmonic (VSH) model. Then, it was suggested that the sign of the IMF B_y component is an important factor which determines how momentum is coupled between high and middle latitudes during substorms. *Crickmore* [1995] calculated the force acting on the high-latitude thermosphere at specific times during two nights with different geomagnetic activities, using data from a Fabry-Perot interferometer and a Dynasonde at Halley (75.5°S , 26.6°W , $L \sim 4.2$), Antarctica. He found that even on a geomagnetically active day, the ion drag force may not be largest, and that advection, pressure and Coriolis forces may all be larger than the ion drag term.

Recently, some significant improvements for the etendue of the Fabry-Perot interferometer have been made by using imaging photon detectors to record the entire Fabry-Perot fringe in the image plane. *Rees and Greenaway* [1983] discussed alternative means of obtaining a higher etendue from an etalon, and described the concept of a Doppler imaging system (DIS) which would have a multiplex advantage of at least 100 times that of the classical interferometer. The DIS is also capable of deducing a two-dimensional velocity field of a suitable line-emitting areal source by independently measuring the Doppler shift at a large number of points within the field of view. *Rees et al.* [1984] presented the results of initial observations of the auroral thermosphere at Kiruna, using a prototype DIS which has an 80° field of view. *Batten et al.* [1988] and *Batten and Rees* [1990] presented new data from the upgraded UCL-DIS, which has been developed specifically for the detection of small-scale thermospheric wind velocity structures with correspondingly short time scales. The data

confirmed that the thermosphere is very dynamic, with a high degree of variability even on small spatial (50 km) and temporal (10 min) scales. Typical eddy scale sizes of 100-300 km were observed near midnight.

The Tohoku University Fabry-Perot Doppler imaging system (FPDIS) has been developed for observations of two-dimensional distributions of thermospheric wind velocities and temperatures. The FPDIS measures the Doppler shift and width of aurora emission lines of atomic oxygen OI557.7 nm and OI630.0 nm over a 165° field of view [Nakajima *et al.*, 1995]. This system was applied to observations of thermospheric wind velocities and temperatures at Syowa Station (69.00°S, 39.58°E, 66° INV), Antarctica for the period of one auroral winter in 1990, and detected large variations in the neutral thermospheric temperatures and wind velocities associated with an auroral break up event. Conde and Smith [1995, 1996] described a new all-sky imaging spectrometer using a separation scanned Fabry-Perot etalon. In this instrument the etalon plate spacing is scanned periodically over one order of interference and each photon detected is assigned to a wavelength interval which is determined from both its arrival location on the detector and the etalon plate spacing prevailing at the detection time. Spectra recorded by this instrument are not distorted by spatial and temporal brightness fluctuation in the aurora.

In addition to the optical observations, there have been a number of thermosphere dynamics observations using high frequency coherent scatter radars (HF radars). The backscattered power, Doppler velocity, and spectral width are computed from the data obtained by HF radars. There have also been many papers on medium-scale acoustic gravity waves observed with HF radars [Samson *et al.*, 1989, 1990; Bristow *et al.*, 1996; Greenwald *et al.*, 1996]. Bristow *et al.* [1996] examined the seasonal dependence of medium-scale atmospheric gravity waves in the super Dual Auroral Radar Network (SuperDARN) HF radar data and through analysis of the gravity wave dispersion relation. Greenwald *et al.* [1996] found a mesoscale convection vortex in the high-latitude postnoon ionosphere, and investigated the features of this phenomenon.

1.4.2 Lower thermosphere

In recent years it has been realized that the motion of the high-latitude E-region neutral atmosphere plays an important role in the electrodynamic interaction between the magnetosphere and the upper atmosphere. Since the neutral gas density at E-region height is usually

very large compared to the density of the ionized gas, it is commonly believed that the ionized gas will be dragged along due to collisional interaction with the neutral gas. In periods of long and steady electric fields the motion of the ionized gas enforced by these electric fields may start to drag the neutrals through collisional interactions. Furthermore, since the neutral gas is always blowing due to the pressure gradients set up by the nonsymmetric global heat input together with the tidal forces in these heights, it will, in general, carry the ions along to form a dynamo in the upper atmosphere. In order to understand the heat exchange in the upper atmosphere due to interactions between magnetospheric plasma and ionospheric plasma, it is essential to know the behavior of the neutral gas in detail.

The Fabry-Perot interferometer (FPI) is capable of measuring directly the line-of-sight component of the neutral wind, but it is not possible to measure three-dimensional wind vectors and moreover the FPI has some ambiguity in the altitudinal resolution since the specific line of an emission inevitably has some finite width in altitude. On the other hand, the IS radar observation allows us to determine the three-dimensional wind vectors with a high (a few km) altitude resolution, but we need some assumption to derive the neutral wind from IS radar data. This assumption may cause significant errors occasionally. Thus, simultaneous observations with FPIs and IS radars are necessary to investigate the characteristics of the neutral winds.

The incoherent scatter radar can measure several characteristics of the plasma in the E-region, from which the neutral wind velocity can be derived. Using the incoherent scatter radar at Chatanika (65°N), Alaska, which was operated from 1971 to 1982, a variety of experiments were performed in order to study the auroral E-region neutral winds [Brekke *et al.*, 1973]. The height resolution of their observations, however, was of the order of 50 km, therefore the E-region wind data obtained by the Chatanika radar included some influence of the F-region neutral winds. In recent years, improved height resolution wind observations were performed using the European incoherent scatter radar (EISCAT). Brekke *et al.* [1994] analyzed quiet time auroral E-region neutral wind data obtained by EISCAT, in order to establish the background mean neutral velocities as well as tidal influences on the wind. Nozawa and Brekke [1995] analyzed auroral E-region neutral wind data obtained by EISCAT on disturbed and quiet days, and examined the differences in the E fields between these days.

Quasi-steady winds may be present in the polar region by the existence of long-period planetary waves and the polar vortex, in addition to the direct circulation forced by UV

and EUV solar radiation absorption in the mesosphere and lower thermosphere. The coordinated measurements of the upper mesosphere winds and temperatures field at South Pole (90°S) and Scott Base (78°S, 165°E) have shown the presence of a 10.1-hour period wave motion ascribable to a Lamb wave of zonal wavenumber one. Since the Scott Base data also showed the existence of a semi-diurnal oscillation with a vertical wavelength of nearly 40 km, appropriate for a semi-diurnal tide at the latitude of Scott Base, the observed 10.1-hour oscillation must belong to other than a tidal motion [Hernandez *et al.*, 1995a]. Hernandez *et al.* [1995b] reviewed ground-based dynamical investigations of the mesosphere made from South Pole (90°S) and Scott Base (78°S, 165°E) at high austral latitudes. Furthermore, wind measurements in the mesopause region at 92 ± 5 km altitudes were performed by a meteor radar at South Pole [Forbes *et al.*, 1995]. Winds were obtained by measuring the Doppler shift of coherent radio reflections from the ionized trails produced by meteor ablation in the upper atmosphere. A large amplitude (± 20 m/s) oscillation in the northward wind was observed with a 12-hour period and zonal wavenumber one.

1.4.3 Vertical winds

Early model simulations showed that the vertical component of thermospheric wind is much smaller than the horizontal wind component. In contrast, more recent spectral models and three-dimensional global circulation models of the thermosphere demonstrated the existence of large vertical winds which, in the high latitude upper thermosphere, are comparable with the horizontal wind component. It was also shown that vertical winds play a significant role in determining the composition, large scale circulation and energy balance of the upper atmosphere. The very existence of vertical winds offers therefore a challenge both to theoreticians with their current global models and to experimenters making line-of-sight measurements under the assumption that the vertical wind component is zero.

Rees *et al.* [1984] measured vertical winds up to 160 m/s (associated with a mean altitude of about 240 km) on the poleward side of the auroral oval. The changes of vertical winds and the horizontal wind field were highly correlated, and responded directly to the local geomagnetic energy input. In recent, observations of vertical winds have been made by Price and Jacka [1991], Price *et al.* [1991], Crickmore *et al.* [1991], Conde and Dyson [1995], Aruliah and Rees [1995], Smith and Hernandez [1995], Sipler *et al.* [1995], and others. Price *et al.* [1995] made high resolution vertical wind measurements of the upper and lower thermosphere at Poker Flat, Alaska, using the OI557.7 nm and OI630.0 nm emission

lines at altitudes of about 130 and 240 km, respectively. Significant upwelling events were measured on the poleward side of the auroral oval during geomagnetically active conditions, and a schematic model was used to describe an event from which the horizontal scale of the upwelling region is estimated to be less than 320 km in the lower thermosphere and less than 800 km in the upper thermosphere.

1.5 Purpose of this thesis

In order to investigate the Earth's thermosphere in which a variety of dynamical and chemical processes take place in response to the variations of energy input, we have made an overall improvement of the prototype Fabry-Perot Doppler imaging system (FPDIS) which had been developed by the Tohoku University optical group in 1989 [Nakajima *et al.*, 1995]. The FPDIS measures the Doppler shifts and widths of aurora and/or airglow emission lines of OI557.7 nm and OI630.0 nm over a wide field of view (165°) to obtain two-dimensional distributions of winds and temperatures in the E- and F-region.

We installed the improved FPDIS at Syowa station (69.00°S , 39.58°E , 66° INV, $L \sim 6.1$) in February 1994, and carried out observations of thermospheric neutral winds for 57 nights covering various auroral conditions in the austral winter period from March to September in 1994. Since Syowa station is located just in the auroral zone, the site is quite suitable to observe the variations of thermospheric winds directly associated with auroral disturbances. Syowa station has also enough facilities to observe auroral, magnetic and ionospheric disturbances; an SIT all-sky camera for auroral observations, fluxgate and search coil magnetometer for geomagnetic field observations, an ionosonde and a multi-beam riometer for ionosphere observations. Further, Syowa station has a satellite tracking and data acquisition system which acquires in-situ measurement data from the Akebono (EXOS-D) satellite passing above the site.

The main purpose of this study is to understand the response of thermospheric neutral winds in the high-latitude E- and F-region to auroral disturbances by the Fabry-Perot Doppler imaging observations characterized by high temporal and spatial resolution in the thermospheric wind measurement. The maximum time resolution of the FPDIS measurement is 1 min for the OI557.7 nm emission and 3 min for the OI630.0 nm emission, while its typical spatial resolution is about 50 km for the OI557.7 nm emission and about 100 km for the OI630.0 nm emission. Several characteristic variations of the thermospheric neutral winds associated with auroral disturbances are examined in detail. The principle and

analytical description of the Fabry-Perot interferometer are given in Chapter 2, along with overall descriptions of the improved FPDIS and several peripheral instruments used in this study. In Chapter 3, the summary of the FPDIS installation and operation at Syowa Station is given. In Chapter 4, the method of data processing is described, and errors in neutral velocity estimation are discussed. Several new findings concerning neutral wind variations caused by auroral disturbances are shown in Chapter 5. These findings are discussed in detail in Chapter 6. Comparison between the obtained wind variations and the wind patterns derived from model simulations is also discussed in this chapter. Finally, the summary and conclusion of this study are presented in Chapter 7.

Chapter 2

Development of the Fabry-Perot Doppler Imaging System

2.1 Basic principle of the Fabry-Perot interferometer

The Fabry-Perot interferometer (FPI) is one of the main tools for observing wind velocities in the upper atmosphere. The basic principle of the FPI is as follows. A standard FPI system consists of a collimation lens, a Fabry-Perot etalon and a focusing lens as shown in Figure 2.1. The Fabry-Perot etalon is a combination of two optical flats which are placed in parallel with a separation d . Their inner surfaces are coated with semi-transparent material of high reflectance, such as dielectric multi-layered films. When a monochromatic light with a wavelength λ falls upon the etalon at an angle ϕ to the normal, the light undergoes a series of transmission and reflections, as shown in Figure 2.1, and pairs of adjoining emergent rays differ in their path lengths by Δl , where

$$\Delta l = 2d \cos \phi \quad (2.1)$$

Constructive interference between the emerging rays will then occur at those wavelength for which

$$n\Delta l = m\lambda \quad (2.2)$$

i.e.,

$$2nd \cos \phi = m\lambda \quad (2.3)$$

where n is the reflective index of the medium between the plates A and B and m is an integer. Since the image of a point source P_1 is still a point at P_2 , only the image of a point source of which the optical path holds equation 2.3 becomes bright.

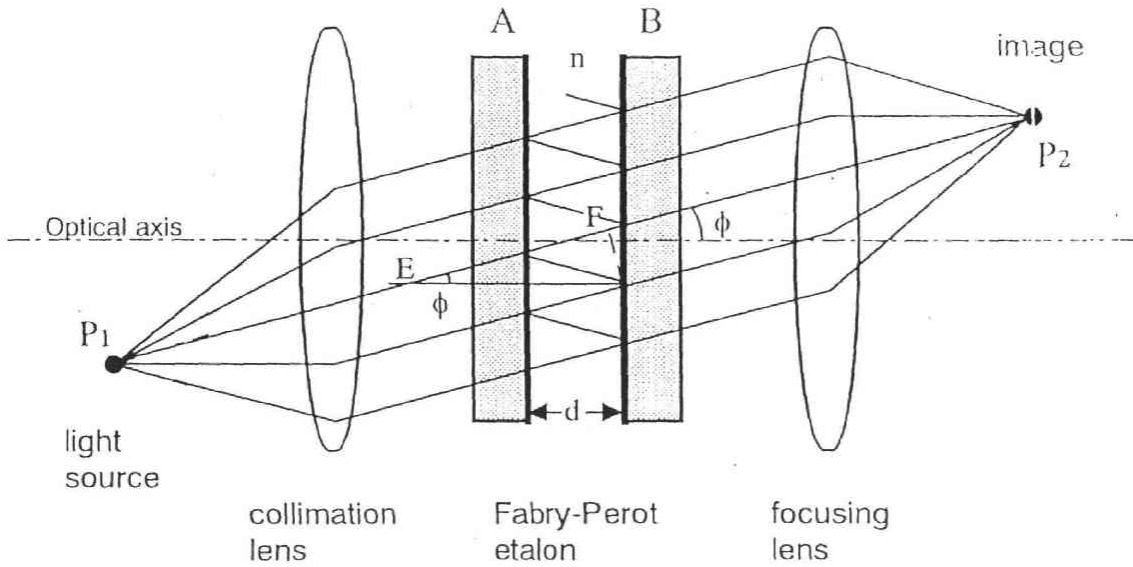


Figure 2.1. Schematic diagram showing the optical path of the Fabry-Perot interferometer. The optical path difference of adjoining rays is given by the relation $m\lambda = 2nd \cos \phi$.

The transmittance of the etalon is calculated as follows. As is indicated in Figure 2.1, we assume that a monochromatic beam falls upon the etalon at an angle ϕ . We also assume that the surfaces of the plates A and B have identical characteristics for reflection. We denote the amplitude transmittance and the amplitude reflectance on the reflective surfaces as t and r respectively. For a unit amplitude of incident light, the amplitudes of the light transmitted from the plate after multiple reflections are given by

$$t^2, t^2 r^2 e^{-i\Phi}, t^2 r^4 e^{-2i\Phi}, \dots \quad (2.4)$$

where Φ denotes the phase difference by $2nd \cos \phi$ in the optical paths of adjoining beams transmitted from the etalon. From equation 2.3, the phase difference Φ is given by

$$\Phi = \frac{2\pi}{\lambda} 2nd \cos \phi. \quad (2.5)$$

The total transmitted amplitude τ is then the sum of the amplitudes given in equation 2.4 as

$$\begin{aligned} \tau &= t^2 + t^2 r^2 e^{-i\Phi} + t^2 r^4 e^{-2i\Phi} + \dots \\ &= \frac{t^2}{1 - r^2 e^{-i\Phi}}. \end{aligned} \quad (2.6)$$

Now the transmittance of light T_F is given by

$$T_F = \tau\tau^* = \frac{(1-R)^2}{1-2R\cos\delta+R^2} \quad (2.7)$$

where

$$R = r^2 = 1 - t^2 \quad (2.8)$$

$$\delta = \Phi - 2\chi = \frac{2\pi}{\lambda} 2nd \cos\phi - 2\chi. \quad (2.9)$$

In the above equations, R is the reflectance at the reflective surfaces on the etalon plates, and δ denotes the total phase difference which includes both the phase difference Φ corresponding to the optical path difference and the phase change χ due to reflection on each surface. Equation 2.7 is called 'Airy function'. Equation 2.7 shows that the transmittance T_F has a maximum at $\delta = 2m\pi$ ($m = 0, 1, 2, \dots$), i.e.,

$$\left(m + \frac{\chi}{\pi}\right) \lambda = 2nd \cos\phi \quad (m = 0, 1, 2, \dots). \quad (2.10)$$

Figure 2.2 shows transmittance curves of the etalon as a function of the phase δ for various values of the reflectance R as parameters. When the value of R is greater than 0.9, the transmittance of the etalon has a very sharp peak around $\delta = 2m\pi$, and is nearly zero for other values of δ .

2.2 Principle of the Fabry-Perot Doppler imaging

The Fabry-Perot Doppler Imaging System (FPDIS) was first developed by our optical group of Tohoku University in 1989. The FPDIS is a two-dimensional Fabry-Perot interferometer system with an extremely high spectroscopic resolution and a high temporal and spatial resolution. Compared with conventional Fabry-Perot interferometers, the FPDIS developed in 1989 has the following characteristics;

- 1) The FPDIS employs an all-sky fish-eye objective lens to match a field of view of the interference fringes on the focal plane to a wide field of view (FOV = 165°) in the sky.
- 2) The FPDIS employs a very sensitive two-dimensional photon detector which consists of a photon counting imager and a charge coupled device (CCD) camera.

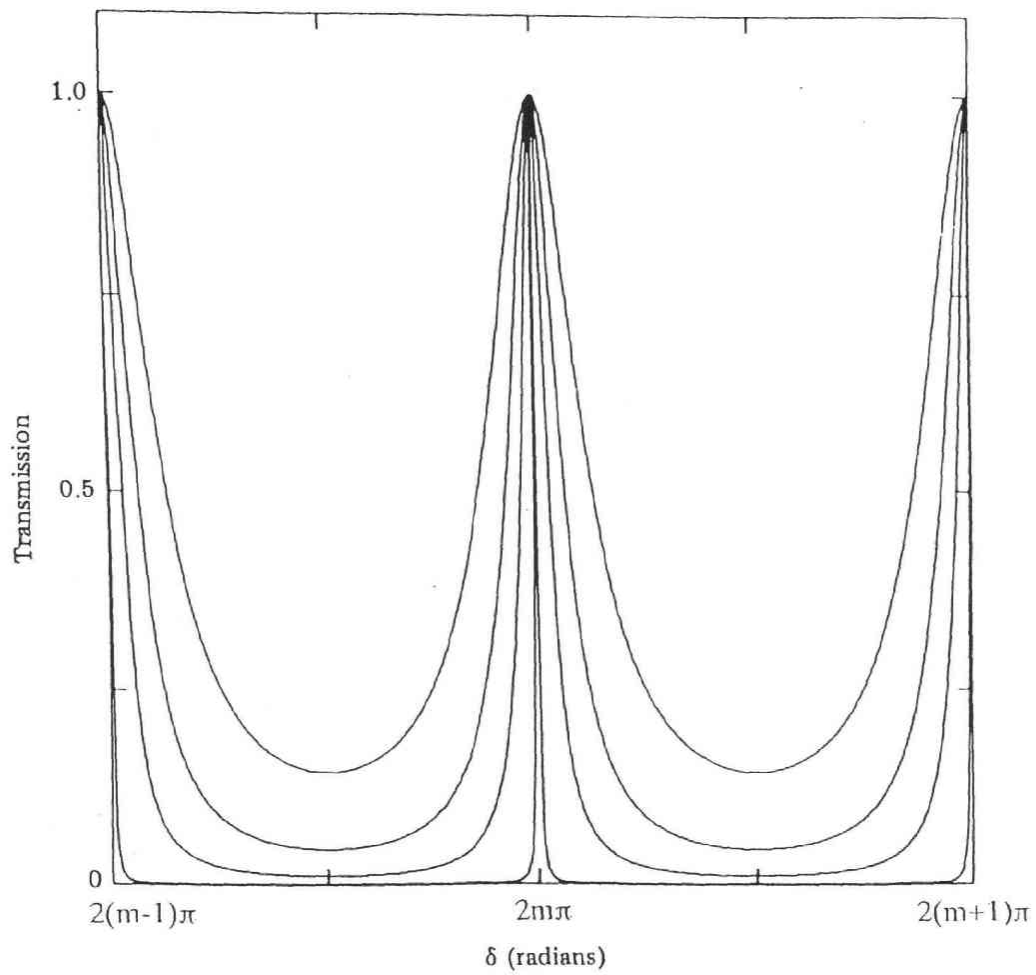


Figure 2.2. Transmittance of a Fabry-Perot etalon as a function of the phase retardation of a beam for various values of the reflectance R . Four profiles from the narrowest to the widest one correspond to the values of R 0.98, 0.81, 0.65 and 0.45, respectively.

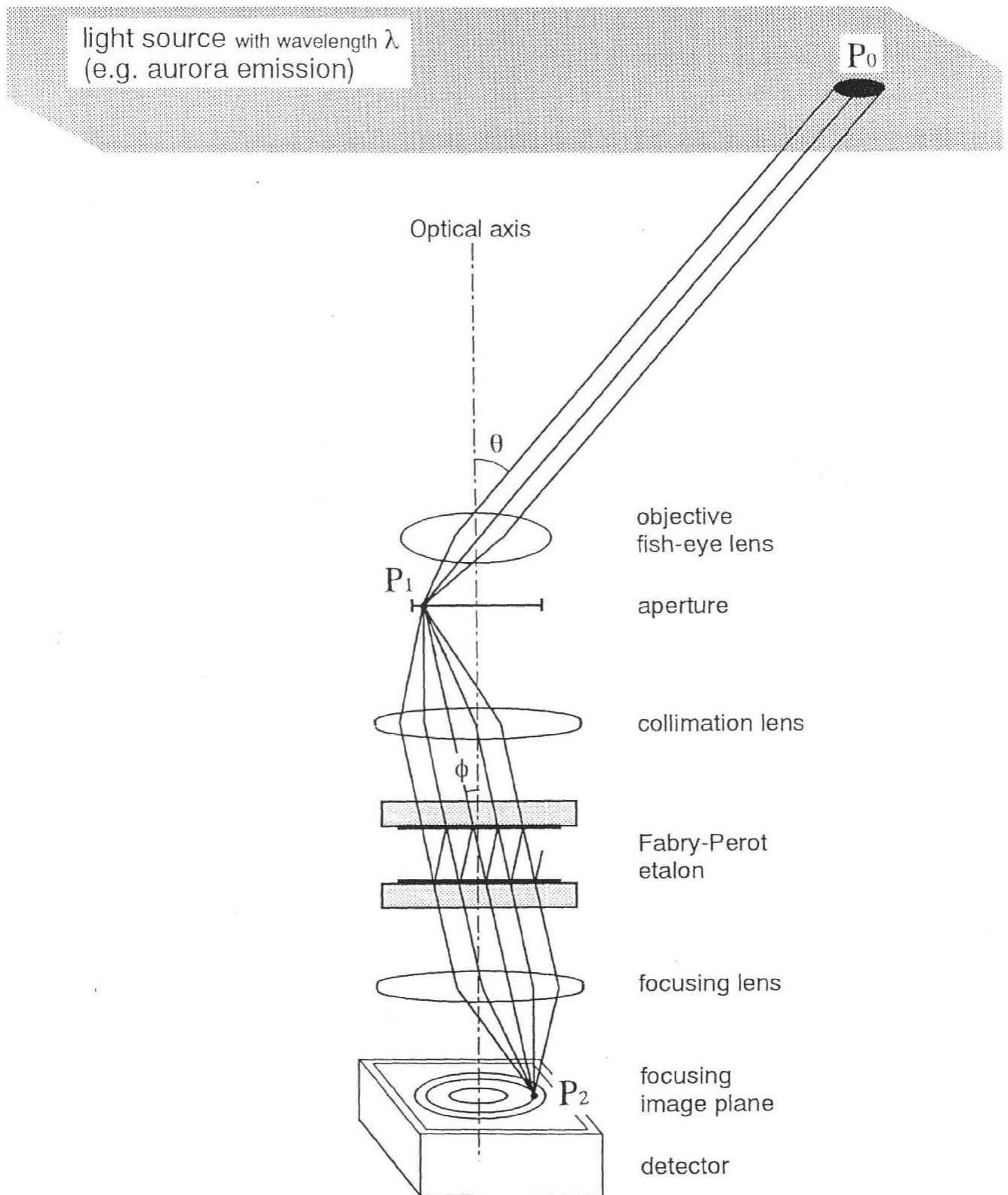


Figure 2.3. Schematic diagram showing the concept of the Fabry-Perot Doppler imaging system.

The principle of the Fabry-Perot Doppler imaging system is as follows. Figure 2.3 shows the basic concept of the Fabry-Perot Doppler imaging system which includes an objective lens, a Fabry-Perot interferometer and an image plane detector. In this geometry, a monochromatic light with a wavelength λ from a point P_0 , which is considered to be a small part of a plane emission surface such as auroral emission, falls upon the objective fish-eye lens with an incident angle θ , and focused on a point P_1 at the 1-st aperture. Then, the light falls upon the Fabry-Perot interferometer with an angle ϕ , and focused at a point P_2 on the image plane. The light intensity at P_2 has a maximum at the light incident angle ϕ , which satisfies equation 2.10, and thus interference fringes are produced on the image plane. Since the transmittance of the FPI is symmetrical about the optical axis, the produced interference fringes become ring shaped. These fringes are called 'etalon fringes'. An example of the etalon fringes is shown in Figure 2.4. It is found that each segment on the fringes is mapped to the different location of the emission source in the sky. On the other hand, if n and d are constant in equation 2.10, the incident angle ϕ and the corresponding fringe radius are decided by the wavelength λ . With this theory, we can estimate a slight change of wavelength such as a Doppler shift of auroral emission by measuring the fringe radius precisely.

A region where the order numbers of fringes do not overlap is called 'a free spectral range' $\Delta\lambda_R$. When an interference fringe of m -th order is formed for an incident angle ϕ with an interference condition of equation 2.10, the interference fringe of $(m+1)$ -th order is formed at the incident angle of $\phi - \Delta\phi$, i.e.,

$$\left(m + 1 + \frac{\chi}{\pi}\right) \lambda = 2nd \cos(\phi - \Delta\phi). \quad (2.11)$$

On the other hand, when a light with a wavelength of $\lambda + \Delta\lambda$ forms the interference fringe of m -th order at the same incident angle of $\phi - \Delta\phi$, the following equation is satisfied.

$$\left(m + \frac{\chi}{\pi}\right) (\lambda + \Delta\lambda) = 2nd \cos(\phi - \Delta\phi). \quad (2.12)$$

From equations 2.10, 2.11 and 2.12, the free spectral range $\Delta\lambda_R$ is given by

$$\Delta\lambda_R = \Delta\lambda = \frac{\lambda^2}{2nd \cos \phi}. \quad (2.13)$$

If the emission line width of an incident light is wider than the free spectral range $\Delta\lambda_R$, it is difficult to isolate each emission line spectrum, since adjoining fringes with different order numbers overlap each other.

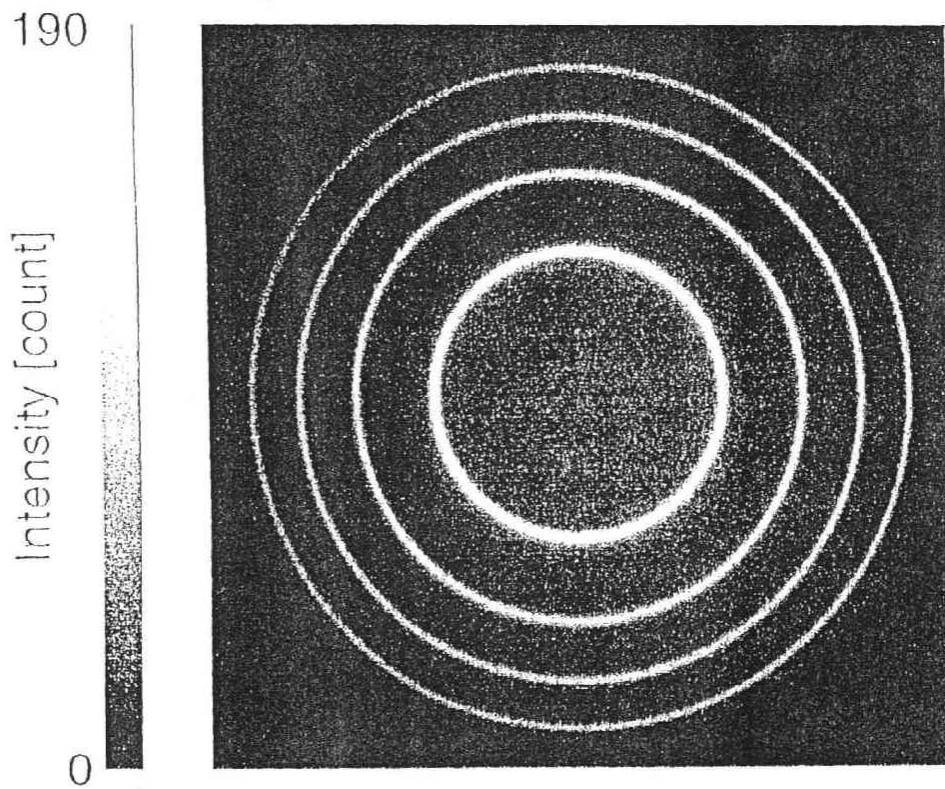


Figure 2.4. An example of interference fringes of a Fabry-Perot etalon. These are fringes of a He-Ne laser source with a etalon of 12 mm spacer and a reflectance of 0.88.

The free spectral range of the FPI used in our system is about $2.63 \times 10^{-5} \cdot \lambda$ for an incident light of the auroral OI630.0 nm emission. In case of the auroral OI630.0 nm emission, the emission line width $\Delta\lambda_T$ is decided by the atmospheric temperature $T \sim 1000$ [K] as follows

$$\begin{aligned} \Delta\lambda_T &= \left(\frac{2kT}{m} \right)^{\frac{1}{2}} \frac{\lambda}{c} \\ &\cong 3.40 \times 10^{-6} \cdot \lambda. \end{aligned} \quad (2.14)$$

Here k is Boltzmann's constant, m is the mass of the emitting species and c is the velocity of light. The emission line width given by equation 2.14 is called 'a thermal width' or 'a Doppler width'. In our system, the thermal width is much narrower than the free spectral range.

2.3 Prototype of the Fabry-Perot Doppler Imaging System

2.3.1 Optics

The system diagram of the prototype of the FPDIS developed in 1989 is shown in Figure 2.5. All-sky images, focused by an objective fish-eye lens, are reduced by a relay lens system and then collimated to nearly parallel beams by a collimating lens. These nearly parallel beams cause interference in an etalon. Then the beams are focused on a photocathode of the photon imaging head (PIH) detector. Two interference filters which are placed between a focusing lens and the PIH are used to select the wavelength of the auroral emission of OI630.0 nm and OI557.7 nm. An output image on a fluorescent screen of the PIH is reduced and finally focused on a CCD camera. The composite video output signal of the CCD camera is monitored and recorded by a video-disk recorder. The image data, recorded on optical video disks, are reproduced and processed further. To check instrumental errors arising from thermal drifts of etalon parameters, a stabilized He-Ne calibration laser is equipped in the FPDIS. A beam of the He-Ne laser is diffused and enters the optical path of the FPDIS by a beam splitter.

In the image plane, there are two complete etalon fringes which are projected onto the full field of view of 165° in the sky. Thus, the fringes of an auroral emission of OI630.0 nm with a peak emission altitude of ~ 240 km cover a region of approximately 900 km in diameter,

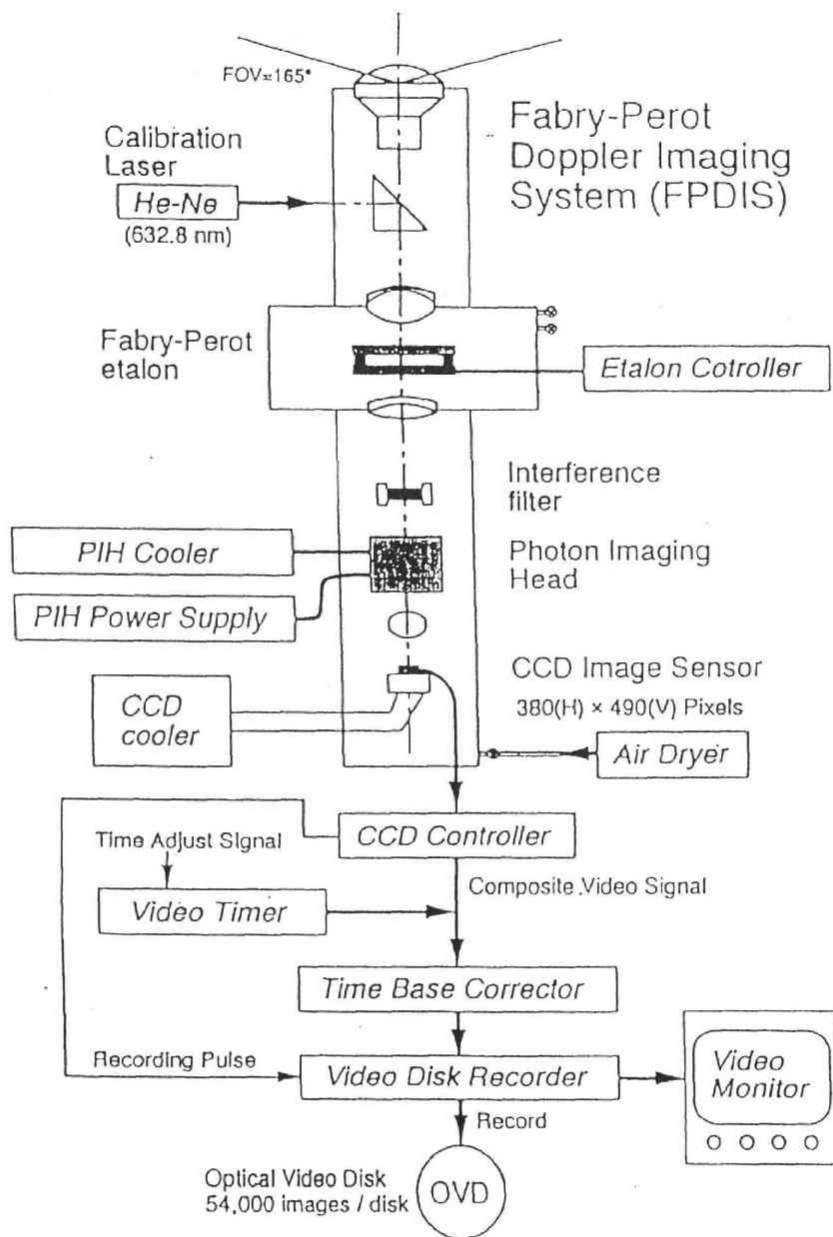


Figure 2.5. System diagram of the prototype of the Fabry-Perot Doppler Imaging System [after Nakajima, 1993]

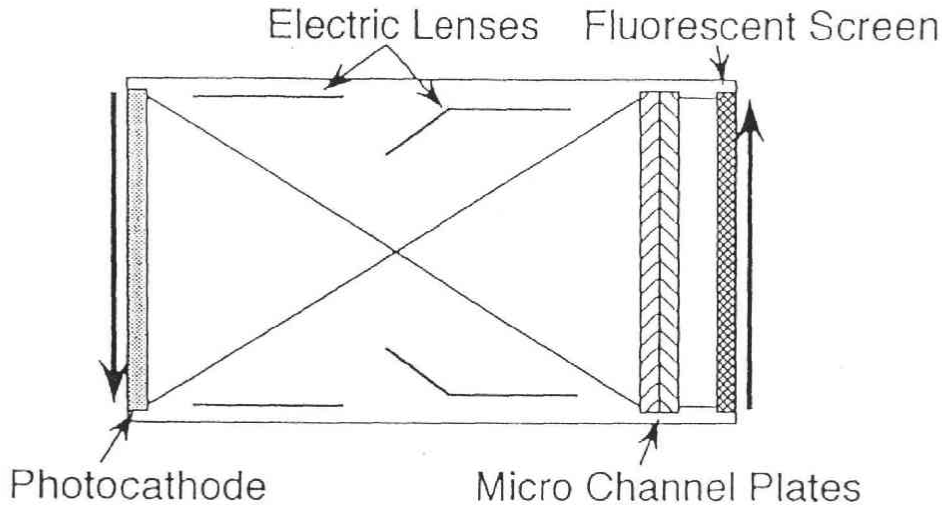


Figure 2.6. Diagram of the photon imaging head (PIH) detector [after Nakajima, 1993]

while the fringes of an auroral emission of OI557.7 nm with a peak emission altitude of ~ 105 km cover a region of approximately 350 km in diameter.

This system was used for observations of thermospheric wind velocities at Syowa Station, Antarctica in 1990. From the analysis of the obtained data, large variations in the neutral thermospheric temperatures and wind velocities during an auroral breakup event on 11 September 1990 were reported [Nakajima, 1993, Nakajima *et al.*, 1995].

2.3.2 Correction of the image distortion caused by the photon imaging head

The photon imaging head (PIH) used in the prototype FPDIS is a highly sensitive two-dimensional photon detector (Model C2166-01, Hamamatsu Photonics Corp.) which consists of a photocathode, a pair of electric lenses, two-stage microchannel plates, and a fluorescent screen, all assembled in a vacuum tube. A schematic diagram of the PIH is shown in Figure 2.6. A slight (less than 5%) geometric distortion was found in the obtained PIH images. Its cause was aberrations of the electric lenses. Precise correction of this distortion is essential to derive thermospheric temperatures and wind velocities from interference-image data. The collection methods called 'the grid calibration' and 'the two-dimensional plane-spline-interpolation', were given by Nakajima [1993] and Nakajima *et al.* [1995].

In the grid calibration, a precise optical grid is placed on the focal plane in the foreoptics of the FPDIS, and images of the grid which is weakly illuminated by a diffused He-Ne laser

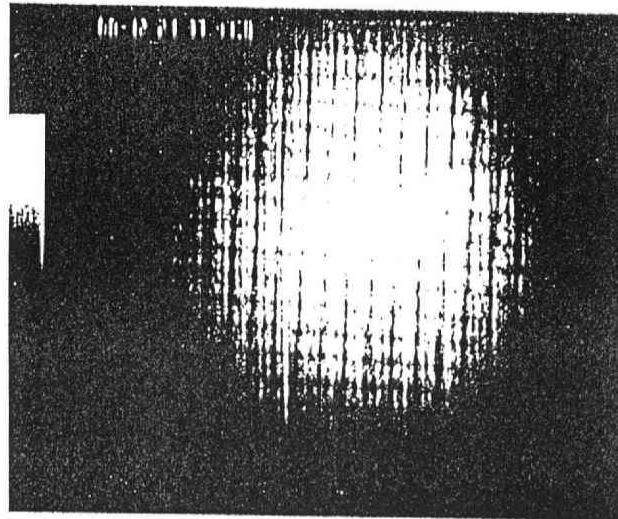
are taken. Next, X and Y coordinates at the intersections of vertical and horizontal grid lines in the image are obtained, and the two-dimensional plane-spline-interpolation method is applied to interpolate the X and Y coordinates over the whole region of the image. Figure 2.7(a) shows an example of the grid image used for the grid calibration, while Figure 2.7(b) shows an image corrected by the two-dimensional plane-spline-interpolation method. It is found that distorted and curved grid lines are mapped to straight lines that are orthogonal to each other.

As described above, the correction procedures for the PIH images are very complicated, and may reduce the accuracies in derivation of thermospheric winds and temperatures. To solve this image distortion problem, we need a different type of imaging detector. In the model developed in 1993, we adopted the proximity focused photon counting imager (PFPCI) which has no electric lenses. Details about the PFPCI are described in Section 2.4.4.

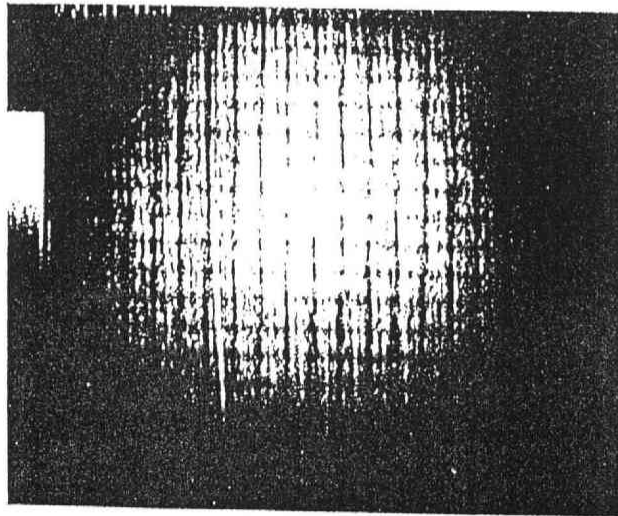
2.3.3 Problems in the image integration

The PIH was operated in the photon counting mode because the luminosity of auroral emission is usually less than 10^6 photons/mm²/s. This mode detects an incident photon as a single photon spot on the output fluorescent screen. A typical diameter of this spot is approximately 60 μ m. Images are then produced by summation of individual photons on the CCD chip. The exposure time of the CCD is selectable among 0.53, 1.06, 2.13, 4.26, and 8.58 s. Then, a thresholding procedure which eliminates CCD thermal and readout noises and an integration procedure are needed to obtain the etalon fringes of the incident light, as shown in Figure 2.8(a). However, photon spots sometimes overlap each other as shown in Figure 2.8(b), since the PIH detects too many photons in the case of bright aurora even if the minimum exposure time of 0.53 s is selected. In this case, obtained fringe peaks are deformed because overlapped photon spots are counted as one spot by a simple thresholding procedure.

To solve this problem, a new image processing system has been adopted for the new version of the FPDIS developed in 1993. Details about this system are described in Section 2.4.5.



(a)



(b)

Figure 2.7. Example of a grid image used for the grid calibration: (a) an image before correction and (b) a corrected image. It is apparent that distortions and nonlinearities of the image are eliminated [after Nakajima, 1995].

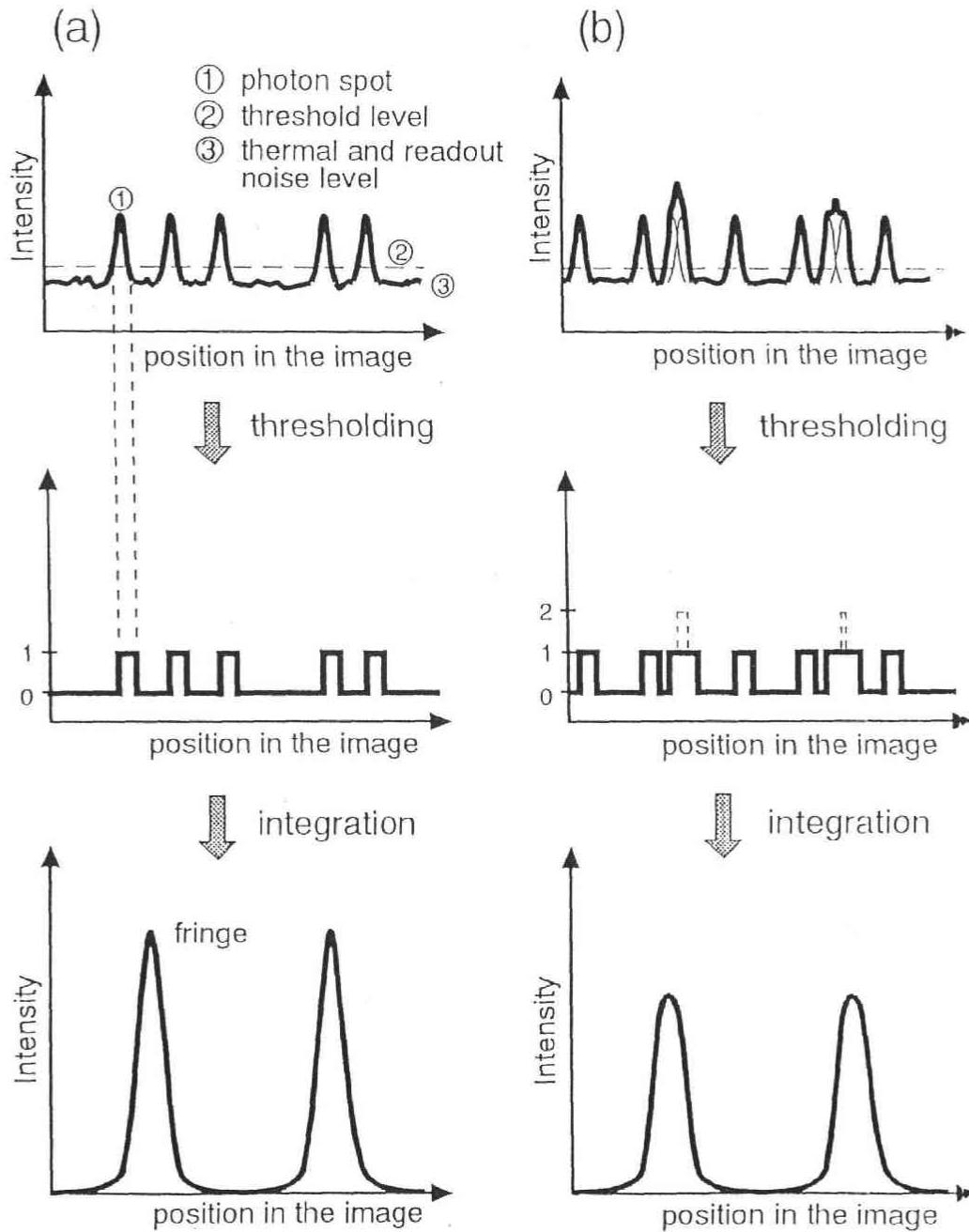


Figure 2.8. Conceptual sketches of the thresholding and integration process: (a) normal photon spots and (b) photon spots which overlap each other because of an overexposure. In both sketches, top, middle and bottom panels show photon spot images, thresholding images and fringe patterns obtained by the integration process, respectively.

2.4 New version of the Fabry-Perot Doppler Imaging System

To eliminate two important problems described in Section 2.2, we developed a new version of the FPDIS in 1993. The system diagram of the new version is shown in Figure 2.9. The instrumental parameters are summarized in Table 2.1. The main characteristics of the improvements are as follows.

- 1) Introduction of a proximity focused photon counting imager (PFPCI) in place of the photon imaging head (PIH) which has the image distortion problem.
- 2) Introduction of a highspeed CCD camera and a fast data processor to solve the overexposure problem.
- 3) Introduction of a digital data recording system in place of optical video-disk recorder, to simplify the data analysis process.
- 4) Development of a computer control program for automatic operation of the FPDIS including the selection of interference filters and the time sequences for image data acquisition.

In the following sections, we will give details on the characteristics of the new version of the FPDIS concerning an optical system, a Fabry-Perot etalon, interference filters, a two-dimensional photon detecting system, an image data processing and recording system, and a calibration laser.

2.4.1 Optical system

Figure 2.10 shows the schematic diagram of the FPDIS. The list of the optical components used for the FPDIS is given in Table 2.2. The optical layout of the FPDIS is as follows. An all-sky image ($FOV = 165^\circ$) is focused with the objective fish-eye lens (1) to an image of 24.0 mm diameter and then reduced to an image of 12.0 mm diameter at the 1-st aperture (3) and 5.5 mm diameter at the 2-nd aperture (5) by using the aspheric lens (2) and the relay lens (4), respectively. The incident light is then collimated to nearly parallel beams by the collimator lens (7). The maximum incident angle of light falling upon the Fabry-Perot etalon (8) is 0.66° . These nearly parallel beams cause interference in the etalon. Then the etalon fringes are focused on the photocathode of the PFPCI (13) with the focusing lens (9).

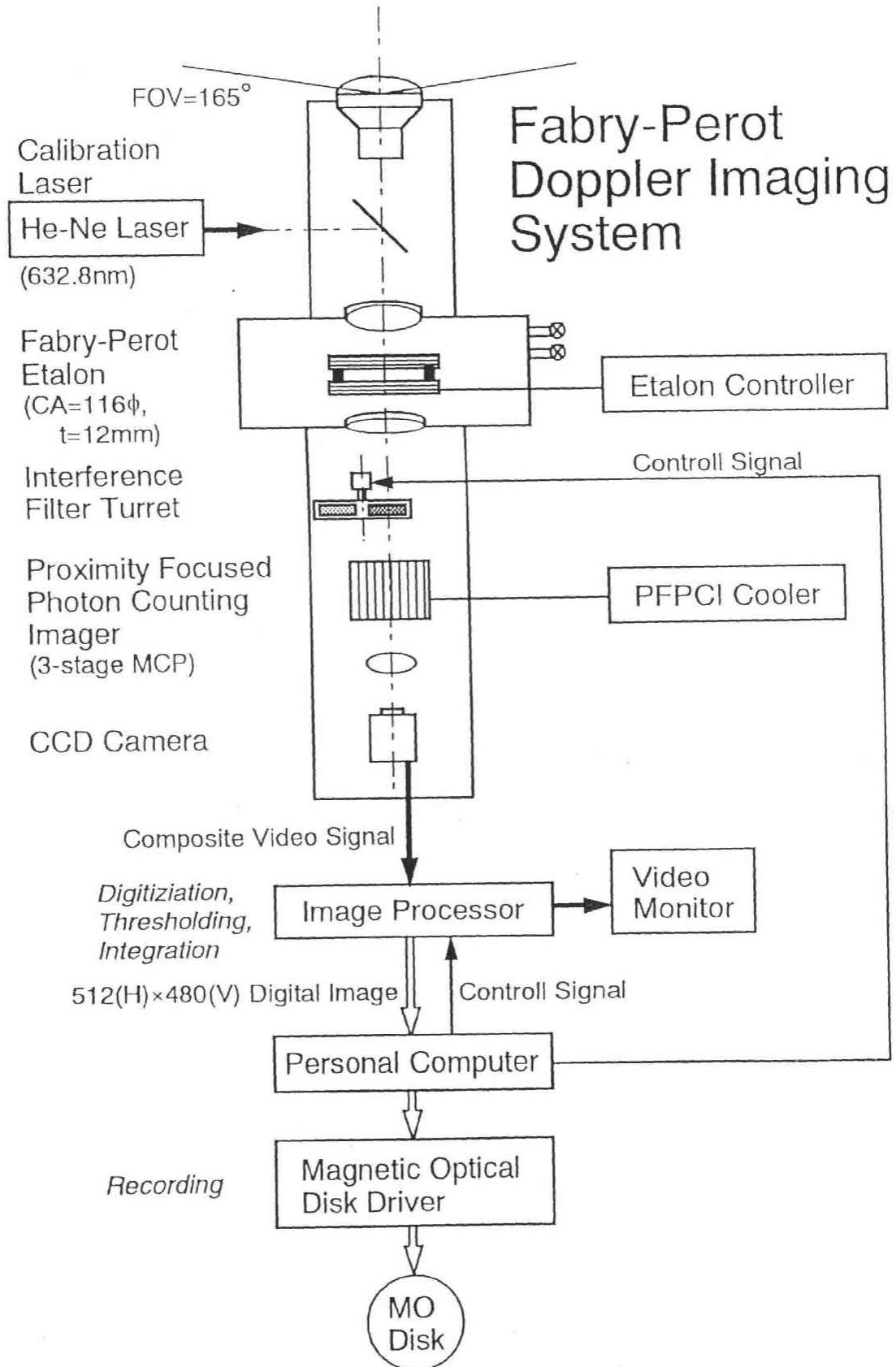


Figure 2.9. System diagram of the further developed Fabry-Perot Doppler Imaging System (FPDIS)

Table 2.1. Summary of the instrumental parameters for the new version of the Fabry-Perot Doppler Imaging System (FPDIS)

Apparatus	Parameter	Value
Foreoptics	Field of view	165 °
	Maximum incident angle onto the etalon	0.66 °
Fabry-Perot etalon (Queensgate Model ET116)	Clear aperture	116 mm
	Reflectivity (at 557.7-630.0 nm)	0.88 ± 0.03
	Theoretical reflective finesse	24.6
	Nominal spacing	12 mm
Interference filters	Center wavelengths of	
	ch.1	557.90 nm
	ch.2	630.11 nm
	ch.3	589.16 nm
	FWHM of	
	ch.1	0.71 nm
ch.2	0.96 nm	
ch.3	0.91 nm	
Proximity Focused Photon Counting Imager (Hamamatsu Model V5102UX)	Minimum useful area	18 ϕ mm
	Gimmitting resolution	20 line pairs/mm
	Luminous gain	1 × 10 ⁷
	Quantum efficiency	
	557.7nm	8 %
	630.0nm	4.5 %
CCD camera (Ikegami Model FCD-10)	Imaging area	8.8 mm horizontal 6.6 mm vertical
	Pixel number	800 (H) × 490 (V)
	Output signal type	NTSC composite video
Stabilized He-Ne laser (Spectra-Physics Model 117A)	Output power	> 1.0 mW
	Frequency	473.61254 THz ($\lambda = 632.3$ nm)
	Frequency stability	± 3.0 MHz / 1day ($\Delta f / f < 10^{-8}$)

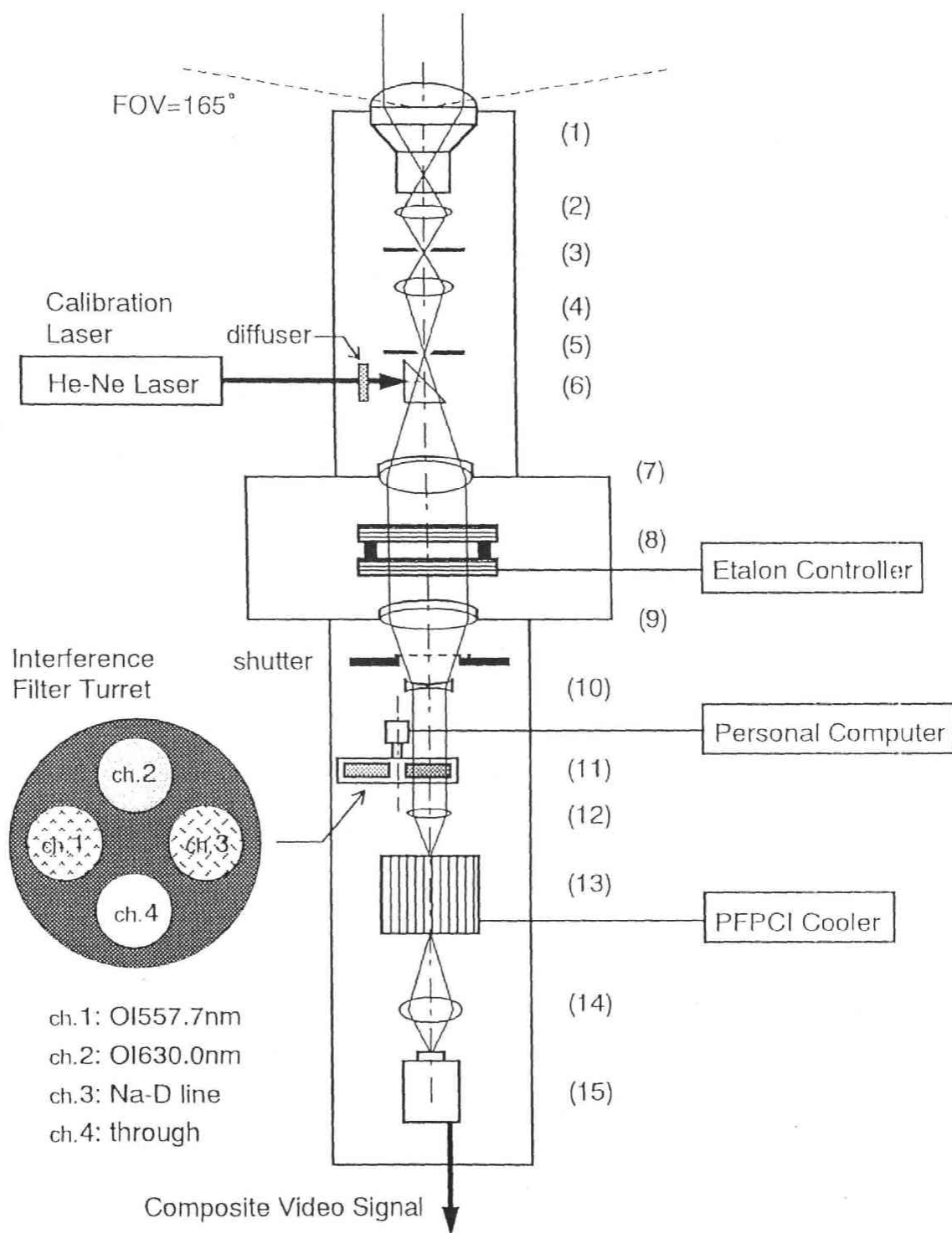


Figure 2.10. Schematic diagram of the Fabry-Perot Doppler Imaging System (FPDIS). The list of the components (1)-(15) is given in Table 2.2.

Table 2.2. List of the optical components used for the FPDIS.

	Name of Components	Data
(1)	fish-eye lens	Nikkor, $f=8$ mm, $F=2.8$
(2)	relay lens 1	Aspheric lens, $f=35.7$ mm, $F=0.89$
(3)	1-st aperture	$\phi = 12$ mm
(4)	relay lens	Nikkor, $f=50$ mm, $F=1.2$
(5)	2-nd aperture	$\phi = 5.5$ mm
(6)	beam splitter	
(7)	collimator lens	$f=240$ mm, $F=2.0$
(8)	Fabry-Perot etalon	Queensgate Model ET116 maximum incident angle= 0.66° , clear aperture= 116 mm,
(9)	focusing lens	$f=600$ mm, $F=5.0$
(10)	concave lens	$f=-125$ mm, $F=-3.13$
(11)	interference filter turret	4 channel, $\phi = 30$ mm
(12)	convex lens	$f=125$ mm, $F=3.13$
(13)	Proximity Focused Photon Counting Imager	Hamamatsu Model V5102UX minimum useful area= 18 mm
(14)	focusing lens	Nikkor, $f=50$ mm, $F=1.2$ + Nikkor macro-ling, 14 mm
(15)	CCD camera	Ikegami Model FCD-10 imaging area 8.8 mm (H) \times 6.6 mm (V)

In the optical path, a pair of concave and convex lenses (10) and (12) and the interference filter turret wheel (11) are placed. Three interference filters are mounted on the filter turret wheel for the selection of wavelengths OI557.7 nm, OI630.0 nm and Na-D589.0 nm as shown in Figure 2.10. The output image on the fluorescent screen of the PFPCI is reduced and finally focused on the CCD camera (15) with the focusing lens (14). The composite video output signal from the CCD camera is further processed by an image data processor which is described in the following section.

2.4.2 Fabry-Perot etalon

The Fabry-Perot etalon used in the FPDIS is a piezoelectrically turned and servo-stabilized etalon (Model ET116, Queensgate Instruments, Ltd). A view of the etalon and its controller is shown in Figure 2.11. The clear aperture of the etalon is 116 mm with a surface quality of $\lambda/100$ at $\lambda = 546.1$ nm. The wedge angle of the etalon plate is set to 10-15 arcmin. The inner surface of the etalon is coated to provide a reflectivity of 0.88 ± 0.03 in the wavelength region between 557.7 nm and 630.0 nm. Figure 2.12 shows the dependence of the reflectivity on the wavelength of incident light. This reflectivity corresponds to a theoretical reflective finesse \mathcal{F} of 24.6. The normal optical spacing of the etalon is selected to be 12.0 mm, which gives a normal free spectral range of 16.5 pm for a wavelength of 630.0 nm to meet the requirements for 1) obtaining the maximum resolution of the interference fringe and 2) obtaining at least two interference fringes within the field of view of 165° for each of 630.0 nm and 557.7 nm wavelengths. The optical spacing of the etalon and the parallelism of the etalon plates are maintained with a stability of better than $\lambda/2000$ by the piezoelectric etalon-stabilization system (Model CS100, Queensgate Instruments, Ltd). The electronic drift of the etalon spacing resulting from temperature changes is less than 0 ± 50 pm $^\circ\text{C}^{-1}$.

2.4.3 Interference filters

Three interference filters are prepared to select the wavelength of the aurora emissions of OI630.0 nm and OI557.7 nm and the airglow emission of Na-D589.0nm. The center wavelengths of these filters are 630.11 nm, 557.90 nm, and 589.16 nm, while the full widths at half-maximum (FWHM) of these filters are 0.96, 0.71, and 0.91 nm, respectively. The auroral emissions of OI630.0 nm and OI557.7 nm were mainly observed at Syowa station. Filter transmission functions of the two filters are presented in Figure 2.13.

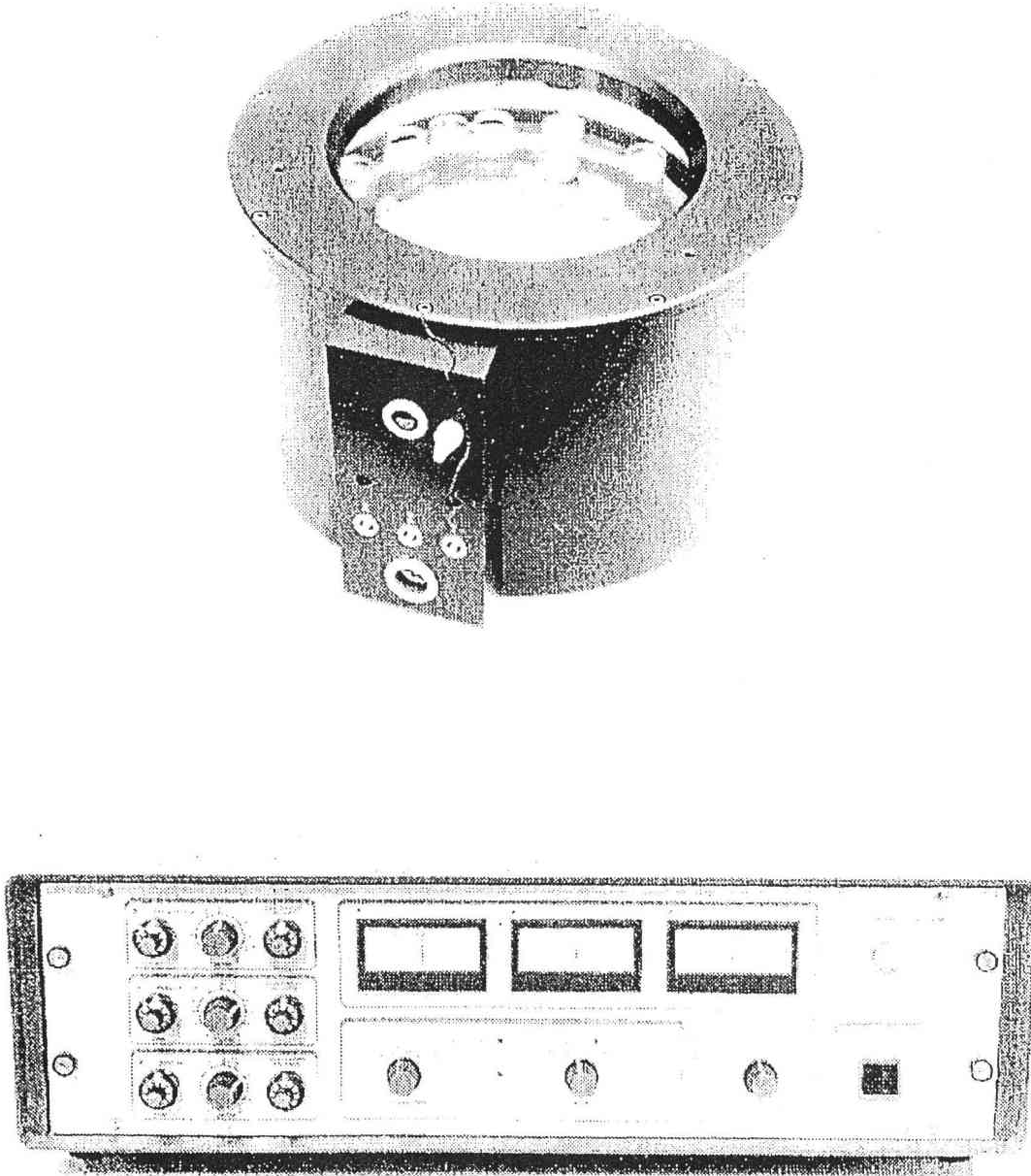


Figure 2.11. View of the servo-stabilized Fabry-Perot etalon and its controller used for the FPDIS. Several connectors which are seen on the side of the etalon container are used for cables connecting the servo-control circuit to keep the parallelism and spacing of the etalon.

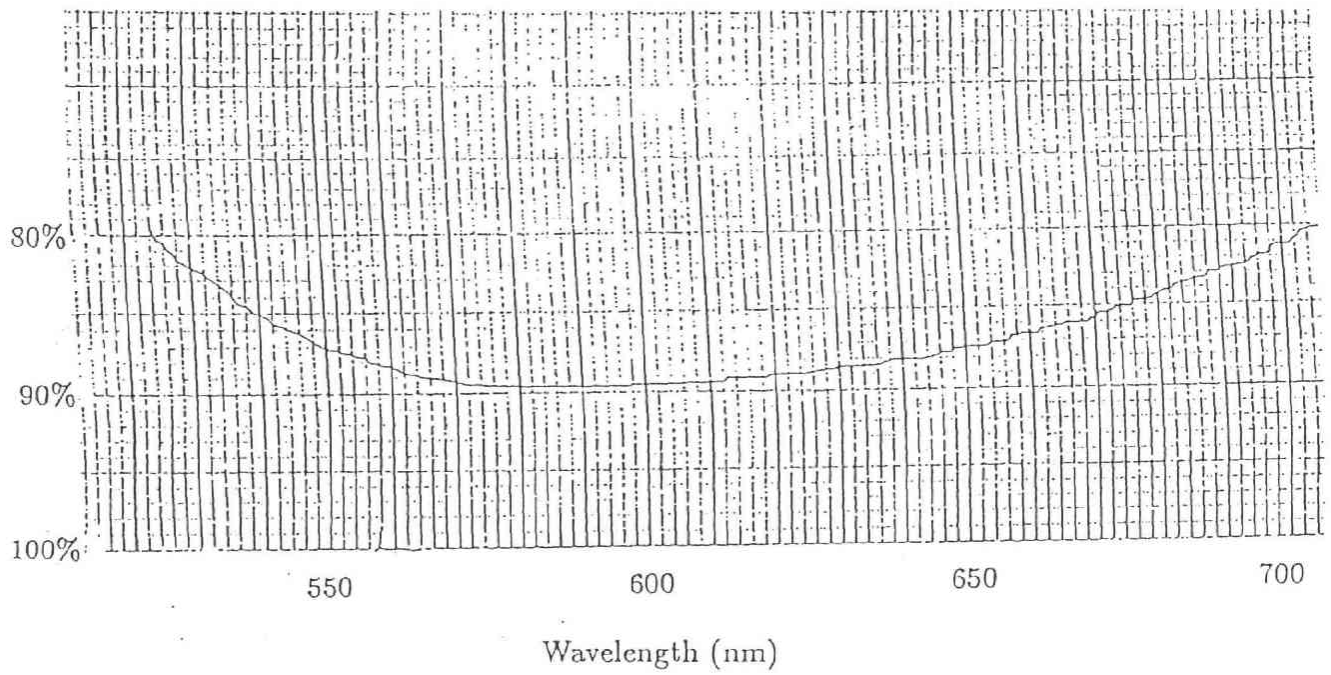


Figure 2.12. Dependence of the reflectivity of the etalon coating on the wavelength of incident light.

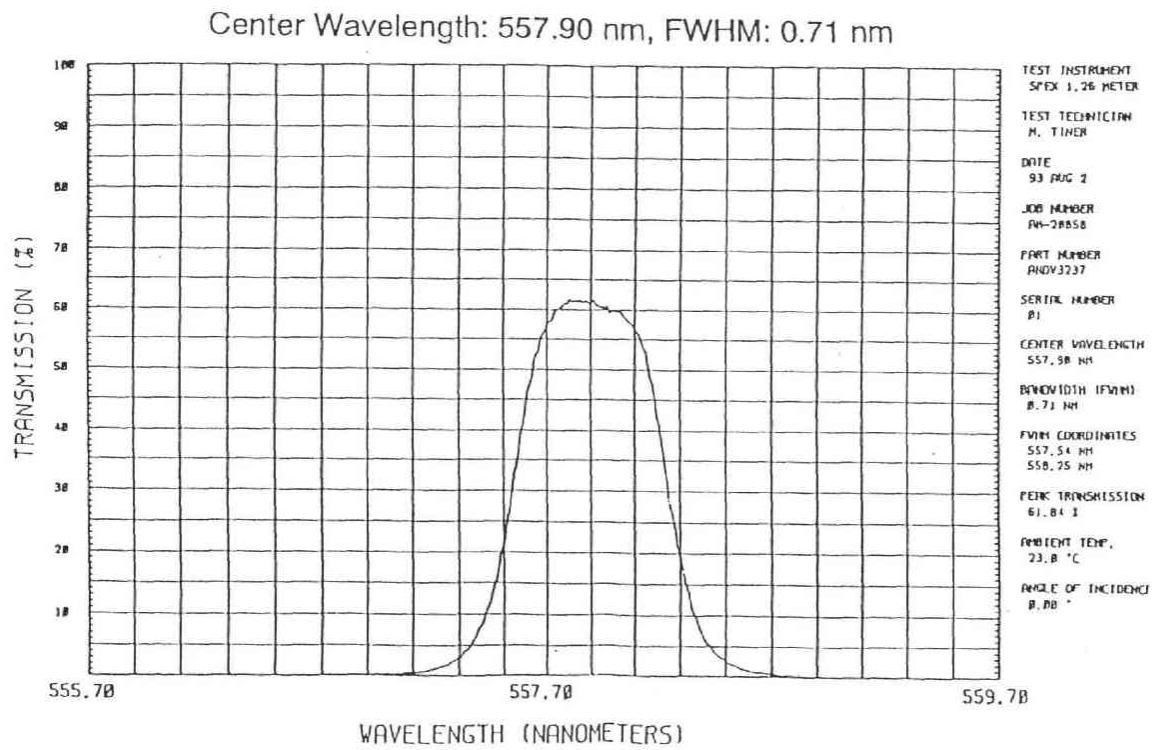
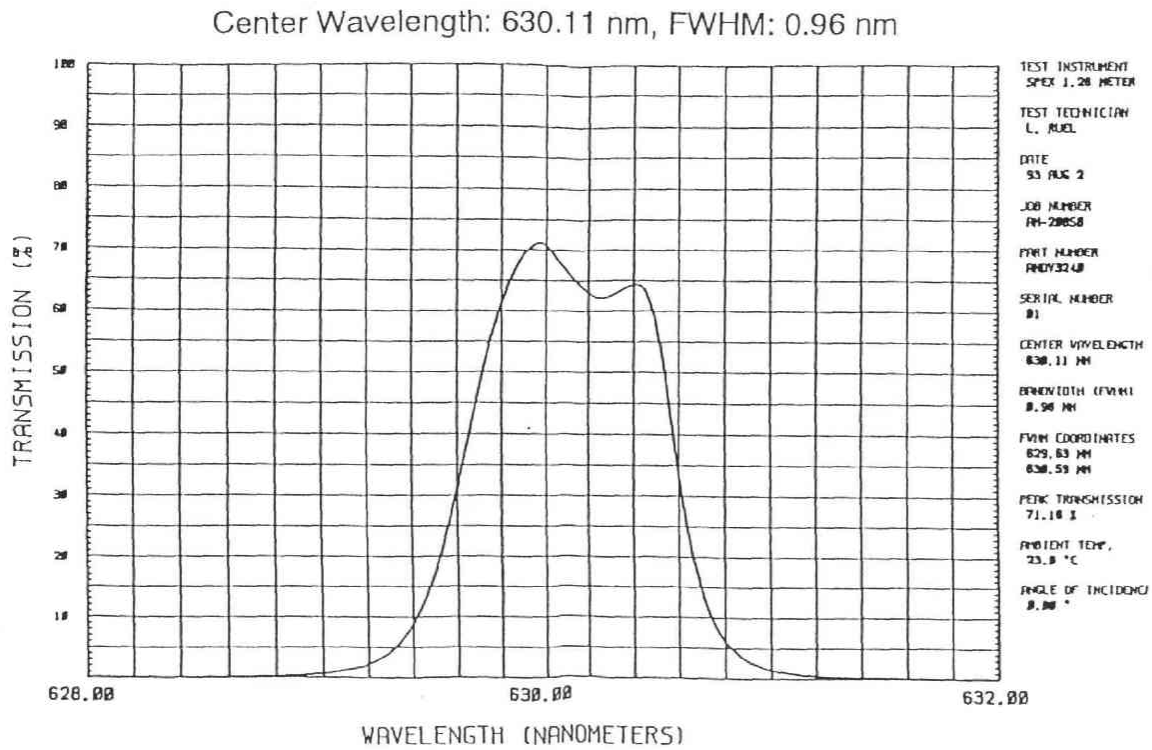


Figure 2.13. Filter transmission functions.

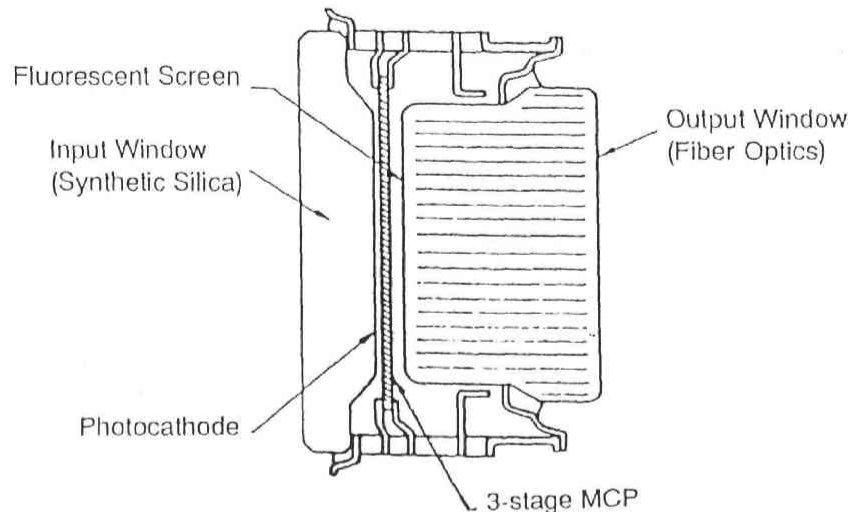


Figure 2.14. Schematic diagram of the proximity focused photon counting imager (PFPCI).

Although the 630.0 nm filter passes an unwanted $\text{OH}(9,3)P_1(3)$ emission line at 630.68 nm, the contribution of this line is considered to be almost negligible because it is much weaker than the $\text{OI}630.0$ nm emission line at high latitudes.

2.4.4 Two-dimensional photon detecting system

Since the spectral brightness of the auroral emissions is extremely low, the FPDIS used a combination of two types of imaging detectors, i.e., PFPCI and CCD detectors. They attain the high signal-to-noise ratio (SNR) and time resolution of the FPDIS due to the use of the photon counting technique.

The PFPCI is a highly sensitive, two-dimensional photon detector (Model V5102UX, Hamamatsu Photonics Corp.). This detector consists of a photocathode, three-stage microchannel plates, and a fluorescent screen, all assembled in a vacuum tube. A schematic diagram of the PFPCI is shown in Figure 2.14. The photocathode and the fluorescent screen of the PFPCI are made of multi-alkali and zinc-cadmium sulfide (P-20), respectively, whereas the input and output windows are made by borosilicate glass and fiber plate, respectively. The effective diameters of the photocathode and the fluorescent screen are both 18 mm. The radiant sensitivity and the quantum efficiency of the photocathode is shown in Figure 2.15. The PFPCI is mounted in a cooling unit, which employs the Peltier effect, as shown in Figure 2.16, and cooled down to -15°C to reduce dark counts at the time of observation. We use

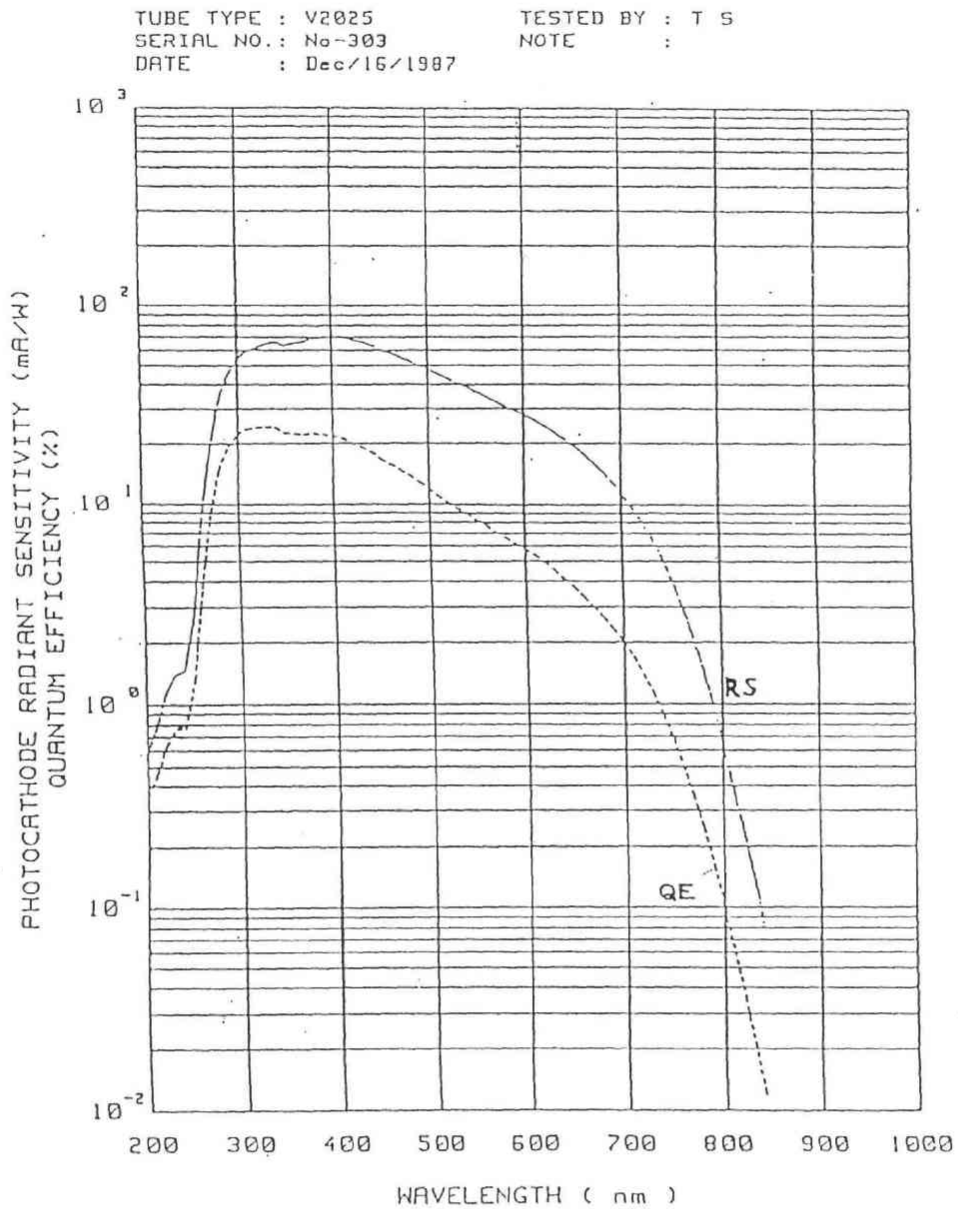


Figure 2.15. Radiant sensitivity and quantum efficiency of the photocathode as a function of wavelength. The photocathode used for the PFPCI is sensitive between 250 and 850 nm.

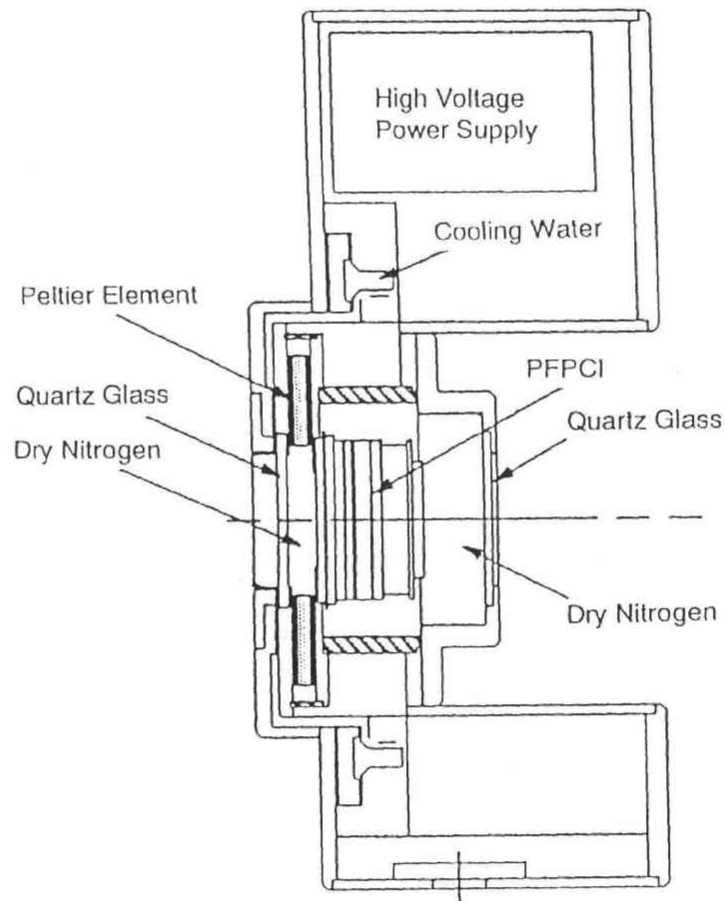


Figure 2.16. Schematic diagram of the PFPCI cooling unit.

the PFPCI in the photon counting mode like the PIH. The typical diameter of photon spots is approximately $50\ \mu\text{m}$, which corresponds to a resolution of 20 line pairs per millimeter.

The image on the fluorescent screen of the PFPCI is reduced and focused with an focusing lens onto the CCD camera located on the bottom of the FPDIS. A flame-transfer-type CCD camera (Ikegami Model FCD-10) with an effective imaging area of $8.8\ \text{mm (H)} \times 6.6\ \text{mm (V)}$ is used to take the image data of the PFPCI. The pixels of the CCD camera are $800\ \text{(H)} \times 490\ \text{(V)}$. The CCD images are read out every 0.033 second and transferred to composite video signals. The composite video output signals are further processed by an image data processor which is described in the following section.

2.4.5 Image data processor and recording system

The composite video signals from the CCD camera are transferred to digital images composed of $512\ \text{(H)} \times 480\ \text{(V)}$ pixels, and are discriminated and integrated by the image data processor where threshold is adjusted to pass the majority of the photoelectron pulses while blocking the majority of the pulses caused by the noise. The integration of image data are usually performed for 600-1800 and 4500-5400 images for auroral OI557.7 nm and OI630.0 nm emissions, respectively. These processes are made with an image processor (Model EXCEL, Nippon Avionics Co., Ltd.), which is controlled by a personal computer (Model PC9801Rx, NEC) (see Figure 2.9).

Thus, each fringe image is given by a 512×480 pixels \times 8 bit binary data with a data size of 245,760 byte. Finally, the fringe image data are recorded on a 5" magnetic optical disk (MO disk) with a magnetic optical disk driver connecting to the personal computer. About 1000 frames of image data, which are equivalent to data amount for three night observations, can be recorded on one side of a MO disk.

2.4.6 Calibration laser

A frequency stabilized He-Ne laser (Model 117A, Spectra-Physics, Inc.) with an output power of 1 mW is used to calibrate the parameters of the etalon and also to monitor the optical spacing drift of the etalon. A view of the laser head and the power supply unit is shown in Figure 2.17. The fluctuation of the laser frequency ($\lambda = 632.8\ \text{nm}$) is less than 1 part in 10^8 , i.e., $\Delta f/f < 1 \times 10^{-8}$, which is small enough to use as a reference wavelength of the FPDIS. The errors in the estimation of the Doppler velocities due to the stability of the calibration laser are less than few meters per second for both OI630.0 nm and OI557.7 nm.

During the laser calibration, skylight is blocked by covering the objective lens with a lens cap. Then, the laser beam enters into the optical path of the FPDIS with an optical fiber and a beam splitter, as shown in Figure 2.10. The beam splitter reflects close to 5% of the incident laser beam, which is diffused with a diffuser to cover the full field of view of the FPDIS.

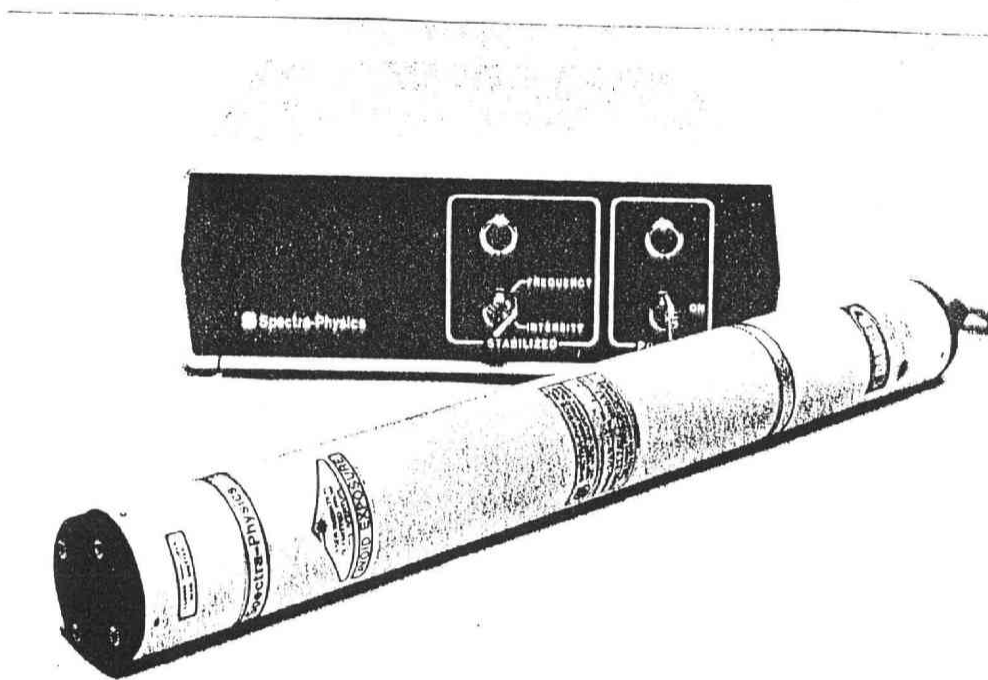


Figure 2.17. View of a laser head and a power supply unit.

Chapter 3

Observations

3.1 Installation of the FPDIS at Syowa station, Antarctica

Fine adjustments of the optics and test observations were performed at Zao observatory, Japan, in August 1993. Then the FPDIS was disassembled and shipped to Syowa station with the research vessel of the Japanese Antarctic Research Expedition 'Shirase'. The installation of the FPDIS at Syowa station was executed in February and March 1994.

The components of the FPDIS were reassembled in the information processing building at Syowa station. Figure 3.1 is an overall view of the optical observation room in the information processing building. The optical system of the FPDIS is seen in the middle of the picture, while the data processing system is seen on the left hand of the picture. Other instruments, e.g., controllers for an SIT all-sky camera and scanning photometers, are seen on the right hand of the picture. Figure 3.2(a) shows the optical system of the FPDIS. A He-Ne laser tube is attached on the left side of the FPDIS, and a monochromatic laser light enters into the optical path with an optical fiber. A CCD camera and a focusing lens are attached at the bottom of the FPDIS. Figure 3.2(b) shows the instruments for image data processing and data storage. An image data processor EXCEL and a monitor are seen in the middle, while a personal computer PC-9801 which controls the EXCEL and a filter selection unit are seen on the right hand of the picture. The top of the FPDIS, i.e., an objective fish-eye lens was set up at a roof opening of the information processing building as shown in Figure 3.3.

Fine adjustments of the optics of the FPDIS were performed by taking the following procedures.

- 1) The adjustment of the fore-optics is performed so as to focus an image on a diffuser paper which was put on the 2-nd aperture.
- 2) The alignment of the optical centers of the optics and the etalon are performed by adjusting a slant angle of the etalon.
- 3) Two etalon plates are adjusted to become exactly parallel by the CS100 etalon controller.
- 4) The adjustment of the imaging-optics is performed so as to focus interference fringes on the photocathode of the PFPCI.
- 5) Finally, the focusing lens which projects the image of the PFPCI onto the CCD is focalized.

3.2 FPDIS observations at Syowa station

We started observations of thermospheric winds and temperatures with the FPDIS in March 1994 when the dark night season began at Syowa station. We obtained FPDIS data for 57 nights during the period from March to September 1994. These data cover various auroral conditions. The dates and times when the FPDIS observations were carried out are listed in Table 3.1 in which selected wavelengths and geomagnetic conditions for each observation are also given. Further, observations for calibration of the FPDIS were carried out occasionally. All-sky star images, which were used to obtain a correct mapping of each point on Fabry-Perot fringes in the CCD images to the sky, were taken on 10 June 1994. To determine the wind-zero position of the interference fringes, fringe data of OI630.0 nm and OI557.7 nm emissions under totally cloudy condition were taken for several nights. The method of calibration using these data is described in Chapter 4.

A conceptual sketch showing a configuration of the FPDIS observation is shown in Figure 3.4. Two auroral emission lines OI630.0 nm and OI557.7 nm, which have peak emission altitudes of ~ 240 km and ~ 105 km, respectively, are observed by the FPDIS. The two fringes of the OI630.0 nm emission cover a region of ~ 700 km in diameter, while the two fringes of the OI557.7 nm emission cover a region of ~ 360 km in diameter. Figure 3.5 is an example of OI630.0 nm fringe images obtained by the FPDIS. Two complete fringes are seen in the image. Note that the intensities of these fringes are not uniform because auroral emissions are not uniform over the sky.

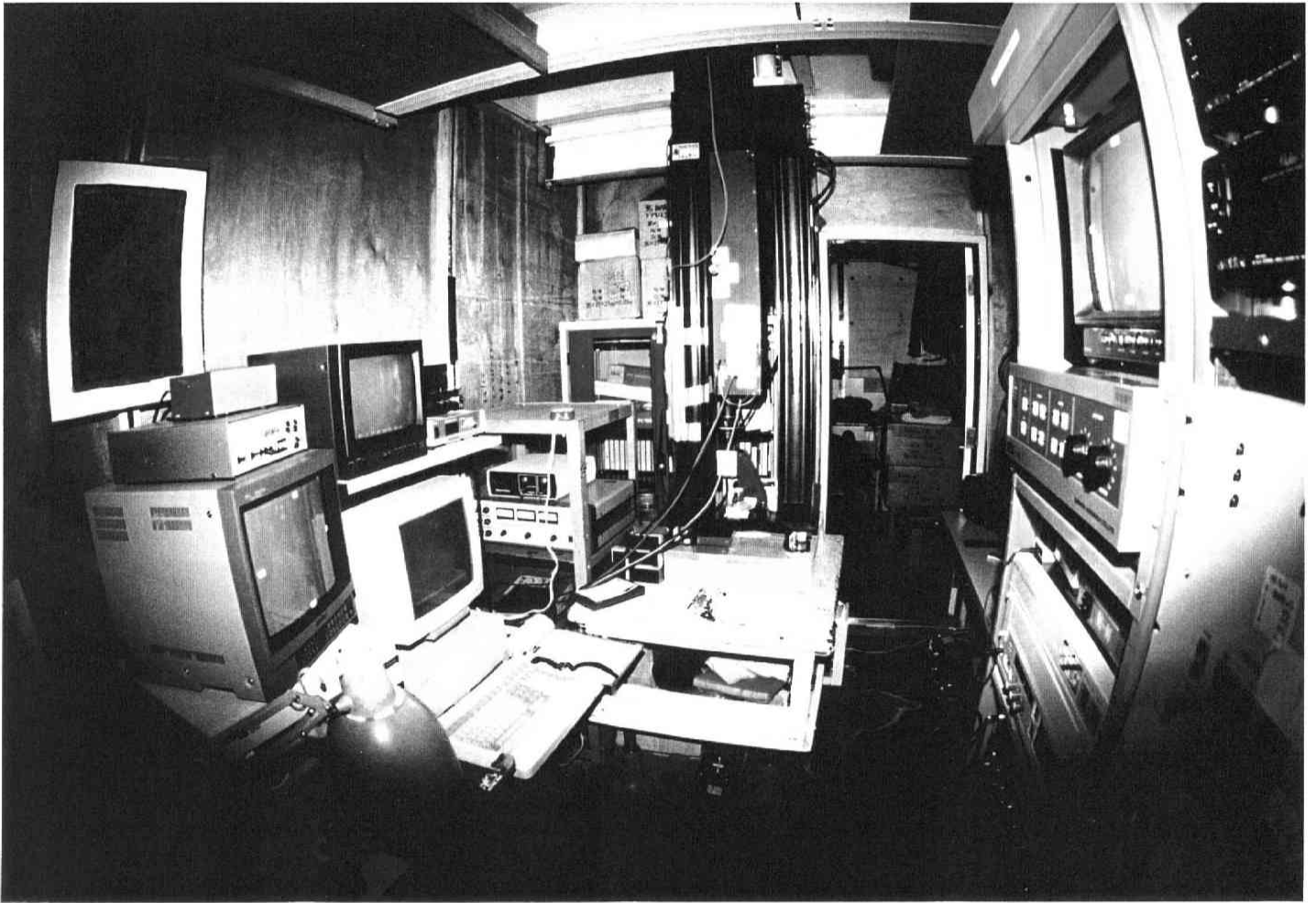


Figure 3.1. Overall view of the FPDIS installed in the information processing building at Syowa station(The picture was taken by a camera with a fish-eye lens). The optical system is seen in the middle, while the data processing system is seen on the left hand.

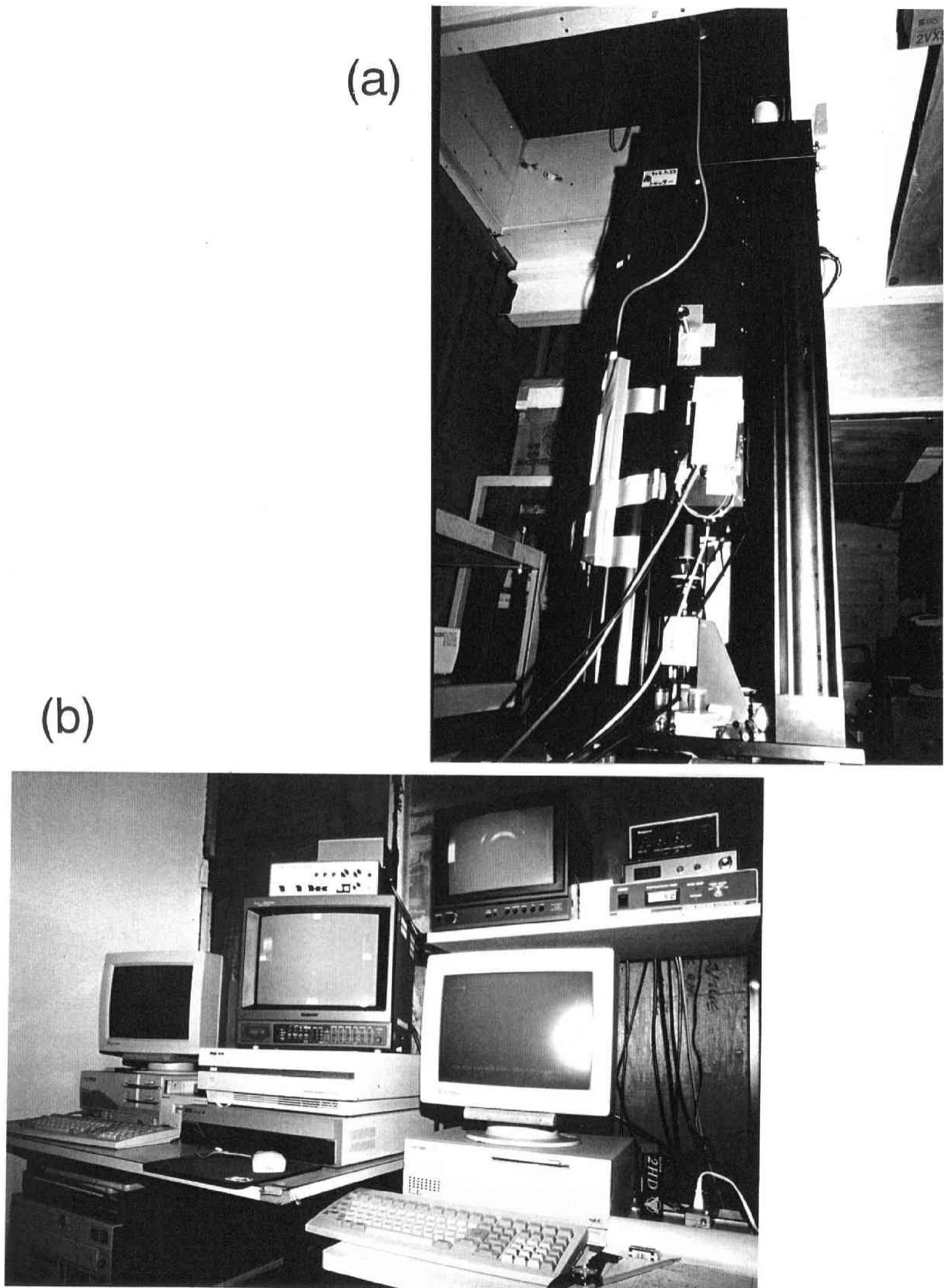


Figure 3.2. (a) The optical system for the FPDIS. A He-Ne laser tube is attached on the left side of the FPDIS, and a monochromatic laser enters into the optical path with an optical fiber which is seen as a blue string on the color picture. A CCD camera and a focusing lens are attached at the bottom of the FPDIS. (b) The instruments for image data processing and data storage of the FPDIS. An image data processor EXCEL and a monitor are seen in the middle, while a personal computer PC-9801 which controls both the EXCEL and a filter selection unit is seen on the right hand.

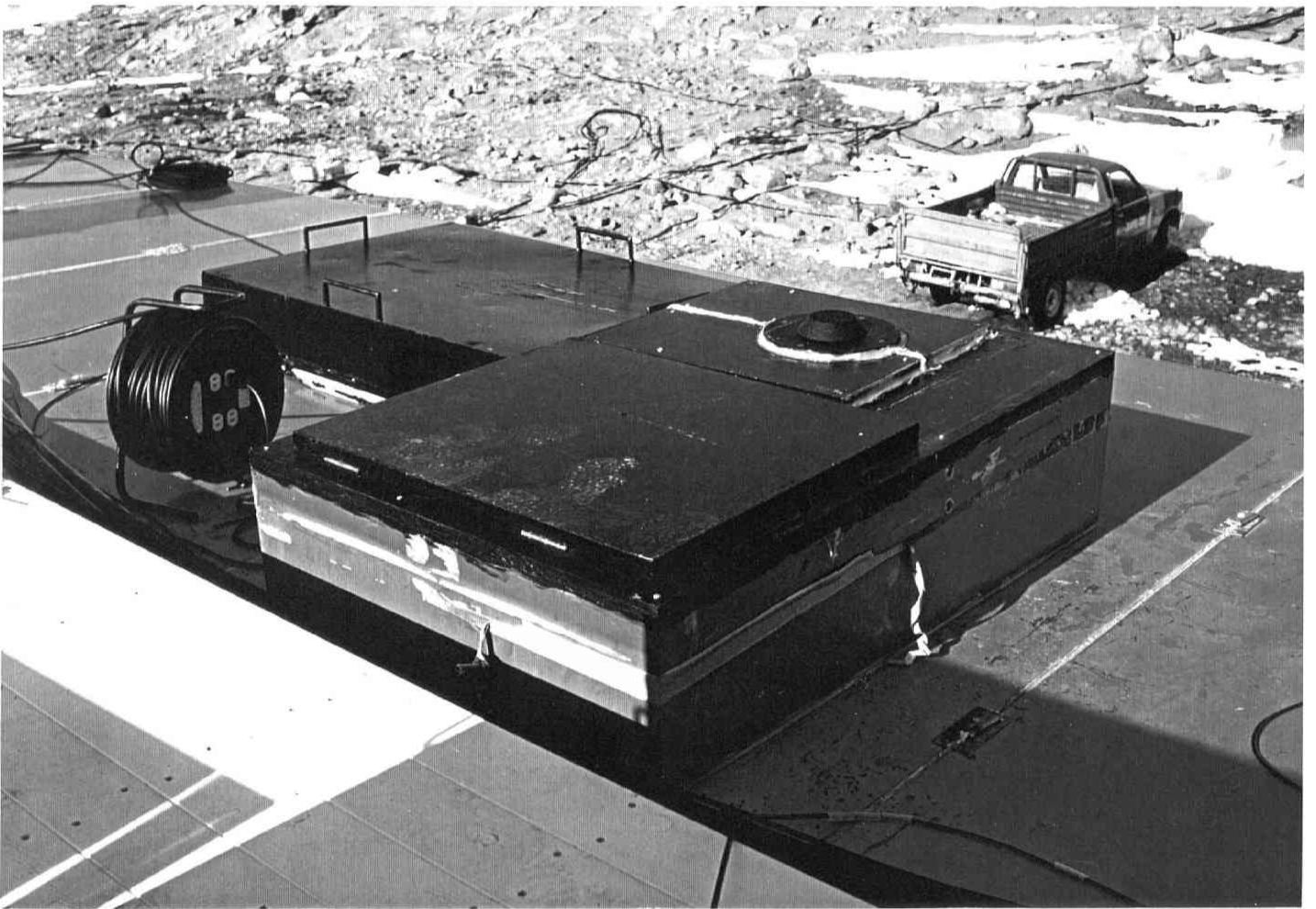


Figure 3.3. View of the roof of the information processing building at Syowa station, Antarctica. A lens projecting from the cover of the roof opening is the objective fish-eye lens of the FPDIS.

Table 3.1. Summary of Fabry-Perot Doppler Imaging observations at Syowa station, Antarctica from March to September, 1994. The symbol 'o' in the column of condition indicates that full observation was made, while the symbol ' Δ ' indicates that observation was made partially. The notation $\sum K_p$ Pre/Next represents the summation of K_p values on the day of observation start and the next day.

Date YYYY/MM/DD	TD	Time(UT) Start End		Total Time	Condi- tion	Obs. 5577	Wave 6300	$\sum K_p$ Pre/Next	comments
1994/ 3/22	81	1827	2252	04h25m	○	◇		26/27	
4/ 4	94	2113	2230	01h17m	○	◇	◇	40/37	
5	95	1707	0148	08h41m	○	◇		37/40	
15	105	1750	0000	06h10m	—	◇	◇	26/31	Cloudy night
17	107	1712	0100	07h48m	○	◇	◇	44/29	
18	108	1647	0249	10h02m	○		◇	29/23	
19	109	1904	0203	06h59m	○	◇		23/16	
20	110	2032	2349	03h17m	○	◇		16/16	
21	111	2232	0056	02h24m	○	◇	◇	16/15	
5/ 6	126	1839	0330	08h51m	○	◇		34/36	
7	127	1645	0350	11h05m	○	◇	◇	36/35	
8	128	1530	0107	09h37m	○	◇	◇	35/31	
11	131	1955	0345	07h50m	—	◇		31/17	Cloudy night
12	132	1817	2353	05h36m	—	◇	◇	17/13	Cloudy night
13	133	1728	2355	06h27m	—	◇		13/26	Cloudy night
18	138	1936	0043	05h07m	Δ	◇	◇	27/18	
30	150	1416	2135	07h19m	○	◇	◇	41/32	
6/ 1	152	1428	0103	10h35m	Δ	◇	◇	30/30	
2	153	1902	0120	06h18m	Δ	◇	◇	30/29	
3	154	1658	0427	11h29m	○	◇	◇	29/27	
4	155	1430	0320	12h50m	○	◇	◇	27/28	
8	159	1510	0440	13h30m	○	◇		17/16	
9	160	1356	0427	14h31m	○	◇	◇	16/24	
10	161	1350	0435	14h45m	○	◇	◇	24/23	All-sky star image
11	162	1400	0453	14h53m	○	◇	◇	23/30	
12	163	1350	0300	13h10m	○	◇	◇	30/22	
16	167	2130	0255	05h25m	Δ		◇	9/15	
29	180	1445	2315	08h30m	○	◇	◇	31/27	
30	181	1415	2205	07h50m	Δ	◇	◇	27/30	

3. OBSERVATIONS

Date YYYY/MM/DD	TD	Time(UT) Start End		Total Time	Condi- tion	Obs. 5577	Wave 6300	Σ Kp Pre/Next	comments
1994/ 7/	1	182	1405 0420	14h15m	○	◇	◇	30/31	
	2	183	1705 1855	01h50m	△	◇	◇	31/20	
	10	192	1605 0420	12h15m	○	◇	◇	8/ 8	
	11	193	1405 0435	14h30m	○	◇	◇	8/ 4	
	12	194	1550 2035	04h45m	△	◇	◇	4/ 8	
	13	195	2110 0325	06h15m	○	◇	◇	8/29	
	15	197	2150 0435	06h45m	○	◇	◇	26/33	
8/ 4	216	216	1720 0345	10h25m	○	◇	◇	5/10	
	5	217	1455 0340	12h45m	○	◇	◇	10/ 8	
	6	218	1455 0340	12h45m	○	◇	◇	8/ 7	
	7	219	1655 1900	02h05m	△	◇	◇	7/ 3	
	10	222	1909 0330	08h21m	○	◇	◇	20/23	
	13	225	2355 0330	03h35m	○	◇	◇	31/30	
	24	236	1550 2003	04h13m	△	◇	◇	11/18	
	26	238	1755 2310	05h15m	○	◇	◇	12/17	
	27	239	1555 0200	10h05m	○	◇		17/12	
	28	240	1555 0221	10h26m	○		◇	12/ 9	
	29	241	1615 0220	10h05m	○	◇		9/ 7	
	30	242	1615 0210	09h55m	○		◇	7/11	
	31	243	1720 0215	08h55m	△	◇		11/19	
9/ 1	244	244	1626 0200	09h34m	○		◇	19/10	
	2	245	1730 0120	07h50m	—	◇		10/13	Cloudy night
	3	246	2015 0120	05h05m	—		◇	13/ 9	Cloudy night
	4	247	1925 0110	05h45m	—	◇		9/18	Cloudy night
	5	248	1705 2200	04h55m	—		◇	18/22	Cloudy night
	9	252	2050 0153	05h03m	○	◇	◇	35/26	
	25	268	1830 0005	05h35m	○	◇		19/26	
	26	269	1810 2355	05h45m	○		◇	26/26	

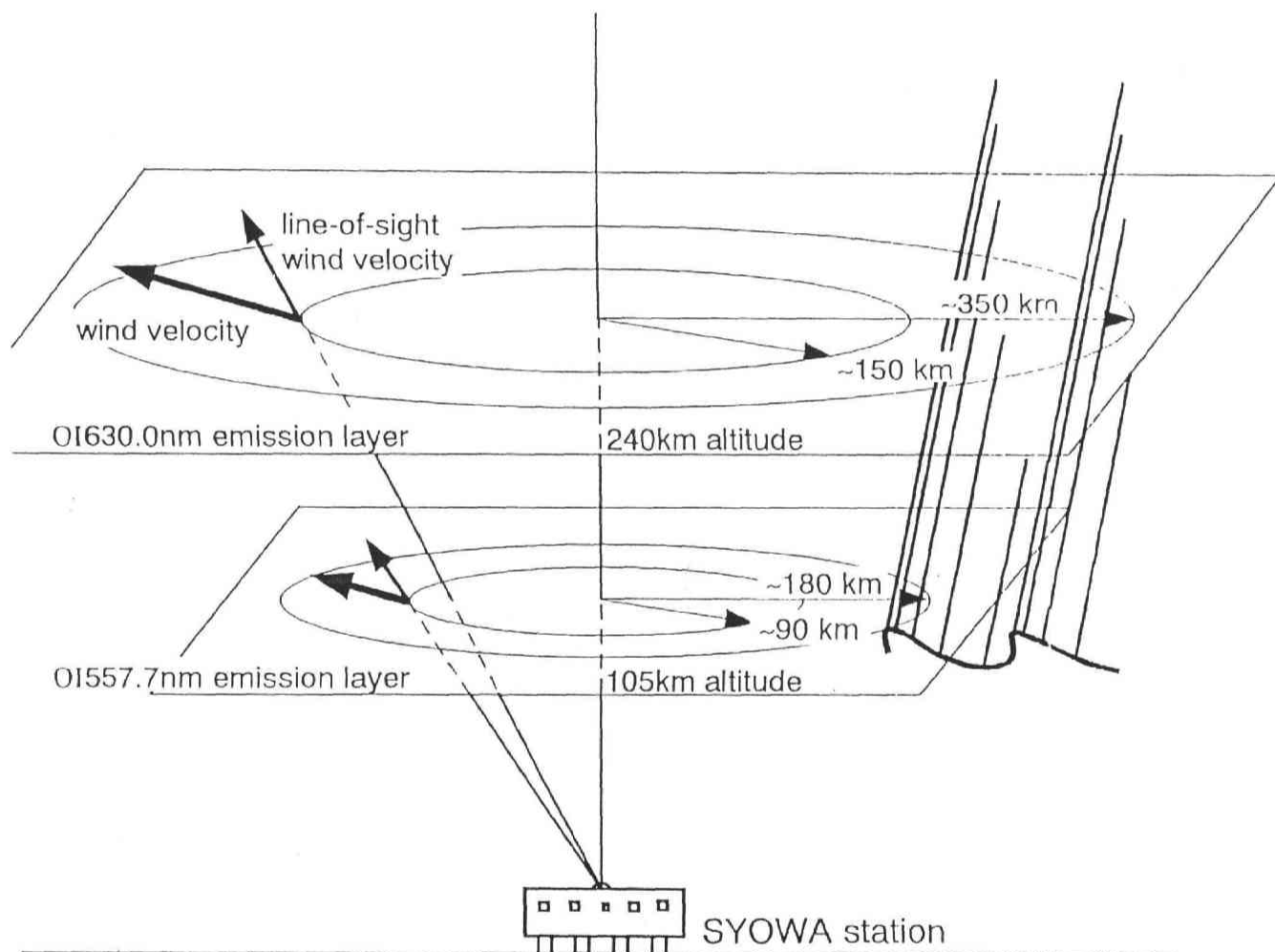


Figure 3.4. Conceptual sketch of the configuration of observations with the FPDIS.

OI630.0nm fringes

94/ 6/11 23:21 UT

SYOWA station

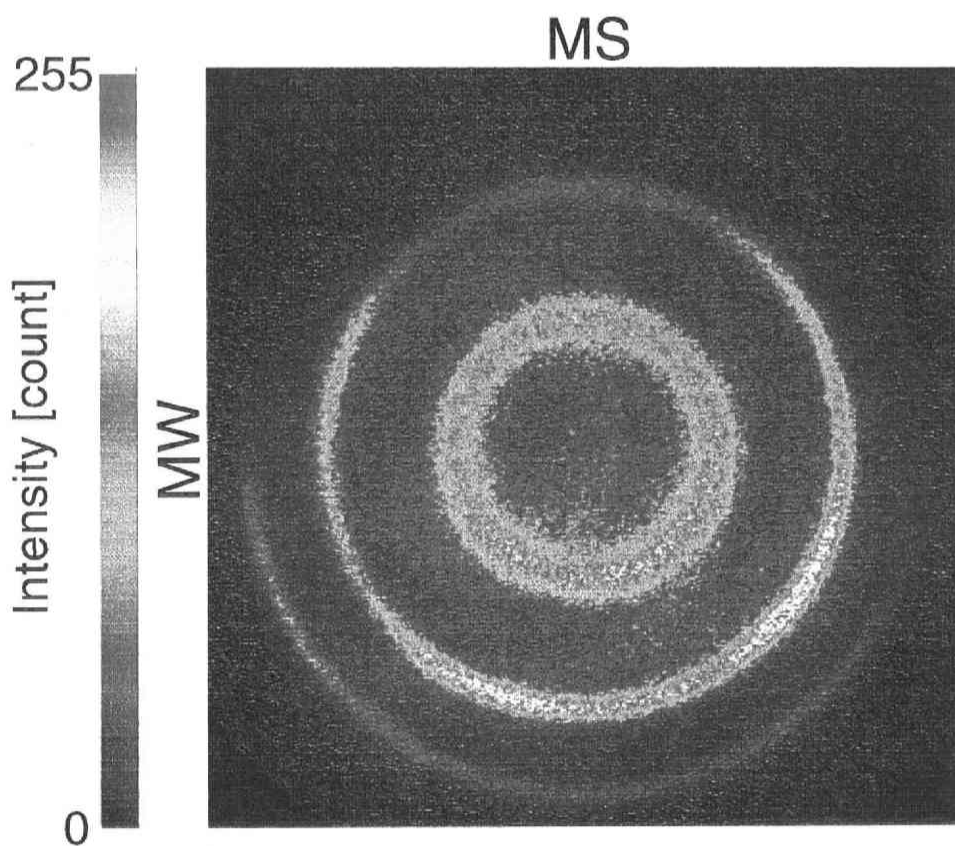


Figure 3.5. Example of OI630.0 nm fringe image obtained by the FPDIS.

All operations of the FPDIS are automatically executed by instructions from a personal computer. For example, the selection of the emission lines OI630.0 nm and OI557.7 nm is automatically performed by rotating the filter wheel. The personal computer also controls the time sequence of the FPDIS operation. Fringe image data read out from the CCD are integrated by the image processor as described in Section 2.4.5. The integration time is usually 150-240 sec for the OI630.0 nm emission and 18-30 sec for the OI557.7 nm emission. To save each image data on a magneto-optical disk, it takes 30 sec. If necessary, the rotation of the filter wheel is performed during this time interval. Figure 3.6 presents three kinds of the time sequences for the FPDIS operation. In the time sequence (a) two fringe images of the He-Ne calibration laser beam are taken at the head of 1-hour interval to check thermal drifts of etalon parameters as described in Chapter 4. Then, the cycle of successive three fringe images, one OI630.0 nm fringe image and two OI557.7 nm fringe images, is repeated. In the time sequence (b) fringe images of only the OI630.0 nm emission are observed, while in the time sequence (c) fringe images of only the OI557.7 nm emission are observed. For 35 nights out of 57 nights, the time sequence (a) was used. The time sequences (b) and (c) were used for 8 and 14 nights, respectively.

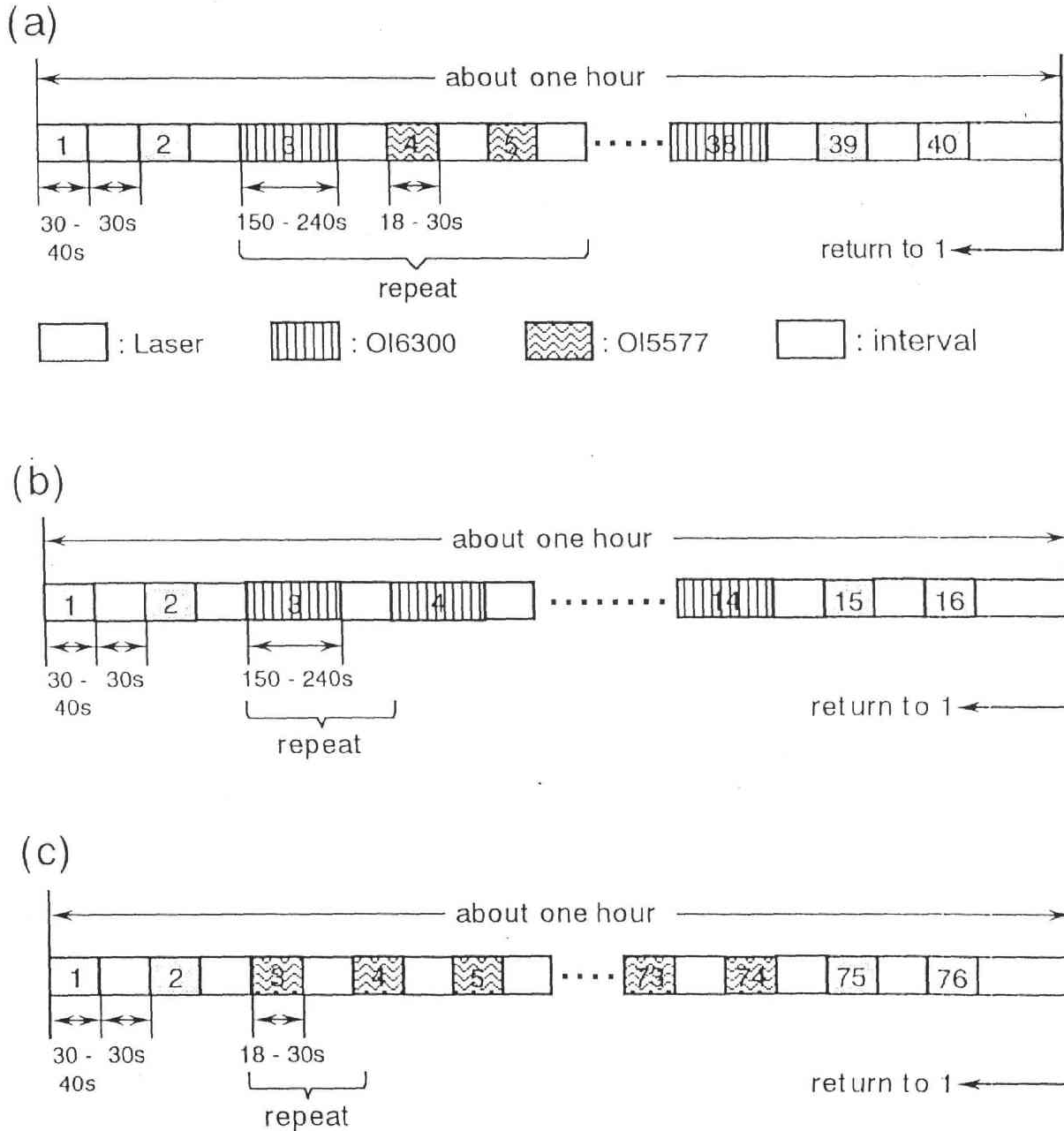


Figure 3.6. Time sequence of the FPDIS observation: (a) alternation of OI630.0 nm and OI557.7 nm, (b) only OI630.0 nm, and (c) only OI557.7 nm. These time sequences are repeated during observations.

Chapter 4

Procedures of Data Analysis

4.1 Determination of etalon parameters and fringe center using a calibration laser

Since the Doppler shifts of auroral emission lines due to neutral winds are extremely small, it is essential to determine both the etalon parameters described in Section 4.1.1 and the center position of fringe with the uppermost accuracy. For this purpose, fringe images of monochromatic light from a frequency-stabilized He-Ne laser were taken every one hour during auroral observation (see Figure 3.6).

4.1.1 Determination of fringe center

The procedure for determining the fringe center position using the He-Ne laser is as follows.

- 1) Four sequential laser fringe images are superposed and sliced in the horizontal direction with an initial guess of the center position on the Y-coordinate, as shown in Figure 4.1. An example of sliced image data is also shown in Figure 4.1 in which the abscissa is represented with the radius-squared coordinate described in Section 4.1.2. In order to reduce noises in the image data, five successive slices data are superposed, so that the count levels of the image data can exceed 256 counts. Since there are two fringes in FPDIS images, four peaks are seen in the sliced data. The 1-st and 4-th peaks from the left hand correspond to the outer fringe, while the 2-nd and 3-rd peaks correspond to the inner fringe.

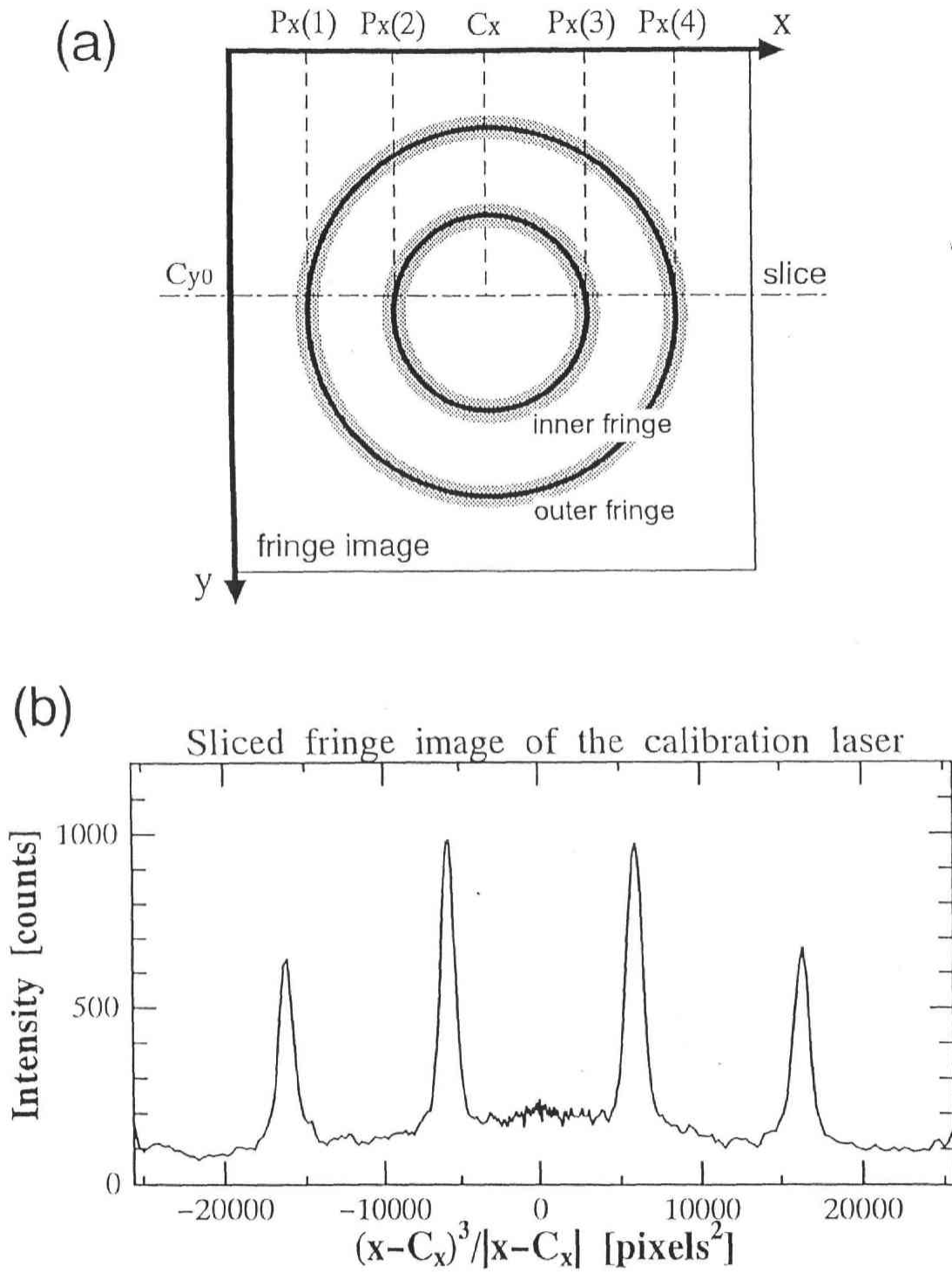


Figure 4.1. (a) Slicing of the fringe image. Here, X and Y-coordinates denote the horizontal and the vertical direction, respectively. C_{y0} is an initial guess for the center position in Y-coordinate. (b) Example of the sliced image data. The abscissa represents the radius-squared coordinate $((x - C_x)^3 / |x - C_x|)$, while the ordinate represents the count number of the image data.

- 2) Each fringe peak in the sliced image data is fitted by Gaussian function with a nonlinear, least-squares method. Gaussian function is given by

$$G(r) = A \exp \left\{ -\frac{(r - P)^2}{B^2} \right\} \quad (4.1)$$

where constants A , B , and P are determined by the fitting. Since, there are four peaks in the sliced image data, four sets of the constants are obtained. If the constants are represented as $A_x(1)$, $B_x(1)$, $P_x(1)$ for the 1-st peak, $A_x(2)$, $B_x(2)$, $P_x(2)$ for the 2-nd peak, and so on, the fringe center position on the X coordinate, C_x , is given by

$$C_x = \frac{1}{2} \left\{ \frac{P_x(3) + P_x(2)}{2} + \frac{P_x(4) + P_x(1)}{2} \right\}. \quad (4.2)$$

The right side of this equation represents a mean value of the four peak positions at the inner and outer fringes.

- 3) Next, the laser fringe image are sliced in the vertical direction at $x = C_x$. In the same way as C_x , the center position for the Y-coordinate, C_y , is given by

$$C_y = \frac{1}{2} \left\{ \frac{P_y(3) + P_y(2)}{2} + \frac{P_y(4) + P_y(1)}{2} \right\}. \quad (4.3)$$

- 4) Then, the laser fringe image is sliced again in the horizontal direction at $y = C_y$. These steps are repeated until the values of C_x and C_y converge to certain values.

4.1.2 Conversion of image coordinates

From equation 2.7, a normalized Airy function, which represents a transmission profile of an ideal etalon, is expressed as

$$A(\delta) = \frac{1}{2\pi} T_F = \frac{1}{2\pi} \left\{ \frac{(1 - R)^2}{1 - 2R \cos \delta + R^2} \right\}, \quad (4.4)$$

where

$$\delta = \frac{2\pi}{\lambda} 2nd \cos \phi - 2\chi. \quad (4.5)$$

Here, R is the reflectance at the surfaces of the etalon plate, δ is the total phase difference between the adjoining rays emerging from the etalon, n is the reflective index of the medium in the etalon cavity, d is the etalon spacing, λ is the wavelength of the incident light, and ϕ is the incident angle of the ray. Expanding equation 4.5 by Taylor series, we get

$$\delta = \frac{4\pi nd}{\lambda} \left(1 - \frac{\phi^2}{2!} + \frac{\phi^4}{4!} - \dots \right) - 2\chi. \quad (4.6)$$

When ϕ is sufficiently small, it can be written as

$$\phi \simeq \tan \phi \simeq r/f, \quad (4.7)$$

where r is the distance from the center of fringe on the detector, and f is the focal length of the focusing lens. Using this relation, equation 4.6 can be rewritten as

$$\delta = \frac{4\pi nd}{\lambda} \left(1 - \frac{r^2}{2!f^2} + \frac{r^4}{4!f^4} - \dots \right) - 2\chi. \quad (4.8)$$

Because $f \gg r$, the third and subsequent terms within parentheses in the right side of equation 4.8 can be neglected, i.e.,

$$\delta = \frac{4\pi nd}{\lambda} \left(1 - \frac{r^2}{2!f^2} \right) - 2\chi. \quad (4.9)$$

When the values of n , d , λ and f are constant, δ is linear to r^2 . Therefore, it is convenient to use r^2 instead of r as a variable to represent the position in the fringe image. This is the conversion of the image coordinates from the real-pixel coordinates (R space) on the image plane into the radius-squared coordinates (X space). Figures 4.2(a) and (b) show examples of sliced fringe images in the R and X space, respectively. The variable r representing the distance from the center of fringes is converted into the squared distance in the X space as $r^3/|r|$.

4.1.3 Correction of drifting etalon parameters

According to equation 4.4, the transmittance of etalon has maxima at $\delta = 2m\pi$ ($m = 0, 1, 2, \dots$), i.e.,

$$\begin{aligned} \left(m + \frac{\chi}{\pi} \right) \lambda &= 2nd \cos \phi \\ &\simeq 2nd \left\{ 1 - \frac{r^2}{2!f^2} \right\}. \end{aligned} \quad (4.10)$$

Here, m is an order number of the interference, and r represents a fringe radius. If the values of n , d , f , χ , and λ are constant, the fringe radius r must be a constant value. However, in actually, the value of r varies during observation. Figure 4.3 shows variations of the fringes of the stabilized He-Ne laser. The radii of both inner and outer fringes are reduced gradually during the observation. This radius variation is considered to be caused by drifts of etalon parameters with a change of room temperature (mainly a drift of the etalon spacing d with temperature).

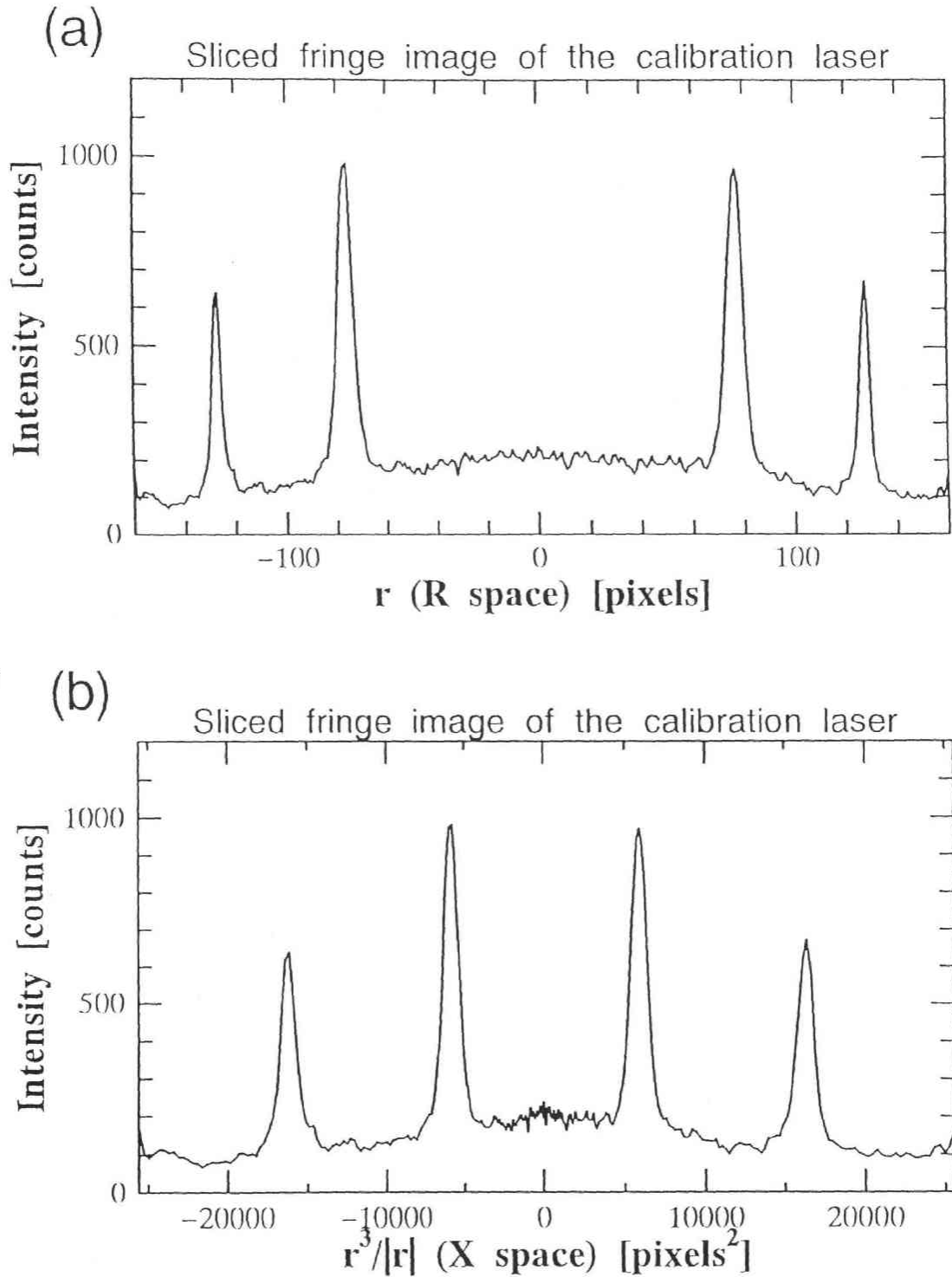


Figure 4.2. Conversion of real-pixel coordinates (R space) on the image plane into radius-squared coordinates (X space). Sliced fringes of a calibration laser image are shown with the abscissa of (a) R space, and (b) X space.

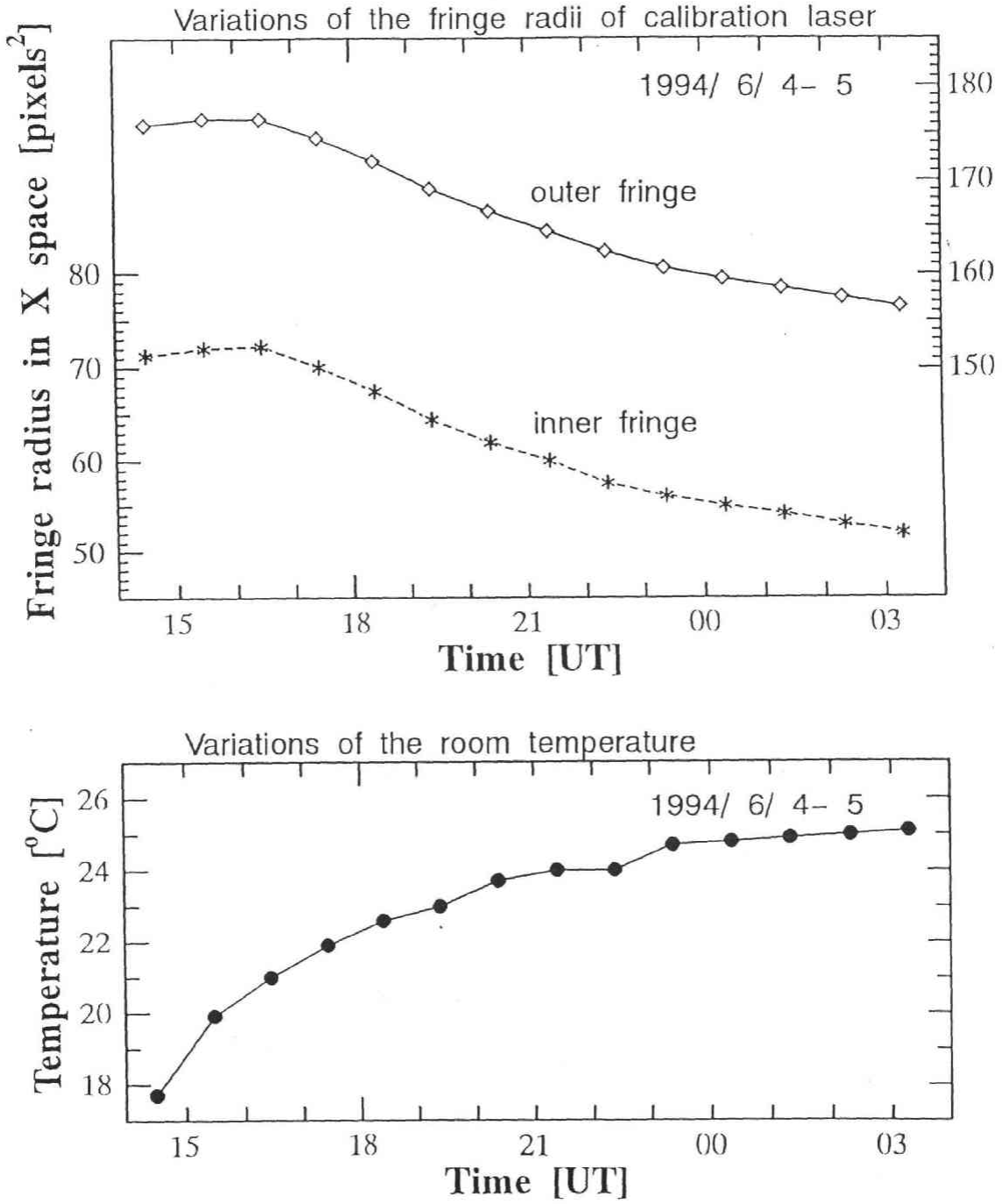


Figure 4.3. Variations of the He-Ne laser fringes over the observation time on 4-5 June, 1994. Laser fringe images are obtained every one hour. The ordinate represents the X-position of the image. The scale for the inner fringe is indicated on the left hand, while the scale for the outer fringe is indicated on the right hand. Symbols '*' and 'o' stand for the radii of inner and outer fringes, respectively. The lower panel shows a variation of room temperature for the same time interval.

Using equation 4.9, two adjacent, inner and outer fringes of the He-Ne laser are described as

$$\left(m + \frac{\chi}{\pi}\right) \lambda_l = 2nd(t) \left(1 - \frac{r_{out}^2}{2!f^2}\right) \quad (4.11)$$

$$\left(m + 1 + \frac{\chi}{\pi}\right) \lambda_l = 2nd(t) \left(1 - \frac{r_{in}^2}{2!f^2}\right) . \quad (4.12)$$

Here, r_{in} and r_{out} are the radii of the inner and outer fringes, respectively, λ_l is the wavelength of the He-Ne laser, f is the focal length of the focusing lens, and $d(t)$ is the etalon spacing at a time t when a fringe image is observed. From equations 4.11 and 4.12, the etalon parameter $2nd(t)$ is given by

$$2nd(t) = \frac{2f^2\lambda_l}{r_{out}^2 - r_{in}^2} . \quad (4.13)$$

Using equation 4.13, we can get the value of the etalon parameter $2nd(t)$ from the radii of the two adjacent fringes of the He-Ne laser. We usually performed measurements of laser fringe images every one hour during observation. These calibration data are necessary to derive wind velocities precisely.

4.2 Derivation of line-of-sight wind velocities from Doppler image data

The Doppler shifts of aurora emission lines are caused by the bulk motion (wind) of the thermospheric neutral atmosphere. Using the Doppler shift data of aurora fringe images obtained by the FPDIS, we can estimate line-of-sight (LOS) wind velocities in the thermosphere. The basic principle and the method to determine the LOS wind velocities are described in this section.

After the determination of the fringe center position by the method described in Section 4.1.1, fringe images obtained by the FPDIS are sliced in the azimuthal directions with every one degree, and the coordinates are converted into the X space (see Section 4.1.2). Then fifteen successive sliced images are superposed to reduce the noise level of the image data. On this way, the fringe images divided with 15 degree separations are converted to 12 sliced profiles. Figure 4.4 shows the divided fringes and the points at which the LOS wind velocities are calculated. The total number of these points is 48 with 24 for each of the inner and outer fringes.

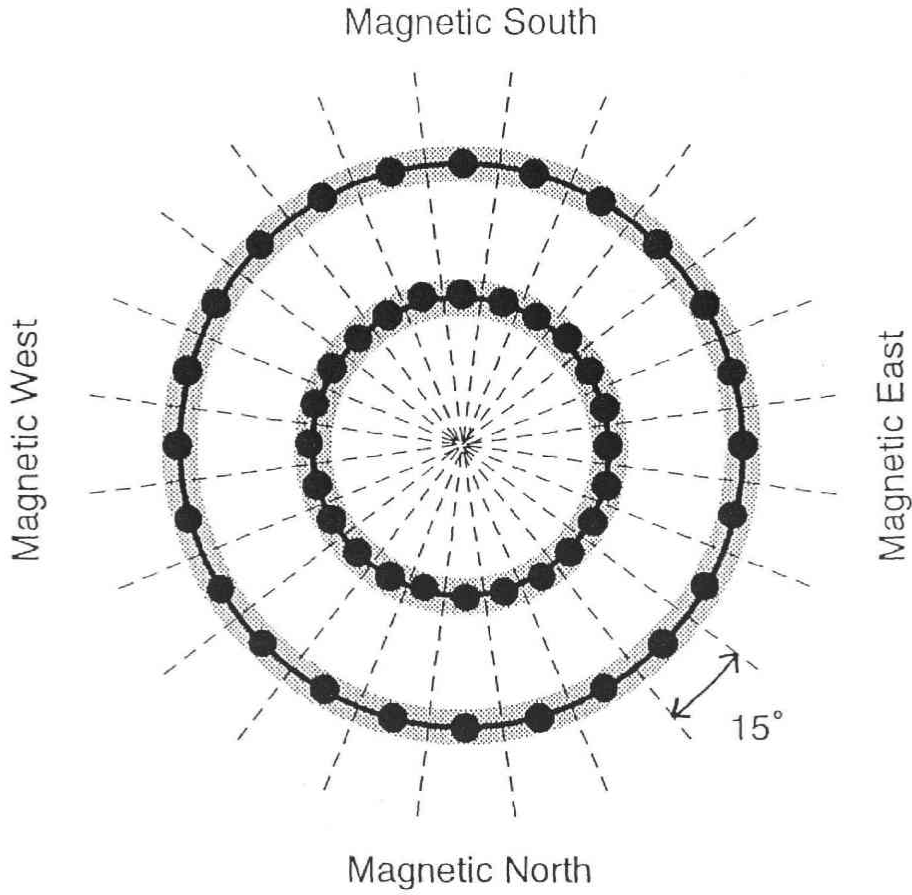


Figure 4.4. Partition of the fringes. Symbol '•' indicates the locations where Doppler wind velocities are derived.

Each sliced fringe profile is fitted by the Gaussian function given by equation 4.1 using a non-linear least squares method, and the peak position is determined. Obtained fringe radius r_{obs} , which is identical with the peak position, satisfies the next equation

$$\left(m + \frac{\chi}{\pi}\right) (\lambda_{au} - \Delta\lambda_{au}) = 2nd(t) \left(1 - \frac{r_{obs}^2}{2!f^2}\right). \quad (4.14)$$

In the above equation, λ_{au} is the wavelength of observed auroral emission, and $\Delta\lambda_{au}$ is the Doppler shift. Further, when the auroral emission has no Doppler shift, the fringe radius r_0 satisfies the next equation

$$\left(m + \frac{\chi}{\pi}\right) \cdot \lambda_{au} = 2nd(t_0) \left(1 - \frac{r_0^2}{2!f^2}\right). \quad (4.15)$$

This fringe is called 'wind-zero fringe'. Here, t_0 is the time when the wind-zero fringe is observed. On the other hand, the relationship between the Doppler shift $\Delta\lambda_{au}$ and the LOS

wind velocity v is given by

$$\frac{\lambda_{au} + \Delta\lambda_{au}}{\lambda_{au}} = \frac{c + v}{c}, \quad (4.16)$$

where c is the velocity of light. From equations 4.14, 4.15 and 4.16, the LOS wind velocity v is given as

$$v = \frac{2nd(t)}{2nd(t_0)} \cdot \frac{2f^2 - r_{au}^2}{2f^2 - r_0^2} \cdot c. \quad (4.17)$$

The wind-zero fringe which is necessary to estimate the Doppler wind velocity is obtained by the following procedure.

Fringe images of aurora obtained during weak auroral activity are selected first. We can assume that there is no vertical wind in such a period. Then the fringe images over a few hours are superposed for improving the signal-to-noise ratio. The superposed fringe image is divided into 24 sectors with 15 degree azimuthal separations, and each fringe radius is determined. The average of the fringe radii in the 24 azimuthal directions is adopted as the wind-zero fringe radius, since divergence or convergence of wind along a closed path of each fringe is considered very small in the case that there is no vertical wind. Thus, we adopt the averaged fringe radius as the zero velocity.

4.3 Error estimation in wind velocity measurement

4.3.1 Photon noise

The technique for error estimation described in this section was originally developed for data processing the prototype FPDIS [Nakajima, 1993, Nakajima et al., 1995]. To estimate the influence of photon noise to wind velocities, we executed the following numerical simulation.

First, noise-free fringe profiles of the calibration laser and OI630.0 nm and OI557.7 nm auroral emissions are generated with an equation given by

$$\begin{aligned} N_r = & C_{or} t \frac{1-R}{1+R} \left(\frac{\partial R}{\partial \lambda_0} \overline{\delta \lambda_F} + R_0 T_{F_0} \right. \\ & \times \left[1 + 2 \sum_{n=1}^{\infty} R^n \cos(n\delta) \operatorname{sinc} \left(\frac{n}{N_f} \right) \right. \\ & \left. \left. \times \exp \left\{ -\frac{n^2(D^2 + G^2)}{4} \right\} \right] \right) + B_r. \end{aligned} \quad (4.18)$$

Here, N_r is the counting rate of the detector at the distance r from the fringe center for a selected auroral emission line, C_{or} represents the sensitivity of the FPDIS corresponding

to the instrumental parameters, t is the integral time period, $\partial R/\partial \lambda|_0$ is the background continuum for a unit wavelength, $\overline{\delta \lambda_F}$ is the filter integral width in nanometers, R_0 is the surface brightness of the source emission, T_{F_0} is the transmittance of the prefilter used to select the emission line, and $1 + 2 \sum_{n=1}^{\infty} R^n \cos(n\delta)$ represents the Airy function. Further, $\text{sinc}(n/N_f)$ comes from the spherical defect and D^2 from microscopic defects of the etalon, respectively, G^2 comes from the Gaussian width corresponding to the kinetic temperature of the source, and B_r is the background noise of the detector. The method of the derivation of equation 4.18 is described by *Hernandez* [1996]. The calculation is made using the values for the effective aperture, spacing and reflectivity of the etalon, transmittance of the filter, transmittance of the optics, quantum efficiency, and background dark-noise count of the detector. The wavelength λ_0 , luminosity of the source R_0 , kinetic temperature T_0 , and line-of-sight velocity v_0 are given in the calculation as variables.

After noise-free fringe profiles have been generated, random noise is superposed on them. The standard deviation (SD) of random noise is determined such that its value is equal to the square root of the model fringe data, as defined by the statistical theory. These model fringe data are then subjected to data analysis to derive the wind velocity v_d . The difference between derived values and assumed values $|v_d - v_0|$ is defined as error in this analysis. The same procedure with the same SD but different random noise is repeated 100 times.

It seems reasonable that the SD of the derived wind velocity represents the error of the FPDIS measurement. These error values have been calculated for various levels of temperature and source luminosity and at various positions on the detector. Figure 4.5 shows SD of derived wind velocities versus the maximum counts at fringe peaks. The result in Figure 4.5 is similar to the result of numerical error analysis conducted by *Hays and Roble* [1971]. It is apparent that errors of the wind velocity increase rapidly as the peak counts become less than 100. The higher the temperature of emission gas becomes, the larger the error becomes. Consequently, we do not use the FPDIS data in the case that peak counts are less than 150. Thus, random errors in wind velocities derived from OI630.0 nm emission fringes are estimated to be less than 25 m/s for the inner fringe, and 35 m/s for the outer fringe.

In this error simulation, however, detector dark noise and CCD readout noise are not included. These noises appear to be discriminated out through photon counting described in Sections 2.3.3 and 2.4.5.

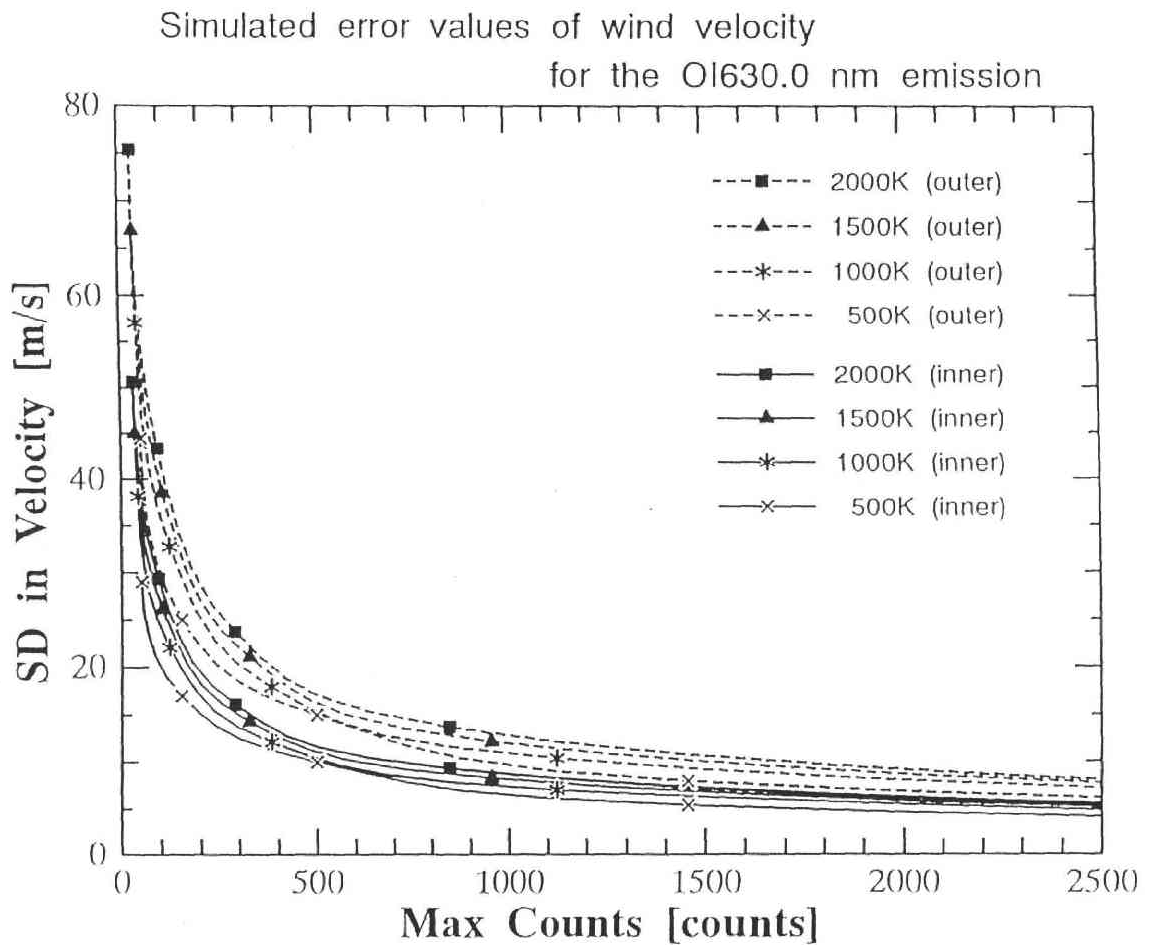


Figure 4.5. Calculated standard deviation (SD) versus maximum counts at fringe peaks. The SD of wind velocities is given for inner (solid lines) and outer (broken lines) fringes of the OI630.0 nm emission. The temperatures assumed in this simulation are 500, 1000, 1500, and 2000 K.

The error simulation presented above has been performed for the OI630.0 nm emission. In the case of the OI557.7 nm emission, errors in derived wind velocities are thought to become smaller, since the kinetic temperature of the OI557.7 nm emission layer at ~ 100 km is lower than that of the OI630.0 nm emission layer at ~ 250 km, and the peak counts of the OI557.7 nm emission fringes are usually larger than those of the OI630.0 nm emission fringes.

4.3.2 Influence of non-uniform auroral emission intensity

A fringe profile of the Fabry-Perot etalon is exactly represented with the Airy function given by equation 4.4 when auroral emission intensity is uniform over the entire field of view of the FPDIS. However, in most cases, the auroral emission intensity is not uniform over the sky. This non-uniformity causes shifts of fringe peak positions. To estimate the influence of non-uniform auroral emission on derived wind velocities, we have executed a numerical simulation. The principle of this simulation is as follows.

First, fringe profiles of the OI630.0 nm or OI557.7 nm emission with a uniform distribution are generated with equation 4.18, and the peak position P_0 is determined by Gaussian fitting. Next, fringe profiles of non-uniform emission source are generated, and the peak position P_x is determined in the same way. Figure 4.6 shows intensity profiles of the OI630.0 nm emission. The source emission intensity R_0 are given by

$$R_0 = \frac{10^5}{1 + \left(\frac{x}{P_0}\right)^\beta} \quad [\text{Rayleigh}] \quad (4.19)$$

where x is the position in the X space, P_0 represents the inner fringe peak position, β is a parameter which decides an emission intensity gradient, and *Rayleigh* is the unit representing the intensity of auroral emission. In this simulation, the calculation has been performed for five kinds of source emission patterns corresponding to $\beta = 0, 1, 2, 4,$ and $8,$ respectively. Figure 4.7 shows examples of the calculated fringe profiles for (a) a uniform emission source and (b) a non-uniform emission source. In Figure 4.7(b), the peak intensity of the outer fringe is weaker than that of the inner fringe, corresponding to the gradient of source emission intensity. Figure 4.8 shows two fringe profiles, one (solid line) for a uniform source and the other (broken line) for a non-uniform source. It is apparent that there is a small difference between the two peak positions of P_0 and P_x in the x space.

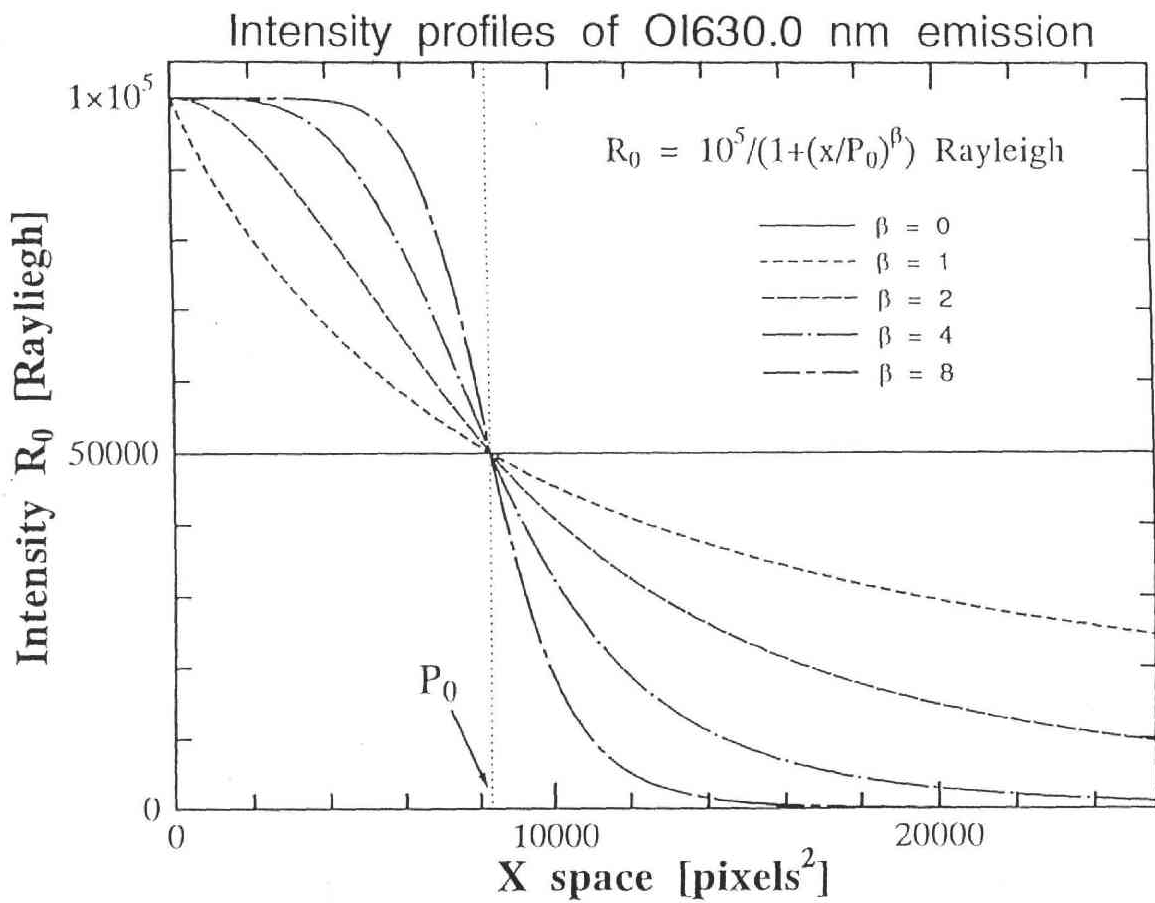


Figure 4.6. Source emission intensity profiles used for investigating the influence of the non-uniformity of auroral emission intensity. Five kinds of source emission patterns corresponding to $\beta = 0, 1, 2, 4,$ and 8 were prepared in this simulation.

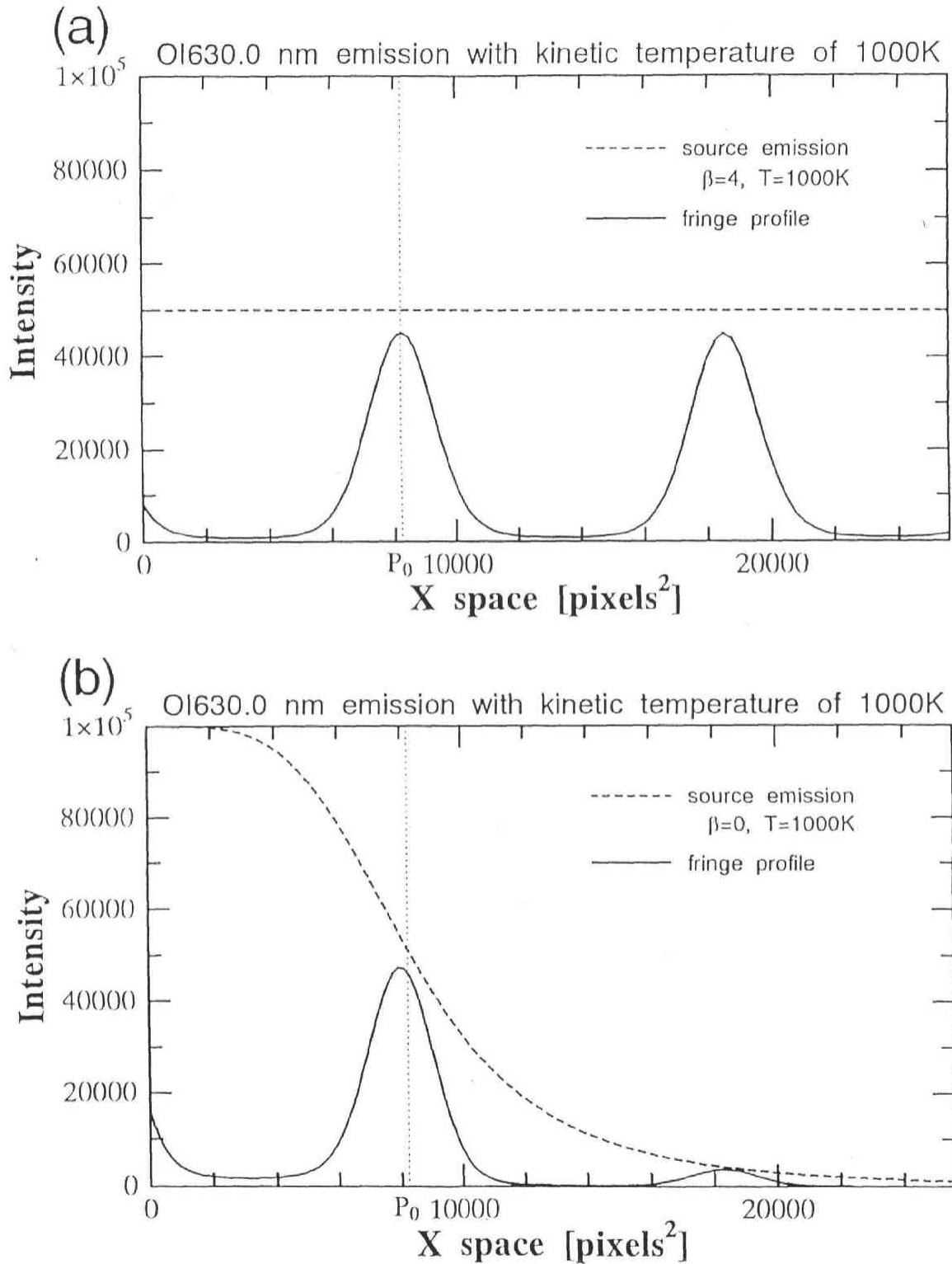


Figure 4.7. Examples of source emission intensity profiles and calculated fringe profiles for (a) a uniform emission source and (b) a non-uniform emission source. The OI630.0 nm emission with a kinetic temperature of 1000 K is assumed as the emission source.

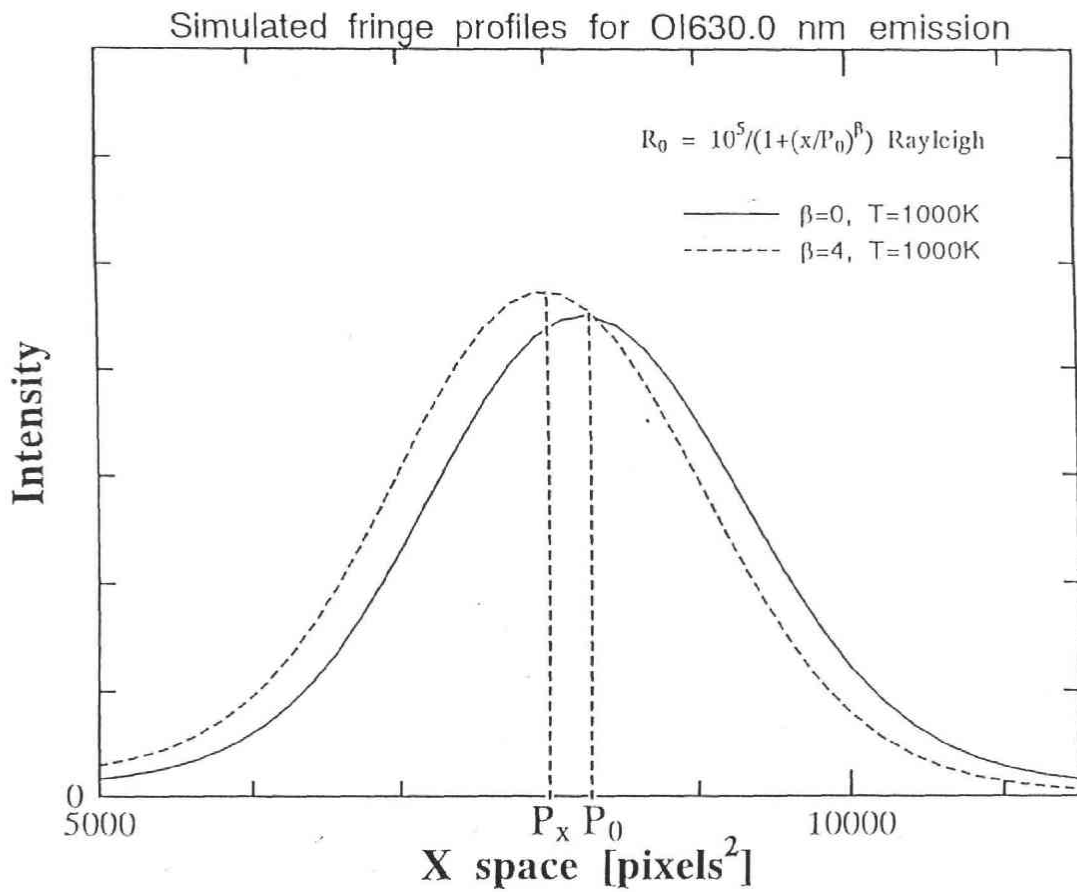


Figure 4.8. Fringe profiles for a uniform source (solid line) and a non-uniform source (broken line). The OI630.0 nm emission with a kinetic temperature of 1000 K is assumed as the emission source.

This difference causes an error dv in the wind velocity estimation as

$$dv = \frac{P_x^2 - P_0^2}{2f^2 - P_0^2} c \quad (4.20)$$

where f is the focal length of the focusing lens and c is the velocity of light. The values of this error are calculated for various kinetic temperatures.

Figure 4.9 shows the error dv as a function of the gradient of source emission intensity. It can be clearly seen from this figure that the error in the wind velocity becomes larger as the gradient of source emission intensity becomes larger. It is also found that the error becomes larger as the temperature becomes higher. Thus, non-uniformity of auroral emission affects the wind velocity estimation when the gradient $(dR_0/dx)_{x=P_0}$ is larger than 2 for the OI630.0 nm emission, or 10 for the OI557.7 nm emission. Actually, it is difficult to know the exact value of $(dR_0/dx)_{x=P_0}$, since monochromatic imaging observations were not carried out simultaneously. It is likely that weak auroras satisfy the condition mentioned above. It is also supposed that bright auroras moving rapidly satisfy the condition because the non-uniform distribution of auroral emission is smoothed due to image integration over an exposure time. However, it is necessary to consider the effect of non-uniform intensity distribution for bright and stable auroras.

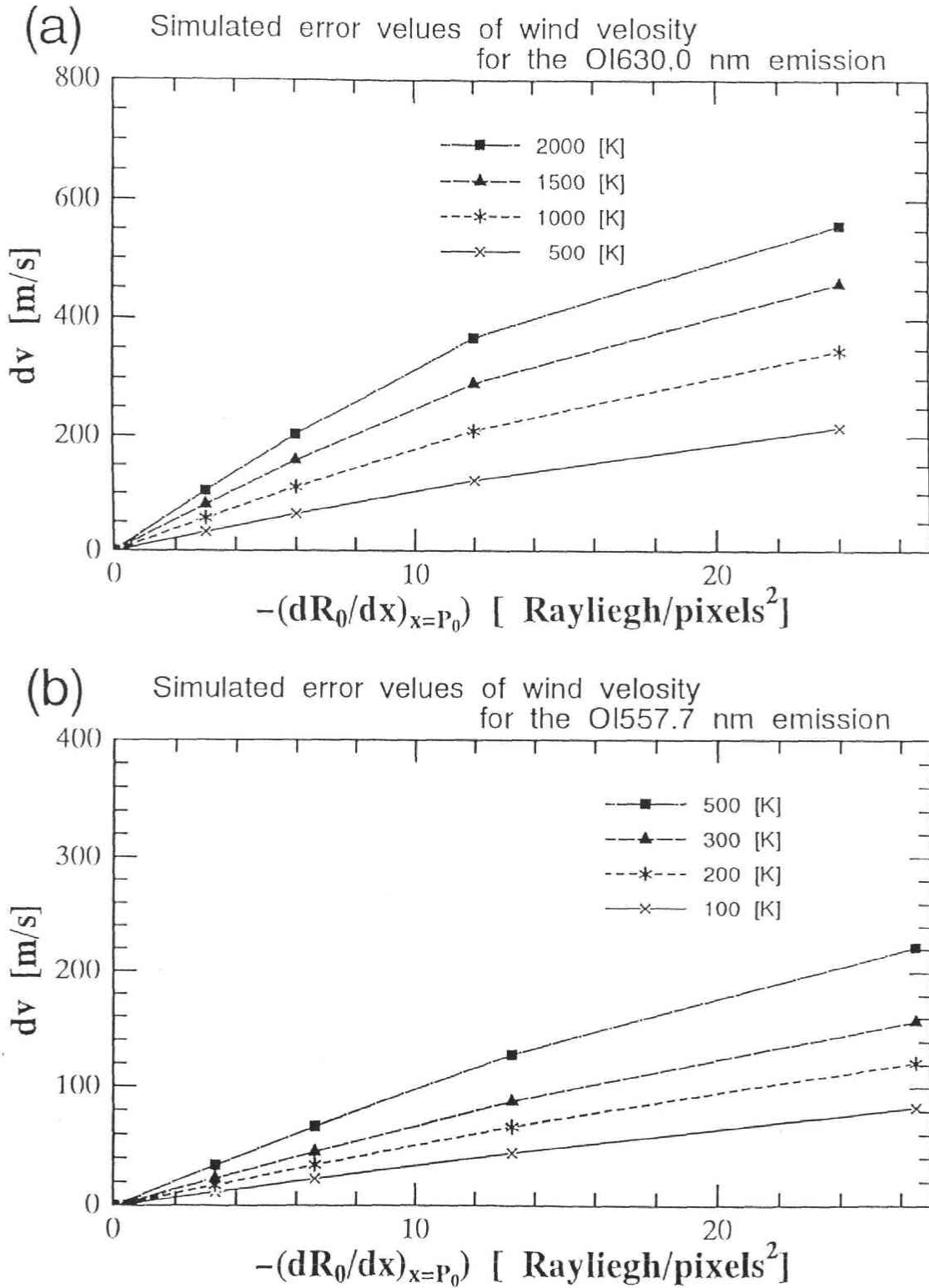


Figure 4.9. Error dv in the wind velocity estimation. (a) Errors calculated for the OI630.0 nm emission with temperatures of 500, 1000, 1500, and 2000 K. (b) Errors are calculated for the OI557.7 nm emission with temperatures of 100, 200, 300, and 500 K.

Chapter 5

Thermospheric Neutral Winds over Syowa Station Derived from Doppler Imaging Data

The thermospheric neutral wind data obtained from the FPDIS observation at Syowa station in 1994 have been analyzed with the procedures described in Chapter 4. From these data analyses, several important features of the thermospheric neutral wind have been found for the first time. In this chapter we present the data of four new findings. They are 1) thermospheric wind patterns in quiet and disturbed times, 2) outward flows from an auroral arc region, 3) quasi periodic variations of meridional winds, and 4) intense upward winds associated with localized auroral intensification.

5.1 F- and E-region wind patterns on quiet and disturbed days

To investigate the thermospheric wind patterns in quiet and disturbed times, FPDIS data obtained in the two periods of 10-13 July 1994 and 1-4 June 1994 have been analyzed in detail. In the former period, geomagnetic activity was very low with the values of Kp ranging from 0 to 2₋, and auroral activity was also very low. In the latter period, geomagnetic activity was high with the values of Kp ranging from 3₋ to 5, and active auroras were observed frequently. The differences in wind patterns on these two periods are shown in the following sections.

5.1.1 F- and E-region wind patterns on quiet days

To derive large scale variations of meridional and zonal winds in the thermosphere, obtained LOS wind velocities are processed as follows.

First, LOS wind velocities are transformed to horizontal wind velocities with the assumption that there is no vertical wind. The horizontal wind velocity v_h is obtained by

$$v_h = \frac{v_{LOS}}{\sin \theta} \quad (5.1)$$

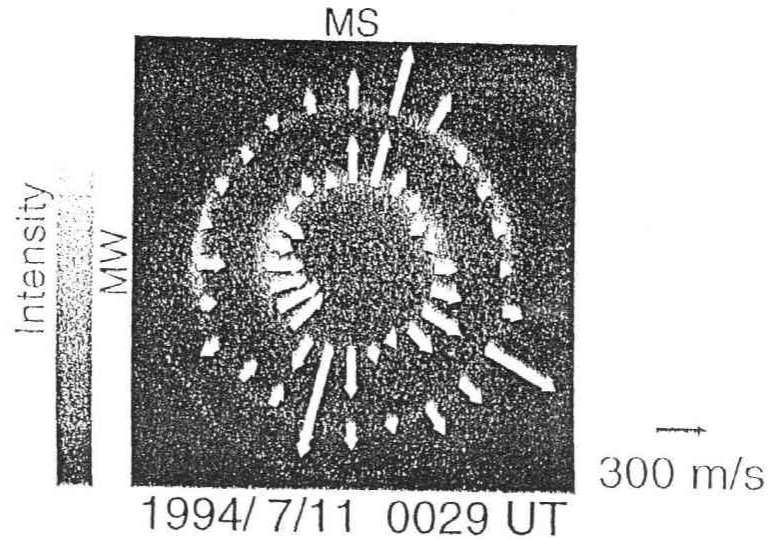
where v_{LOS} is the LOS wind velocity and θ is the zenith angle. Next, these horizontal wind velocities are averaged in the sectors shown in Figures 5.1 and 5.2, to reduce fluctuations due to small scale wind variations. Here, we must note that geomagnetic coordinates are rotated by 42 degrees against geographical coordinates at Syowa station.

Figures 5.3 and 5.4 show the variations of meridional and zonal winds observed by the OI630.0 nm and OI557.7 nm emissions, respectively. In these figures, wind velocity variations on the 4 nights from 10 July 1994 to 13 July 1994 are displayed together. On these nights, wind velocities are derived in every ~ 5 min, but they are smoothed by the boxcar average of a 5-point width. The values of Kp ranged from 0 to 2₋, while the values of F10.7 solar flux ranged from 84.1 to 88.9 during this period. We can see the following features in the wind velocity variations.

- 1) At the F-region OI630.0 nm emission layer (~ 240 km altitude), the meridional wind velocity is almost zero around 1800 UT, and after that, northward wind velocity increases gradually, attaining ~ 150 m/s at about 2300 UT.
- 2) The zonal wind at the OI630.0 nm emission layer is eastward around 1800 UT with a velocity of ~ 120 m/s, and then the wind velocity decreases gradually showing a turning into westward after 0000 UT.
- 3) At the E-region OI557.7 nm emission layer (~ 105 km altitude), the meridional wind is northward throughout the night, and its velocity ranges from ~ 40 m/s to ~ 100 m/s with a slight maximum around 2300 UT.
- 4) On the other hand, the zonal wind at the OI557.7 nm emission layer is eastward before 1800 UT, and turns to westward at ~ 1900 UT. Then it turns again to eastward at ~ 0100 UT. Its velocity is always smaller than ~ 50 m/s.

When geomagnetic activity is low, thermospheric wind should be mainly driven by both the pressure gradient force along the 14-02 LT plane and the convective ion drag force. The obtained wind patterns are consistent in the result of TIGCM model simulations during geomagnetically quiet time. More detailed discussions will be presented in Chapter 6.

(a) Horizontal Neutral Wind Velocities
Syowa Station, OI630.0 nm



(b)

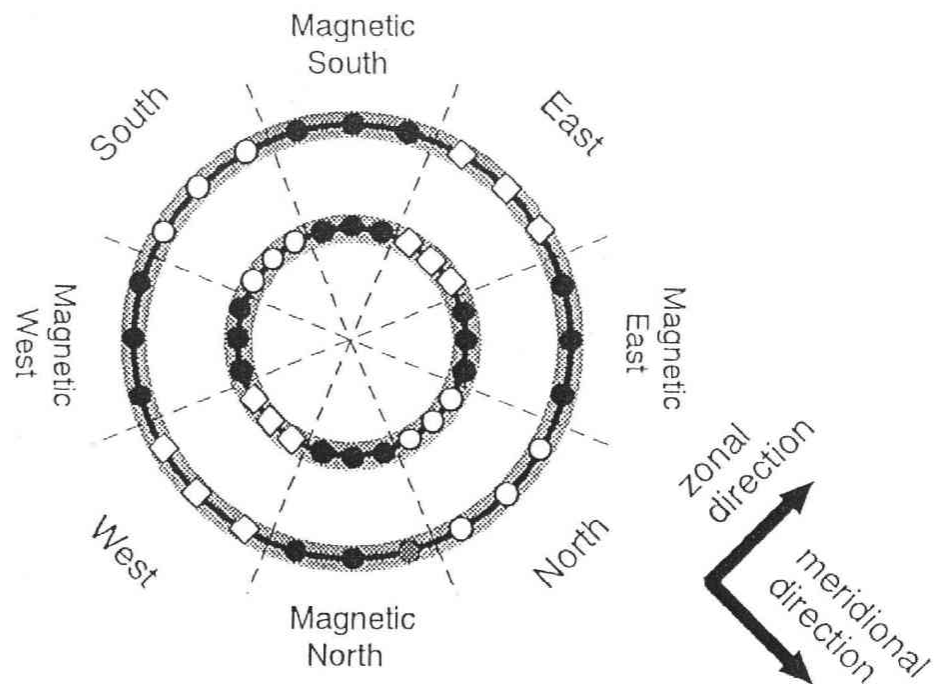
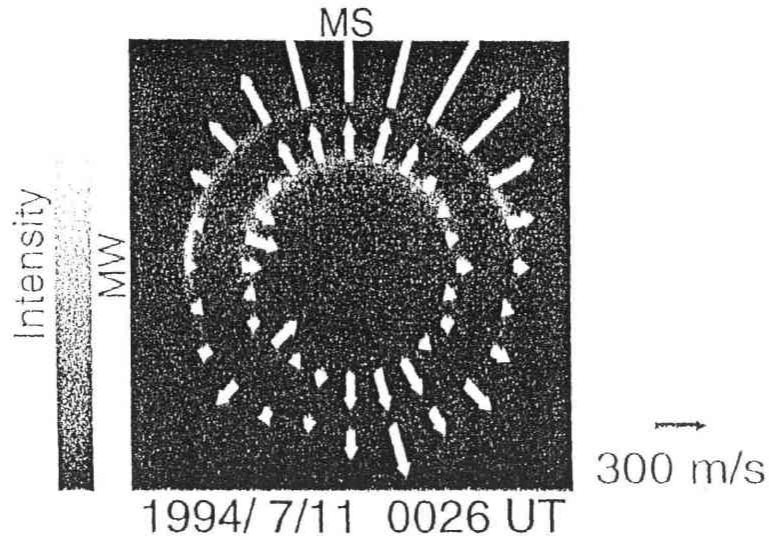


Figure 5.1. Geometry for deriving the averaged meridional and zonal wind velocities from the OI630.0 nm fringe image data. The average values of horizontal wind velocities at the positions indicated by symbols of 'o' or 'o' are adopted as the averaged meridional or zonal wind velocities, respectively. Note that geomagnetic coordinates are rotated by 42 degrees against geographical coordinates at Syowa station.

(a) Horizontal Neutral Wind Velocities
Syowa Station, OI557.7 nm



(b)

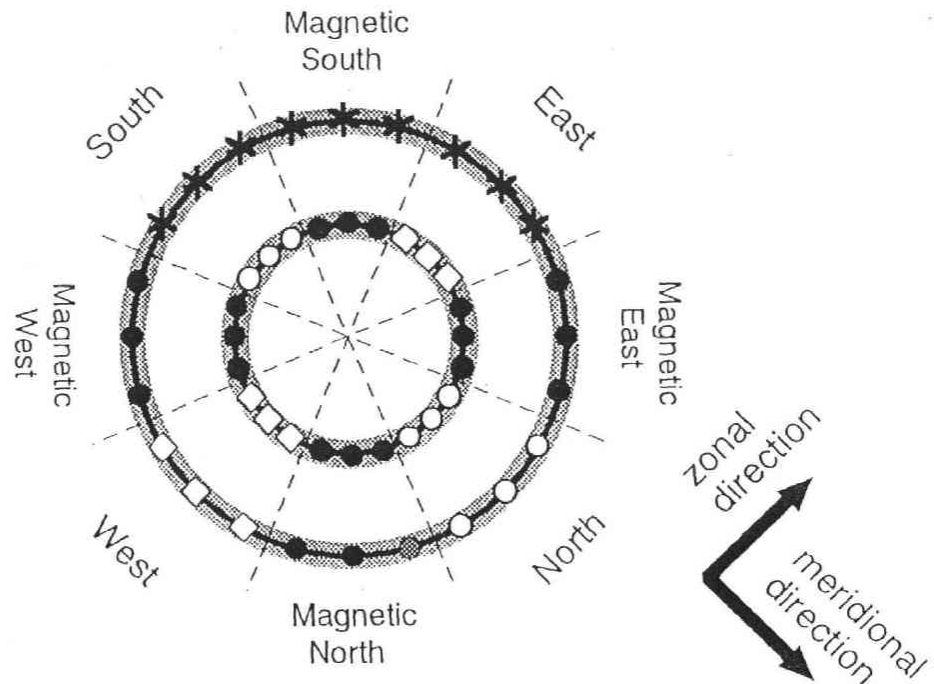


Figure 5.2. Geometry for deriving the averaged meridional and zonal wind from the OI557.7 nm fringe image. The average values of horizontal wind velocities at the positions indicated by symbols of 'o' or 'o' are adopted as the averaged meridional or zonal wind velocities, respectively. The wind velocities in the magnetic southern sector of the OI557.7 nm fringe, which are represented with the symbol '*', are excluded from the averaging, because these data have a deviation caused by an instrumental problem.

Horizontal wind variations at the OI630.0 nm emission height
 1994/ 7/10-13 Kp: 0- 2₋, F10.7: 84.1-88.9

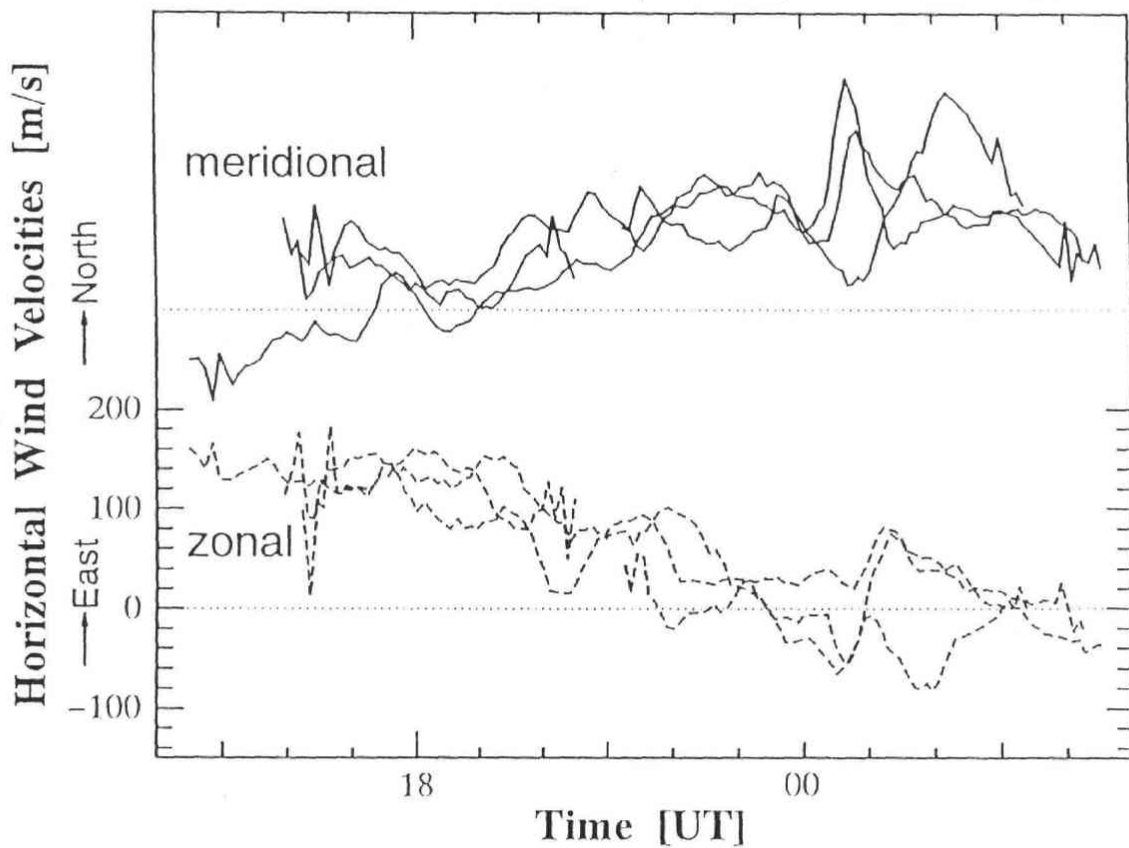


Figure 5.3. Variations of meridional (solid lines) and zonal (broken lines) winds derived from Doppler imaging data of OI630.0 nm emission. Wind velocity data on the 4 nights from 10 July 1994 to 13 July 1994 are displayed together. The values of Kp during this period ranged from 0 to 2₋, while the values of F10.7 solar flux ranged from 84.1 to 88.9.

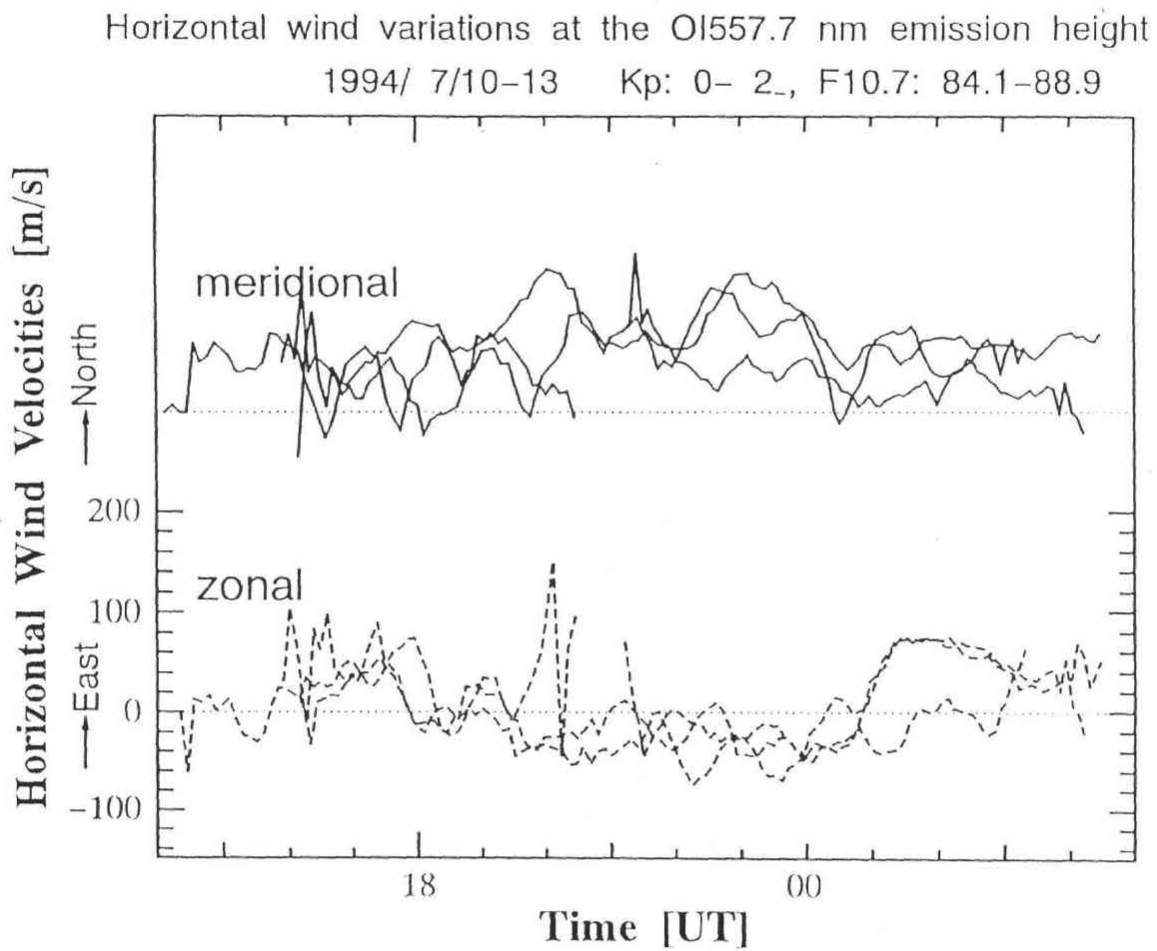


Figure 5.4. Variations of meridional (solid lines) and zonal (broken lines) winds derived from Doppler imaging data of OI557.7 nm emission in the period of 10-13 July 1994.

5.1.2 F- and E-region wind patterns on disturbed days

The FPDIS wind data which observed on the 4 nights from 1 June 1994 to 4 June 1994 during geomagnetically active period are processed with the same procedure as described in the previous section. Figures 5.5 and 5.6 show the variations of meridional and zonal winds derived from the OI630.0 nm OI557.7 nm emission data, respectively. In these figures, wind velocity variations on the 4 nights from 1 June 1994 to 4 June 1994 are displayed together. On these nights, wind velocities were derived in every ~ 5 min, and smoothed by the boxcar average of a 5-point width. The values of Kp ranged from 3₋ to 5, while the values of F10.7 solar flux ranged from 69.5 to 70.3 during this period. We can see the following features in the wind velocity variations.

- 1) The meridional wind at the F-region OI630.0 nm emission layer is slightly northward before ~ 1900 UT, and then turns to southward at ~ 1900 UT. Fluctuations of the meridional wind velocity on each day are large compared with the geomagnetically quiet period.
- 2) The zonal wind at the OI630.0 nm emission layer is eastward throughout the night, and its velocity is over ~ 70 m/s. Fluctuations of wind velocities are large after 2300 UT.
- 3) At the E-region OI557.7 nm emission layer, both the meridional and zonal winds change in the same way as the winds at the F-region OI630.0 nm emission layer. However, fluctuations of wind velocities are smaller than those at the OI630.0 nm emission layer.

When geomagnetic activity is high, the features of wind variations do not agree with the results of TIGCM model simulations. More detailed discussion on this point will be presented in Chapter 6.

5.2 Strong outward flows from the auroral arc region

In this section, we show an example of strong outward flows from the auroral arc region often observed at both the F-region OI630.0 nm emission layer and the E-region OI557.7 nm emission layer. Figures 5.7, 5.8 and 5.9 show line-of-sight neutral wind velocities and all-sky images observed at Syowa station on the night of 10-11 July 1994. Upper and middle panels show sequences of LOS wind velocity distributions superposed on the OI630.0 nm and OI557.7 nm emission fringes, respectively. Note that LOS wind velocities are displayed for only inner fringes to easily compare between the wind patterns at the F- and E-region

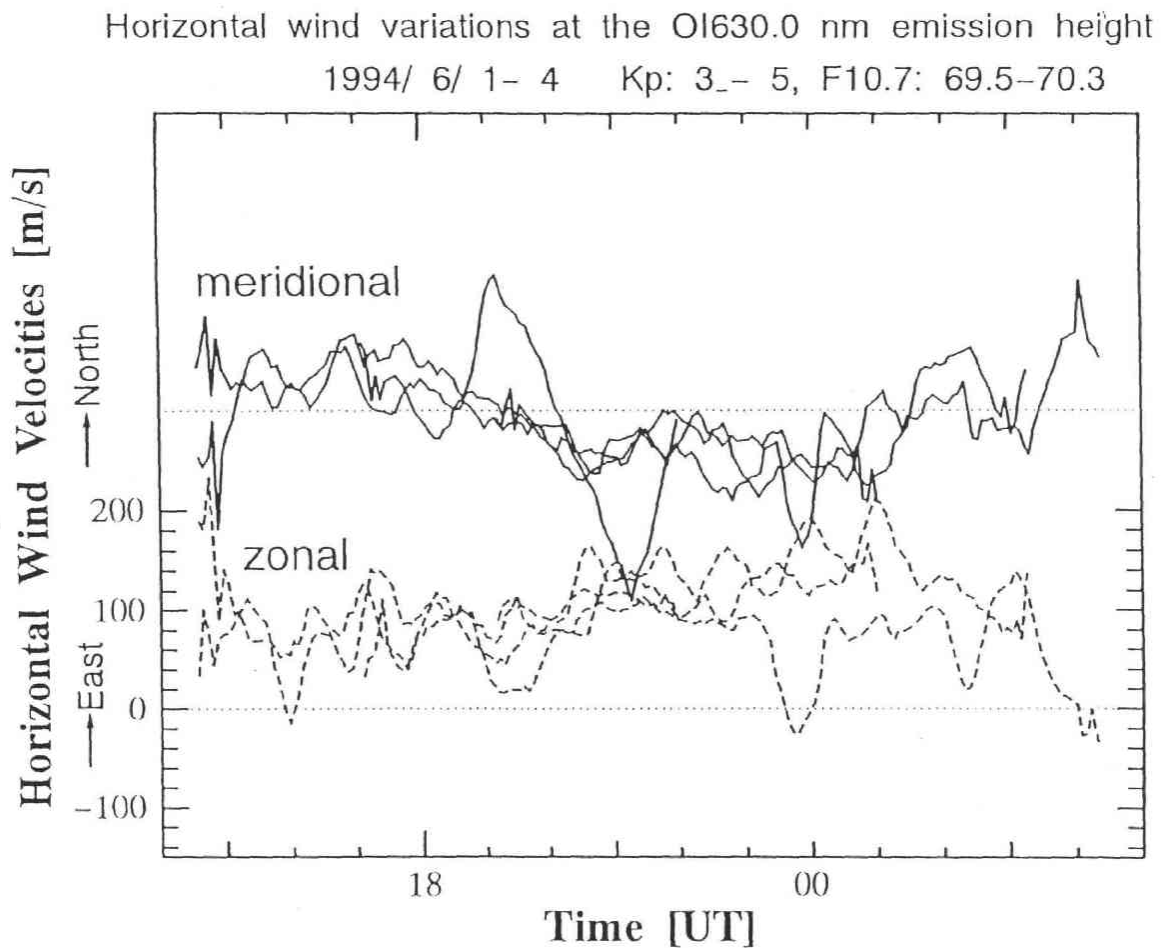


Figure 5.5. Variations of meridional (solid lines) and zonal (broken lines) winds derived from Doppler imaging data of OI630.0 nm emission. Wind velocity data on the 4 nights from 1 June 1994 to 4 June 1994 are displayed together. The values of Kp during this period ranged from 3₋ to 5, while the values of F10.7 solar flux ranged from 69.5 to 70.3.

Horizontal wind variations at the OI557.7 nm emission height
1994/ 6/ 1- 4 Kp: 3- 5, F10.7: 69.5-70.3

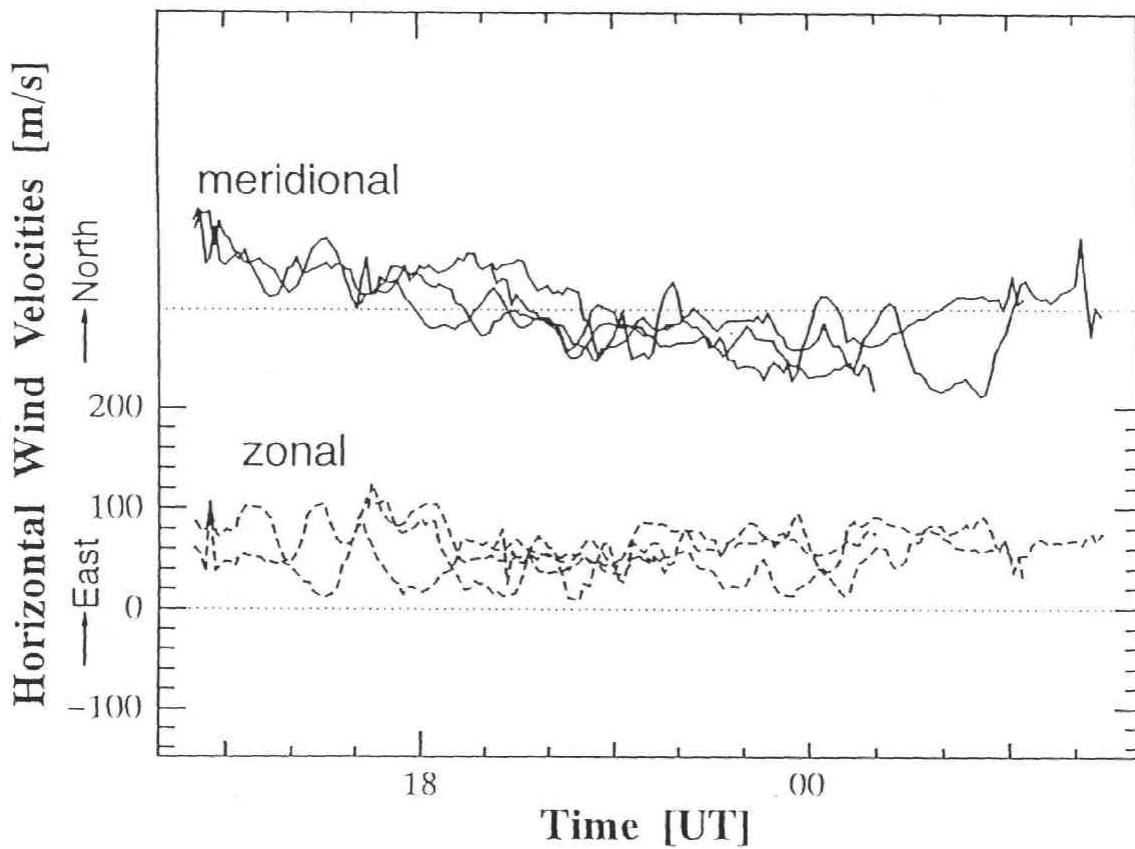


Figure 5.6. Variations of meridional (solid lines) and zonal (broken lines) winds derived from Doppler imaging data of OI557.7 nm emission in the period of 1-4 June 1994.

altitude. The span of one side of each image is 480 km, and the top is magnetic south and the left is magnetic west. Lower panels show a sequence of all-sky images of aurora obtained simultaneously with an SIT camera. Two circles displayed by red and green dots in these images indicate the positions corresponding to the inner fringes of the OI630.0 nm and OI557.7 nm emissions, respectively.

On the night of 10-11 July 1994, geomagnetic activity was very low and the values of K_p ranged from 0 to 1_+ during the observation period. Before 0000 UT, auroral activity was very low and weak auroral emissions were occasionally seen on the magnetic south. However, at \sim 0000 UT, an auroral arc appeared on the magnetic south, and then moved northward (equatorward) as its intensity increased. After 0044 UT, the latitudinal width of the auroral emission region expanded rapidly, accompanying intensity enhancements and occurrences of complicated structures including N-S segments. The intensity enhancement attained its peak at 0054 UT, and then weakened although the equatorward edge of auroral occurrence region continued to move northward. Note that magnetic local time at Syowa station is almost coincides with universal time, therefore 0000 UT corresponds to magnetic midnight.

Neutral winds in the F- and E-region observed at the same time have the following features. In the F-region, strong equatorward wind with the LOS velocity of \sim 300 m/s appeared on the magnetic south at 0001 UT, and then the enhanced wind area moved northward (equatorward) corresponding to the equatorward movement of the auroral arc before 0044 UT. Although the auroral form changed from arcs to more complicated structures after 0044 UT, equatorward winds were observed until the end of observation at 0134 UT, as the wind speed was decreasing gradually. Further, it was found that the poleward wind appeared between 0029 UT and 0040 UT on the magnetic south of Syowa station. During this period, the northern edge of the OI630.0 nm arc was located inside the inner fringe. /par In the E-region, strong equatorward wind with a LOS velocity of \sim 200 m/s appeared on the magnetic north at 0021 UT with a delay of a few minutes against the enhancement of equatorward wind in the F-region. Such equatorward wind was observed until 0104 UT, similarly to the F-region wind. The poleward wind appeared after 0026 UT on the magnetic south of Syowa station. It is found that, in the time interval of 0026-0040 UT, the southern edge of the OI557.7 nm arc was located near the inner fringe.

In order to investigate the relation of LOS winds on the inner fringe with those on the outer fringe, we selected four locations as shown in Figure 5.10. Figures 5.11 and 5.12 show the variations of LOS wind velocities at the four locations for the F- and E-region,

Line-of-Sight Neutral Wind Velocities and All-sky Images

Syowa Station 1994/ 7/10-11

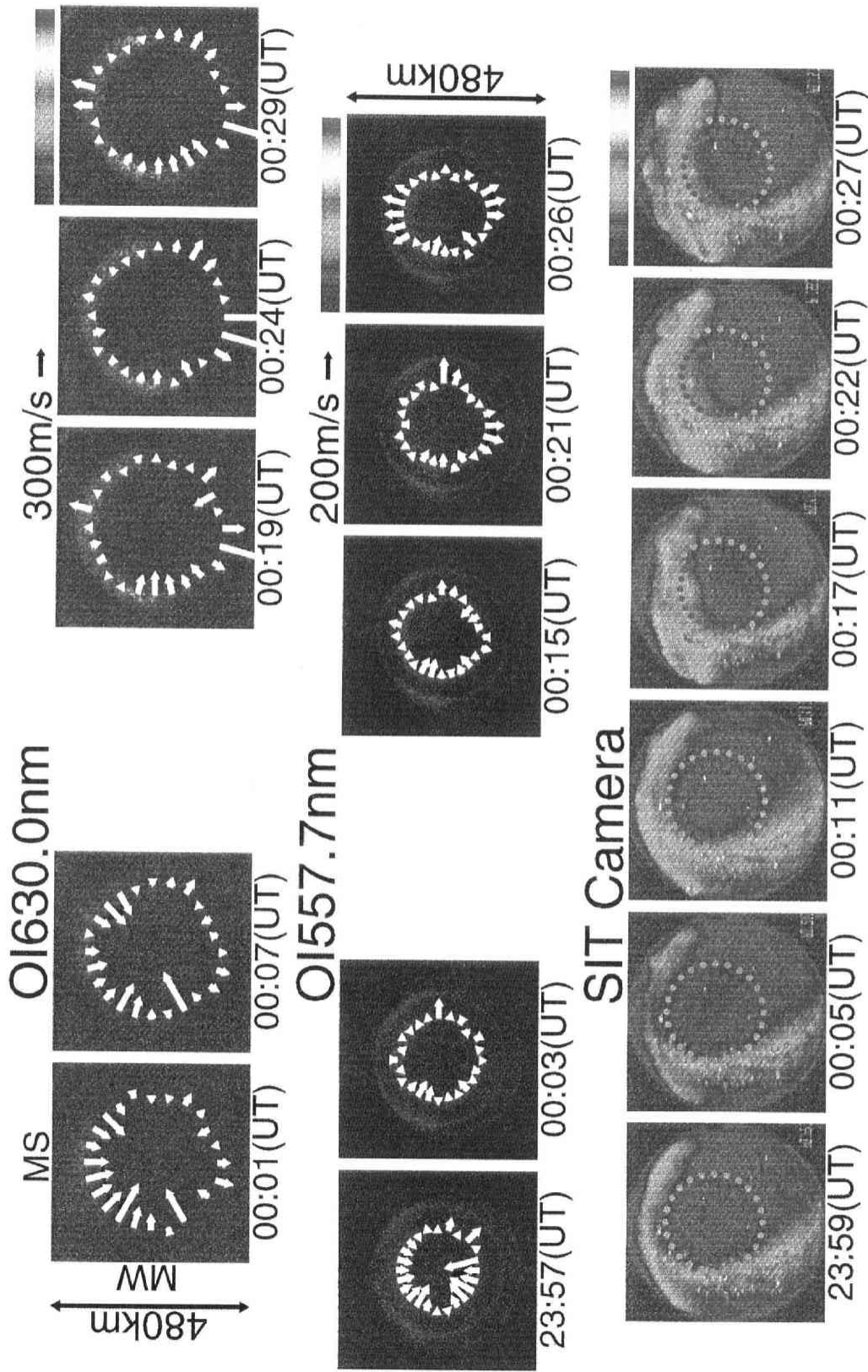


Figure 5.7. Line-of-sight neutral wind velocities and all-sky images observed at Syowa station in the nighttime from 2357 UT to 0029 UT on July 10-11, 1994. Upper panels, LOS wind velocities superposed on OI630.0 nm fringes; middle panels, LOS wind velocities superposed on OI557.7 nm fringes; lower panels, all-sky images obtained simultaneously by the SIT camera.

Line-of-Sight Neutral Wind Velocities and All-sky Images

Syowa Station 1994/ 7/11

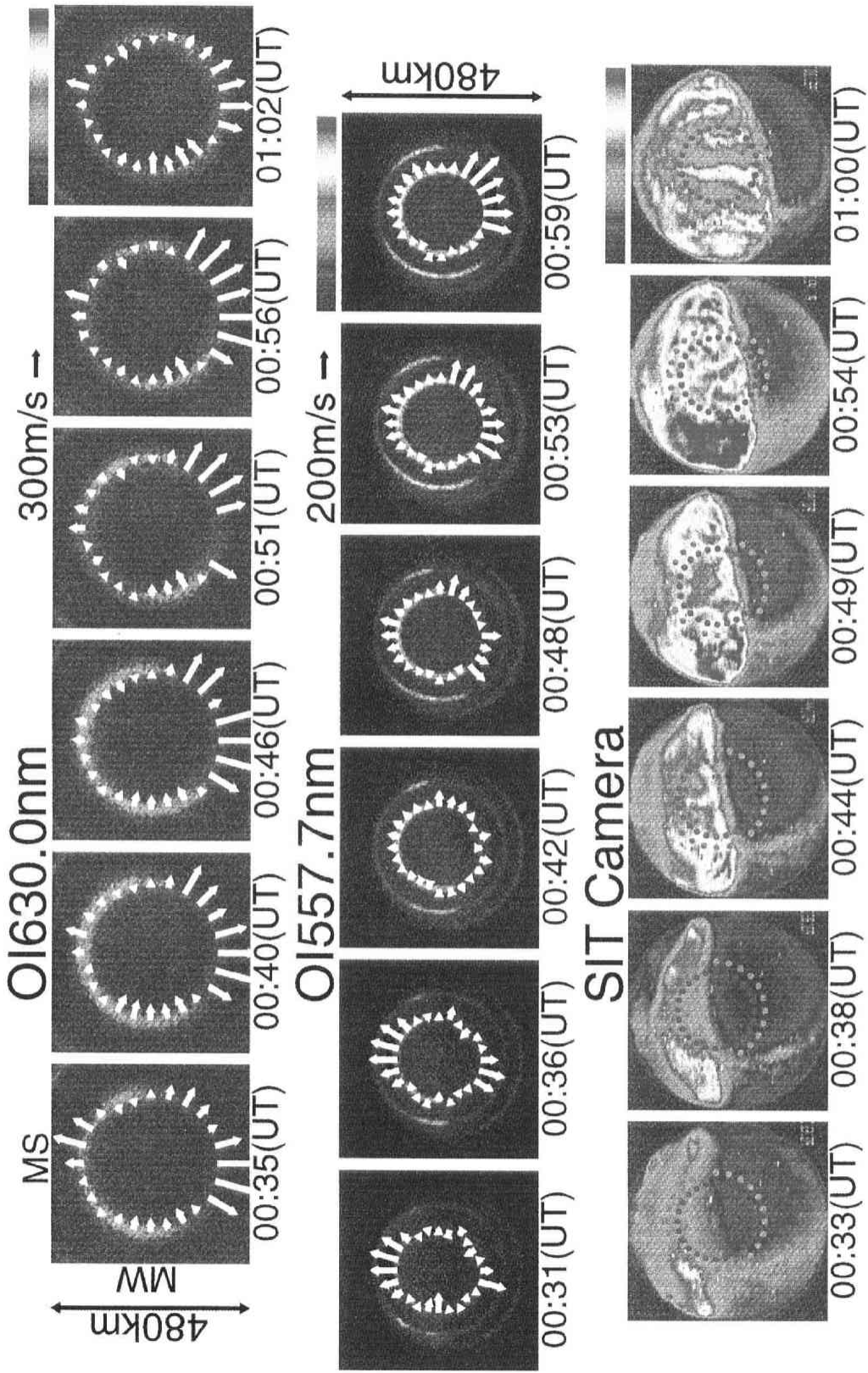


Figure 5.8. Line-of-sight neutral wind velocities and all-sky images observed at Syowa station in the nighttime from 0031 UT to 0102 UT on July 10-11, 1994. The format is the same as Figure 5.7.

Line-of-Sight Neutral Wind Velocities and All-sky Images

Syowa Station 1994/ 7/11

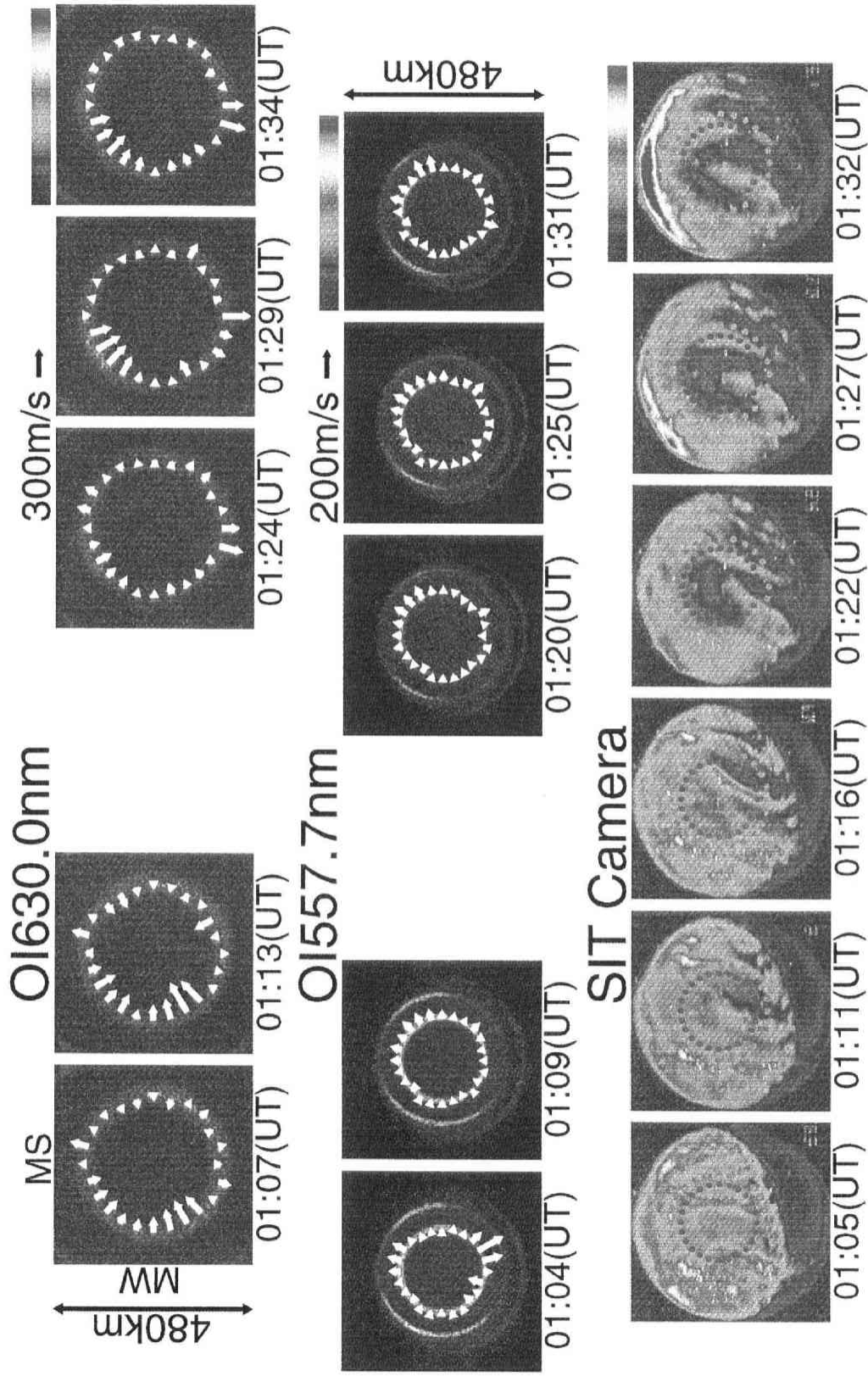


Figure 5.9. Line-of-sight neutral wind velocities and all-sky images observed at Syowa station in the nighttime from 0104 UT to 0134 UT on July 10-11, 1994. The format is the same as Figure 5.7.

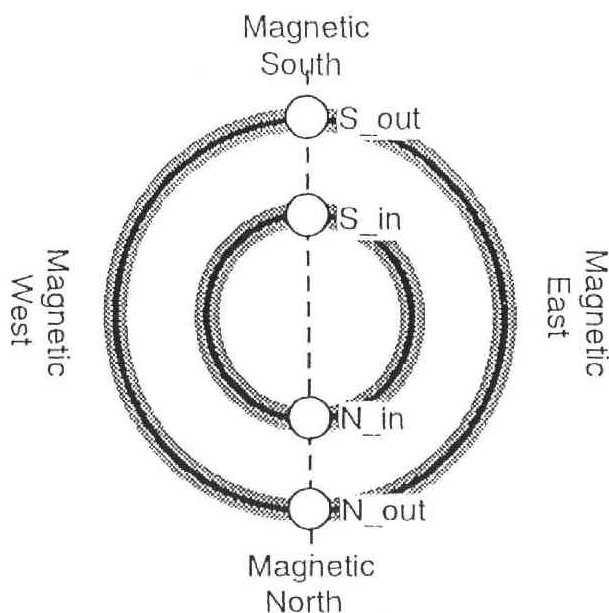


Figure 5.10. Location of four points at which wind velocities and aurora emission intensities are investigated.

respectively, on the night of 10-11 July 1994. On this night, wind velocities were derived in every ~ 5 min, but obtained data were smoothed by the boxcar average of a 5-point width. Figures 5.13 and 5.14 show variations of relative intensities of the OI630.0 nm and OI557.7 nm emissions, respectively, on this night at the same four locations illustrated in Figure 5.10. These values were obtained by fringe peak heights.

Hatched areas in Figures 5.11 and 5.12 represent the time intervals of enhanced equatorward and poleward winds which appear to be related to the stable aurora arc before 0044 UT and the following diffuse aurora activity. As indicated by solid lines in these figures, there is a tendency that both the enhanced equatorward and poleward wind regions move equatorward corresponding to the equatorward shift of the auroral emission region.

5.3 Periodic enhancements of meridional winds on 3-4 June 1994

In this section, we will present an example of periodic enhancements of meridional wind velocities which observed in the F- and E-region on the night of 3-4 June 1994. Unlike the phenomenon described in the previous section, these wind variations were observed during a geomagnetically activity period with Kp values ranging from 3 to 5.

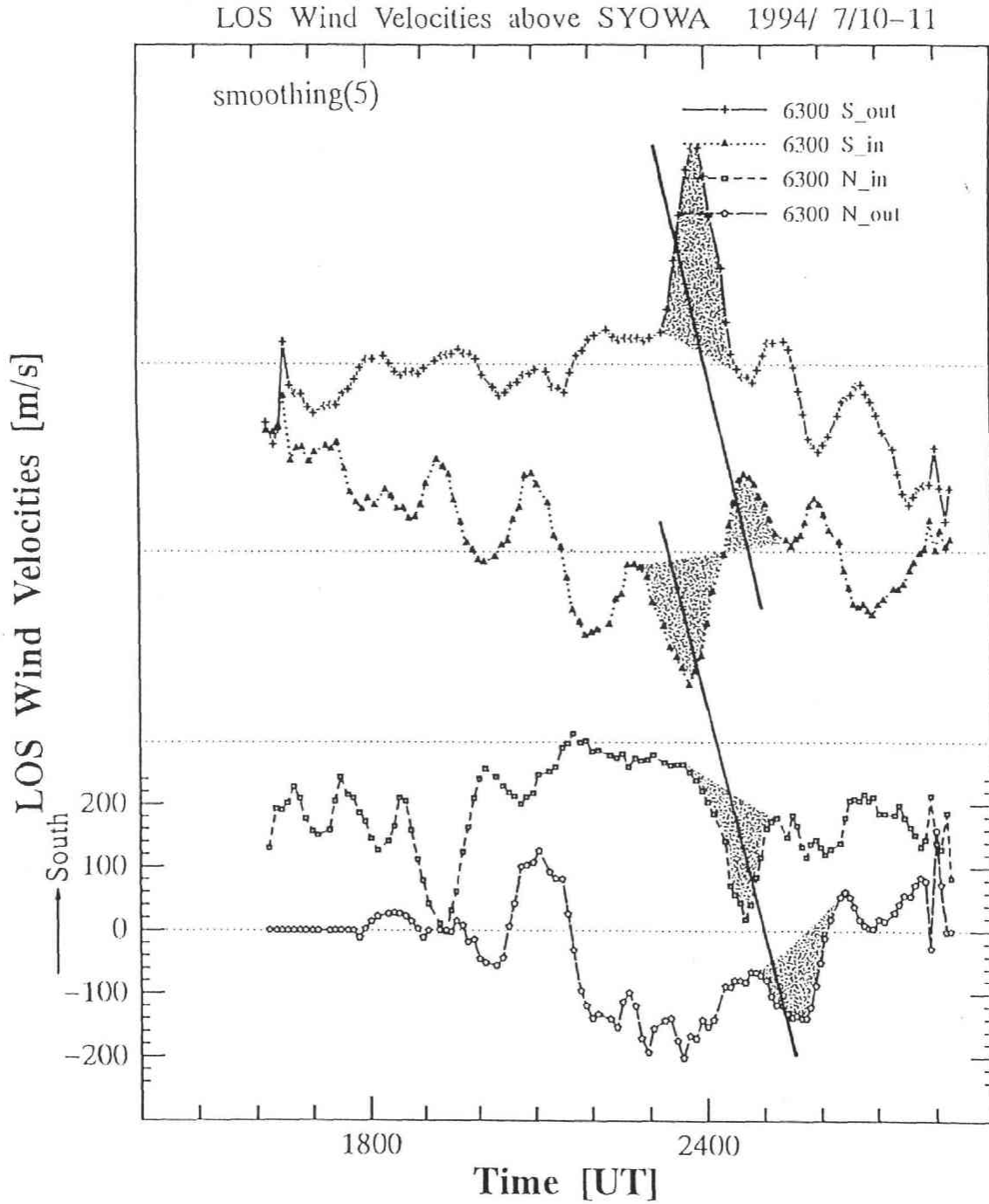


Figure 5.11. Variations of LOS wind velocities at four locations on the inner and outer fringes illustrated in Figure 5.10, for the OI630.0 nm emission in the nighttime on 10-11 July 1994.

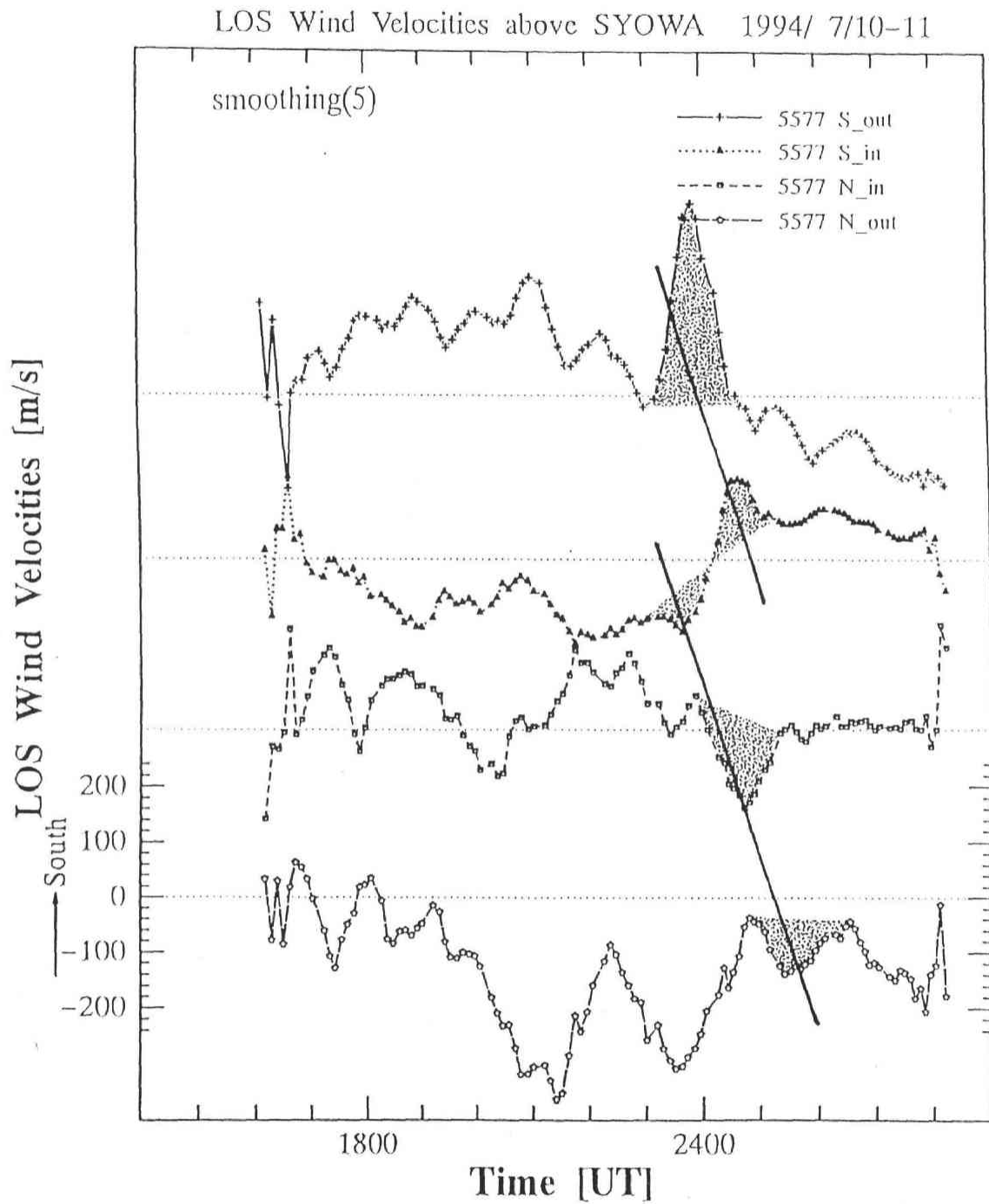


Figure 5.12. Same as Figure 5.11 except for the OI557.7 emission.

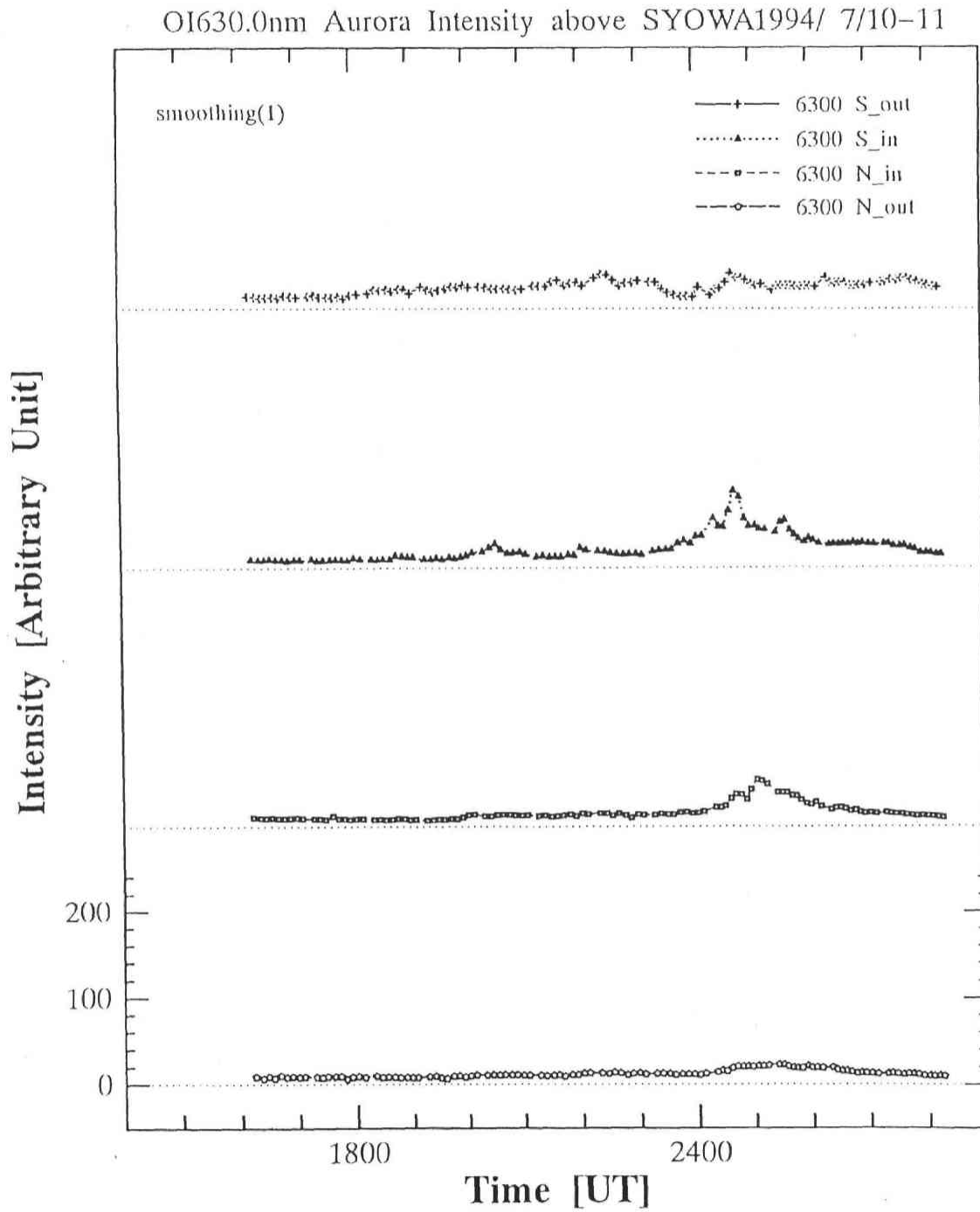


Figure 5.13. Variations of the OI630.0 nm emission intensities at four locations on the inner and outer fringes illustrated in Figure 5.10, for the night of 10-11 July 1994.

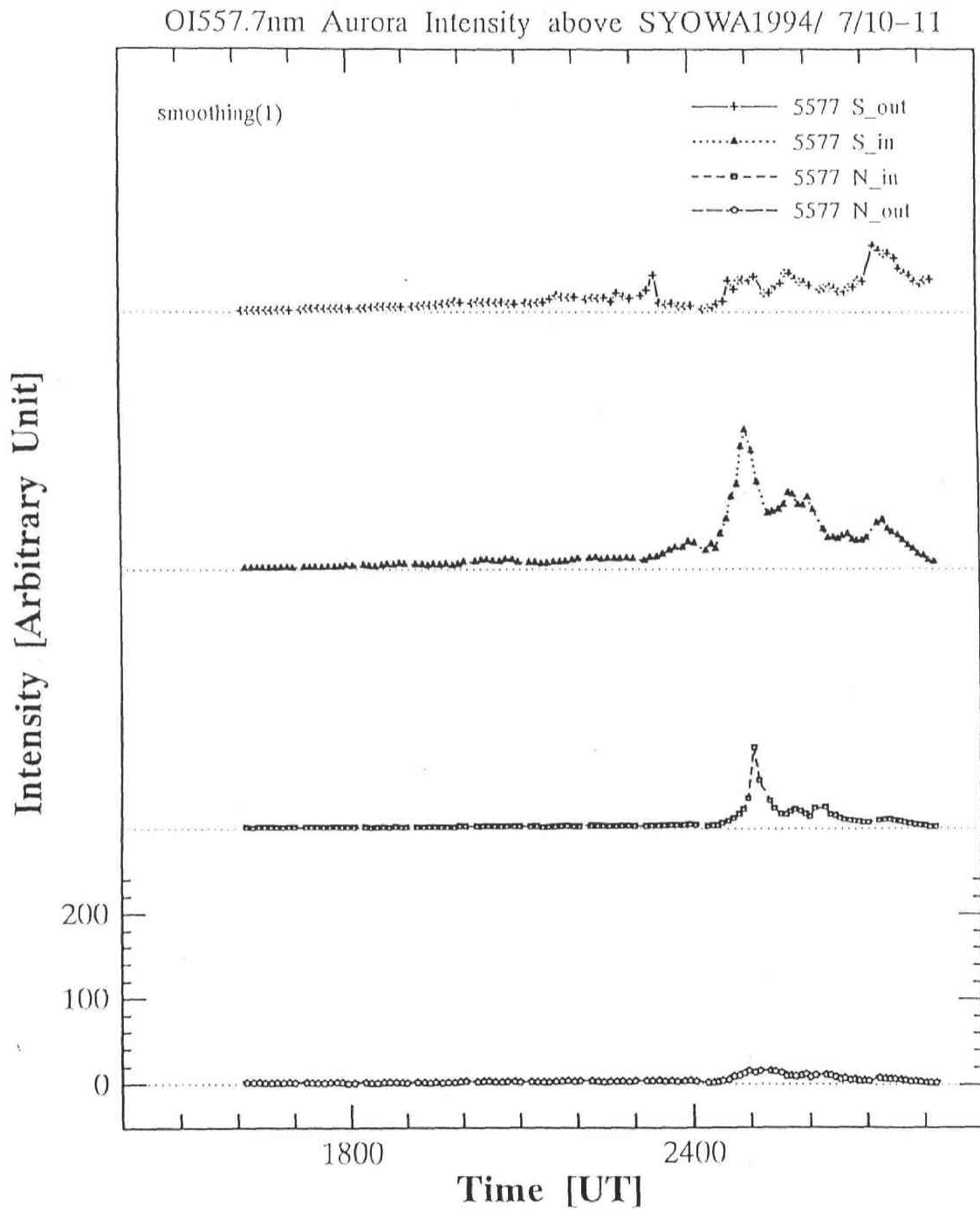


Figure 5.14. Same as Figure 5.13 except for the OI557.7 nm emission intensities.

Figures 5.15 and 5.16 show variations of LOS wind velocities in the F- and E-region, respectively, on this night at the four locations illustrated in Figure 5.10. On this night, wind velocities were derived in every ~ 5 min, but obtained data were smoothed by the boxcar average of a 5-point width. Figures 5.17 and 5.18 show variations of emission intensities of the OI630.0 nm and OI557.7 nm emissions, respectively, on this night at the four locations illustrated in Figure 5.10. Hatched areas between 2300 UT and 0400 UT in Figures 5.15 and 5.16 indicate the periodic enhancements of poleward winds in the F- and E-region, respectively, and solid lines connecting peaks show that the variations are propagating from north to south (poleward). The period of the variations is 1.3 – 2 hr and 1.2 hr in the F- and E-region, respectively, while the phase velocity of the poleward propagation is ~ 80 m/s and ~ 110 m/s in the F- and E-region, respectively. These wave parameters in the F- and E-region are similar each other. Figure 5.19 shows auroral all-sky images observed by the SIT camera at Syowa station on the same night. When the periodic enhancements of poleward winds appeared, there was aurora activity at a few hundred kilometers south of Syowa station.

5.4 Strong divergent winds observed simultaneously with an enhancement of auroral emission

After 0300 UT on 4 June 1994, auroral emission intensities above Syowa station began to increase, and interesting wind variations were observed. Figures 5.20, 5.21, 5.22 and 5.23 show line-of-sight neutral wind velocities and all-sky images observed at Syowa station on this night, similarly to Figures 5.7-5.9 for the night of 10-11 July 1994. About 0300UT, the aurora emission area, which had been staying a few hundred kilometers equatorward of Syowa station, began to spread toward Syowa station, and strong poleward winds appeared on the magnetic south from 0309 UT to 0329 UT in both the F- and E-region, similarly to the example shown in Section 5.2. Then, these poleward winds weakened as the auroral emission region overspread across Syowa station. In these Figures, we can see strong divergent wind patterns at 0246 UT, 0404 UT, 0409 UT, and 0413 UT in F-region, and at 0302 UT in E-region, which suggest the existence of strong upward thermospheric winds. In particular, the 0409 UT event shows a dramatic enhancement of the divergent wind. From 0359 UT, the enhancements of auroral activity occurred, and the OI630.0 nm emission intensity attained its peak at 0409 UT. Strong divergent winds appeared in the F-region at 0404 UT, 0409

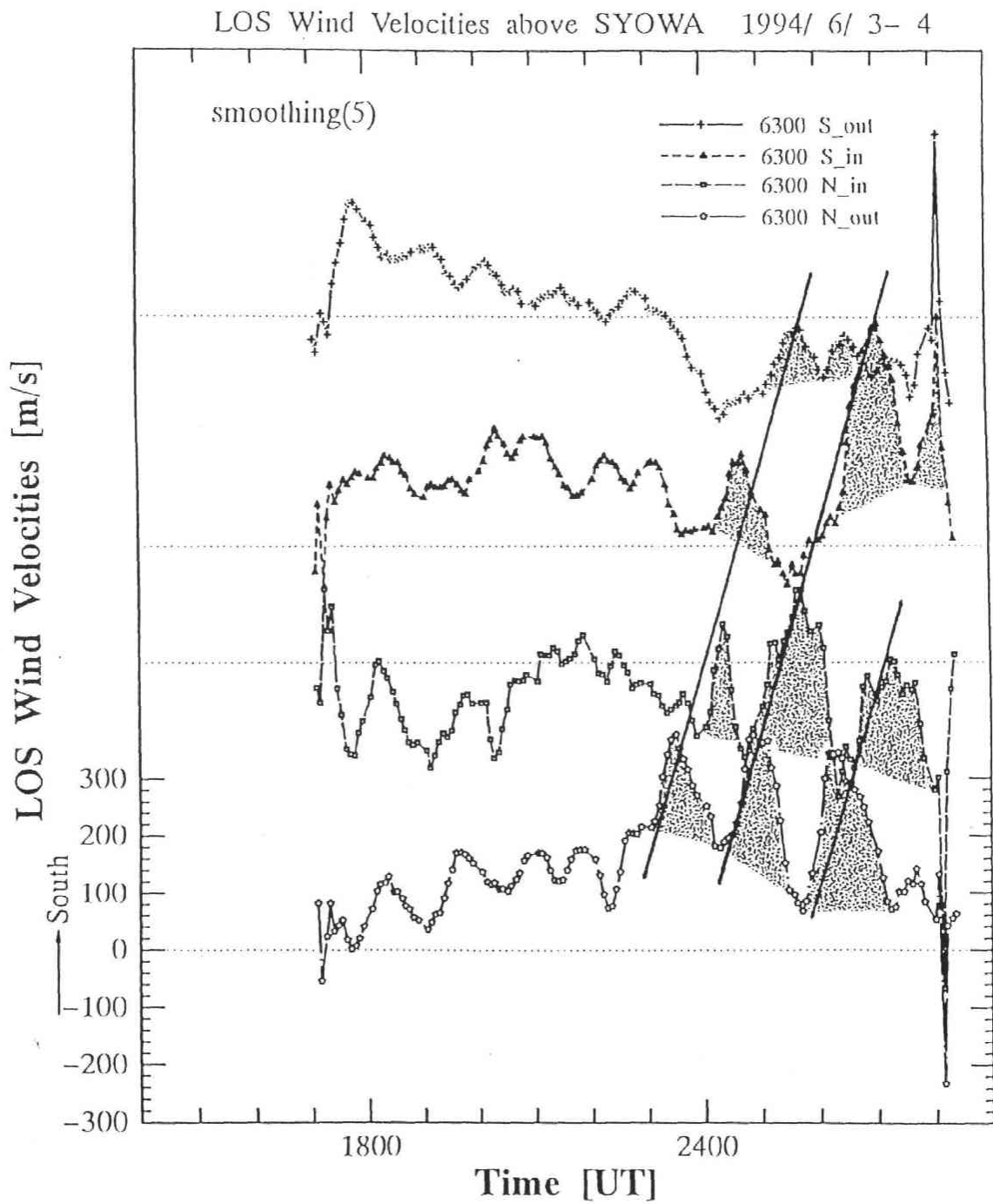


Figure 5.15. Same as Figure 5.11 except for the night of 3-4 June 1994.

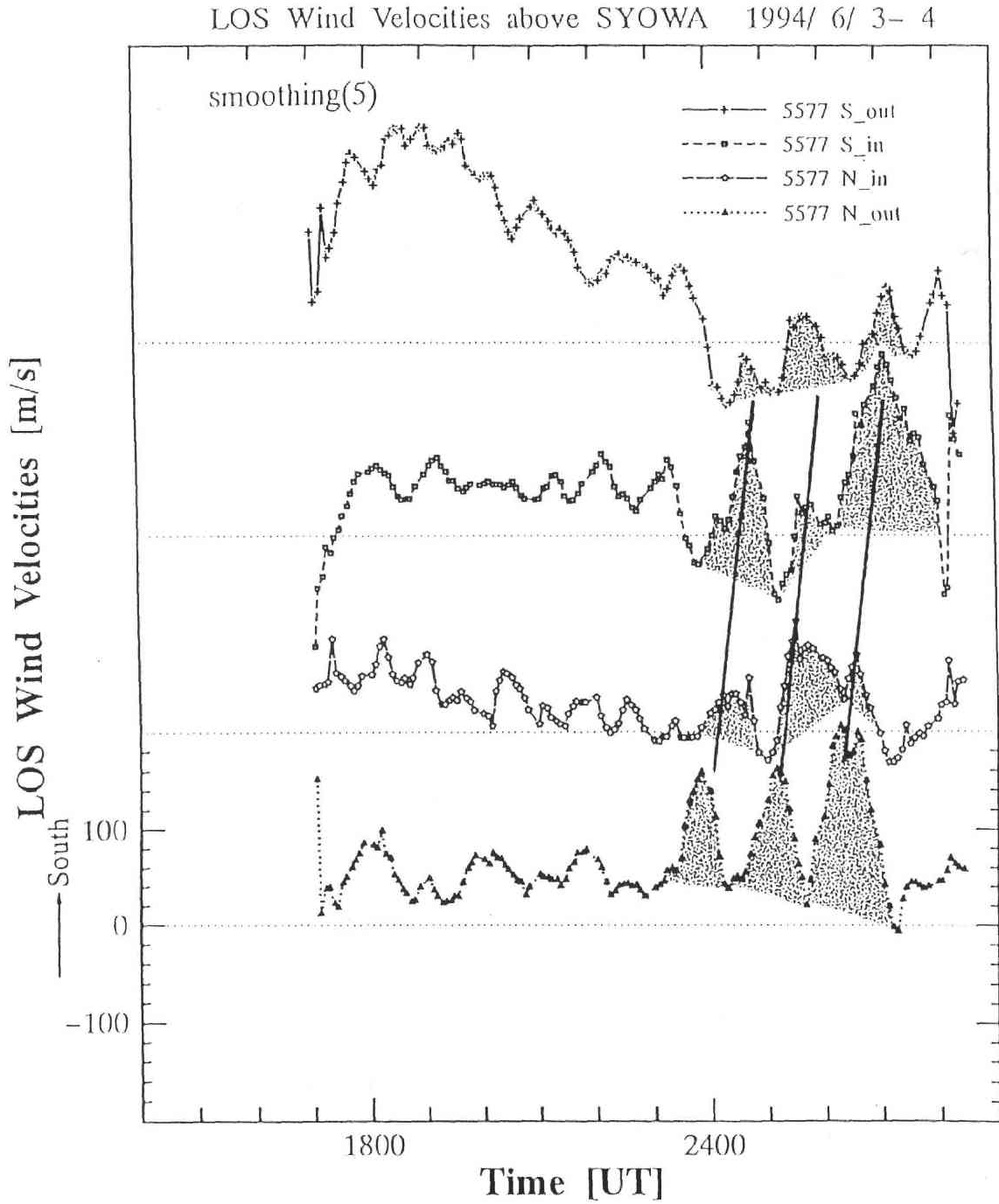


Figure 5.16. Same as Figure 5.12 except for the night of 3-4 June 1994.

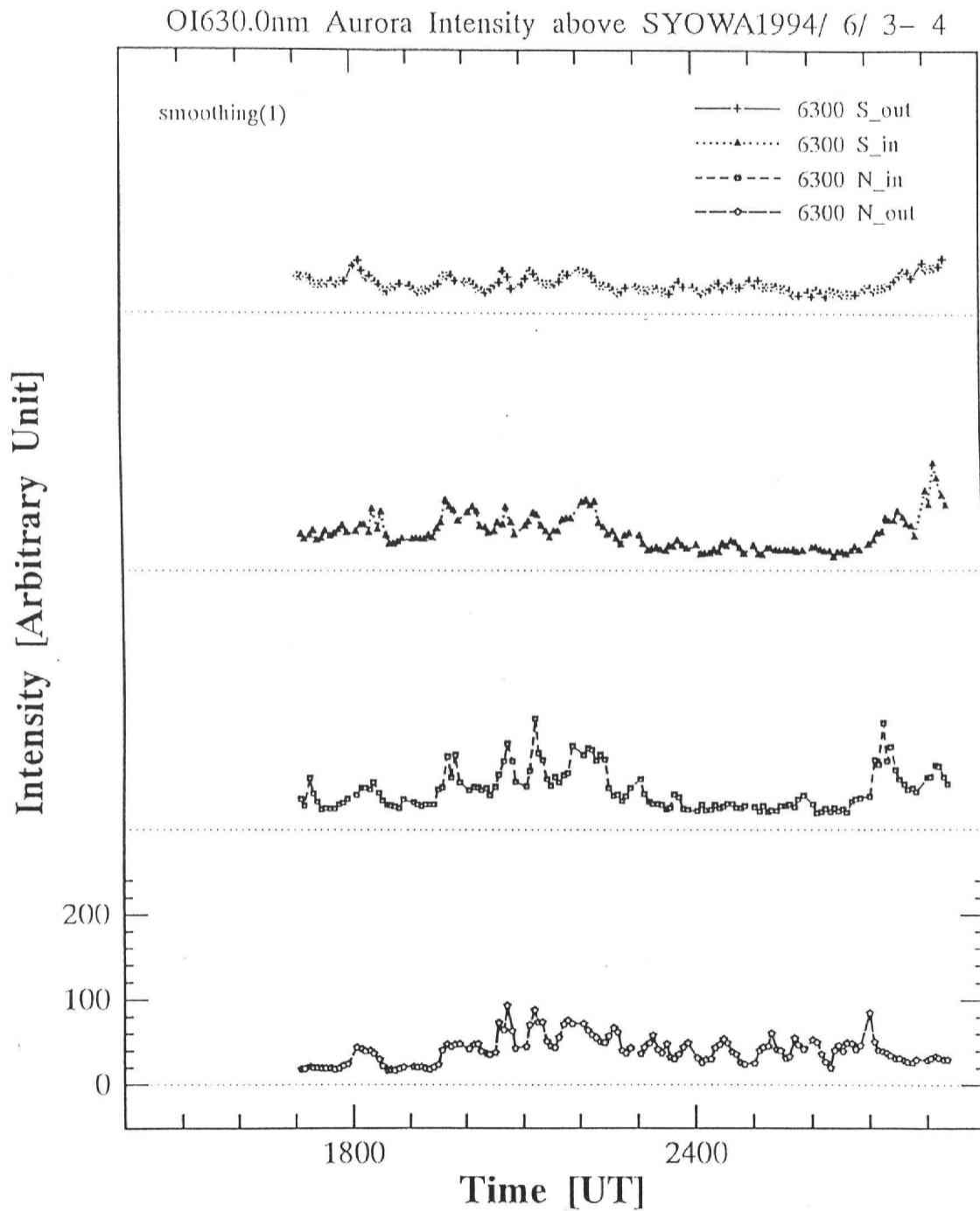


Figure 5.17. Same as Figure 5.13 except for the night of 3-4 June 1994.

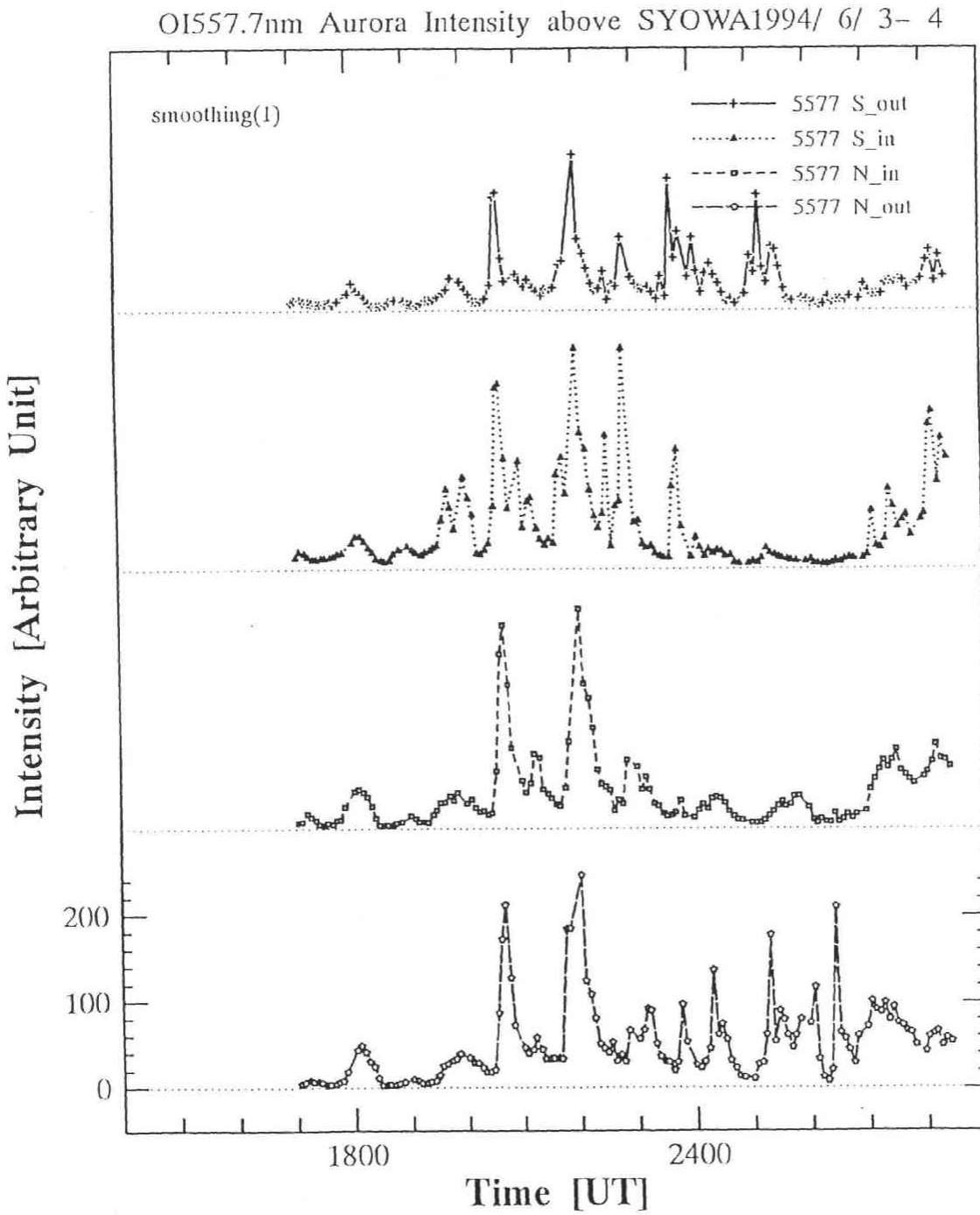


Figure 5.18. Same as Figure 5.14 except for the night of 3-4 June 1994.

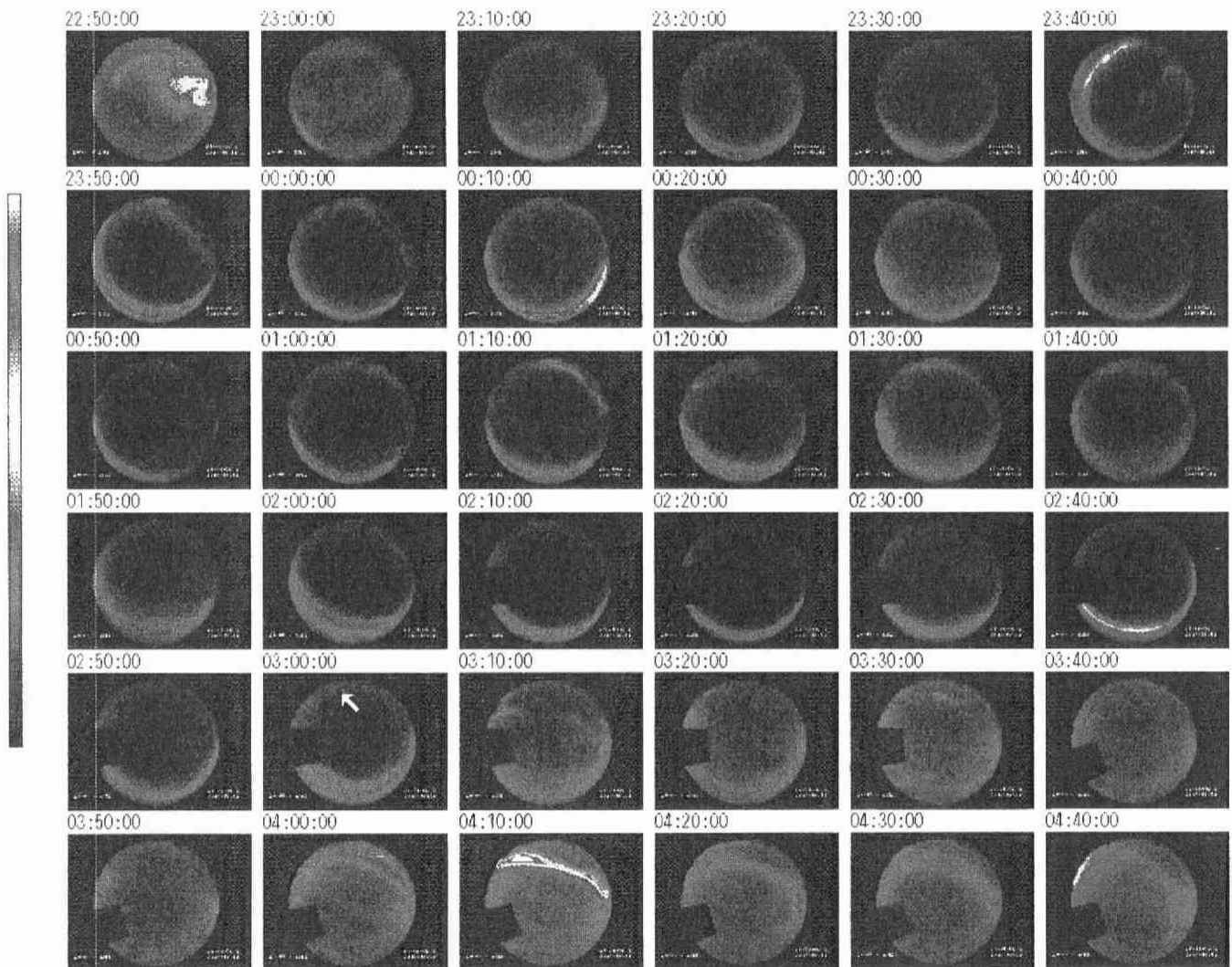


Figure 5.19. All-sky images between 2250 UT and 0440 UT on the night of 3-4 June 1994, observed by the SIT camera at Syowa station.

Line-of-Sight Neutral Wind Velocities and All-sky Images

Syowa Station 1994/ 6/ 4

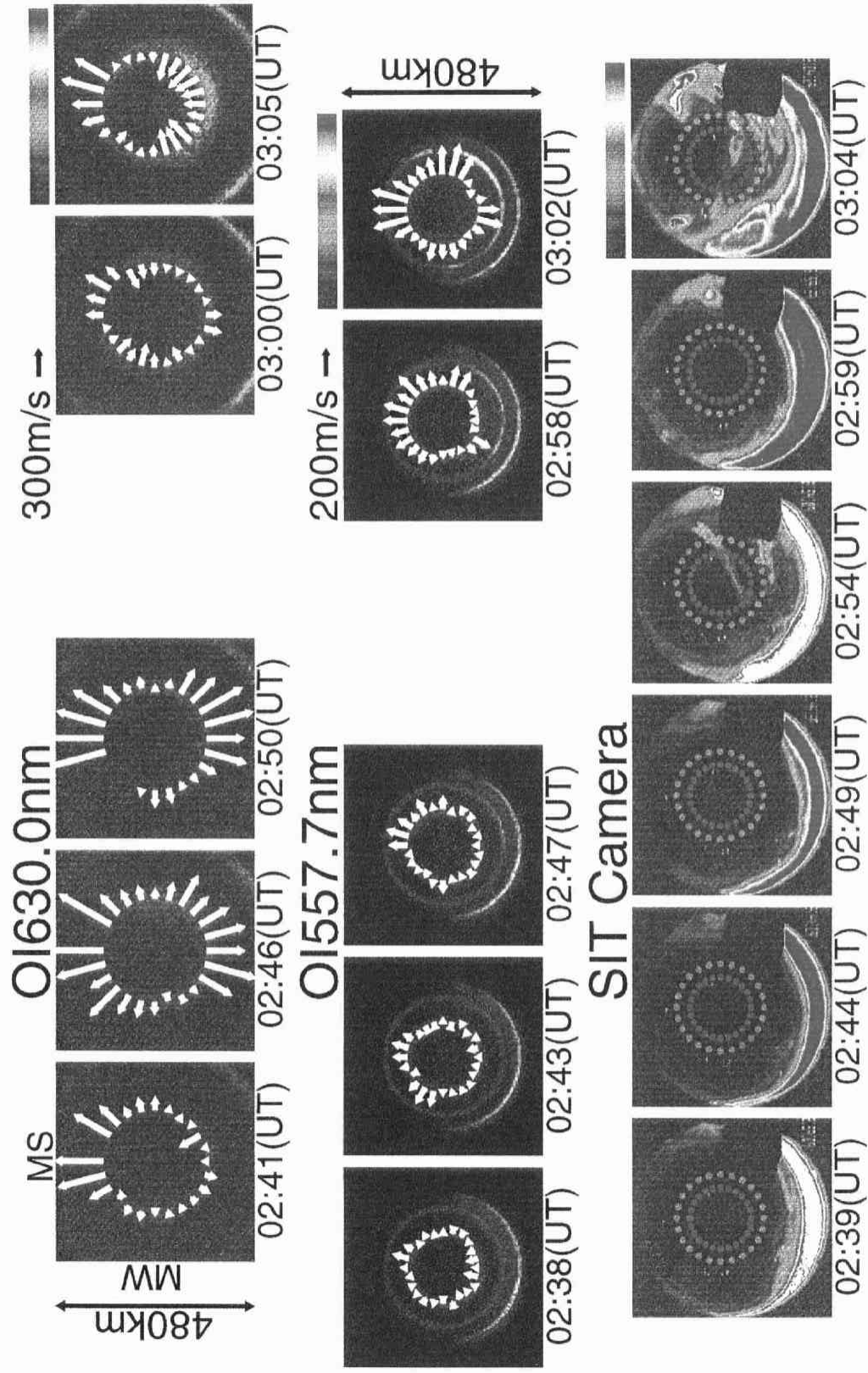


Figure 5.20. Same as Figure 5.7 except for the time interval from 0238 UT to 0305 UT on 3-4 June 1994.

Line-of-Sight Neutral Wind Velocities and All-sky Images

Syowa Station 1994/ 6/ 4

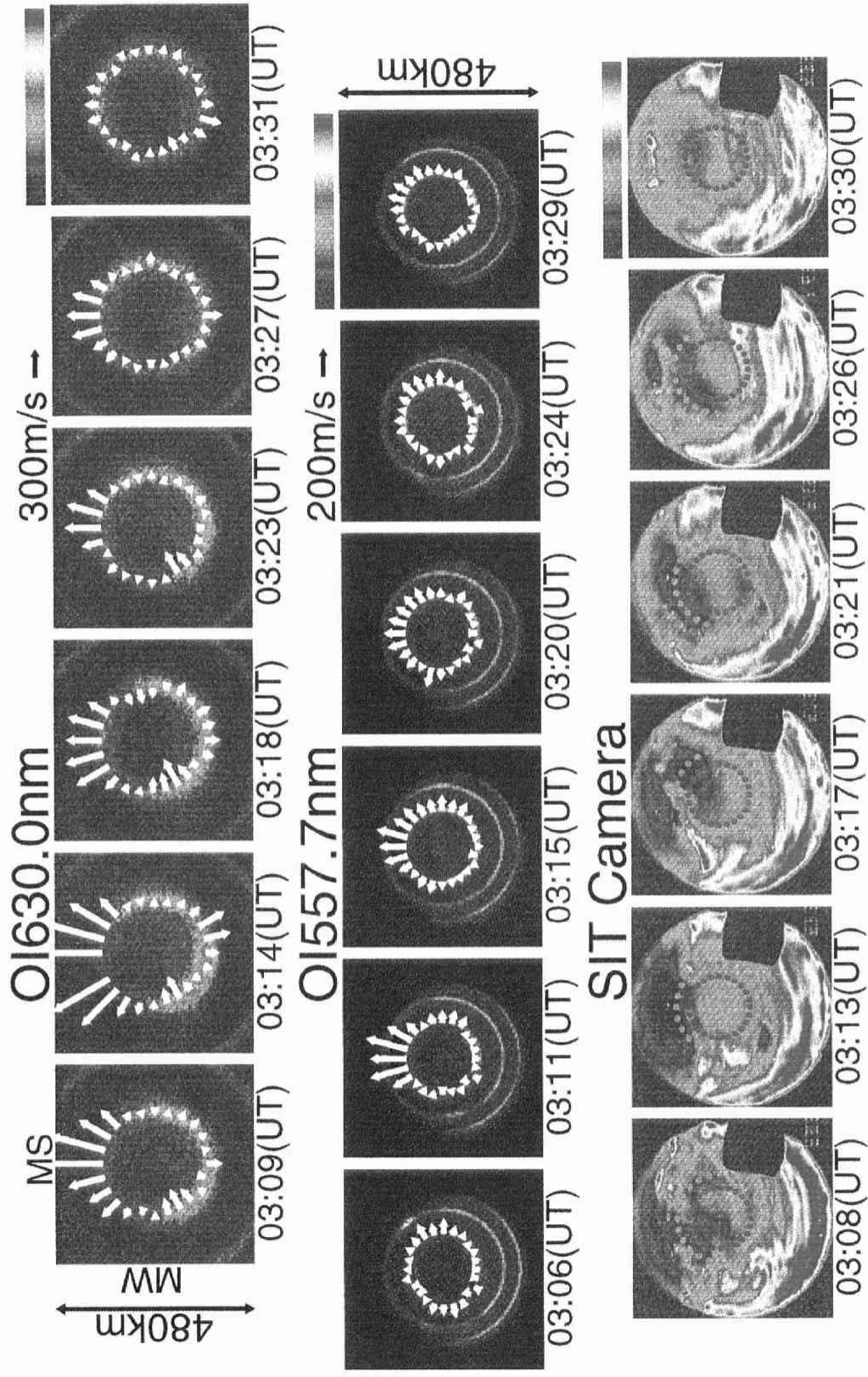


Figure 5.21. Same as Figure 5.20 except for the time interval from 0306 UT to 0331 UT.

Line-of-Sight Neutral Wind Velocities and All-sky Images

Syowa Station 1994/ 6/ 4

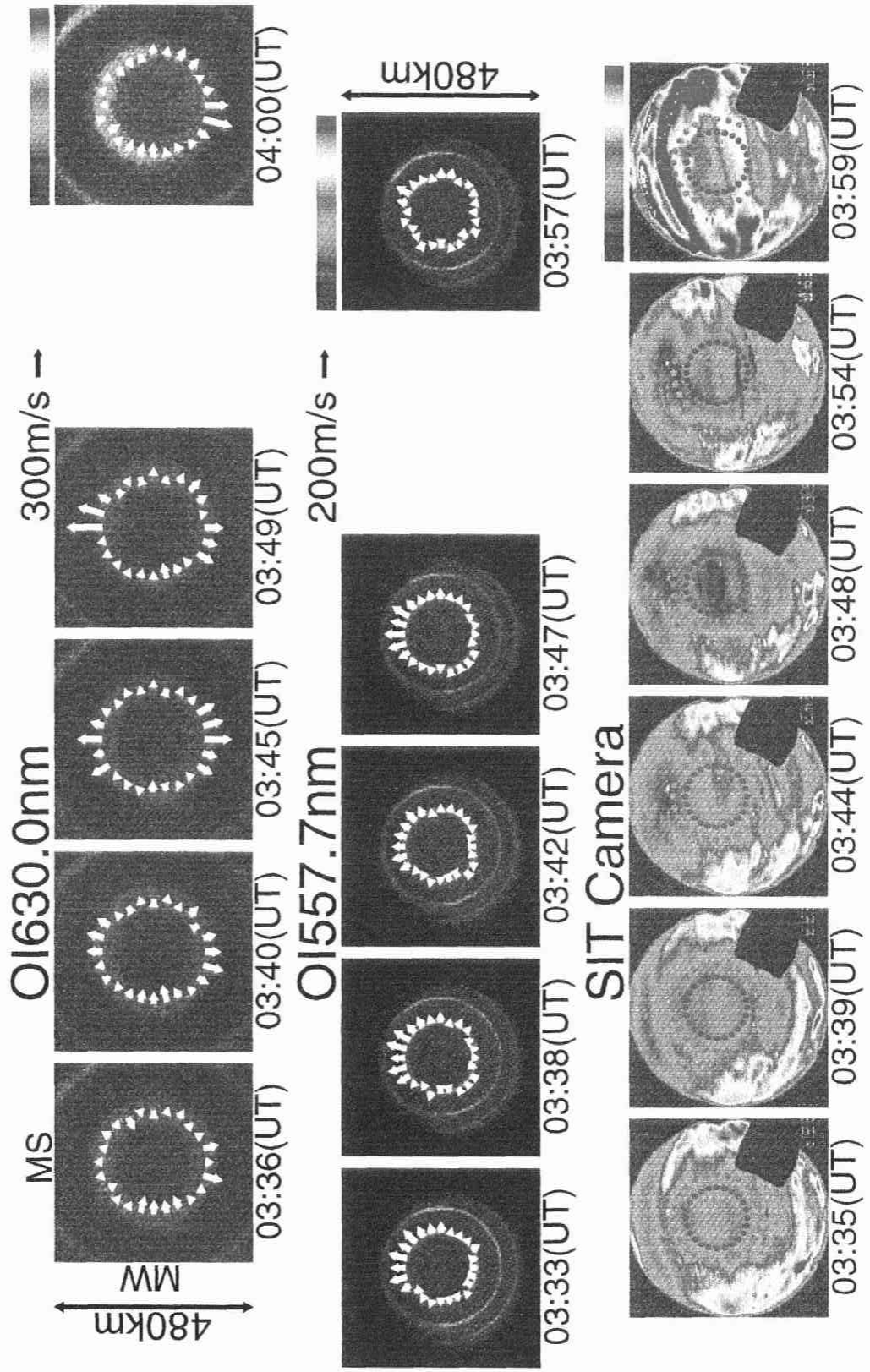


Figure 5.22. Same as Figure 5.20 except for the time interval from 0333 UT to 0400 UT.

Line-of-Sight Neutral Wind Velocities and All-sky Images

Syowa Station 1994/ 6/ 4

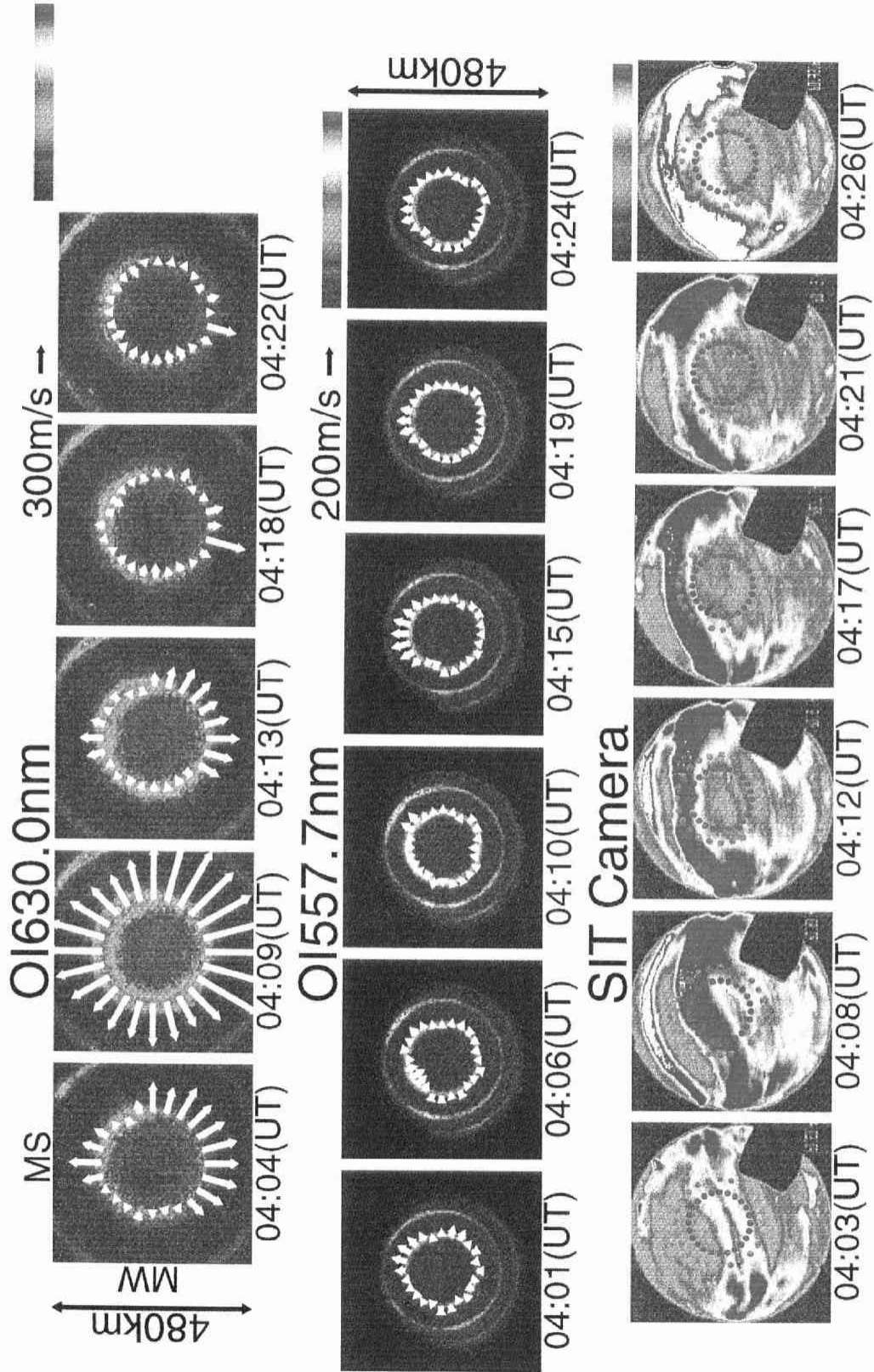


Figure 5.23. Same as Figure 5.20 except for the time interval from 0401 UT to 0426 UT.

UT, and 0413 UT as shown in the upper panels in Figure 5.23. The maximum LOS wind velocity, which was observed at 0409 UT, was about 1000 m/s. This wind pattern suggests the existence of strong upward wind in the F-region. The occurrence of upward winds associated with auroral activity enhancements will be discussed farther in Section 6.4.

Chapter 6

Discussions

6.1 Nighttime variations of thermospheric winds on quiet and disturbed days

Nighttime variations of thermospheric neutral winds during geomagnetically quiet periods obtained by the FPDIS at Syowa station are presented in Section 5.1.1. A comparison of these observational results with TIGCM simulation results shows a good agreement. The TIGCM was run for conditions of winter solstice in the southern hemisphere and $F_{10.7}=90$ by R. G. Roble in the National Center of Atmospheric Research. Figures 6.1 and 6.2 shows calculated meridional and zonal neutral winds above Syowa station, respectively. These simulation results have the following features. At the OI630.0 nm emission layer (~ 240 km altitude) in the F-region, the meridional wind velocity is almost zero at 1800 UT, and after that, northward wind velocity increases gradually, attaining to ~ 100 m/s at about 2300 UT, while the zonal wind is eastward around 1800 UT with a velocity of ~ 110 m/s, and then the wind velocity decreases gradually showing a turning into westward at 0000 UT. At the OI557.7 nm emission layer (~ 105 km altitude) in the E-region, the meridional wind velocity is always very small and not variable, while the zonal wind is eastward with a velocity of ~ 15 m/s at about 1800 UT, and turns into westward at 2000 UT, and eastward again at about 0100 UT. The relation between geographic local time (LT) at the longitude of Syowa station (40°E) and universal time (UT) is given by $LT=UT+2.7$ hr as shown at the bottom in Figures 6.1 and 6.2, while the relation between geomagnetic local time (MLT) at Syowa station and UT is given by $MLT \simeq UT$. To compare between the model calculation and the observation, the calculated winds at the altitudes of 240 km (F-region) and 105 km (E-region) are superposed on the meridional and zonal wind variations shown in Figures 5.3

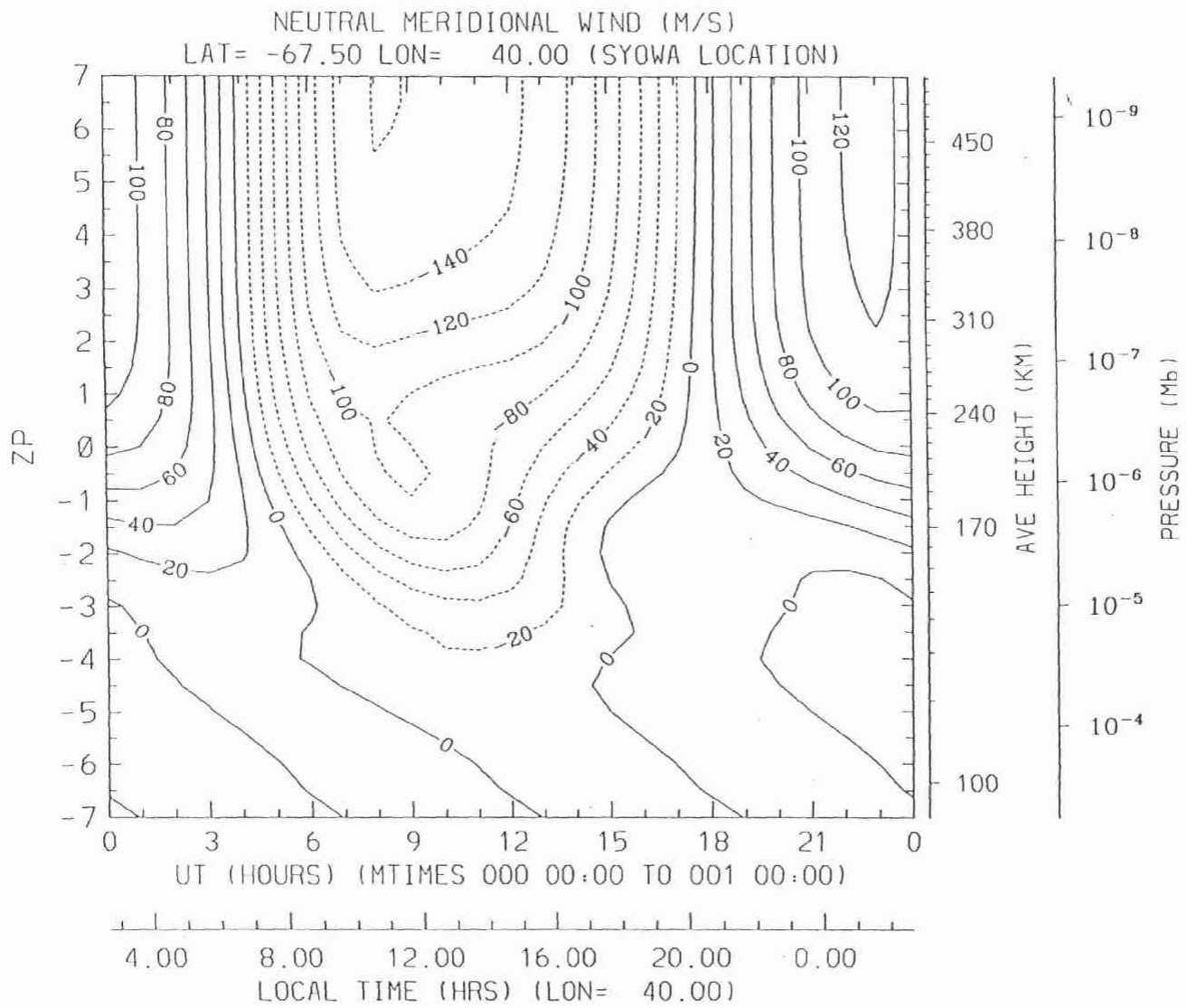


Figure 6.1. Diurnal variation of the meridional neutral wind in the altitude range of 97 - 500 km above Syowa station calculated by the TIGCM.

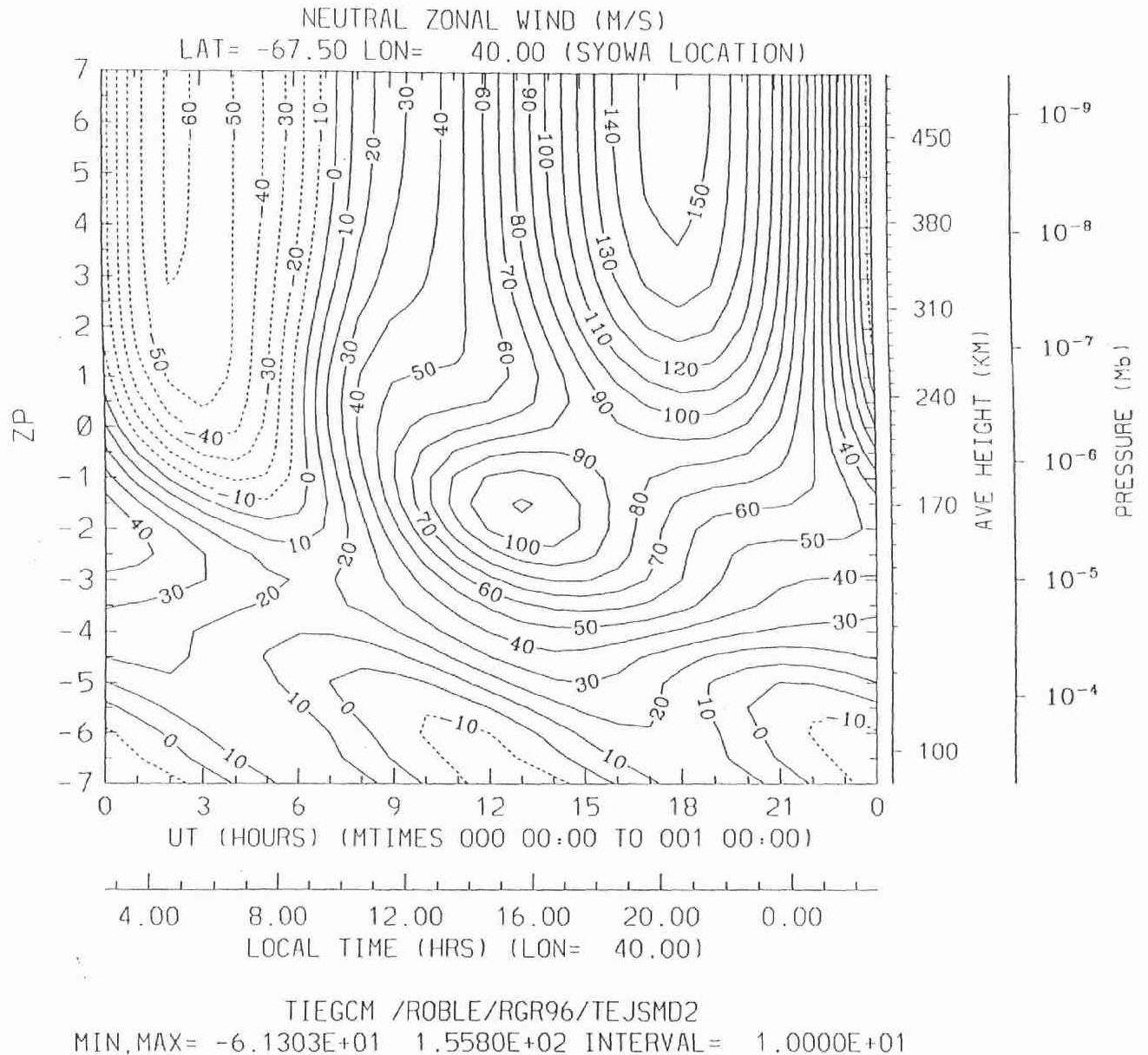


Figure 6.2. Diurnal variation of the zonal neutral wind in the altitude range of 97 – 500 km above Syowa station calculated by the TIGCM.

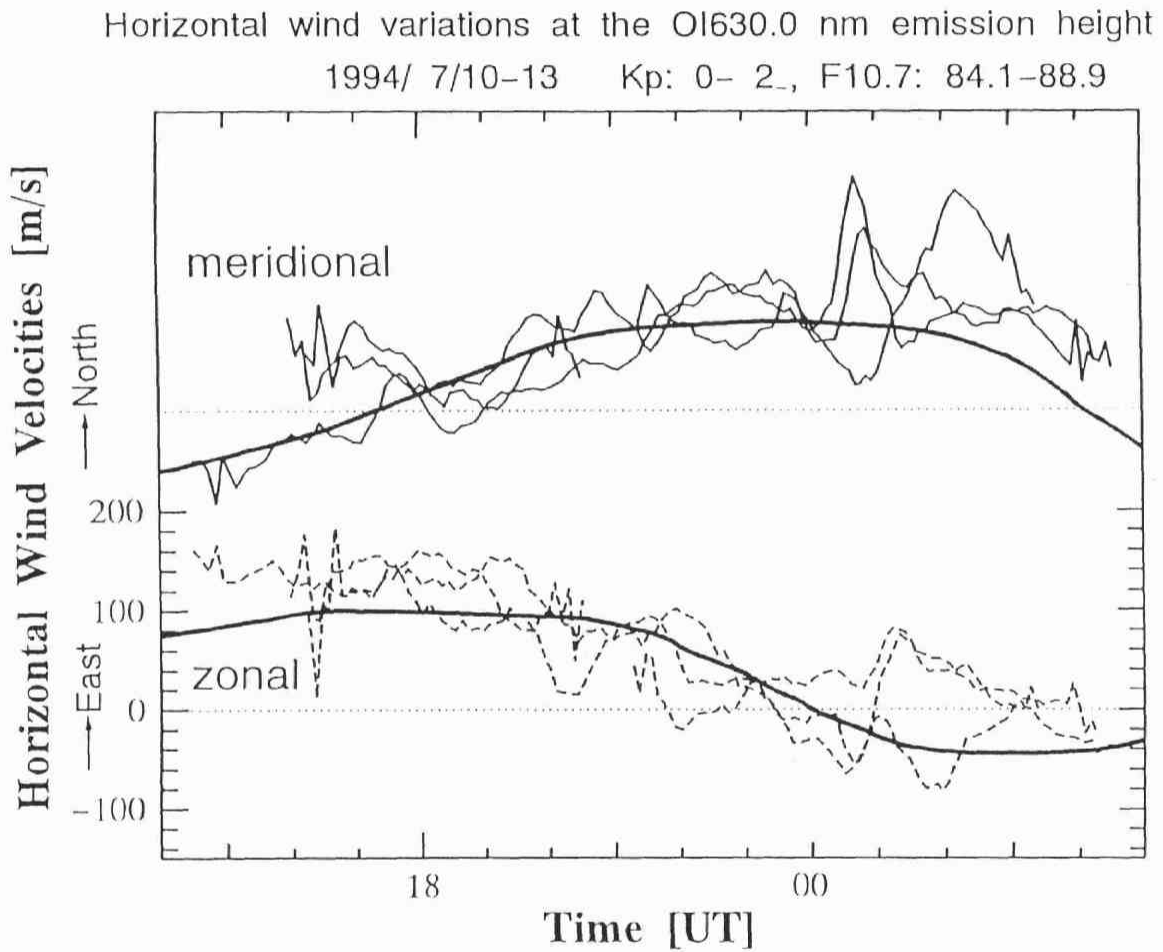


Figure 6.3. Comparison between the meridional and zonal winds in the F-region calculated by the TIGCM model (thick lines) and the observed wind variations given in Figure 5.3.

Horizontal wind variations at the OI557.7 nm emission height
1994/ 7/10-13 Kp: 0- 2₋, F10.7: 84.1-88.9

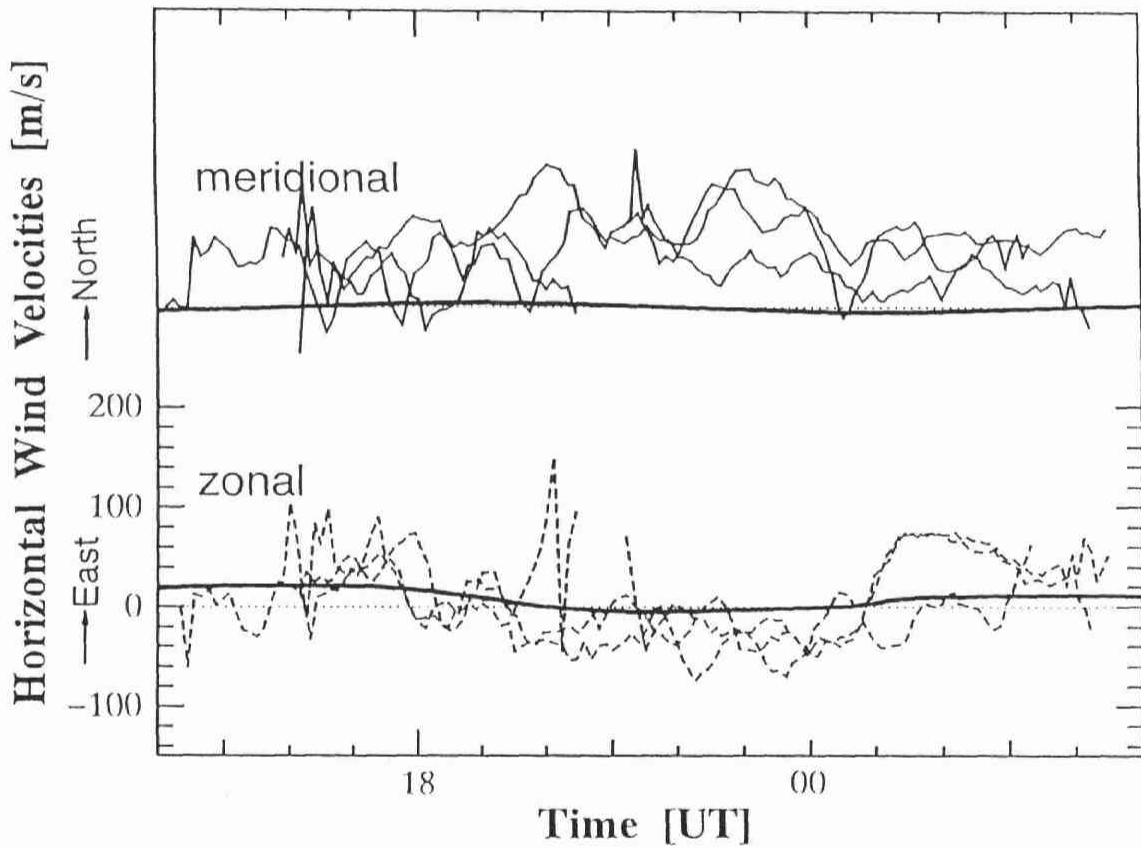


Figure 6.4. Comparison between the meridional and zonal winds in the E-region calculated by the TIGCM model (thick lines) and the observed wind variations given in Figure 5.4.

and 5.4, respectively. The results are shown in Figures 6.3 and 6.4. It is apparent that wind variations obtained from the TIGCM simulation agree with the observed meridional and zonal winds in the F-region, as shown in Figure 6.3. However, in the E-region, there is slight difference between the model prediction and the observed winds, as shown in 6.4, i.e., the model generally underestimates the wind velocity. This disagreement may be associated with the lower boundary condition of the model, given at 97 km altitude.

On the other hand, nighttime wind variations observed during geomagnetically active periods, presented in Figures 5.5 and 5.6 of Section 5.1.2, are quite different from those during geomagnetically quiet periods. The F-region winds during active periods, which are shown in Figure 5.5, are more southward and eastward as compared with the winds during quiet periods shown in Figure 5.3. The similar difference is also seen in the E-region winds shown in Figures 5.4 and 5.6. To investigate the difference in wind patterns on quiet and disturbed days further, we plotted the F-region neutral winds in geomagnetic coordinate. Figures 6.5 and 6.6 represent the magnetic north-south and east-west components of the F-region winds on quiet and disturbed days presented in Figures 5.3 and 5.5. From these figures, it is found that the nighttime variations of the magnetic east-west winds are roughly the same on disturbed days and quiet days, but magnetic north-south winds are apparently more southward (poleward) on disturbed days than on quiet days. Around midnight, the difference in the wind velocities becomes largest and exceed 100-200 m/s.

We suppose that the difference is associated with auroral energy injection and the relative location between the auroral oval and Syowa station. The size of the auroral oval enlarges with increasing geomagnetic activity [*Feldstein and Starkov, 1967; Aruliah and Rees, 1995*]. In the nighttime on quiet days, Syowa station is usually located equatorward of the mean auroral oval. However, during moderately active conditions, Syowa appears to be located mostly within the oval in the nighttime. Under significantly active conditions, it is possible that Syowa enters into the polar cap region around magnetic midnight. In the auroral oval, the heating of the neutral atmosphere occurs through Joule heating and auroral particle precipitation, and pressure gradients are produced. Such pressure gradients can drive a divergent wind field, such as poleward winds on the higher latitude side of the auroral oval, and equatorward winds on the lower latitude side of it. These winds could be enhanced during disturbed periods and affect the neutral circulation pattern of the thermosphere. The poleward wind enhancement in the polar cap caused by the substorm energy injection

Horizontal wind variations at the OI630.0 nm emission height
 1994/ 7/10-13 Kp: 0- 2₋, F10.7: 84.1-88.9

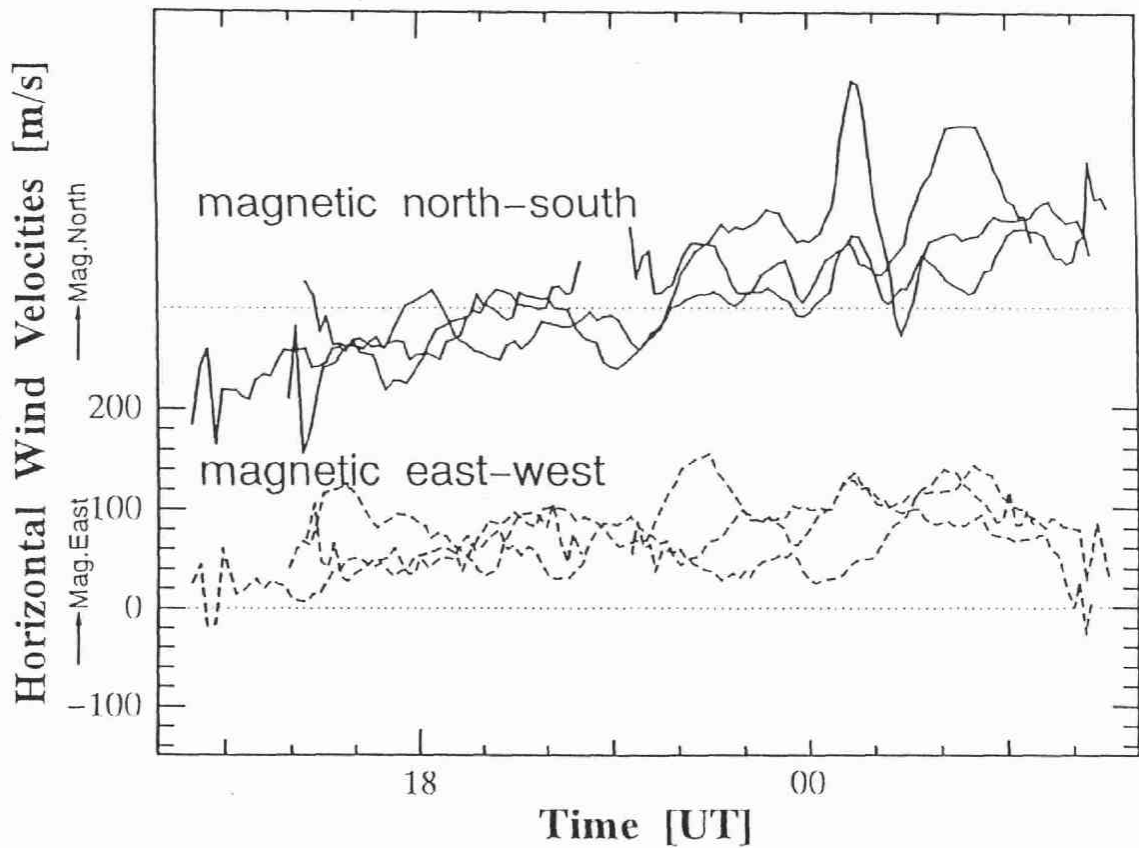


Figure 6.5. Variations of magnetic north-south (solid lines) and east-west (broken lines) winds derived from the FPDIS OI630.0 nm emission data. Wind velocities on the 4 nights of 10-13 July 1994 are displayed together. The values of Kp ranged from 0 to 2₋, and the value of F10.7 solar flux ranged from 84.1 to 88.9 during this period.

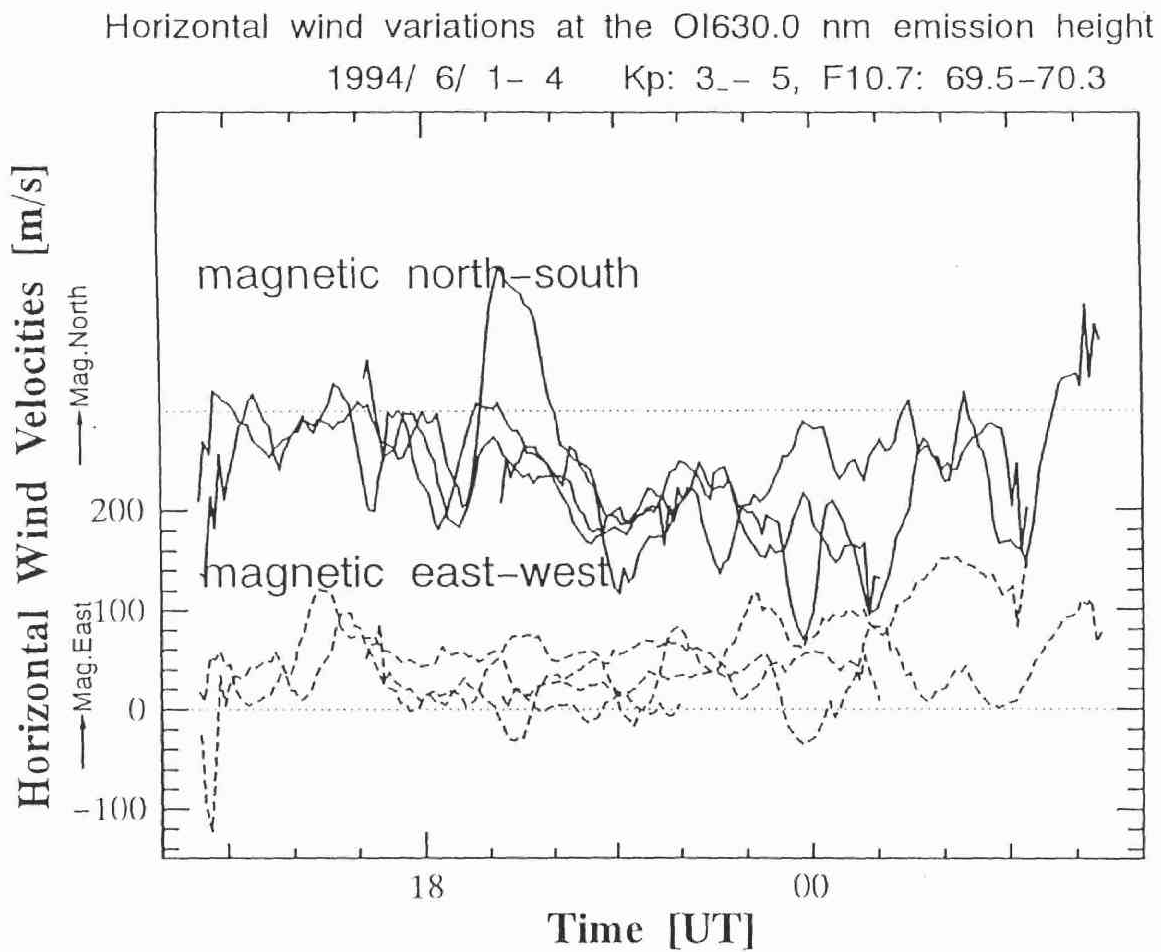


Figure 6.6. Same as Figure 6.5 except for the 4 nights of 1-4 June 1994 with Kp values of 3- to 5 and F10.7 solar flux of 69.5 to 70.3.

is seen in numerical simulation presented by *Fujiwara et al.* [1996]. However, investigations of such poleward winds have scarcely done so far.

To interpret the neutral wind patterns during active periods, we must consider the dependence of the wind pattern on the IMF B_y component [*Thayer et al.*, 1987; *Meriwether et al.*, 1988; *Sica et al.*, 1989]. *Sica et al.* [1989] found a significant IMF B_y -dependence in their Fabry-Perot data from the auroral zone station College, Alaska. The temperatures are higher and winds exhibit stronger sunward zonal flow in the evening (morning) sector for IMF B_y negative (positive) conditions. Furthermore, the nighttime zonal wind changed from westward to eastward earlier for B_y positive than for B_y negative, consistent with the Harang discontinuity shifting to earlier magnetic local times in the northern hemisphere as B_y becomes more positive.

We can use the IMF data obtained by several satellites, from national space science data center (NSSDC) through the world wide web (WWW) interface. Unfortunately, the IMF data during the periods of 1 to 4 June 1994 and 10 to 13 July 1994 are not available due to data gaps. Therefore, it is difficult to discuss the IMF B_y -dependence of our FPDIS wind data. From recent studies, it is known that the changes of thermospheric winds associated with the changes of the IMF B_y component are seen in the morning and evening sectors. However, in our observational results, the wind velocities drastically changed in the midnight sector, therefore this results suggest that the generations of poleward winds during active periods is not related to the IMF B_y effect.

6.2 Thermospheric neutral winds in the vicinity of auroral arcs

In Section 5.2, we showed an example of strong outward flows from the auroral arc region. These flows were observed in both the F- and E-region. One possible driving force for these flows is a forced convection proposed by *Walterscheid et al.* [1985]. The forced convection is the response to heating or the divergent component of ion drag. The circulation cells driven by heating and ion drags illustrated schematically in Figure 6.7. The convection forced by heating will consist of meridional circulation cells with rising motion in the region of heating and sinking motion outside. The convection forced by the meridional ion drag forces consists of circulation cells with horizontal flows along the axis of maximum forcing and return flows above and below. *Walterscheid et al.* [1985] have simulated the perturbation

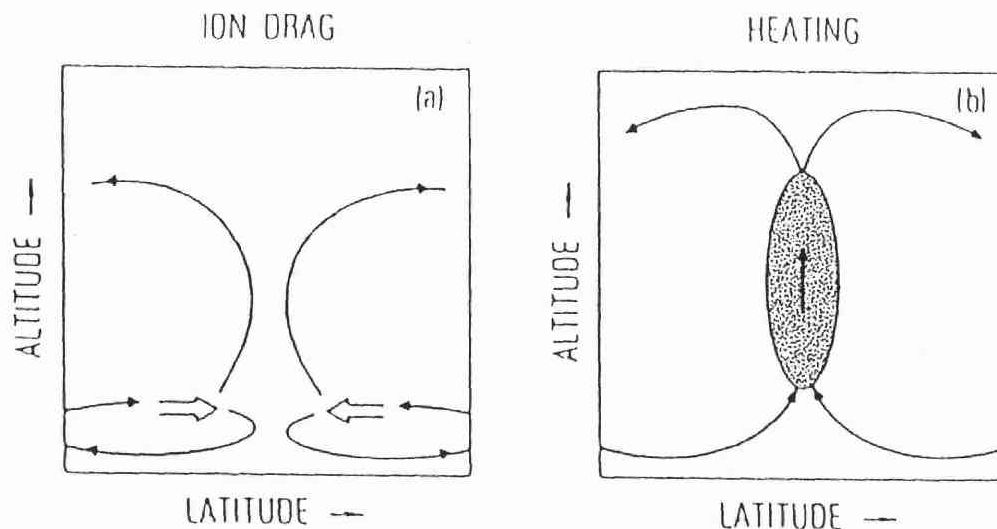


Figure 6.7. Schematic representation of meridional circulation forced by (a) the ion drag momentum force and (b) the heat source. The broad open arrows denote axes of maxima in the north-south ion drag force. The shaded area represents a strongly heated region [Walterscheid *et al.*, 1985].

in the neutral circulation due to the enhanced electrodynamical forcing associated with the appearance of a stable auroral arc. In their simulation, the meridional circulation established by the forcing is not so strong (≤ 15 m/s) but it is quite extensive in latitude. However, the outward flows observed by the FPDIS were strong, and their velocities reached ~ 200 m/s in the E-region, and ~ 300 m/s in the F-region. Therefore, we need further investigation before we conclude that such high speed winds can be derived by the same mechanism as proposed by Walterscheid *et al.* [1985].

It is also necessary to examine the errors in the wind velocity estimation from the FPDIS data in the case of non-uniform distribution of auroral emission intensity as described in Section 4.2.2. Since strong outward flows were observed in the vicinity of auroral arcs, we have to pay attention to this possibility. However, we think that this factor cannot be a major cause. Because, in some panels of Figures 5.7, 5.8, and 5.9, we can see outward flows not only in the edge of auroral arc but also in the outside of the arc where there is no gradient of auroral emission. Further, northward winds appeared in the upper panels of 0001 UT and 0007 UT are opposite to the wind direction expected from an assumption of the influence of non-uniformity.

6.3 Middle-scale atmospheric gravity waves generated by auroral energy injection

In Section 5.3, we presented periodic enhancements of meridional winds on 3-4 June 1994. The period of the variations is 1.3 – 2 hr and the phase velocity of the poleward propagation is ~ 80 m/s in the F-region. Further, these phenomena are observed in both the F- and E-regions simultaneously with the similar phase velocity. They may be middle-scale atmospheric gravity waves (AGWs) with the commonly accepted size classification nomenclature [Francis, 1975; Richmond and Roble, 1979; Hunsucker, 1982]. As a possible source of the middle-scale AGWs, auroral energy appears to be important. When these periodic enhancements appeared in the time interval between 2300 UT and 0300 UT, Syowa station was located on the poleward side of the auroral oval, and there was auroral activity at a distance of a few hundred kilometers north of Syowa station. Therefore, it is likely that middle-scale AGWs were generated in the auroral oval and propagated southward (poleward) across Syowa station. This is the first case that the generation and propagation of middle-scale AGWs were clearly observed by the imaging Fabry-Perot interferometer.

Figure 6.8 shows another event observed on the night of 12-13 June 1994. Hatched areas in Figure 6.8 indicate the enhancements of equatorward winds in the F-region OI630.0 nm emission layer, and a solid line connecting peaks shows that the variations are propagating northward (equatorward). The period of the variations is about 2 hr, and the phase speed is ~ 80 m/s. Auroral all-sky images obtained by the SIT camera at Syowa station on the same night are shown in Figure 6.9. When this phenomenon appeared, Syowa station was located on the equatorward side of the auroral oval, and there was aurora activity at a few hundred kilometers south of Syowa station. Therefore, it seems that middle-scale AGWs were generated in the auroral oval and propagated northward (equatorward) across Syowa station.

In recent study, similar phenomena were presented by *Fagundes et al.* [1995]. They performed measurements of the OI630.0 nm emission line intensity profile and meridional wind velocities at Kiruna using an imaging Fabry-Perot interferometer, and determined the location of auroral electrojet from magnetic field measurement. Their observational results indicated that a large perturbation in the thermospheric winds is generated when the OI630.0 nm line intensity showed an enhancement and/or auroral electrojet was close to, or over, Kiruna latitude. The gravity waves observed were propagating equatorward with speeds of

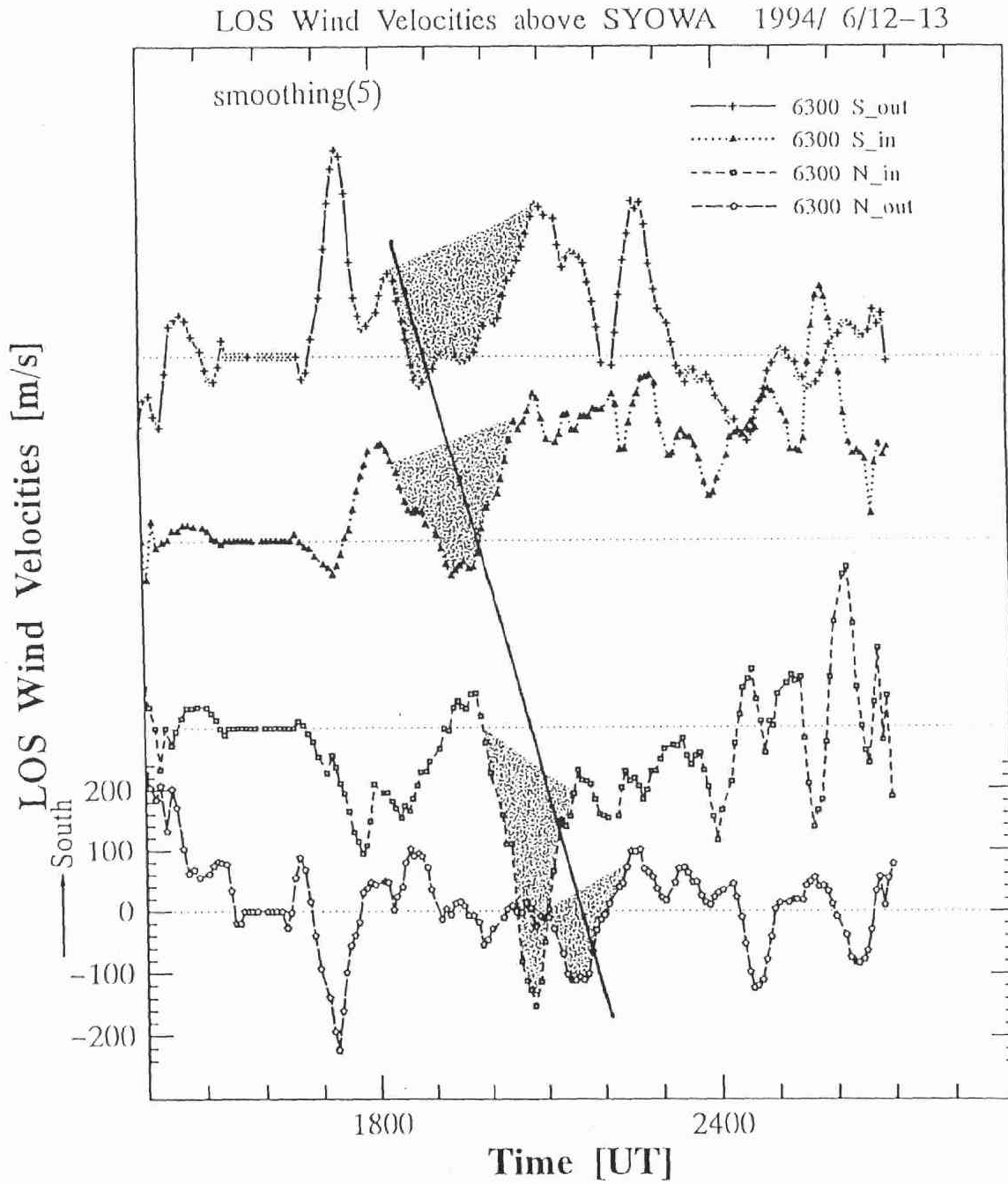


Figure 6.8. Variations of LOS wind velocities observed at Syowa station on the night of 12-13 June 1994. The format is the same as Figure 5.15.

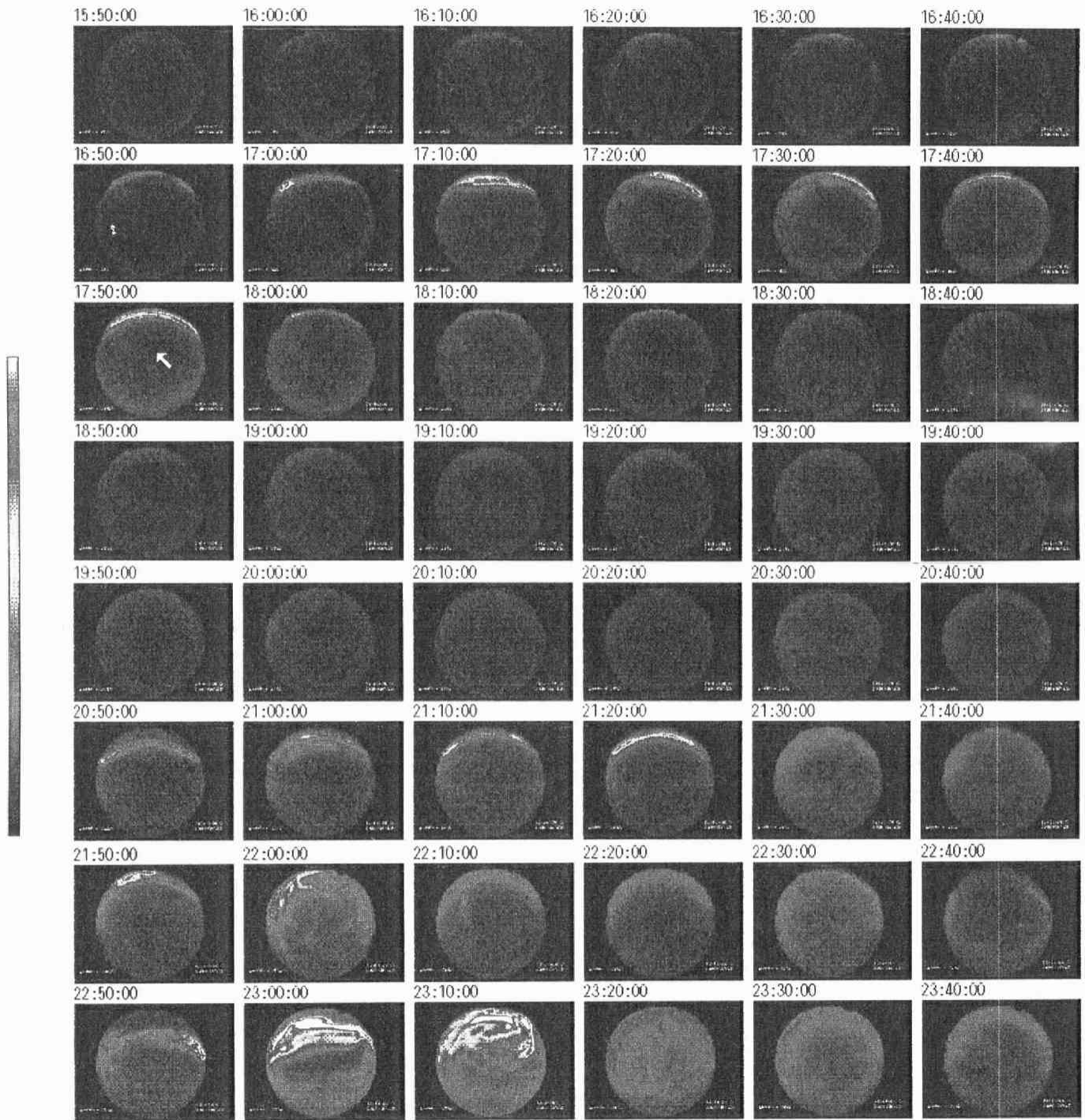


Figure 6.9. All-sky images observed in the nighttime of 12-13 June 1994 using the SIT camera at Syowa station.

890 m/s and 530 m/s or northward with a speed of 380 m/s. These phenomena were thought to be large-scale atmospheric gravity waves.

In Figures 5.15, 5.16, and 6.8, we can find many complex variations of winds besides the middle-scale AGWs. It suggests that various kinds of waves are generated in the auroral oval. Most of them could be dissipated then and there, and only a few variations propagate to different place. It is known that the AGWs are the essential auroral energy transfer process in the high-latitude thermosphere. To investigate the generation and propagation mechanisms of AGWs in detail, simultaneous observations at several points which are located along a meridian with a distance of several hundred kilometers are effective.

6.4 Localized vertical winds associated with auroral activity

Rees et al. [1984] measured vertical winds up to 160 m/s at a mean altitude of about 240 km and on the poleward side of the auroral oval. The changes of vertical winds and the horizontal wind field were highly correlated, and responded directly to the local geomagnetic energy input. *Price et al.* [1995] made high resolution vertical wind measurements of the upper and lower thermosphere at Poker Flat, Alaska, using the OI557.7 nm and OI630.0 nm emission lines at altitudes of about 130 and 240 km, respectively. Significant upwelling events were measured on the poleward side of the auroral oval in geomagnetic active conditions, and a schematic model was used to describe an event from which the horizontal scale of the upwelling region was estimated to be less than 320 km in the lower thermosphere and less than 800 km in the upper thermosphere.

In Section 5.4, we presented the appearance of strong divergent wind pattern which suggests the existence of strong upward thermospheric winds. On the night of 4 June 1994, upward wind patterns appeared at 0246 UT, 0404 UT, 0409 UT, and 0413 UT in the F-region, and at 0302 UT in the E-region (see Figures 5.19, 5.20, 5.21, and 5.22). 0246 UT – 0302 UT events appeared on the poleward side of the auroral oval during geomagnetically active conditions, and they seem to be similar events as those reported by *Price et al.* [1995]. The duration is ~ 10 min, and the horizontal scale of the upwelling region, which is estimated by the extent of the divergent wind in the FPDIS data, is more than 350 km in the E-region and more than 380 in the F-region. However, estimation of the vertical wind velocity is difficult, because we measured only LOS wind velocity.

It is very interesting that the middle-scale AGWs which have been discussed in the previous section are observed on the same night. This result demonstrates that the upwelling motion observed near the active auroral oval is closely related to the AGW generation. Figure 6.10 schematically shows our suggestion of the relation between these phenomena. During geomagnetically disturbed period, the upwelling region with the horizontal scale of ~ 400 km appears on the poleward side of the auroral oval and causes the middle-scale AGWs which propagate poleward. On the night of 3-4 June 1994, Syowa station was located on the poleward side of the auroral oval around magnetic midnight, and therefore it is superposed that AGWs which were generated in the auroral oval propagated poleward over Syowa station. When the upward wind was observed at about 0300 UT, Syowa station approached the auroral oval, and then entered the auroral oval.

On the other hand, the divergent wind pattern observed at 0409 UT shows a dramatic enhancement of a divergent wind which has not been reported yet. Upwelling region overlaps the OI630.0 nm auroral emission region, and strong divergent wind occurred simultaneously with an auroral emission enhancement. Its duration was only ~ 15 min, and the horizontal scale of the upwelling region was estimated to be more than 680 km in the F-region. Figure 6.11 shows flux-gate magnetometer data obtained at Syowa station on this night. It can be seen in this figure that a negative bay in the H-component with a magnitude of 300 nT occurred from 0400 UT to about 0420 UT. It indicates the appearance of an ionospheric current over Syowa station. We suppose that this current caused the heating of atmosphere and the thermospheric upward wind.

From this study, it is shown that the FPDIS observation is very useful to detect the vertical thermospheric winds. Further, we will be able to determine the vertical wind velocities by triangular measurements from two points located with a separation of a few hundred kilometers.

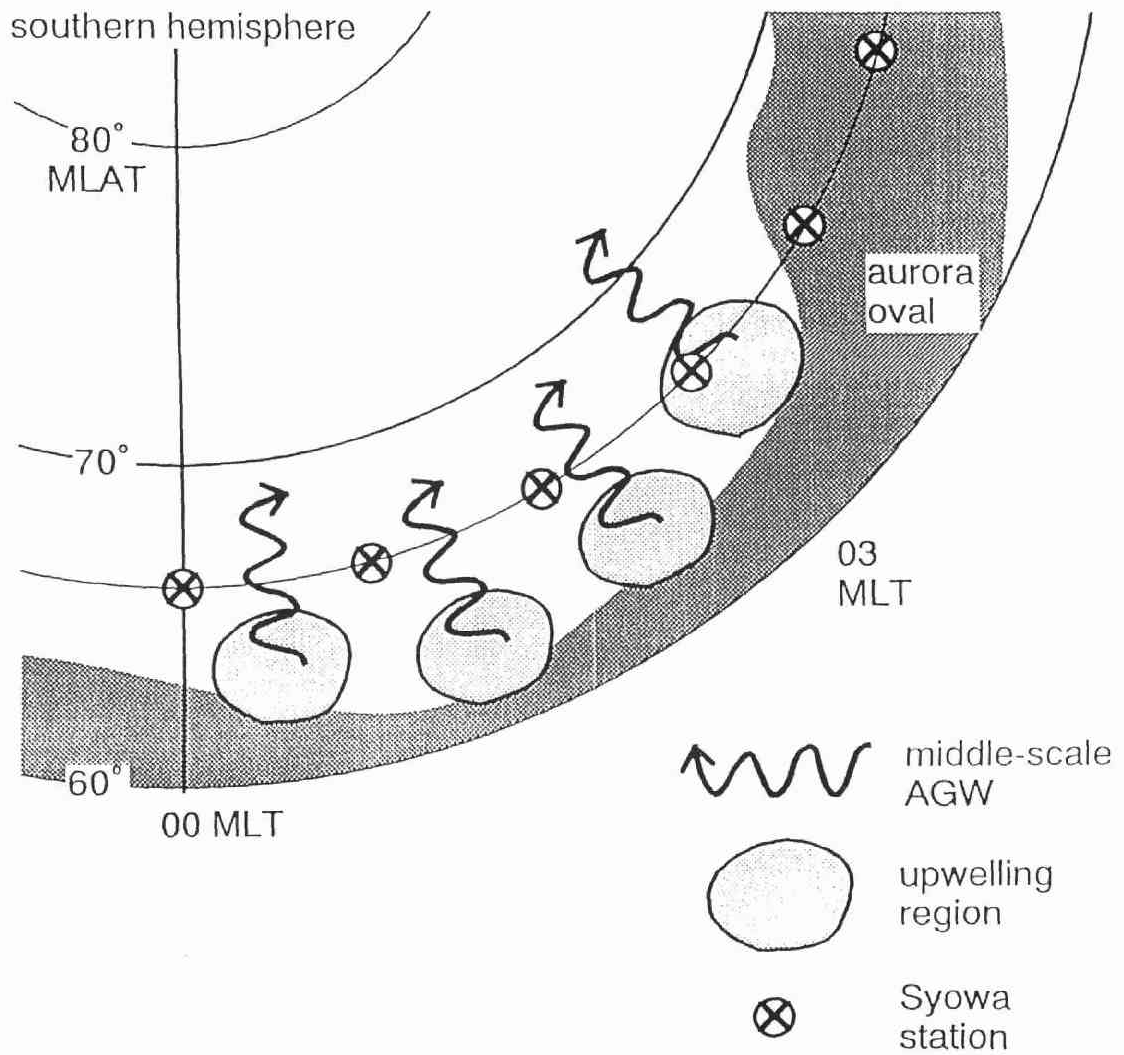


Figure 6.10. Schematic model showing the location of the aurora oval and the events observed on the night of 3-4 June 1994. Symbols '⊗' indicate the location of Syowa station.

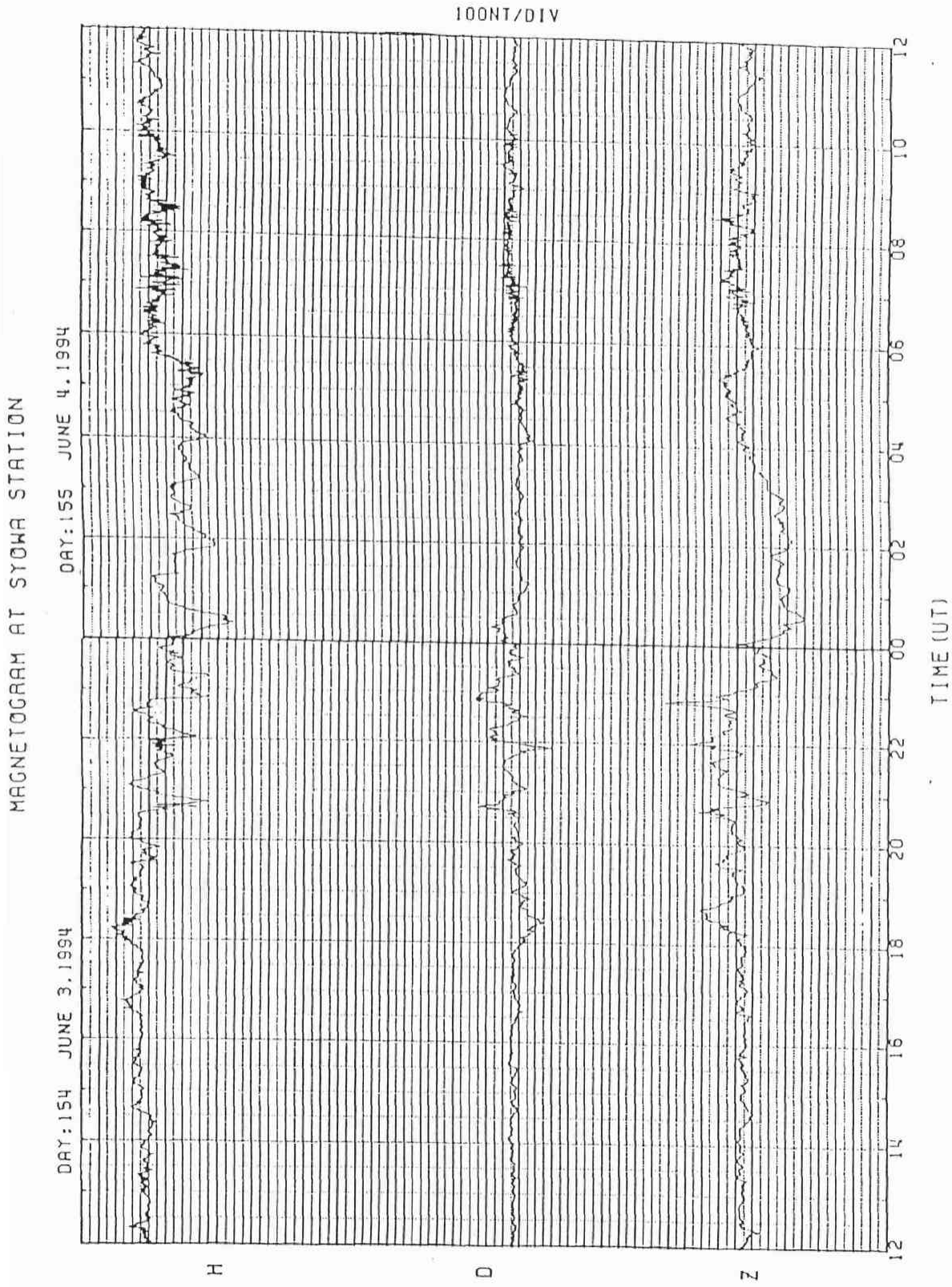


Figure 6.11. Triaxial magnetometer data at Syowa station on the night of 3-4 June 1994.

Chapter 7

Conclusions

In order to investigate the earth's thermosphere in which a variety of dynamical and chemical processes take place in response to the variations of energy input, we made an overall improvement of the prototype Fabry-Perot Doppler imaging system (FPDIS) which had been developed by the Tohoku University optical group in 1989, and performed measurements of thermospheric neutral winds at Syowa station, Antarctica in 1994. The conclusions of this thesis are summarized as follows:

- 1) The FPDIS measures the Doppler shifts and widths of aurora and/or airglow emission lines of OI557.7 nm and OI630.0 nm over a wide field of view (165°) to obtain two-dimensional distributions of winds and temperatures in the E- and F-region. The characteristic of the Fabry-Perot Doppler imaging system used in this study is high temporal and spatial resolution in the thermospheric wind measurements. The maximum time resolution is 1 min for the OI557.7 nm emission and 3 min for the OI630.0 nm emission, while the typical spatial resolution is about 50 km for the OI557.7 nm emission and about 100 km for the OI630.0 nm emission.
- 2) The main improvement of the prototype FPDIS is to adopt the proximity focused photon counting imager (PFPCI) in place of the photon imaging head which caused image distortion. The advanced CCD camera and data processor are also adopted to avoid overexposure.
- 3) The improved FPDIS was installed at Syowa station (69.00°S , 39.58°E in geographic coordinates; -66.23° , 71.75° in corrected geomagnetic coordinates; $L=6.15$), Antarctica, and observations of thermospheric neutral winds were carried out for 57 nights covering various auroral conditions during one austral winter period in 1994.

- 5) Nighttime variations of the thermospheric neutral winds are found to depend on geomagnetic activity. The magnetic southward winds during geomagnetically active periods are stronger than during quiet periods, and the difference in the wind velocities on active and quiet days is largest around midnight. The difference is supposed to be associated with auroral energy injection level and the relative location between the auroral oval and Syowa station.
- 6) In the vicinity of aurora arcs, strong outward flows are often observed. These outward flows seem to be caused by forced convection which is the response to heating or the divergent component of ion drag around aurora arcs. However, the velocity of outward flows is much greater than the prediction of numerical models.
- 7) Poleward propagating, middle-scale atmospheric gravity waves (AGWs) are observed on geomagnetically disturbed days. These AGWs appear to be generated in the auroral oval staying at a few hundred kilometers north of Syowa station. This is the first observation of the generation and propagation of middle-scale AGWs by an optical method.
- 8) Strong divergent wind patterns which suggest the existence of strong upward thermospheric winds are often observed near the active auroral region. The horizontal scale of the upwelling region is several hundred kilometers, and the duration is ~ 10 min.

These observational results demonstrate that the FPDIS is an outstanding tool for remote sensing of rapid variations of the thermospheric neutral winds associated with auroral activity, and make clear the several types of thermospheric responses to auroral activity. Furthermore, it is demonstrated that the upwelling motion observed near the active auroral region is closely related to the AGW generation.

To investigate the generation and propagation mechanisms of AGWs and the upwelling motion in detail, simultaneous observations at several points located along a meridian with a distance of several hundred kilometers are effective. Further, simultaneous observations of thermosphere and ionosphere by the FPDIS and various kind of radars are useful to achieve more clear and comprehensive understanding of the thermosphere.

References

- Andreassen, O., C. E. Wasberg, D. C. Fritts, and J. R. Isler, Gravity wave breaking in two and three dimensions, 1, Model description and comparison of two-dimensional evolutions, *J. Geophys. Res.*, **99**, 8,095–8,108, 1994.
- Armstrong, E. B., Doppler shifts in the wavelength of the OI λ 6300 line in the night airglow, *Planet. Space Sci.*, **17**, 957–974, 1969.
- Aruliah, A. L., D. Rees, The trouble with thermospheric vertical winds: geomagnetic, seasonal and solar cycle dependence at high latitudes, *J. Atmos. Terr. Phys.*, **57**, 597–609, 1995.
- Banks, P. M., Magnetospheric processes and the behavior of the neutral atmosphere, *Space Res.*, **12**, 1,051–1,067, 1972.
- Batten, S., D. Rees, D. Wade, and A. Steen, Observations of thermospheric neutral winds by the UCL Doppler imaging system at Kiruna in northern Scandinavia, *J. Atmos. Terr. Phys.*, **50**, 861–888, 1988.
- Batten, S., and D. Rees, Thermospheric winds in the auroral oval: Observations of small scale structures and rapid fluctuations by a Doppler imaging system, *Planet. Space Sci.*, **38**, 675–694, 1990.
- Brekke, A., S. Nozawa, and T. Sparr, Studies of the E region neutral wind in the quiet auroral ionosphere, *J. Geophys. Res.*, **99**, 8,801–8,825, 1994.
- Brinkman, D. G., R. L. Walterscheid, L. R. Lyons, D. C. Kayser, J. R. Sharber, R. A. Frahm, and M. F. Larsen, E region neutral winds in the postmidnight diffuse aurora during the atmospheric response in aurora 1 rocket campaign, *J. Geophys. Res.*, **100**, 17,309–17,320, 1995.
- Burnside, R. G., F. A. Herrero, J. W. Meriwether Jr., and J. C. G. Walker, Optical observations of thermospheric dynamics at Arecibo, *J. Geophys. Res.*, **86**, 5,532–5,540, 1981.
- Burrage, M. D., N. Arvin, W. R. Skinner, and P. B. Hays, Observations of the O₂ atmospheric band nightglow by the high resolution Doppler imager, *J. Geophys. Res.*, **99**, 15,017–15,023, 1994.

- Conde, M., and R. W. Smith, "Phase compensation" of a separation scanned, all-sky imaging Fabry-Perot spectrometer for auroral studies, *Appl. Opt.*, , submitted, 1996.
- Conde, M., and R. W. Smith, Mapping thermospheric winds in the auroral zone, *Geophys. Res. Lett.*, **22**, 3,019–3,022, 1995.
- Conde, M., and P. L. Dyson, Thermospheric vertical winds above Mawson, Antarctica, *J. Atmos. Terr. Phys.*, **57**, 589–596, 1995.
- Crickmore, R. I., J. R. Dudeney, and A. S. Rodger, Vertical thermospheric winds at the equatorward edge of the auroral oval, *J. Atmos. Terr. Phys.*, **53**, 485–492, 1991.
- Crowley, G., Dynamics of the earth's thermosphere: a review, *Rev. Geophys.*, **29**, 1,143–1,165, 1991.
- Deng, W., T. L. Killeen, A. G. Burns, and R. G. Roble, The flywheel effect: Ionospheric currents after a geomagnetic storm, *Geophys. Res. Lett.*, **18**, 1,845–1,848, 1991.
- Deng, W., T. L. Killeen, A. G. Burns, R. G. Roble, J. A. Slavin, and L. E. Wharton, The effects of neutral inertia on ionospheric currents in the high-latitude thermosphere following a geomagnetic storm, *J. Geophys. Res.*, **98**, 7,775–7,790, 1993.
- Fagundes, P. R., A. L. Aruliah, D. Rees, and J. A. Bittencourt, Gravity wave generation and propagation during geomagnetic storms over Kiruna (67.8°N, 20.4°E), *Ann. Geophys.*, **13**, 13,358–13,366, 1995.
- Fagundes, P. R., Y. Sahai, H. Takahashi, D. Gobbi, and J. A. Bittencourt, Thermospheric and mesospheric temperatures during geomagnetic storms at 23°S, *J. Atmos. Terr. Phys.*, **58**, 1,963–1,972, 1996.
- Forbes, J. M., N. A. Makarov, and Yu. I. Portnyagin, First results the meteor radar at South Pole: a large 12-hour oscillation with zonal wavenumber one, *Geophys. Res. Lett.*, **22**, 3,247–3,250, 1995.
- Foster, J. C., J.-P. St.-Maurice, and V. J. Abreu, Joule heating at high latitudes, *J. Geophys. Res.*, **88**, 4,885, 1983.
- Francis, S. H., Global propagation of atmospheric gravity waves: a review, *J. Atmos. Terr. Phys.*, **37**, 1,011, 1975.
- Fritts, D. C., J. F. Garten, and O. Andreassen, Wave breaking and transition to turbulence in stratified shear flows, *J. Atmos. Sci.*, **53**, 1,057–1,085, 1996.
- Fritts, D. C., J. R. Isler, J. H. Hecht, R. L. Waltersheid, and O. Andreassen, Wave breaking signatures in sodium densities and OH nightglow, Part II: Simulation of wave and instability structures, *J. Geophys. Res.*, submitted, 1996b.
- Fujiwara, H., A simulation study of the thermospheric response to substorm forcing, *Master Thesis*, Tohoku University, 1993.

- Fujiwara, H., S. Maeda, H. Fukunishi, T. J. Fuller-Rowell, and D. S. Evans, Global variations of thermospheric winds and temperatures caused by substorm energy injection, *J. Geophys. Res.*, **101**, 225–239, 1996.
- Fuller-Rowell, T. J., and D. S. Evans, Height-integrated Pedersen and Hall conductivity patterns inferred from the TIROS-NOAA satellite data, *J. Geophys. Res.*, **92**, 7,606–7,618, 1987.
- Fuller-Rowell, T. J., M. V. Codrescu, R. J. Moffett, and S. Quegan, Response of the thermosphere and ionosphere to geomagnetic storms, *J. Geophys. Res.*, **99**, 3,893–3,914, 1994.
- Fuller-Rowell, T. J., M. V. Codrescu, H. Rishbeth, R. J. Moffett, and S. Quegan, On the seasonal response of the thermosphere and ionosphere to geomagnetic storms, *J. Geophys. Res.*, **101**, 2,343–2,353, 1996.
- Garcia, R. R., and S. Solomon, The effect of breaking gravity waves on the dynamics and chemical composition of the mesosphere and lower thermosphere, *J. Geophys. Res.*, **90**, 3,850–3,868, 1985.
- Hays, P. B., and R. G. Roble, Direct observations of thermospheric winds during geomagnetic storms, *J. Geophys. Res.*, **76**, 5,316–5,321, 1971.
- Hays, P. B., J. W. Meriwether, and R. G. Roble, Nighttime thermospheric winds at high latitudes, *J. Geophys. Res.*, **84**, 1,905–1,913, 1979.
- Hedin, A. E., N. W. Spencer, and T. L. Killeen, Empirical globe model of upper thermosphere winds based on Atmosphere and dynamic explorer satellite data, *J. Geophys. Res.*, **93**, 9,959–9,989, 1988.
- Hedin, A. E., Revised global model of thermosphere winds using satellite and ground based observations, *J. Geophys. Res.*, **96**, 7,657–7,688, 1991.
- Hedin, A. E., E. L. Fleming, A. H. Manson, F. J. Schmidlin, S. K. Avery, R. R. Clark, S. J. Franke, G. J. Fraster, T. Tsuda, F. Vial, and R. A. Vincent, Empirical wind model for the upper, middle and lower atmosphere, *J. Atmos. Terr. Phys.*, **58**, 1,421–1,447, 1996.
- Heelis, R. A., J. C. Foster, O. de la Beaujardiere, and J. Holt, Multistation measurements of high-latitude ionospheric convection, *J. Geophys. Res.*, **88**, 10,111–10,121, 1983.
- Hernandez, G., and R. G. Roble, Direct measurement of nighttime thermospheric winds and temperatures. 1. Seasonal variations during geomagnetic quiet periods, *Geophys. Res. Lett.*, **81**, 2,065–2,074, 1976.
- Hernandez, G., Solar, geomagnetic and long term effects on thermospheric neutral kinetic temperatures at midlatitude, *Adv. Space Res.*, **3**, 129–136, 1983.

- Hernandez, G., R. W. Smith, R. G. Roble, J. Gress, and K. C. Clark, Thermospheric dynamics at the south pole, *Geophys. Res. Lett.*, **17**, 1,255–1,258, 1990.
- Hernandez, G., R. W. Smith, G. J. Fraser, and W. L. Jones, Large-scale waves in the upper-mesosphere at antarctic high-latitude, *Geophys. Res. Lett.*, **19**, 1,347–1,345, 1992.
- Hernandez, G., R. W. Smith, and G. J. Fraser, Antarctic high-latitude mesospheric dynamics, *Adv. Space Res.*, **16**, 71–80, 1995.
- Hunsucker, R. D., Atmospheric gravity waves generated in the high-latitude ionosphere: a review, *Rev. Geophys.*, **20**, 293–315, 1982.
- Jacka, F., A. R. D. Bower, and P. A. Wilksch, Thermospheric temperatures and winds derived from OI λ 630 nm night airglow line profiles, *J. Atmos. Terr. Phys.*, **41**, 397–407, 1979.
- Killeen, T. L., P. B. Hays, N. W. Spencer, and L. E. Wharton, Neutral winds in the polar thermosphere as measured from Dynamics Explorer, *Geophys. Res. Lett.*, **9**, 957–960, 1982.
- Killeen, T. L., R. Roble, R. G. Roble, R. W. Smith, N. W. Spencer, J. W. Meriwether Jr., D. Rees, G. Hernandez, P. B. Hays, L. L. Cogger, D. P. Sipler, M. A. Biondi, and C. A. Tepley, Mean neutral circulation in the winter polar F region, *J. Geophys. Res.*, **91**, 1,633–1,649, 1986.
- Killeen, T. L., R. Roble, and R. G. Roble, An analysis of the high-latitude thermospheric wind pattern calculated by a thermospheric general circulation model, 2, Neutral parcel trajectories, *J. Geophys. Res.*, **91**, 11,291–11,307, 1986.
- Killeen, T. L., R. Roble, and N. W. Spencer, A computer model of global thermospheric winds and temperature, *Adv. Space Res.*, **7**, 207–215, 1987.
- Killeen, T. L., Energetics and dynamics of the earth's thermosphere, *Rev. Geophys.*, **25**, 433–454, 1987.
- Killeen, T. L., and R. G. Roble, Thermosphere Dynamics: Contributions from the first 5 years of the dynamics explorer program, *Rev. Geophys.*, **26**, 329–367, 1988.
- Killeen, T. L., F. G. McCormac, A. G. Burns, J. P. Thayer, R. M. Johnson, and R. J. Niciejewski, On the dynamics composition of the high-latitude thermosphere, *J. Atmos. Terr. Phys.*, **53**, 797–815, 1991.
- Lu, G., A. D. Richmond, B. A. Emery, and R. G. Roble, Magnetosphere-ionosphere-thermosphere coupling: effect of neutral winds on energy transfer and field-aligned current, *J. Geophys. Res.*, **100**, 19,643–19,659, 1995.
- McLandress, C., G. G. Shepherd, and B. H. Solheim, Satellite observations of thermospheric tides: Results from the wind imaging interferometer on UARS, *J. Geophys. Res.*, **101**, 4,093–4,114, 1996.

- McCormac, F. G., T. L. Killeen, J. P. Thayer, G. Hernandez, C. R. Tschan, J.-J. Ponthieu, and N. W. Spencer, Circulation of the polar thermosphere during geomagnetically quiet and active times as observed by dynamics explore 2, *J. Geophys. Res.*, **92**, 10,133–10,149, 1987.
- Meriwether Jr., J. W., T. L. Killeen, F. G. McCormac, A. G. Burns, and R. G. Roble, Thermospheric winds in the geomagnetic polar cap for solar minimum conditions, *J. Geophys. Res.*, **93**, 7,478–7,492, 1988.
- Morton, Y. T., R. S. Lieberman, P. B. Hays, D. A. Ortland, A. R. Marshall, D. Wu, W. R. Skinner, M. D. Burrage, D. A. Gell, and J.-H. Yee, Global mesospheric tidal winds observed by the high resolution Doppler imager on board the upper atmosphere research satellite, *J. Geophys. Res.*, **20**, 1,263–1,266, 1993.
- Murty, G. S., and J. S. Kim, Temperatures and meridional winds in the vicinity of the SAR-arc as observed from Albany, New York, *Planet. Space Sci.*, **35**, 1,077–1,085, 1987.
- Nakajima, H., A study on auroral Zone Thermospheric Neutral Temperatures and winds using Fabry-Perot Doppler imaging observations at Syowa stations, Antarctica, *Doctor Thesis*, Tohoku University, 1993.
- Nakajima, H., Observations of thermospheric wind velocities and temperatures by the use of a Fabry-Perot Doppler imaging system at Syowa Station, Antarctica, *Appl. Opt.*, **34**, 8,382–8,395, 1995.
- Nozawa, S., and A. Brekke, Studies of the E region neutral wind in the disturbed auroral ionosphere, *J. Geophys. Res.*, **100**, 14,717–14,734, 1995.
- Okano, S., and J. S. Kim, Observations of a SAR-arc associated with an isolated magnetic substorm, *Planet. Space Sci.*, **35**, 475–482, 1987.
- Price, G. D., and F. Jacka, The influence of geomagnetic activity on the upper mesosphere/lower thermosphere in the auroral zone. I. Vertical winds, *J. Atmos. Terr. Phys.*, **53**, 909–922, 1991.
- Price, G. D., F. Jacka, R. A. Vindent, and G. B. Burns, The influence of geomagnetic activity on the upper mesosphere/lower thermosphere in the auroral zone. II. Horizontal winds, *J. Atmos. Terr. Phys.*, **53**, 923–947, 1991.
- Price, G. D., R. W. Smith, and G. Hernandez, Simultaneous measurements of large vertical winds in the upper and lower thermosphere, *J. Atmos. Terr. Phys.*, **57**, 631–643, 1995.
- Reber, C. A., and C. E. Trevathan, The upper atmosphere research satellite(UARS) mission, *J. Geophys. Res.*, **98**, 10,643–10,647, 1993.
- Rees, M. H., B. A. Emery, R. G. Roble, and K. Stamnes, Neutral and ion gas heating by auroral particle precipitation, *J. Geophys. Res.*, **88**, 6,289–6,300, 1983.

- Rees, D., and A. H. Greenaway, Doppler imaging system; an optical device for measuring vector winds. 1: General principles, *Appl. Opt.*, **22**, 1,078–1,083, 1983.
- Rees, D., R. W. Smith, P. J. Charleton, F. G. McCormac, and A. Steen, The generation of vertical thermospheric winds and gravity waves at auroral latitudes-I. Observations of vertical winds, *Planet. Space Sci.*, **32**, 667–684, 1984.
- Rees, D., A. H. Greenaway, R. Gordon, I. McWhirter, P. J. Charleton, and A. Steen, The Doppler imaging system: Initial observations of the auroral thermosphere, *Planet. Space Sci.*, **32**, 273–285, 1984.
- Rees, D., P. Charleton, M. Carlson, and P. Rounce, Latitude thermospheric circulation during the energy budget campaign, *J. Atmos. Terr. Phys.*, **47**, 195–232, 1985.
- Richmond, A. D. and R. G. Roble, Dynamic effects of aurora generated gravity waves on the mid-latitude ionosphere, *J. Atmos. Terr. Phys.*, **41**, 841, 1979.
- Richmond, A. D., The ionospheric wind dynamo: effects of its coupling with different atmospheric regions, *The upper mesosphere and lower thermosphere: a review of experiment and theory (Geophysical Monograph 87)*, The American Geophysical Union, 49–64, 1995.
- Roble, R. G., T. L. Killeen, N. W. Spencer, R. A. Heelis, P. H. Reiff, and J. D. Winningham, Thermospheric dynamics during November 21–22, 1981: Dynamics explorer measurements and thermospheric general circulation model predictions, *J. Geophys. Res.*, **93**, 209–225, 1988.
- Shepherd, G. G., G. Thuillier, B. H. Solheim, Y. J. Rochon, J. Criswick, W. A. Gault, R. N. Peterson, R. H. Wiens, and S.-P. Zhang, WINDII on UARS - status report and preliminary results, *The upper mesosphere and lower thermosphere: a review of experiment and theory (Geophysical Monograph 87)*, The American Geophysical Union, 297–304, 1995.
- Sica, R. J., G. Hernandez, B. A. Emery, R. G. Roble, R. W. Smith, and M. H. Rees, The control of auroral zone dynamics and thermodynamics by the interplanetary magnetic fields dawn-dusk (Y) component, *J. Geophys. Res.*, **94**, 11,921–11,932, 1989.
- Sipler, D. P., and M. A. Biondi, Midlatitude F region neutral winds and temperatures during the geomagnetic storm of March 26, 1976, *J. Geophys. Res.*, **84**, 37–40, 1979.
- Sipler, D. P., M. A. Biondi, and M. E. Zipf, Vertical winds in the midlatitude thermosphere from Fabry-Perot interferometer measurements, *J. Atmos. Terr. Phys.*, **57**, 621–629, 1995.
- Smith, R. W., G. Hernandez, K. Price, G. Fraser, K. C. Clark, W. J. Schulz, S. Smith, and M. Clark, The June 1991 thermospheric storm observed in the southern hemisphere, *J. Geophys. Res.*, **99**, 17,609–17,615, 1994.

- Smith, R. W., and G. Hernandez, Upper thermospheric temperatures at southpole, *Adv. Space Res.*, **16**, 31–35, 1995.
- Smith, R. W., and G. Hernandez, Vertical winds in the thermosphere within the polar cap, *J. Atmos. Terr. Phys.*, **57**, 611–620, 1995.
- Solomon, S. C., Optical aeronomy, *Rev. Geophys.*, **29**, 1,089–1,109, 1991.
- Steen, A, D. Rees, P. N. Collis, and J. S. Murphree, What role does the F-region neutral wind play in auroral intensifications?, *Space Sci. Rev.*, **36**, 851–868, 1988.
- Thayer, J. P., T. L. Killeen, F. G. McCormac, C. R. Tschan, J.-J. Ponthieu, and N. W. Spencer, Thermospheric neutral wind signatures dependent on the east-west component of the interplanetary magnetic field for northern and southern hemispheres as measured from DE-2, *Ann. Geophys. Gauthier Villars*, **5A**, 363–368, 1987.
- Thayer, J. P., and T. L. Killeen, A kinematic analysis of the high-latitude thermospheric neutral circulation pattern, *J. Geophys. Res.*, **98**, 11,549–11,565, 1993. Titheridge, J. E., Winds in the Ionosphere - a review, *J. Atmos. Terr. Phys.*, **57**, 1,681–1,741, 1995.
- Torr, M. R., P. G. Richards, and D. G. Torr, A new determination of the ultraviolet heating efficiency of the thermosphere, *J. Geophys. Res.*, **85**, 6,819–6,826, 1980.
- Torr, M. R., D. G. Torr, and P. G. Richards, The solar ultraviolet heating efficiency of the midlatitude thermosphere, *Geophys. Res. Lett.*, **7**, 373–376, 1980.
- Walterscheid, R. L., L. R. Lyons, and K. E. Taylor, The perturbed neutral circulation in the vicinity of a symmetric stable aurora arc, *J. Geophys. Res.*, **90**, 12,235–12,248, 1985.
- Walterscheid, R. L., and L. R. Lyons, The neutral E region zonal winds during intense postmidnight diffuse aurora: Response to observed particle fluxes, *J. Geophys. Res.*, **94**, 3,703–3,712, 1989.
- Walterscheid, R. L., and L. R. Lyons, The neutral circulation in the vicinity of a stable aurora arc, *J. Geophys. Res.*, **97**, 19,489–19,499, 1992.
- Wu, Q., T. L. Killeen, and N. W. Spencer, Dynamics explorer 2 observations of equatorial thermospheric dependence, *J. Geophys. Res.*, **99**, 6,277–6,288, 1994.

Appendix A

Sequential wind data in the F-region

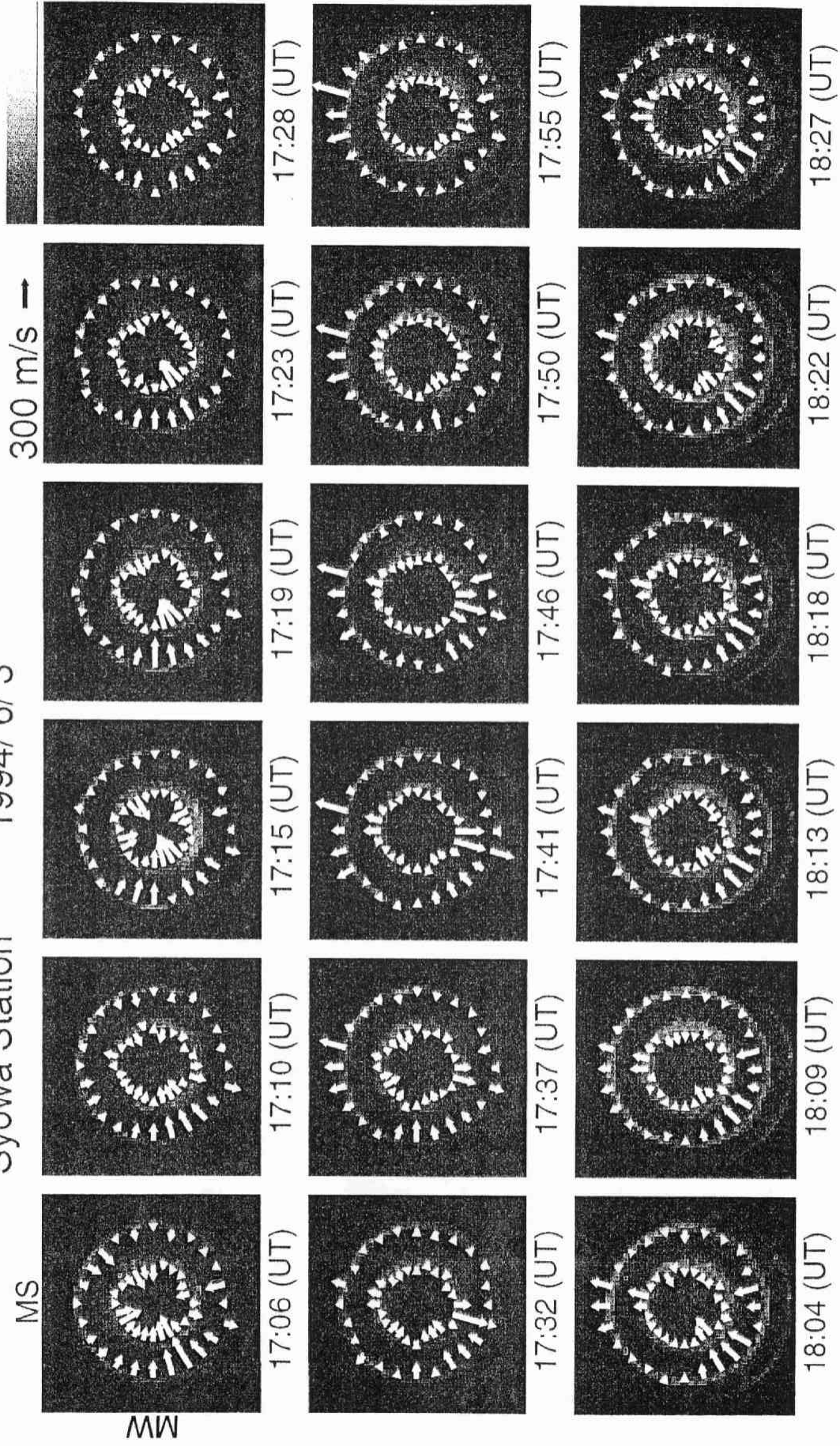
We present sequential wind data in the F-region and OI630.0 nm fringe images between 1705 UT and 0423 UT on the night of 3-4 June 1994. These data were obtained by measurements of the OI630.0 nm emission line using the FPDIS at Syowa station, Antarctica. Each panel shows the line-of-sight wind velocity distributions in 24 directions superposed on the OI630.0 nm emission fringes. The top of the panel is magnetic south and the left is magnetic west, and the time at the midst of exposure is denoted under the panel. Similar data for the OI557.7 nm emission line observed simultaneously are shown in Appendix B.

The FPDIS wind data obtained at Syowa station in 1994 are opened to the public tentatively. They are kept in an anonymous ftp site, so that anyone can get them by ftp commands. Address and account of the server are as follows.

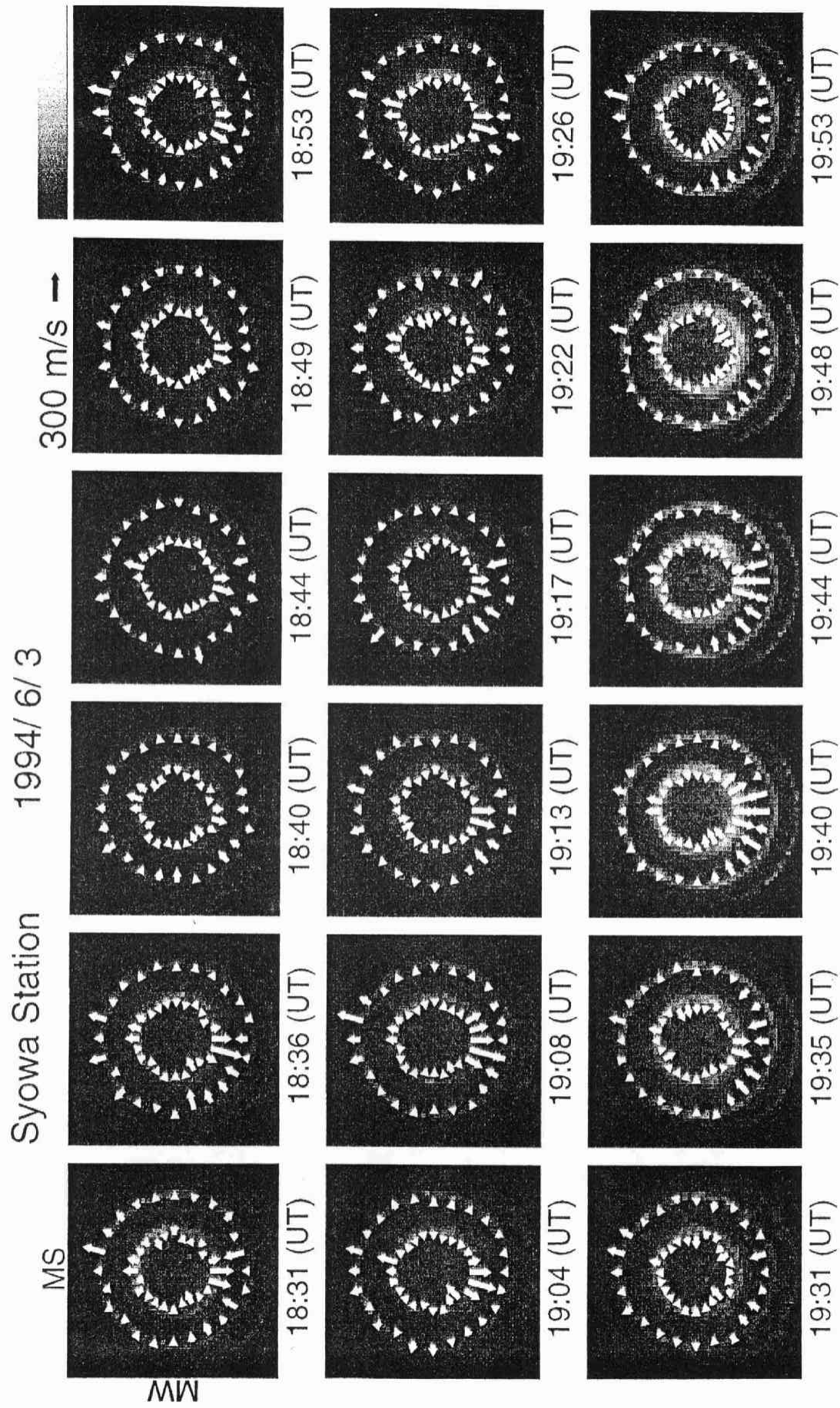
IP address: 130.34.117.150
account: ftp
password: your e-mail address
directory: fpdis/

Line-of-sight neutral wind velocities and auroral fringes measured by the OI630.0 nm emission line

Syowa Station 1994/ 6/ 3

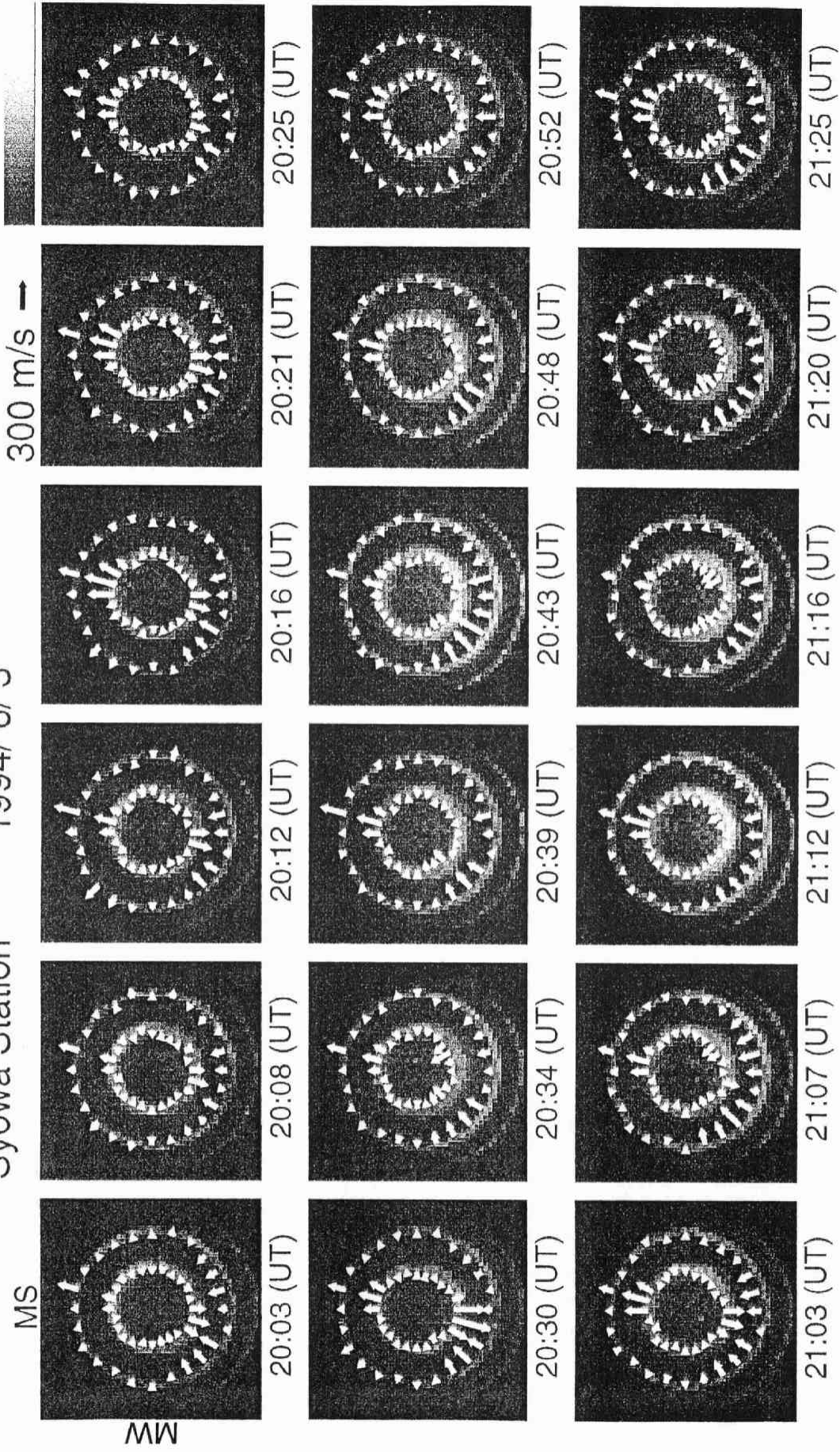


Line-of-sight neutral wind velocities and auroral fringes measured by the OI630.0 nm emission line



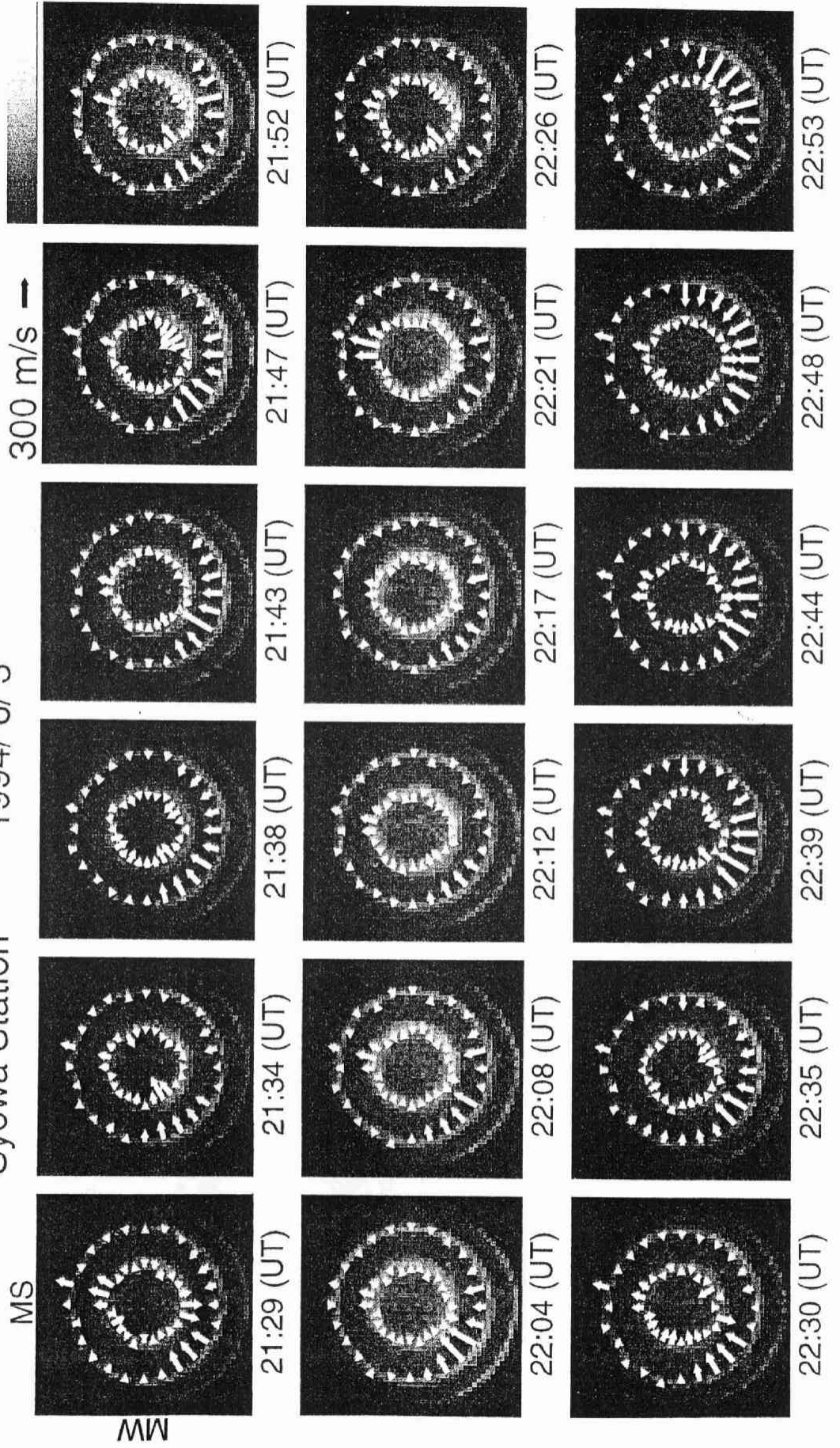
Line-of-sight neutral wind velocities and auroral fringes measured by the OI630.0 nm emission line

Syowa Station 1994/6/3



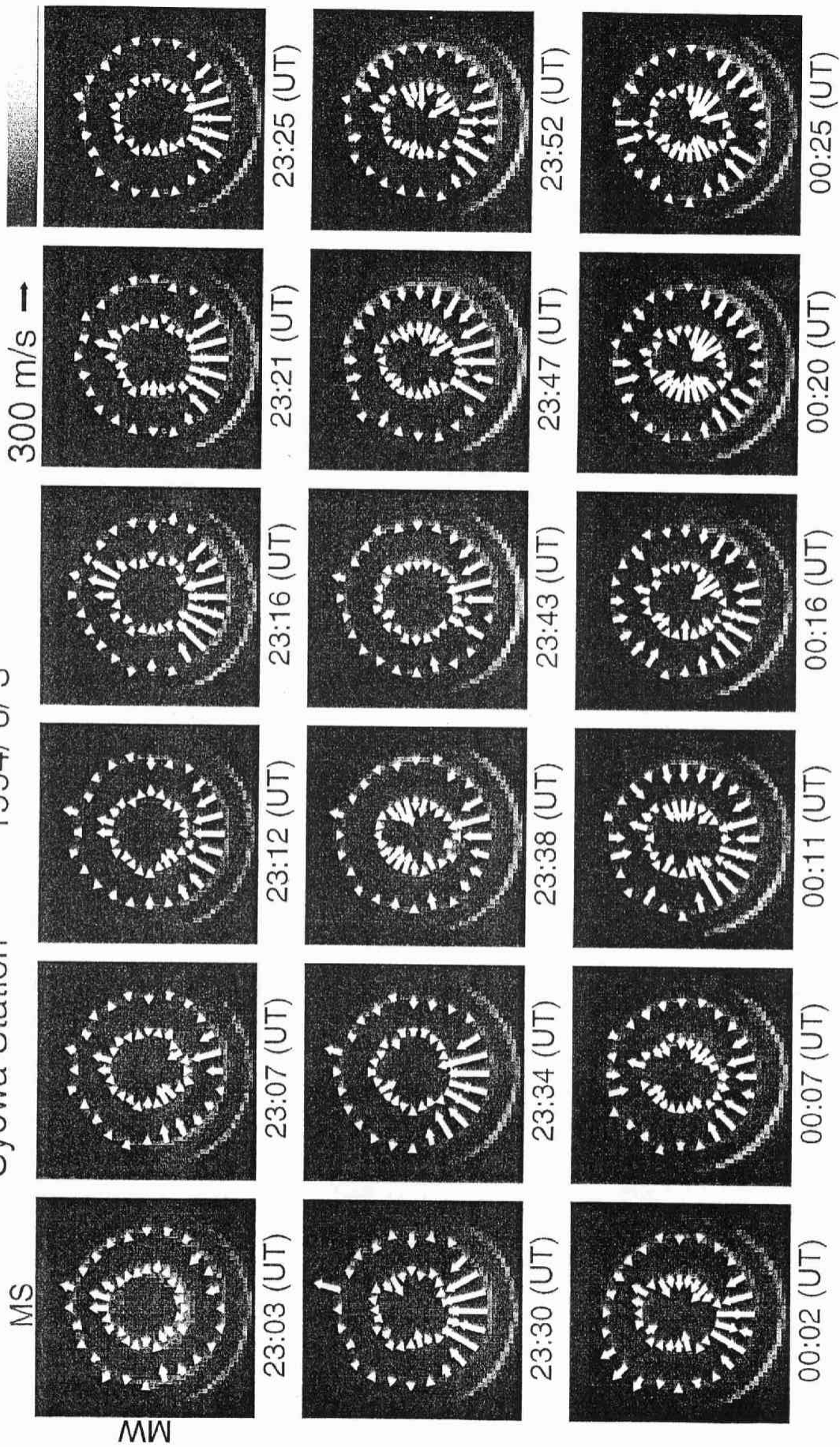
Line-of-sight neutral wind velocities and auroral fringes measured by the OI630.0 nm emission line

Syowa Station 1994/6/3

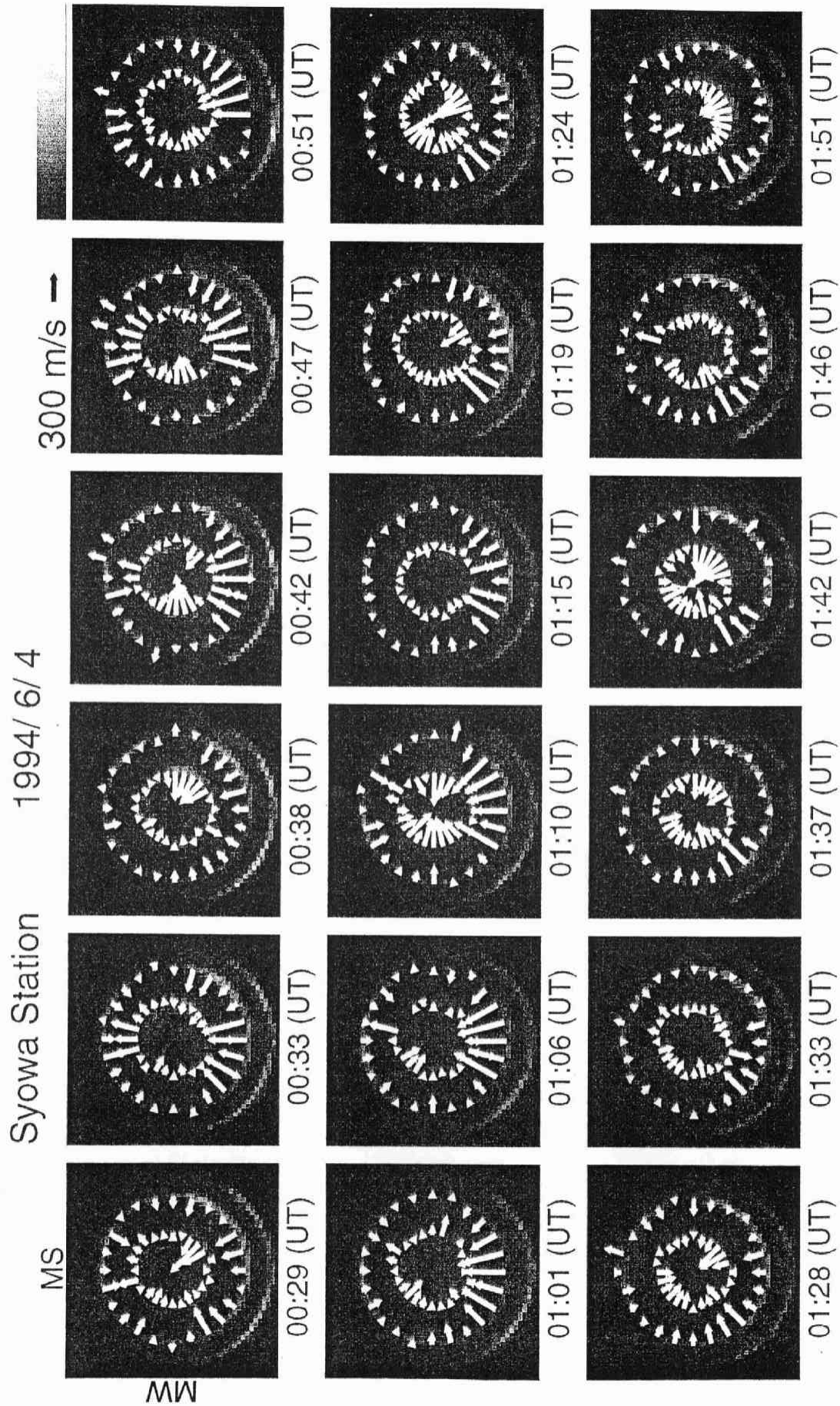


Line-of-sight neutral wind velocities and auroral fringes measured by the OI630.0 nm emission line

Syowa Station 1994/ 6/ 3

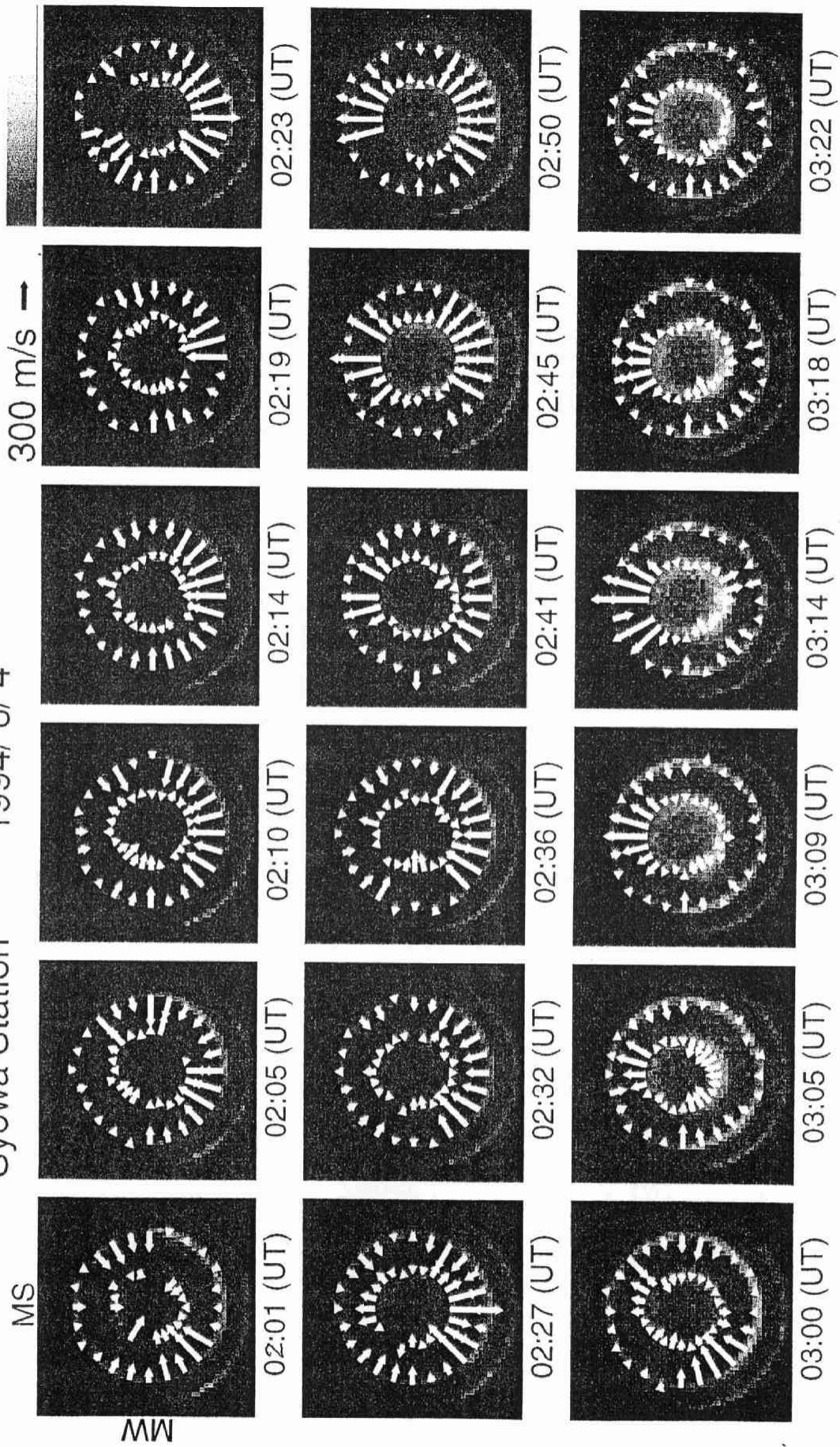


Line-of-sight neutral wind velocities and auroral fringes measured by the OI630.0 nm emission line



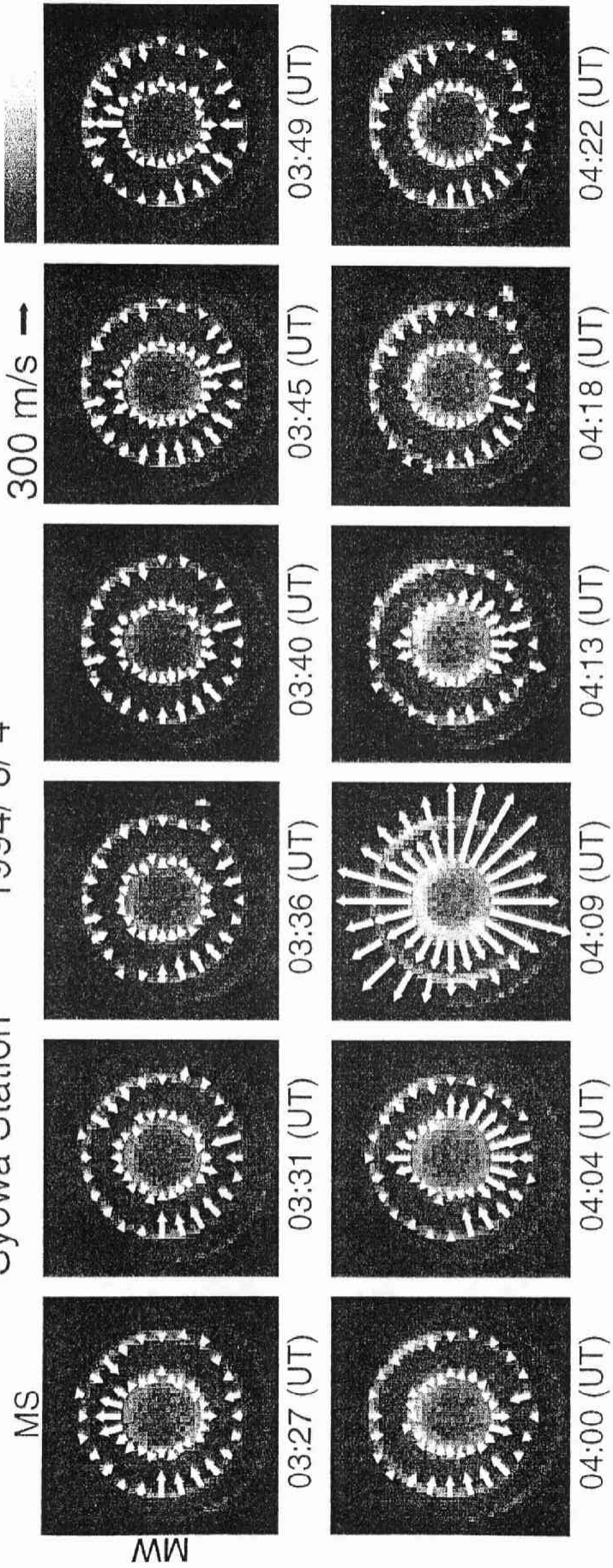
Line-of-sight neutral wind velocities and auroral fringes measured by the OI630.0 nm emission line

Syowa Station 1994/ 6/ 4



Line-of-sight neutral wind velocities and auroral fringes measured by the OI630.0 nm emission line

Syowa Station 1994/6/4



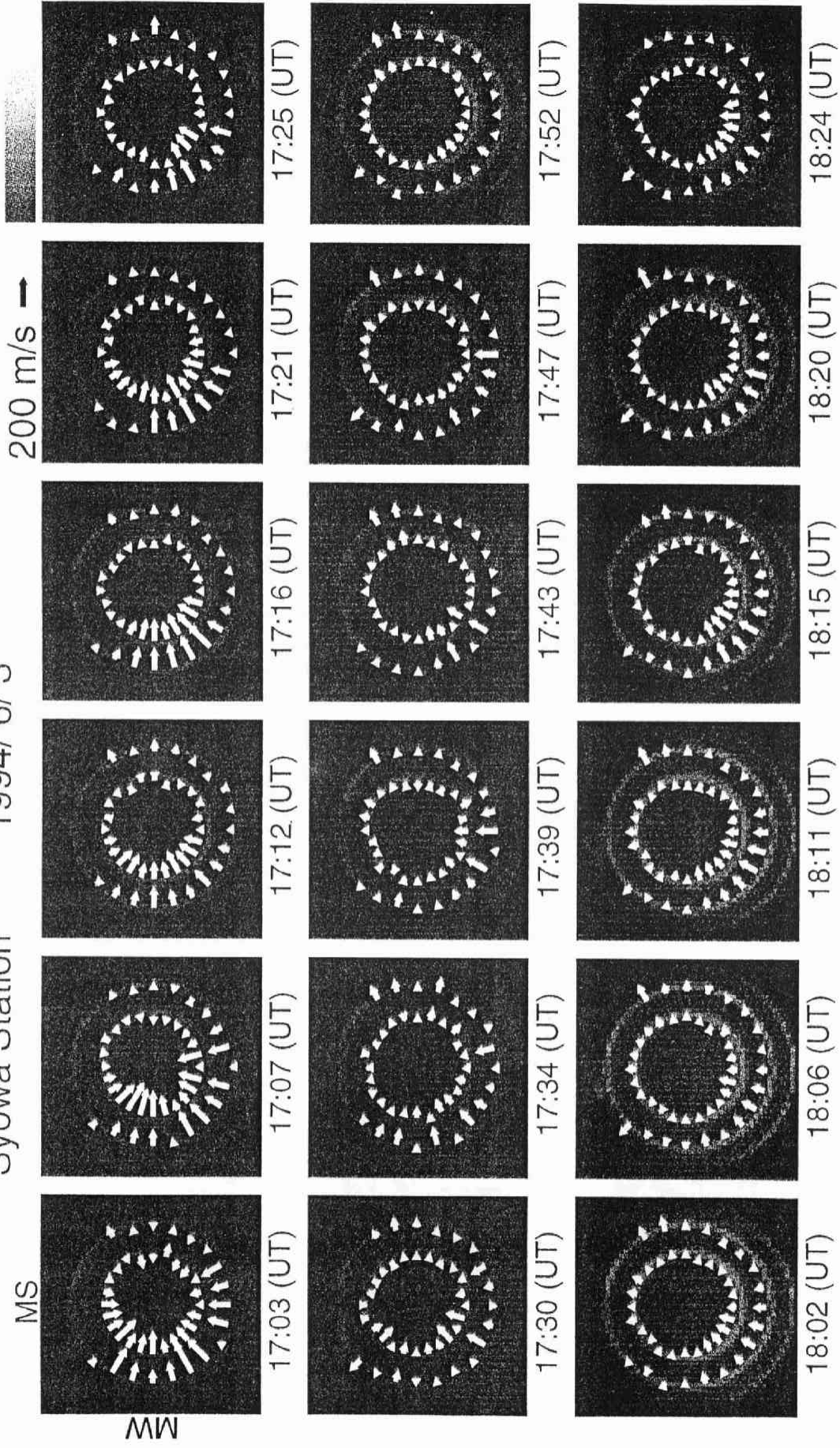
Appendix B

Sequential wind data in the E-region

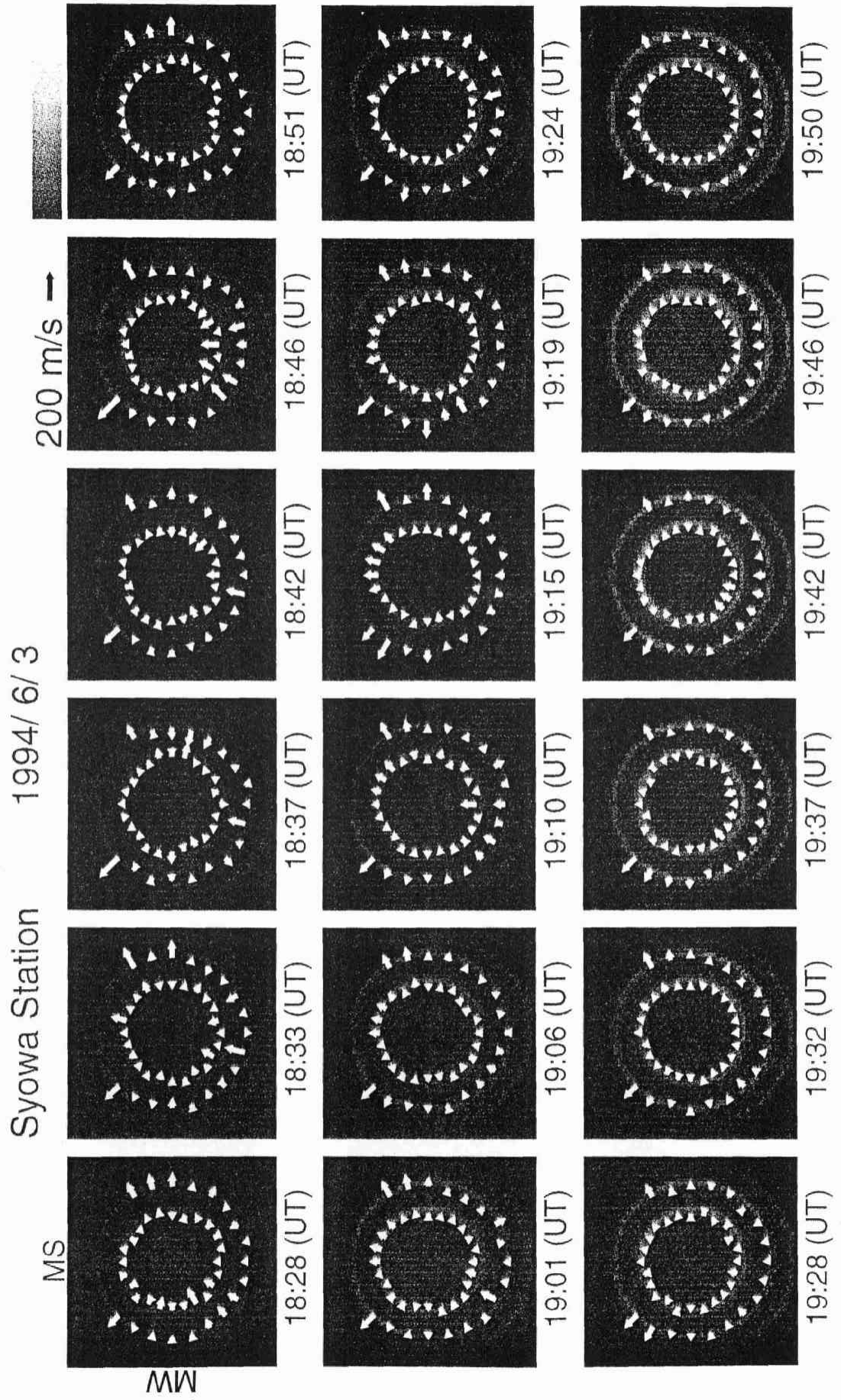
We present sequential wind data in the E-region and OI557.7 nm fringe images between 1703 UT and 0425 UT on the night of 3-4 June 1994. These data were obtained by measurements of the OI557.7 nm emission line using the FPDIS at Syowa station, Antarctica. Each panel shows the line-of-sight wind velocity distributions in 24 directions superposed on the OI557.7 nm emission fringes. The top of the panel is magnetic south and the left is magnetic west, and the time at the midst of exposure is denoted under the panel.

Line-of-sight neutral wind velocities and auroral fringes measured by the OI557.7 nm emission line

Syowa Station 1994/ 6/ 3

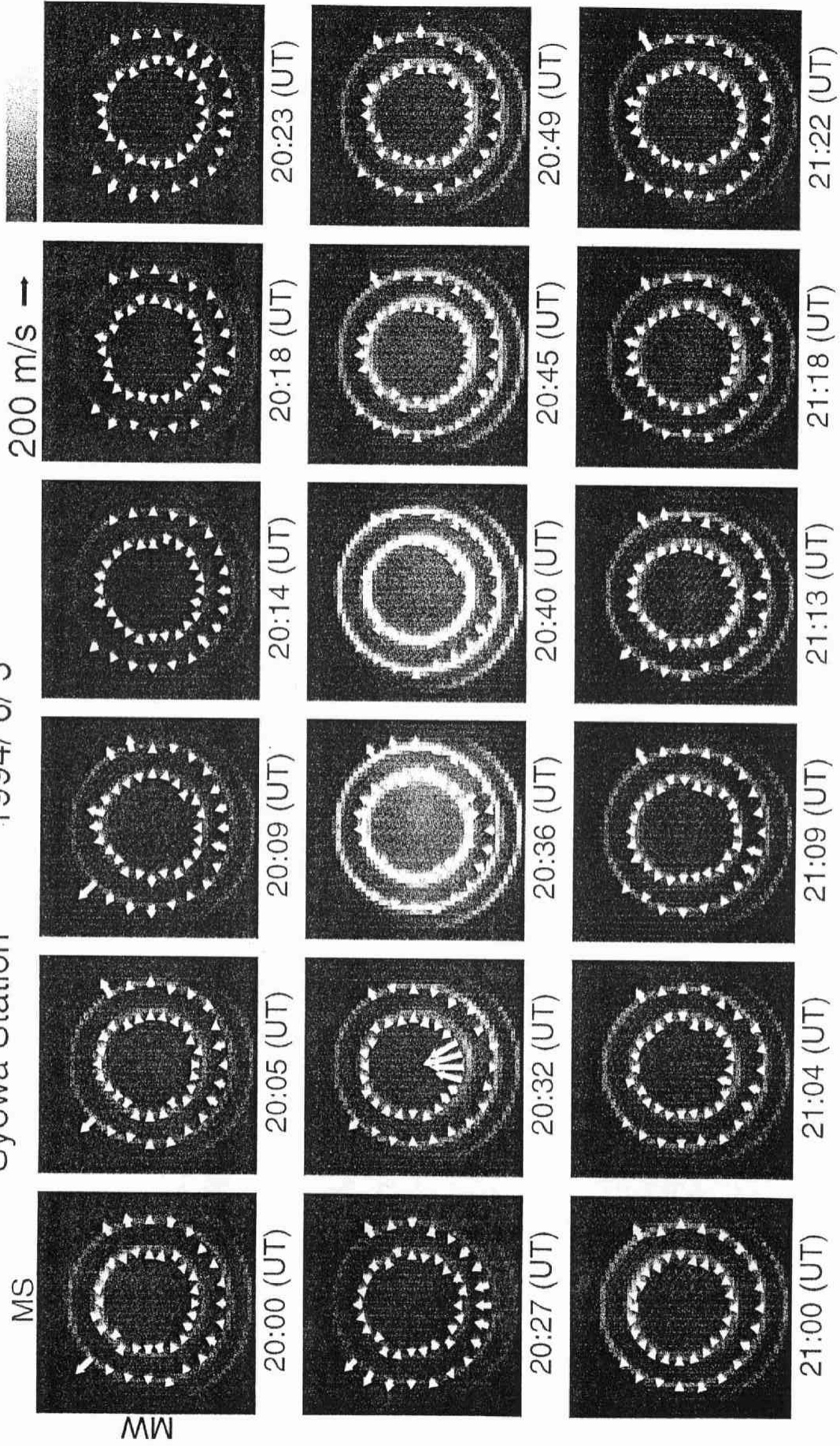


Line-of-sight neutral wind velocities and auroral fringes measured by the OI557.7 nm emission line

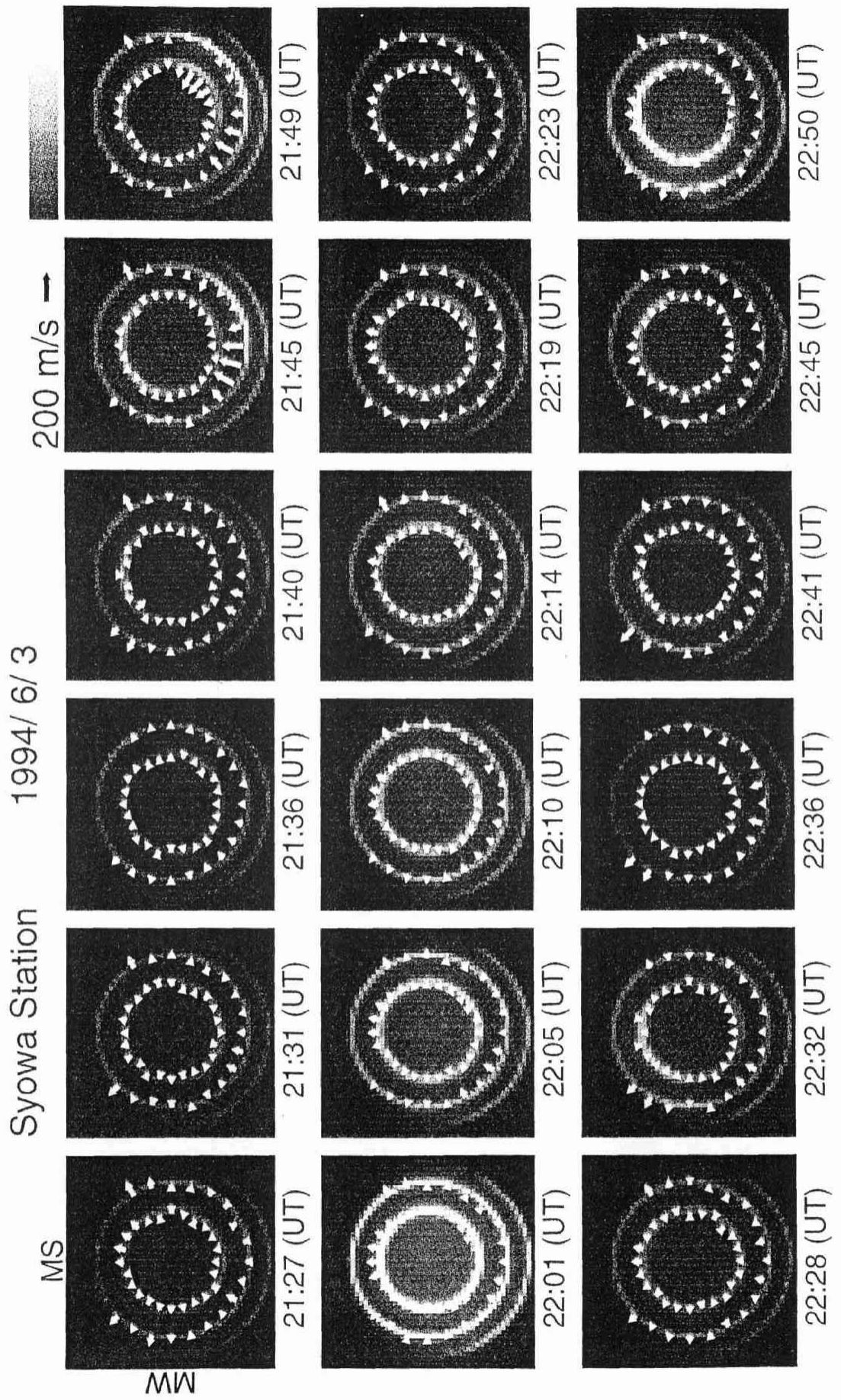


Line-of-sight neutral wind velocities and auroral fringes measured by the OI557.7 nm emission line

Syowa Station 1994/6/3

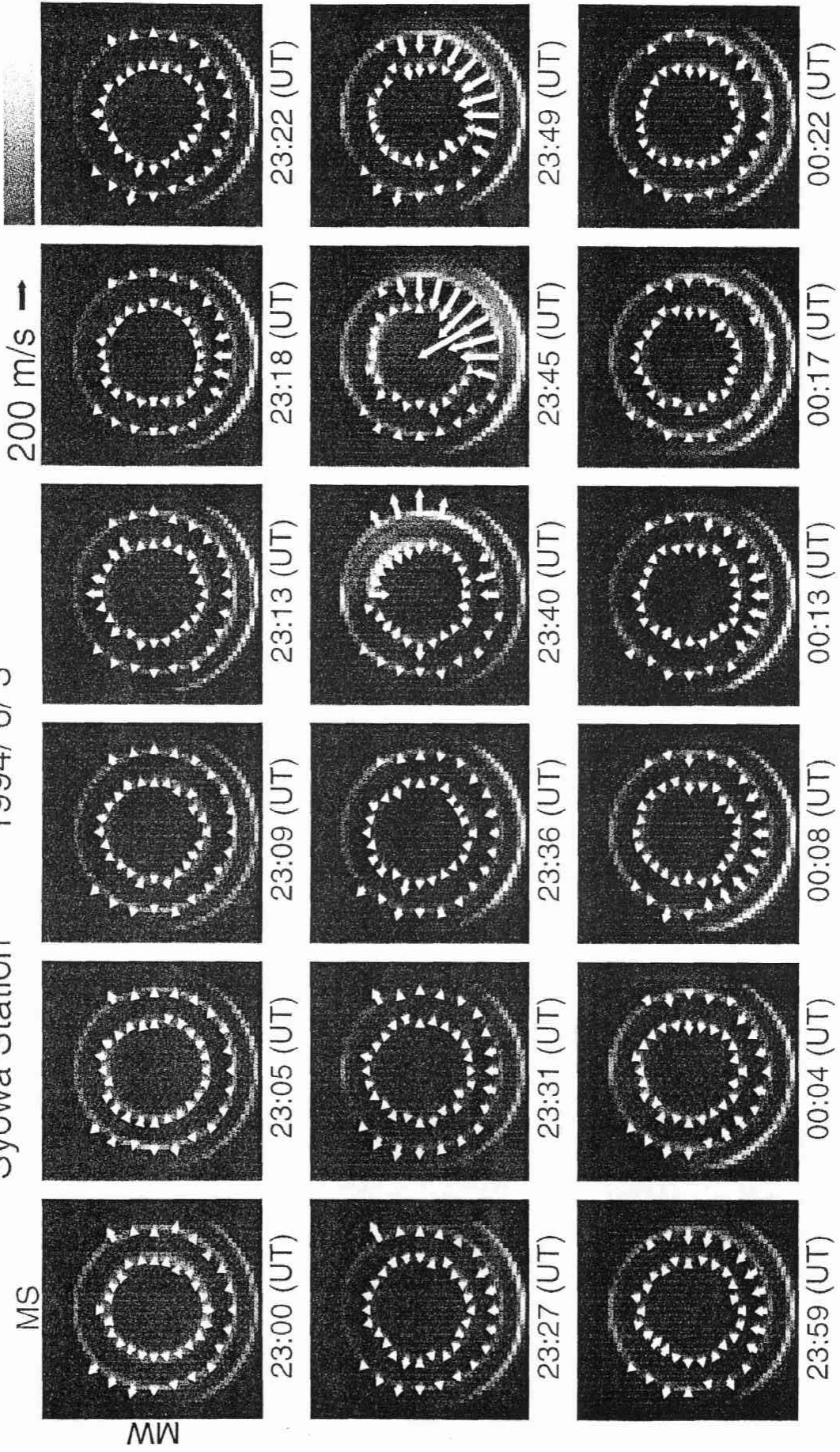


Line-of-sight neutral wind velocities and auroral fringes measured by the OI557.7 nm emission line

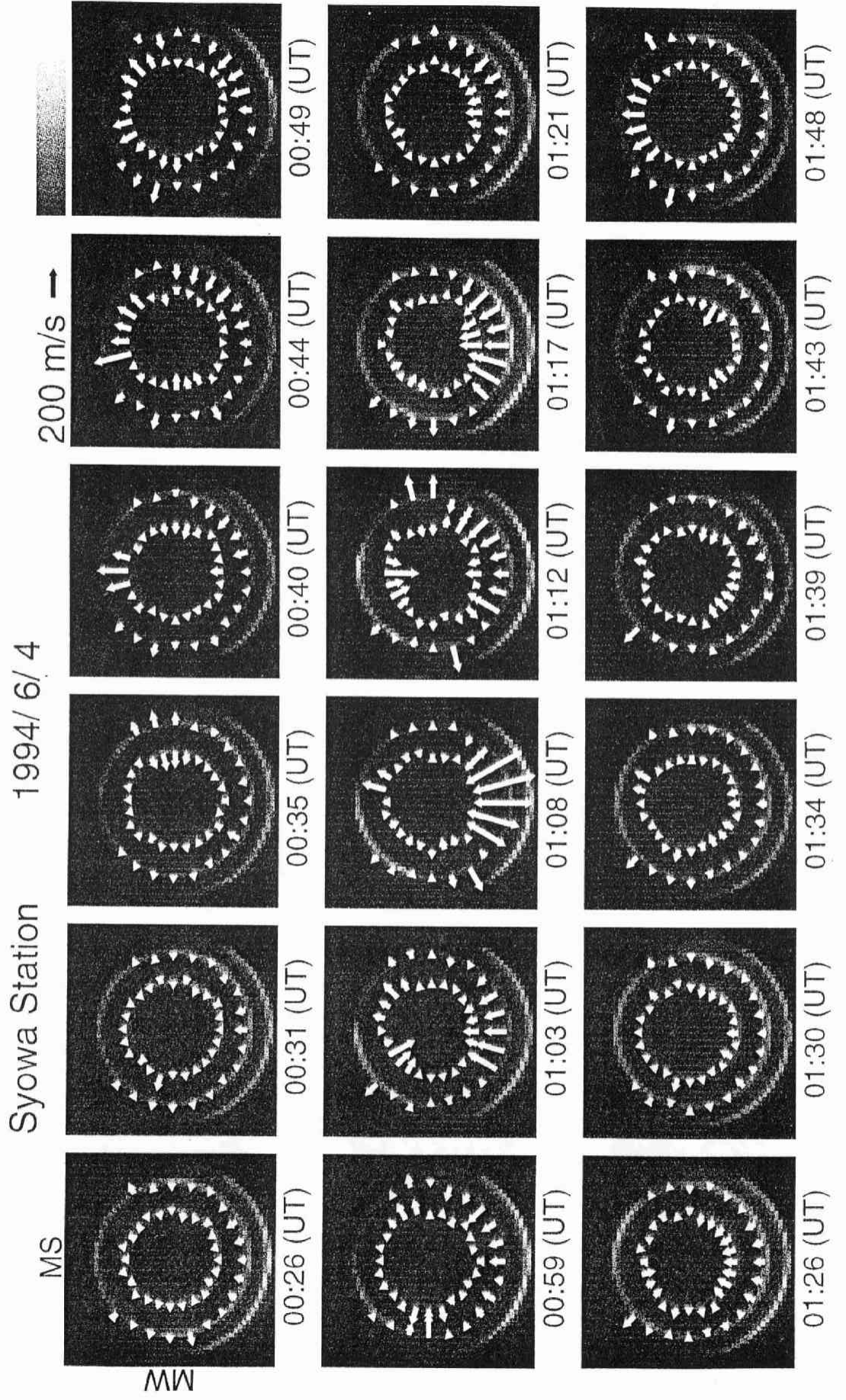


Line-of-sight neutral wind velocities and auroral fringes measured by the OI557.7 nm emission line

Syowa Station 1994/ 6/ 3

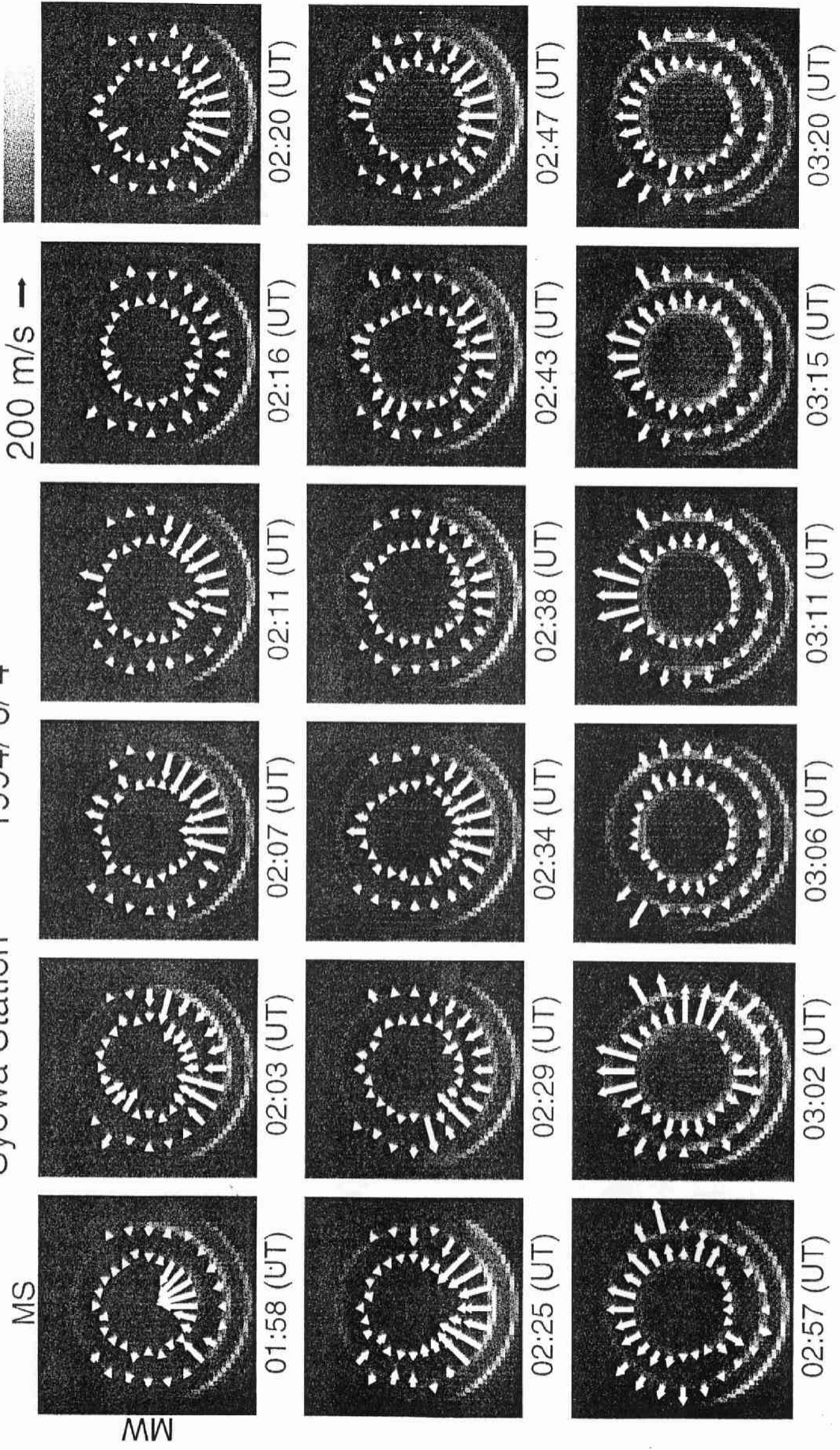


Line-of-sight neutral wind velocities and auroral fringes measured by the OI557.7 nm emission line



Line-of-sight neutral wind velocities and auroral fringes measured by the OI557.7 nm emission line

Syowa Station 1994/ 6/ 4



Line-of-sight neutral wind velocities and auroral fringes measured by the OI557.7 nm emission line.

